Aix*Marseille université
Socialement engagée

NNT : 2023AIXM0001

THÈSE DE DOCTORAT

Soutenue à Aix-Marseille Université
le 22 Février 2024 par

Srijoyee DATTA

Titre de la thèse :
Fabrication laser de nanostructures périodiques dans la silice fondue par faisceau de Bessel segmenté ultrabref

Discipline
Physique et Sciences des Matériaux

Spécialité
Optique, Photonique et Traitement d'Image

École doctorale
(ED 352) Physique et Sciences des Matériaux

Laboratoire/Partenaires de recherche
Laboratoire LP3

Composition du jury

Inka MANEK - HöNNINGER Université de Bordeaux, Laboratoire CELIA	Rapporteure
Cyril MAUCLAIR Université Jean-Monnet, Saint-Étienne, Laboratoire Hubert Curien	Rapporteur
Aurélie JULLIEN Université Côte d'Azur, Laboratoire INPHYNI	Présidente du jury
Olivier UTéZA Aix-Marseille University, Laboratoire LP3	Directeur de thèse
Nicolas SANNER Aix-Marseille University, Laboratoire LP3	Co-directeur de thèse

LP3

Affidavit

Je soussigné, Srijoyee Datta, déclare par la présente que le travail présenté dans ce manuscrit est mon propre travail, réalisé sous la direction scientifique de Olivier Utéza et Nicolas Sanner, dans le respect des principes d'honnêteté, d'intégrité et de responsabilité inhérents à la mission de recherche. Les travaux de recherche et la rédaction de ce manuscrit ont été réalisés dans le respect à la fois de la charte nationale de déontologie des métiers de la recherche et de la charte d'Aix-Marseille Université relative à la lutte contre le plagiat.

Ce travail n'a pas été précédemment soumis en France ou à l'étranger dans une version identique ou similaire à un organisme examinateur.

Fait à Marseille le 11 Décembre, 2023.



Cette œuvre est mise à disposition selon les termes de la Licence Creative Commons Attribution - Pas d'Utilisation Commerciale - Pas de Modification 4.0 International.

List of publications and participation in conferences

List of Publications

1. S. Datta, R. Clady, O. Utéza, N. Sanner, “Direct bulk laser-machining of scalable nanochannel assemblies for fabricating integrated metaphotonic structures inside glass” submitted to Laser & Photonics Reviews. => following recommendation of Editor, we are currently revising the manuscript before resubmitting.

2. S. Datta, R. Clady, O. Utéza, N. Sanner, “Submicron-spaced ultradeep nanohole arrays on glass machined by ultrafast laser ablation”, in preparation.

List of Conferences

Accepted Oral Presentations

1. S Datta, R Clady, O Utéza, N Sanner, Laser-fabrication of submicrometer periodic structures in the bulk of fused silica, Photonics West 2023, LAMOM, Jan 28 – Feb 02, 2023, San Francisco, USA.

2. S. Datta, R. Clady, O. Utéza, and N. Sanner. Laser machining of sub-micrometric-pitch structures with a truncated ultrafast Bessel beam in the bulk of fused silica. CLEO/Europe 2023, Paper CM-3.4, 26-30 June 2023, Munich, Germany.

Contributed International & National Conferences

1. N. Sanner, X. Liu, S. Datta, R. Clady, O. Utéza, Engraving depth-controlled nanohole arrays at the surface of glass by tailored laser beam processing, Photonics West 2022, LASE, San Francisco, USA, 22–27 January 2022 (online).
2. N. Sanner, X. Liu, S. Datta, R. Clady, O. Utéza, Processing arrays of deep nanoholes at the surface of glass by short-length micro-Bessel beams, 9th European Conference on Applications of Femtosecond Lasers in Materials Science - Femtomat 2022, Mauterndorf, Salzburg, Austria. 14-16 March 2022.
3. N. Sanner, X. Liu, S. Datta, R. Clady, O. Utéza, Processing arrays of deep nanoholes at the surface of glass by short-length micro-Bessel beams, 29th International Conference on Advanced Laser Technologies, ALT’22, Arcachon, France, 11-16 September 2022.
4. N. Sanner, X. Liu, S. Datta, R. Clady, O. Utéza, Single-step laser-fabrication of arrays of deep holes of submicrometer diameter on dielectrics surface, Photonics West 2023, LASE, Jan 28 – Feb 02, 2023, San Francisco, USA.

5. N. Sanner, X. Liu, S. Datta, R. Clady, O. Utéza, “Writing nanohole arrays with controllable depth in fused silica by ultrafast laser ablation”, MNA 2022 (Meeting on Nanosciences Advances), Porquerolles, 22 au 29 Sept. 2022.
6. N. Sanner, X. Liu, S. Datta, R. Clady, O. Utéza, Faisceaux de Bessel tronqués pour la fabrication de matrices de nanotrous profonds, LaserAP 2022, Semur-en-Auxois, 10-14 octobre 2022.

Proceedings

1. N. Sanner, X. Liu, S. Datta, R. Clady, O. Utéza, Engraving depth-controlled nanohole arrays at the surface of glass by tailored laser beam processing, Proc. SPIE Nanoscale and Quantum Materials : From Synthesis and Laser Processing to Applications, paper PC1199007.
2. N. Sanner, X. Liu, S. Datta, R. Clady, O. Utéza, Processing arrays of deep nanoholes at the surface of glass by short-length micro-Bessel beams, 9th European Conference on Applications of Femtosecond Lasers in Materials Science - Femtomat 2022.
3. N. Sanner, X. Liu, S. Datta, R. Clady, O. Utéza, Processing arrays of deep nanoholes at the surface of glass by short-length micro-Bessel beams, 29th International Conference on Advanced Laser Technologies, ALT’22.
4. N. Sanner, X. Liu, S. Datta, R. Clady, O. Utéza, “Writing nanohole arrays with controllable depth in fused silica by ultrafast laser ablation”, MNA 2022 (Meeting on Nanosciences Advances), Porquerolles, 22 au 29 Sept. 2022.
5. N. Sanner, X. Liu, S. Datta, R. Clady, O. Utéza, Faisceaux de Bessel tronqués pour la fabrication de matrices de nanotrous profonds, LaserAP 2022, Semur-en-Auxois, 10-14 octobre 2022.
6. N. Sanner, X. Liu, S. Datta, R. Clady, O. Utéza, Single-step laser-fabrication of arrays of deep holes of submicrometer diameter on dielectrics surface, Proc. SPIE 2023, Nanoscale and Quantum Materials : From Synthesis and Laser Processing to Applications 2023, paper PC1241002.
7. S. Datta, R Clady, O Utéza, N Sanner, Laser-fabrication of submicrometer periodic structures in the bulk of fused silica, Proc. SPIE 2023, Laser Applications in Microelectronic and Optoelectronic Manufacturing (LAMOM) XXVIII, paper PC1240808.
8. S. Datta, R. Clady, O. Utéza, and N. Sanner. Laser machining of sub-micrometric-pitch structures with a truncated ultrafast Bessel beam in the bulk of fused silica. CLEO/Europe 2023, Paper CM-3.4.

Participation in Seminar

— Internal seminar on the topic of "Towards the laser-fabrication of nanostructures in dielectrics by customized Bessel beams", LP3, 5/4/2022.

Résumé

L'ablation directe par laser femtoseconde est un outil prometteur pour fabriquer des composants nanométriques pour la mise au point de circuits intégrés photoniques. Il est cependant nécessaire de développer cette technique pour conduire à l'obtention de caractéristiques d'une qualité similaire à celles obtenues avec les techniques lithographiques traditionnelles. Pour cela, une approche de mise en forme de faisceau laser innovante a été développée pour générer un faisceau de Bessel segmenté. Cela nous a permis de fabriquer des nanocanaux de longueur contrôlée à la surface et dans le volume d'un matériau diélectrique. L'étude démontre ainsi la structuration des surfaces avant et arrière de la silice fondue avec une périodicité spatiale sub-micrométrique ajustable. Travailler en face arrière du matériau se révèle aussi plus favorable à la fabrication de nanocanaux de haute qualité. En ajustant la durée et l'énergie de l'impulsion laser, l'écriture de nanocanaux dans le matériau est ensuite étudiée, démontrant des réseaux avec un pas aussi petit que 0,7 μm, adaptés aux composants photoniques dans la plage spectrale de l'infrarouge moyen. Pour preuve de principe, des motifs sont fabriqués pour imiter des dispositifs à cristaux photoniques tels que des guides d'ondes, des coupleurs en Y et des structures métaphotoniques. Les calculs d'indice numérique efficace suggèrent que les structures métaphotoniques peuvent fonctionner comme un gradient de composantes d'indice, manipulant la phase optique du faisceau incident avec un changement de $\frac{\pi}{2}$. Cela démontre l'applicabilité potentielle des structures fabriquées pour manipuler les phases optiques dans les dispositifs photoniques.

Mots clés : Usinage laser ultrarapide, Mise en forme de faisceau, Écriture laser directe, Cristaux Photoniques et Métamatériaux, Structuration sub-micrométrique.

Abstract

Direct femtosecond laser ablation is a promising tool used for fabricating micrometric components required for developing photonic integrated circuits. Its further optimization can achieve sub-micrometric features with quality similar to those obtained with traditional lithographic techniques. This research presents an optimized femtosecond laser ablation technique for creating micro and sub-micrometric photonic structures. A dedicated beam-shaping configuration has been developed to generate a segmented Bessel beam. This allowed us a length-controlled fabrication of single-shot nanochannels on the surface and in the bulk of dielectrics. The study successfully demonstrates the structuring of the front and rear surfaces of fused silica, analyzing hole-like structures with varying spatial periodicity. We identify the rear surface configuration as a better strategy for the fabrication of high-quality nanochannels. Channels are then machined in the bulk of fused silica by adjusting laser pulse duration and energy, demonstrating arrays with a pitch as small as 0.7 μm, suitable for writing photonic components in the mid-infrared (MIR) spectral range. As a proof-of-principle, embedded patterns are fabricated to mimic photonic-crystal devices like waveguides, Y-couplers, and metaphotonic structures. Numerical effective index calculations suggest that the meta-photonic structures can function as a gradient of index components, manipulating the optical phase of the incident beam with a phase change of $\frac{\pi}{2}$. This demonstrates the potential applicability of the fabricated structures for manipulating optical phases in photonic devices.

Keywords: Ultrafast laser machining, Beam shaping, Direct laser writing, Photonic crystals and Metamaterials, Sub-micrometric structuring.

Synopsis

De par les propriétés non linéaires uniques induites lors de l'interaction laser-matière, l'usinage par laser femtoseconde est incontournable pour réaliser un dépôt d'énergie précis permettant d'obtenir des modifications contrôlées et calibrées à la surface ou à l'intérieur d'un matériau. Cette capacité a contribué de manière significative à la miniaturisation des fonctionnalités de la micro-électronique et de la photonique, un aspect crucial pour la croissance de l'industrie et des technologies optiques avancées. À mesure que l'accent se déplace vers le remplacement des composants électroniques par des composants photoniques, la demande de fabrication pour des composants photoniques de dimension caractéristiques micro et nanométriques, tels que guides d'ondes, coupleurs, réseaux, lentilles et autres éléments micro-optiques, a considérablement augmenté. Les méthodes lithographiques traditionnelles permettent de façonner la matière à ces échelles extrêmement petites mais elles souffrent d'inconvénients comme le fait d'être lentes, coûteuses et insuffisamment agiles pour écrire des structures 3D complexes sur des matériaux divers. L'usinage laser femtoseconde est une technique d'écriture permettant de résoudre ces problèmes en offrant rapidité, flexibilité et capacité à travailler dans des géométries 3D variées sur différents types de matériaux, cette agilité lui étant permise grâce à l'aspect nonlinéaire de l'absorption sous tendu par l'emploi de ce type d'impulsions laser. De plus, cette approche se révèle rentable et respectueuse de l'environnement car elle ne nécessite pas de salle blanche, d'étapes chimiques ou d'environnement sous vide et qu'elle peut aussi être opérée à taux de répétition très élevé (≥MHz). Malgré des progrès significatifs dans l'usinage laser femtoseconde pour les composants micro/nano photoniques, il existe cependant un besoin continu d'améliorer les performances et la robustesse des outils d'usinage laser pour une production de structures miniaturisées (jusqu'au domaine sub-micrométrique) de très haute qualité, intégrables dans des systèmes photoniques viables et performants. En particulier, une brique de base pour la réalisation de composants photoniques (ainsi pour des métamatériaux optiques ou cristaux photoniques) implique la manipulation de la permittivité diélectrique aux échelles sub-micrométriques (≤ longueur d'onde) à la surface ou en volume d'un matériau, par exemple impliquant la formation de structures périodiques dans le domaine nanométrique. Par exemple, des réseaux de nano-trous, s'étendant sur plusieurs micromètres de profondeur, ont le potentiel pour définir des conceptions et des fonctionnalités dans des structures nanophotoniques. Cependant, y parvenir de manière simple, adaptable et universelle dans divers matériaux n'a pas encore été pleinement démontré par usinage laser femtoseconde. Des résultats prometteurs ont été observés avec des faisceaux de Bessel femtoseconde pour la réalisation précise de nanocanaux. Dans ce travail, nous utilisons ce type de

stratégie de mise en forme spatiale d'un faisceau laser pour progresser vers un outil d'écriture laser capable d'écrire à terme un guide d'onde pouvant être intégré dans un cristal photonique ou de manière générale dans des structures métaphotoniques, qui permettent de manipuler la phase optique d'un faisceau incident avec une précision et une versatilité sans précédent. À cette fin, nous avons tout d'abord construit un dispositif expérimental (voir Figure A) comprenant une méthode de mise en forme spatiale du faisceau par transformation du faisceau gaussien incident de notre système laser (ASUR) en faisceau de type Bessel. Cette mise en forme spatiale permet d'obtenir un avantage décisif en matière d'usinage de gabarit cylindrique contrôlé et de très petite dimension ($\leq 1\ \mu m$), exprimé par son paramètre de longueur "non diffractante" appelée profondeur de champ (DOF) du faisceau. Ce fin pinceau de lumière laser, que l'on obtient par transformation spatiale de type Bessel, est en effet l'outil de choix pour usiner des diélectriques aux échelles sub-micrométriques.

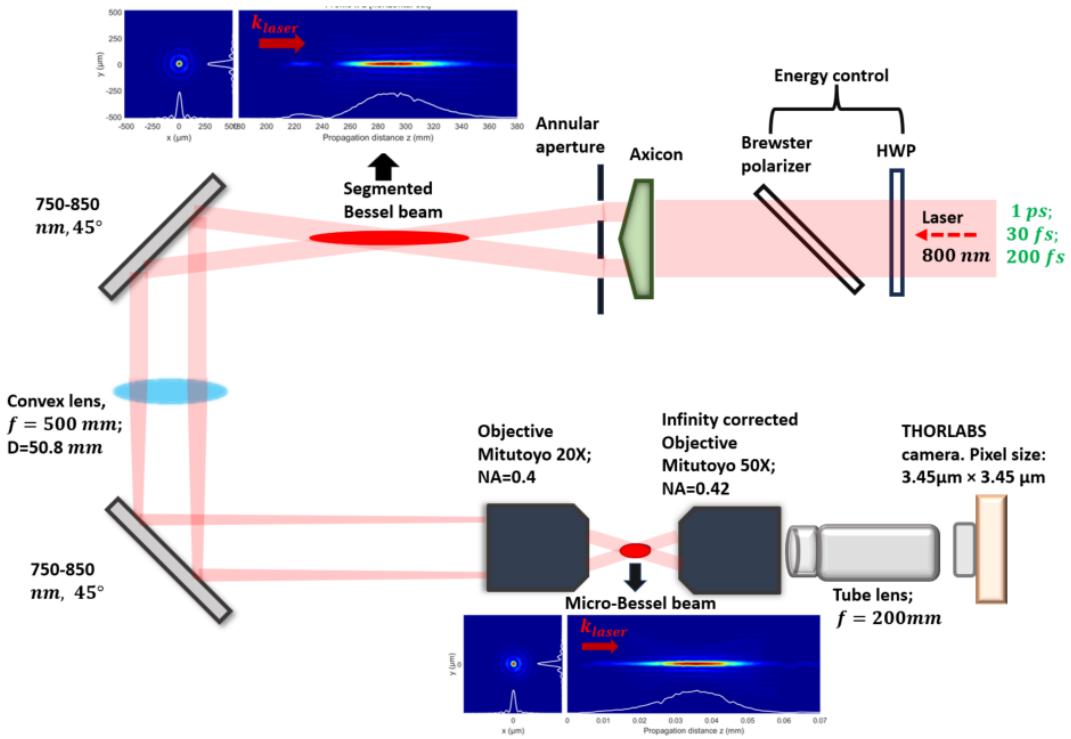

Figure A – Schéma du montage expérimental montrant le dispositif de mise en forme Bessel du faisceau laser femtoseconde ASUR s'appuyant sur un axicon d'angle de base de 1°. La configuration de dé-magnification (× 1/50) composée d'une lentille de 500 mm et un objectif $20X$ permet de former un micro-faisceau de Bessel sur la cible. Le faisceau est imagé avec un système télescopique composé d'un objectif $50X$ et d'une lentille tube de 200 mm ainsi que d'une caméra Thorlabs pour la détection.

D'un point de vue expérimental, nous avons utilisé un axicon avec un angle de base de 1° pour générer un faisceau de Bessel avec une longueur non-diffractante

(DOF) de ~30 cm (avant démagnification). Pour augmenter les capacités de cette technique de mise en forme, nous avons placé une ouverture annulaire devant l'axicon pour créer un faisceau Bessel segmenté. Cela permet de mettre en forme la longueur non-diffractante du faisceau de Bessel (ajustement de la DOF, positionnement et obtention d'un ou plusieurs segments selon l'axe optique, etc.) sans sacrifier sa distribution d'intensité transverse (largeur du faisceau inchangée) et d'introduire ainsi un paramètre de sélectivité pour augmenter les caractéristiques de cette méthode d'usinage comme le montre la Figure B. Ainsi, par exemple en modifiant le positionnement de l'ouverture (d'une largeur constante) devant l'axicon, nous sommes capables d'usiner à n'importe quelle profondeur un bloc de silice fondue.

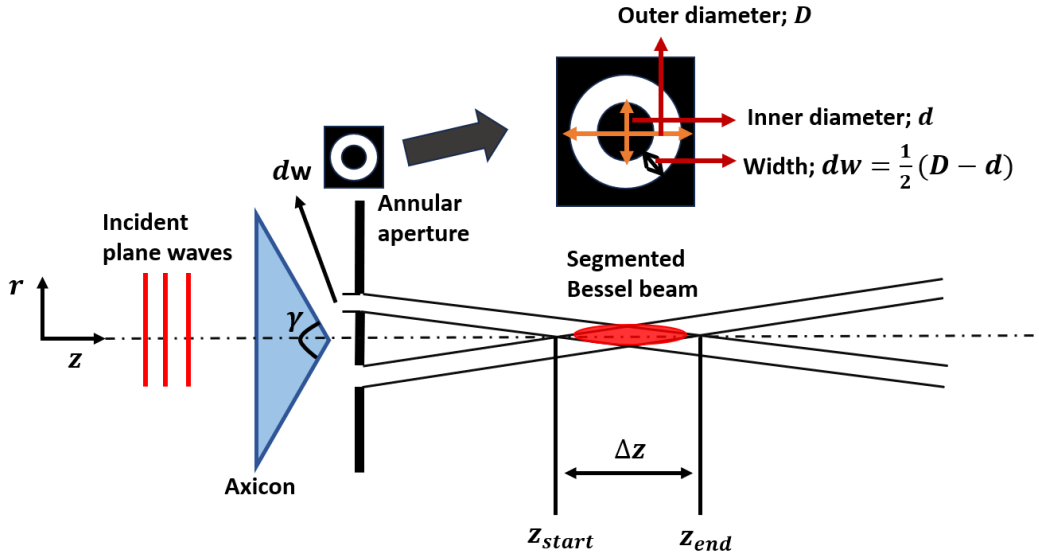

Figure B – Principe schématique d'un faisceau de Bessel segmenté obtenu à l'aide d'un anneau d'ouverture de largeur dw. L'angle de l'axicon est γ. L'ouverture annulaire à l'avant de l'axicon restreint la région du faisceau de Bessel de telle sorte que nous obtenons une région de faisceau de Bessel segmentée plus petite Δz, se positionnant à la coordonnée de l'axe optique Z_{start} jusqu'à Z_{end}.

Afin d'obtenir un contrôle le plus précis possible sur ce faisceau d'écriture, nous avons étudié le faisceau de Bessel segmenté en caractérisant la propagation du faisceau (à la fois expérimentalement et numériquement) à travers différentes caractéristiques d'ouverture annulaire (largeurs et positionnement de l'anneau par rapport au faisceau incident Gaussien). Nous avons identifié la largeur d'ouverture de 600 μm (avec un positionnement des rayons Interne/Externe en mode 2/3,2 mm par rapport au centre du faisceau et du prisme), comme étant la caractéristique optimale pour avoir un paramètre DOF favorable pour atteindre un très petit rapport d'aspect (~ 1:10 avec un diamètre transverse du faisceau de Bessel < 1 μm) pour les structures usinées. Le rapport d'aspect est le rapport entre le diamètre et la longueur du canal.

Par ailleurs, la littérature a montré que ce rapport largeur/hauteur dans la gamme 1-10 est adapté à l'usinage de structures photoniques et de type métamatériaux. Le système de dé-magnification $4f$ (composé d'une lentille de 500 mm et d'un objectif $20X$) placé après la mise en forme du faisceau système (voir Figure A) conduit ensuite à un faisceau de Bessel, mesuré avec une taille transverse de 0,96 µm et un DOF de ~15 μm par le système d'imagerie installé sur notre dispositif expérimental (voir Figure A).

Nos premières démonstrations (chapitre 3) ont consisté tout d'abord à usiner la surface d'un échantillon de silice fondue avec une longueur d'onde de 800 nm et une durée d'impulsion de 1 ps (le faisceau d'ASUR de durée nominale de 25 fs étant étiré par dérèglement du compresseur), comme indiqué dans la Figure C.

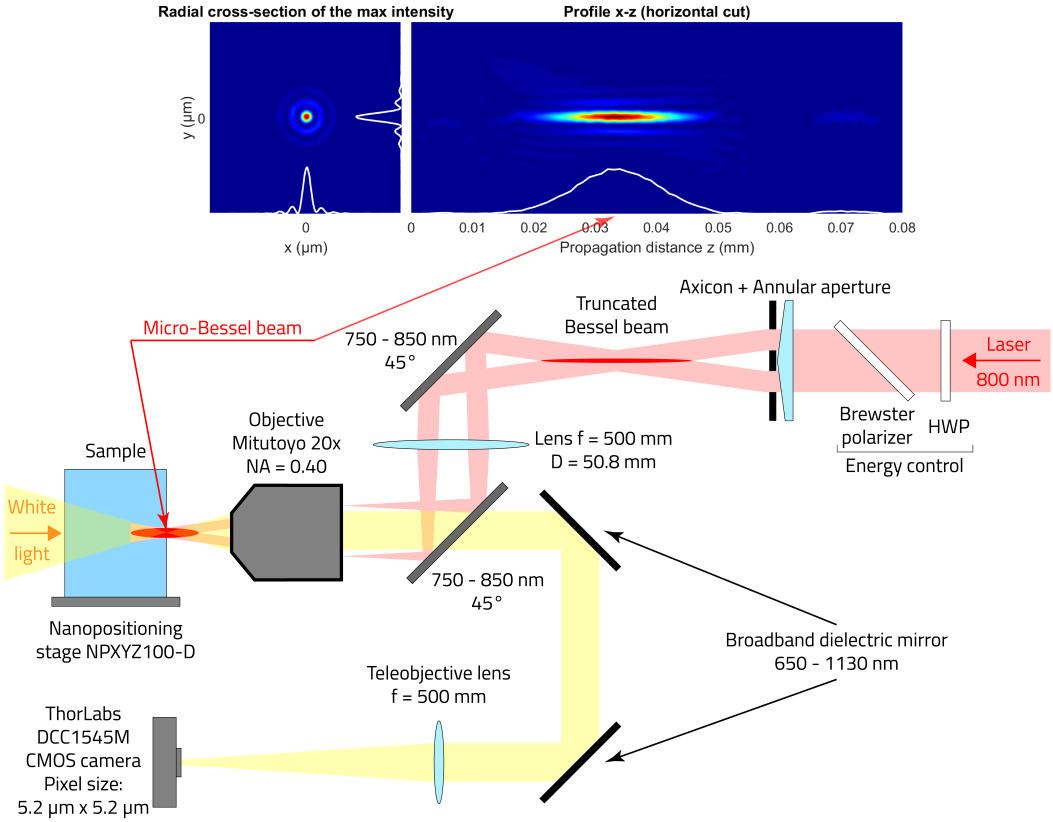

Figure C – Montage expérimental montrant la configuration expérimentale d'usinage et d'imagerie in-situ pour imager la surface de l'échantillon pendant le traitement laser.

Notre travail vise tout d'abord à réduire la périodicité spatiale d'écriture dans la gamme submicronique. Lors de l'usinage de la surface, outre l'obtention d'une telle périodicité, le défi est aussi d'obtenir des profils de canaux adjacents parfaitement cylindriques, avec un diamètre d'ouverture de haute qualité et de calibrer ces caractéristiques pour différentes énergies d'impulsion. Pour atteindre une qualité et une efficacité supérieures, nous mettons l'accent sur l'obtention de telles structures

élémentaires en un seul tir laser. Les résultats d'une première étude pour déterminer l'évolution de la plus petite périodicité spatiale possible des canaux en fonction de l'énergie des impulsions est présentée sur la Figure D.

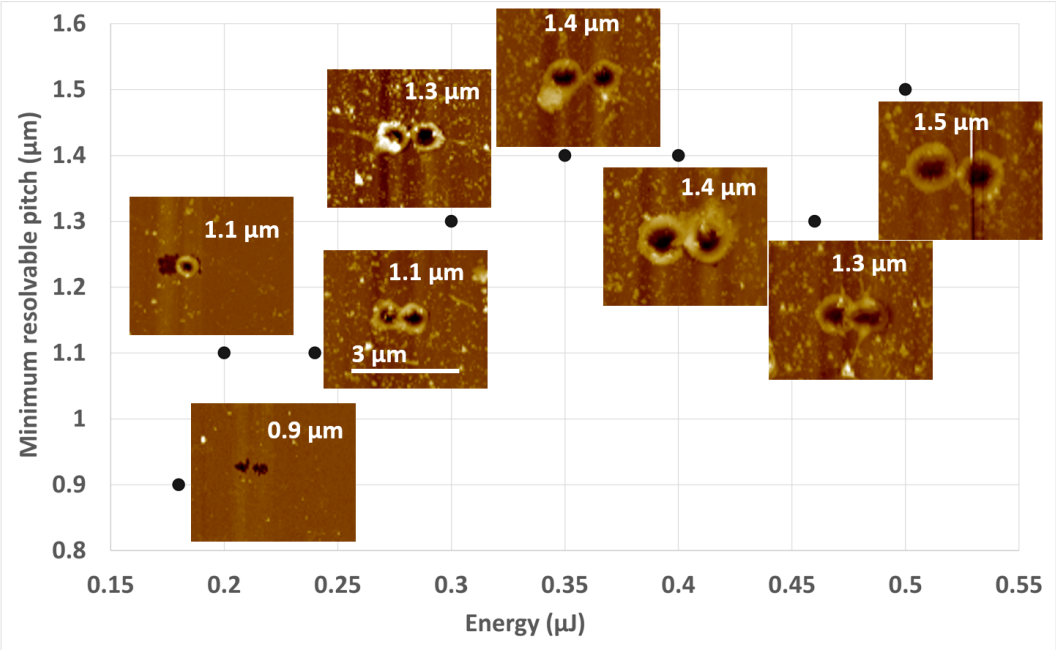

Figure D – Evolution de la résolution spatiale accessible en fonction de l'énergie. La résolution spatiale accessible est déterminée par l'écriture de motifs adjacents identiques (sans recouvrement).

Cette étude confirme qu'un pas de résolution spatiale submicronique (0,9 μm) peut être atteint pour une énergie proche du seuil d'ablation (caractéristique que nous déterminons par des méthodes classiques dans chacune de nos conditions d'expérience, exprimée par la suite par le paramètre énergétique E_{th}). Sur la base de cette étude, nous avons ensuite exploré l'usinage des surfaces avant et arrière d'un échantillon de silice fondue pour déterminer si une géométrie d'interaction est plus favorable qu'une autre à l'obtention de nos objectifs de structuration. A partir du pas de 5 μm, nous réduisons progressivement le pas d'écriture vers la plage submicronique (environ 0,9 μm), comme le montre la Figure E. Nous identifions tout d'abord la présence d'un bourrelet (en bords des cratères d'ablation) qui limite l'empilement des nanocanaux au niveau de la surface avec une densité spatiale importante. Nous avons également identifié que la configuration d'irradiation en surface arrière est la plus favorable pour l'empilement de canaux avec une périodicité spatiale sub-micrométrique.

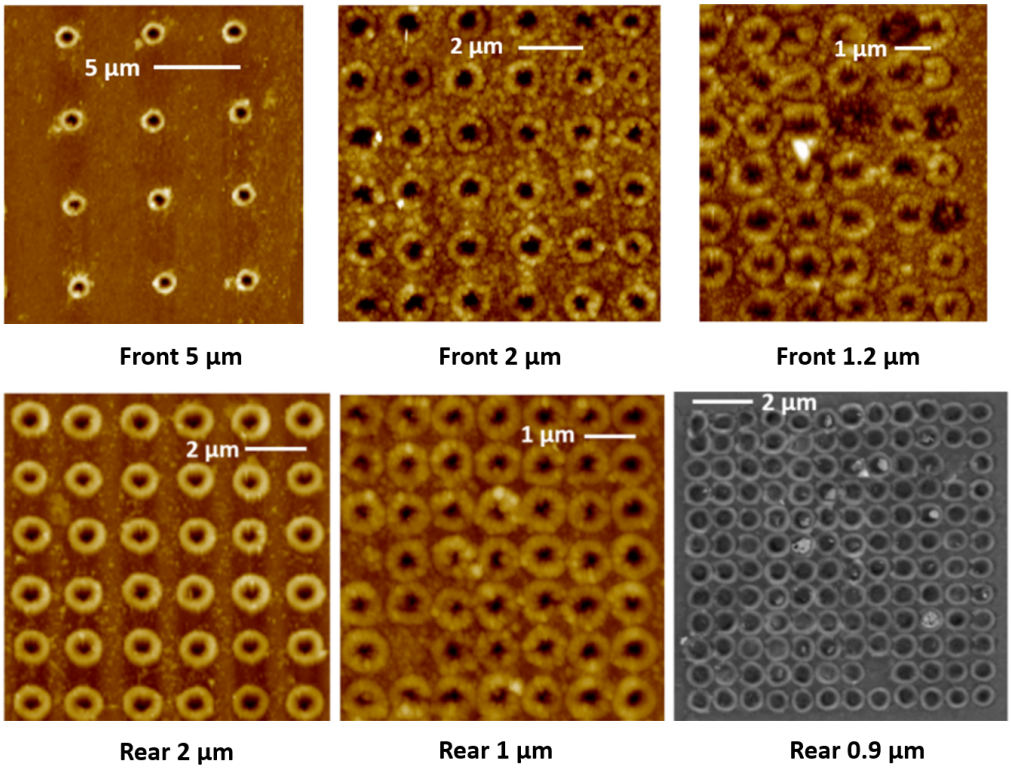

Figure E – (Haut) Usinage de type matriciel de la surface avant de l'échantillon avec un pas de 5 μm à E~0,3 μJ (imagerie AFM) ; avec un pas de 2 μm à E~0,35 μJ ; avec un pas de 1,2 μm à E~0,23 μJ ; (Bas) Usinage de type matriciel de la surface arrière de l'échantillon avec un pas de 2 μm à E~0,55 μJ; avec un pas de 1 μm à E~0,33 μJ; avec un pas de 0,9 μm à E~0,33 μJ (imagerie MEB).

Après la caractérisation des canaux à la surface, notre objectif est aussi d'évaluer leur longueur afin d'être en mesure de définir pleinement aussi leur rapport d'aspect. Pour cela, nous avons besoin de techniques permettant d'accéder à ces canaux en profondeur. Employant la technique de fraisage utilisant un faisceau d'ions focalisé (FIB) en conjonction avec l'analyse SEM pour accéder à l'information requise, nous évaluons la qualité de l'entrée des canaux juste sous la surface, leur longueur, leurs caractéristiques de cylindricité et rugosité de leurs parois latérales et leur séparabilité, permettant ainsi d'évaluer la résolution obtenue. L'analyse FIB-SEM a aussi confirmé que la configuration de la surface arrière est avantageuse pour obtenir des canaux de haute qualité avec un diamètre de canal d'environ 200 nm et une longueur d'environ 5 μm à une énergie proche du seuil (voir Figure F et Figure G).

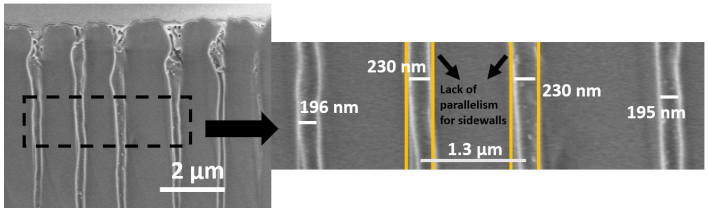

(a) Front face

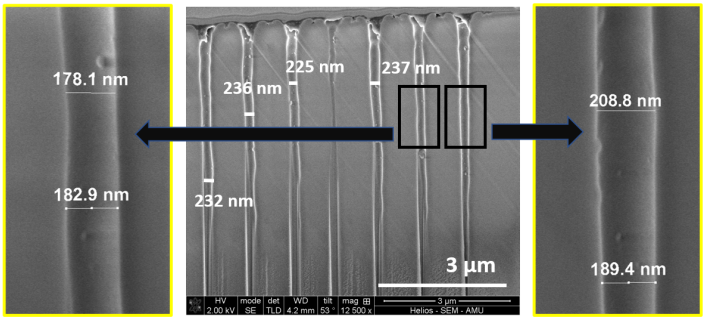

(b) Rear face

Figure F – Profil de canal cylindrique d'un diamètre de ~200 nm pour a) la surface avant et avec un pas de 1,3 μm à E~0,3 μJ et b) pour la configuration d'irradiation en surface arrière avec un pas de 1 μm à E~0,33 μJ. Les canaux obtenus en configuration d'irradiation sur la surface avant n'ont clairement pas de parois latérales et parallèles alors que les résultats obtenus en face arrière sont bien meilleurs.

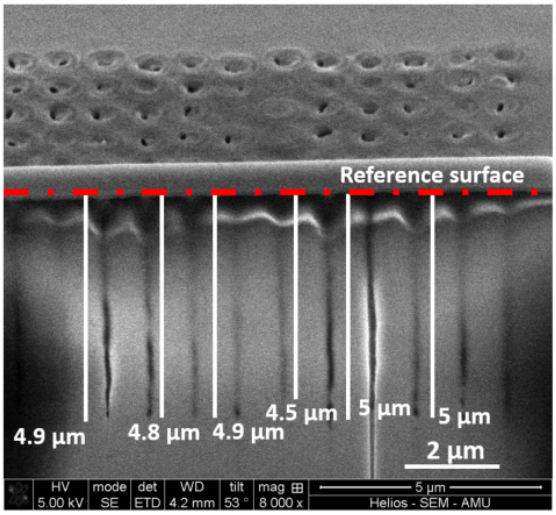

(a) Rear face

Figure G – Longueur des canaux mesurée en transparence obtenue en écriture face arrière ; pas de 1 μm et E~0,33 μJ. Ce mode d'imagerie en transparence permet d'éviter des artefacts d'imagerie (effet de rideau) liée à l'utilisation du mode FIB-SEM et ainsi d'obtenir des résultats robustes et fiables.

En utilisant la technique de caractérisation FIB-SEM, nous avons également analysé des cas de structuration spatiale dense (correspondant à des pas submicroniques comme 0,8 μm et 0,7 μm) obtenus dans la configuration d'irradiation en surface arrière. Cette évaluation vise aussi à comprendre les caractéristiques des canaux sous la surface et à évaluer les performances de très haute résolution spatiale permises par un faisceau de Bessel dans ce régime d'écriture difficile. Nous avons en particulier observé une perturbation de diaphonie induite par les canaux pré-usinés sur les suivants. Les matrices écrites avec des pas inférieurs ou égaux à la longueur d'onde (800 nm) ne sont plus effectivement séparables, comme le montre la Figure H et également la Figure 3.29 du chapitre 3. La diffraction de la lumière joue ici un rôle crucial, indiquant la nécessité d'un espacement minimum d'écriture entre deux canaux adjacents équivalent à la longueur d'onde.

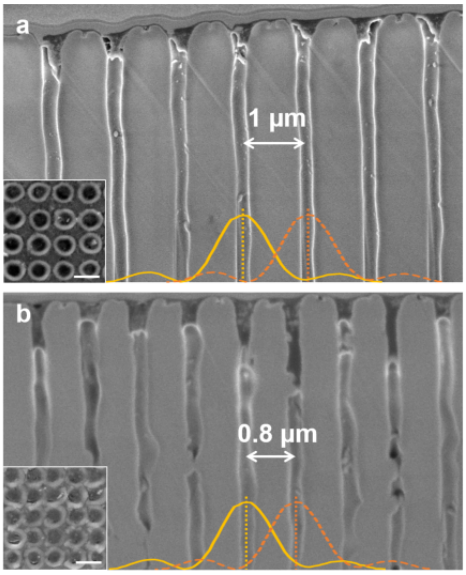

Figure H – Canaux avec un pas de a) 1 μm et b) 0,8 μm à E~0,33 μJ usinés en face arrière.

La partie suivante des travaux (chapitre 4) consiste à usiner un bloc de silice fondue non plus à la surface mais en volume afin d'étudier les caractéristiques de structuration que l'on peut obtenir dans cette configuration. L'objectif principal a été en particulier d'évaluer l'impact de la durée d'impulsion sur l'écriture laser par le faisceau de Bessel. Ceci est motivé par la nécessité de déposer l'énergie de manière non-linéaire dans le volume d'un milieu diélectrique pour le structurer localement. Cependant, cela soulève également des questions sur la propagation non linéaire au sein d'un matériau, phénomène intrinsèquement influencé par la durée de l'impulsion. Pour étudier cela, nous avons réalisé une étude paramétrique d'écriture laser de canaux en volume pour différentes durées d'impulsion de 1 *ps*, 30 *fs* et 200 *fs* (voir Figure I). Les canaux ont été fabriqués en mode mono-coup pour plusieurs pas, à partir de 5 μm et jusqu'à 0,5 μm. L'énergie varie sur une plage allant du seuil ($E_{th} \sim 0{,}2\ \mu J$) à cinq fois le seuil (5 E_{th}).

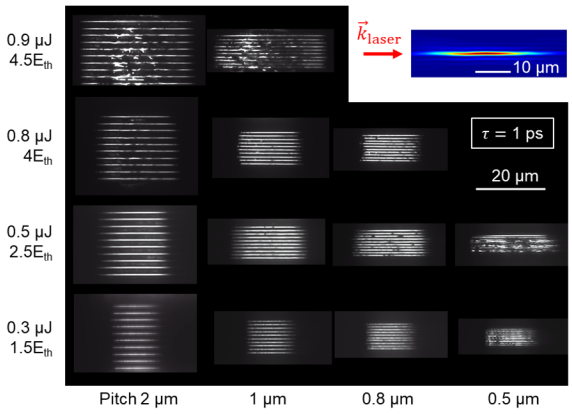

(a) 1 ps

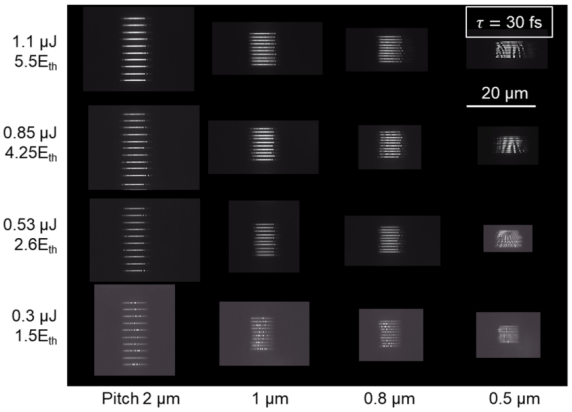

(b) 30 fs

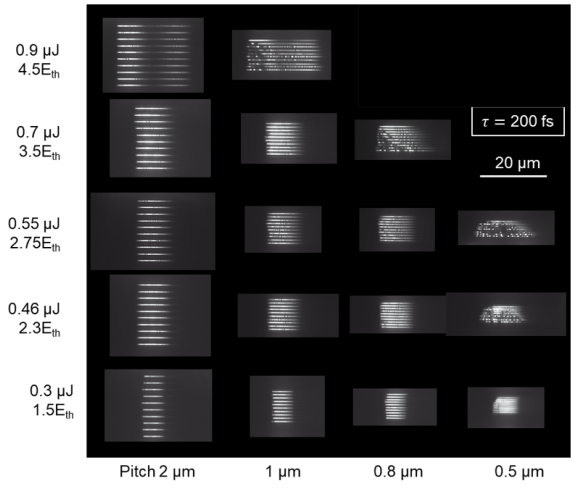

(c) 200 fs

Figure I – Etude paramétrique des canaux en volume pour a)1 ps ; b)30 fs ; c)200 fs. Pour 1 ps, les pas de 0,8 μm et de 0,5 μm n'ont pas été réalisés pour les énergies les plus élevées. La plage d'énergie explorée ici est comprise entre E_{th}=0,25 μJ et $5E_{th}$=1,1 μJ. Le pas a varié de 5 μm à 0,5 μm pour les trois différentes durées.

Cette étude paramétrique réalisée avec des paramètres laser variés (durée d'impulsion, énergie) permet de cerner les potentialités d'écriture laser par faisceau de Bessel ultra-court et de progresser vers un outil polyvalent pouvant fabriquer des structures variées (en particulier dans le domaine sub-micrométrique). La synthèse de ces capacités d'écriture est exprimée dans la Figure J montrant les périodicités spatiales accessibles avec succès et qualité (en vert), simplement en ajustant la durée d'impulsion et/ou l'énergie incidente du faisceau. Ainsi, la plage efficace énergétique pour l'écriture de structures est identifiée vers E $\cong 2E_{th} \sim 0{,}5\ \mu J$.

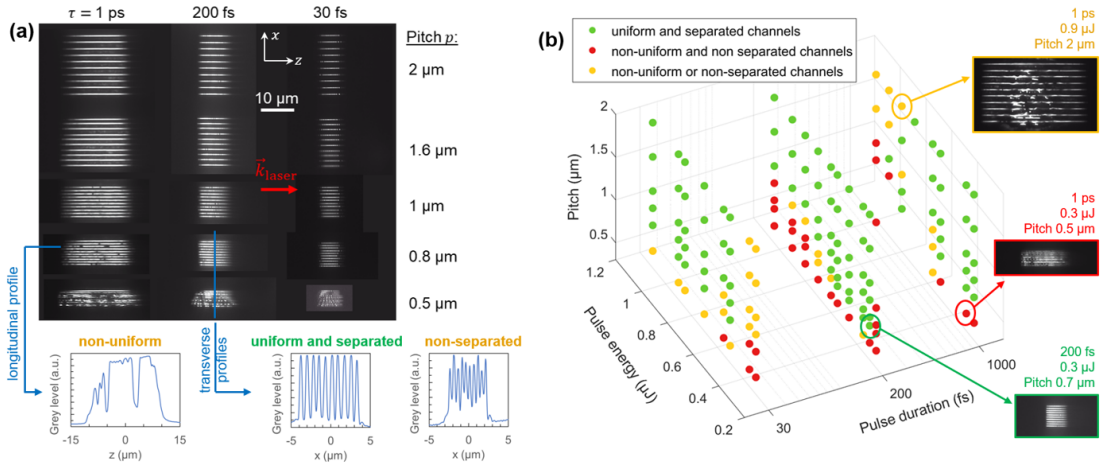

Figure J – Synthèse de l'étude paramétrique pour atteindre des résolutions spatiales d'écriture dans les domaines micrométriques et sub-micrométriques. (a) Série de 10 canaux dans le volume de silice fondue, avec un pas variable (de 2 μm à 0,5 μm) et pour différentes durées d'impulsion. Chaque canal est réalisé par ablation en un seul tir laser, avec une énergie constante (ici E $\approx 0{,}5\ \mu J$). Les profils longitudinaux et transversaux des canaux sont caractérisés par imagerie (a - en bas), permettant de définir et d'évaluer des critères pour définir des canaux uniformes et séparés (en vert). Ces critères expriment une condition nécessaire pour assurer des capacités optiques fonctionnelles (fonctions non mesurées ou vérifiées dans le cadre de cette thèse). (b) Résultats de l'étude paramétrique intégrés dans un espace 3D liant la périodicité spatiale, l'énergie et la durée d'impulsion. Les points verts correspondent à des canaux intègres et fonctionnels (séparés et uniformes) et identifient ainsi les conditions expérimentales correspondantes permettant cette structuration. Les points jaunes et rouges expriment un rejet, les critères de qualité (uniformité, séparabilité) n'étant pas obtenus. Les encarts montrent des exemples de canaux correspondants (même échelle que pour la Figure a).

Utilisant ces données, nous avons ensuite réussi à écrire des structures métaphotoniques intégrées et un guide d'ondes à cristaux photoniques en faisant varier hauteur et durée d'impulsion comme le montre la Figure K.

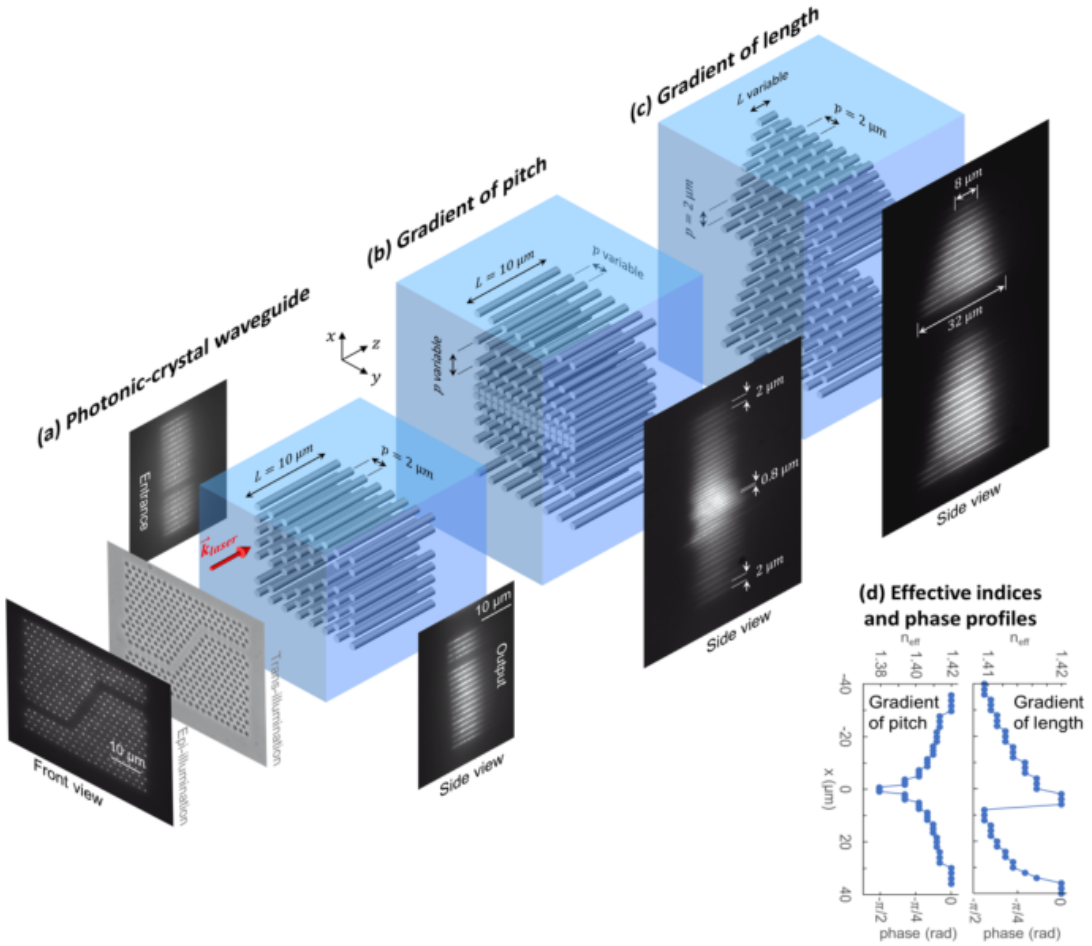

Figure K – Conception schématique (et structures correspondantes obtenues par écriture par faisceau de Bessel femtoseconde) de métastructures photoniques intégrées composées de nanocanaux usinés à l'intérieur du volume de silice fondue. (a) Configuration de guides d'ondes à cristaux photoniques, composés de canaux de longueur de 10 μm (durée d'impulsion 200 *fs*, énergie d'impulsion 0,5 μJ) avec un pas de 2 μm. (b) Métastructure impliquant un gradient de périodicité spatiale (ou pas) le long de la verticale (direction x), obtenue par variation progressive de l'espacement intercanal de 2 μm à 0,8 μm (durée d'impulsion 200 *fs*, énergie 0,5 μJ). (c) Métastructure impliquant un gradient de longueur de canal dans la direction verticale (x), de L=8 μm à L=32 μm, obtenue par variation d'énergie de l'impulsion laser de 0,2 μJ à 0,9 μJ (durée d'impulsion 1 *ps*). (d) Indices de réfraction effectifs calculés et profils de phase correspondants le long de l'axe vertical (x) pour les deux métastructures réalisées (cas b et c).

Le calcul de l'indice effectif à partir des structures observées montre une variation progressive de ce dernier. L'indice varie ainsi de n_{eff} = 1,40 au centre de la structure à n_{eff} = 1,41 aux extrémités. De plus, en calculant la phase correspon-

dante, $\phi(r)= \frac{2\pi}{\lambda} \times n_{eff} L$ accumulée sur toute la longueur de la structure (L=10 μm), on constate qu'on peut atteindre une différence de phase substantielle d'environ $\frac{\pi}{2}$. Ainsi, la longueur du canal sert de moyen direct pour manipuler le retard de phase optique et, par conséquent, pour déterminer l'ampleur du retard généré. En résumé, l'approche d'écriture numérique développée permet une mise à l'échelle indépendante ou ajustable pour chaque canal (à noter que ceci serait impossible avec un faisceau gaussien en raison de la zone confocale limitée de la zone focale d'un tel faisceau). Cette caractéristique offre ainsi une grande flexibilité de conception, notamment par rapport aux métamatériaux 2D conventionnels ou des cristaux photoniques. Contrairement aux approches qui modifient uniquement le diamètre ou la périodicité spatiale des structures (trou, etc.), notre méthode permet des ajustements nombreux et variés (dans des grands domaines d'amplitude) de tous les paramètres importants (pas spatial, diamètre et profondeur), conduisant à une grande versatilité des structures accessibles. Les exemples fournis démontrent le potentiel de création de méta-prismes ou de structures permettant le guidage directionnel de faisceaux, par exemple en faisant varier le gradient d'écriture dans une direction latérale.

A titre de perspective, les conceptions futures pourront incorporer des gradients radiaux en hauteur ou en longueur, ouvrant la voie à la fabrication de méta-lentilles 2D. La combinaison des gradients de hauteur et de longueur pourront permettre d'adresser un large éventail de possibilités de conception en utilisant des élémentaires de type cellules unitaires ou "méta-atomes", auxquels un tel outil d'écriture peut permettre d'accéder.

Acknowledgement

> Là où d'autres proposent des oeuvres, je ne pretends pas autre chose que de montrer mon esprit. La vie est de brûler des questions.
>
> *Antonin Artaud,*
> *L'Ombilic des Limbes*

I want to begin by extending my appreciation to Dr. Olivier Utéza and Dr. Nicolas Sanner, my supervisors, for their invaluable guidance and substantial support throughout the last three years. Special thanks are extended to Dr. Mario García Lechuga, Dr. Raphaël Clady, Jean-Luc Bellemain, Emmanuel Andre, and Fabrice Dessolis for their unwavering support in the laboratory during experiments. I am deeply grateful to my thesis committee members, Dr. Catalin-Daniel Constantinescu, Dr. David Grojo, and Dr. Anne-Patricia Alloncle, for their cooperation during the critical stage of this thesis. I am also grateful to my jury members, for taking their valuable time to read my thesis. A heartfelt appreciation goes to Andrei, Anjali, Pol, and Clarissa, who consistently listened to me and supported me during challenging times.

I am particularly grateful to all my comrades, friends, and people who never forget to show me genuine love and care, and who stood by me, encouraging me to embrace each moment. Also, I owe a debt of gratitude to my parents for showing their patience and understanding towards me.

Finally, my heartfelt thanks extend to Marseille and all the unfamiliar faces who never failed to provide brief solace during moments of despair.

Contents

Introduction 22

1 Introduction to Micro/Nano-structuring with Short Pulse lasers 26
- 1.1 Fundamental aspects of light-matter interaction . . . 26
  - 1.1.1 Carrier excitation . . . 27
  - 1.1.2 Nonlinear propagation . . . 30
  - 1.1.3 Relaxation mechanism . . . 32
  - 1.1.4 Modification regimes . . . 32
  - 1.1.5 Nonlinear interaction for Bessel beam . . . 34
- 1.2 Beam shaping . . . 35
  - 1.2.1 A Brief History . . . 35
  - 1.2.2 Necessity for Beam Shaping . . . 36
  - 1.2.3 Beam shaping methods . . . 37
- 1.3 Material structuring at micrometric scale . . . 40
  - 1.3.1 Conventional Fabrication techniques . . . 41
  - 1.3.2 Non-conventional fabrication method . . . 43
  - 1.3.3 Micro-structuring application with Bessel beam . . . 46
  - 1.3.4 Micro-structuring of photonic components and devices . . . 47
- 1.4 Structuring at nanoscale using conventional methods . . . 49
- 1.5 Towards the direct laser writing at sub-micrometric scale . . . 50
- 1.6 Summary . . . 51

2 Bessel beam and additional shaping method 54
- 2.1 Bessel beam . . . 54
  - 2.1.1 Generation of Bessel Beam . . . 54
  - 2.1.2 Fundamentals of Bessel beam . . . 55
  - 2.1.3 Axicon generated Bessel beam . . . 57
  - 2.1.4 Simulation tool . . . 61
- 2.2 Further beam shaping method: Segmented Bessel Beam . . . 67
  - 2.2.1 Customization of the depth of focus . . . 68
- 2.3 Experimental arrangements . . . 71
  - 2.3.1 Beam waist retrieval of incident Gaussian beam . . . 71
  - 2.3.2 Experimental Set-up . . . 72
  - 2.3.3 Annular aperture calibration . . . 74
  - 2.3.4 Beam characterization through various aperture widths . . . 74
  - 2.3.5 Micro-Bessel beam characterization . . . 84
- 2.4 Summary . . . 85

3 Material processing at the surface of the dielectrics **87**
3.1 Introduction . . . 87
3.2 Experimental arrangement . . . 89
3.3 Crater Morphology . . . 92
3.3.1 Determination of ablation threshold . . . 93
3.3.2 Crater Characterization . . . 94
3.4 Towards sub-micron spacing of channels . . . 95
3.5 High Spatial density matrices of channels . . . 99
3.6 Post Processing techniques . . . 103
3.6.1 Cleaning with Plasma torch . . . 103
3.6.2 Ultrasonic Cleaning . . . 105
3.7 Channel characteristics determination below the surface . . . 106
3.7.1 FIB milling procedure for SEM analysis . . . 106
3.7.2 Analysis of Channel Entrance . . . 108
3.7.3 Channel diameter, quality of sidewalls . . . 110
3.7.4 Channel Length . . . 111
3.7.5 Crosstalk effect . . . 113
3.8 Summary . . . 119

4 Material processing in the bulk of the dielectrics **120**
4.1 Introduction . . . 120
4.2 Experimental arrangements . . . 122
4.2.1 Adjustment to the shortest pulse duration . . . 123
4.3 Parametric study of channels . . . 124
4.3.1 Individual channel characterization . . . 129
4.4 Dense stacking of channels down to sub-micron pitch . . . 130
4.5 Fabrication of embedded basic and meta-photonic structures . . . 133
4.5.1 Fabrication of embedded meta-photonic structure . . . 133
4.6 Summary . . . 140

References **145**

Introduction

The generation of femtosecond ultrashort pulses with the invention of chirped pulse amplification (CPA) [1] revolutionized the laser-matter interaction field and unleashed their potential in micro-machining applications, such as cutting, drilling, and structuring materials with unprecedented precision. Among the first demonstrations, we note that femtosecond laser micro-machining was reported on silica and silver surfaces by [2] [3]. An ongoing demand for increased compactness from the micro-machining industry required further downsizing of the feature size. Several researches started to grow to achieve feature sizes ranging from sub-micron to just a few nanometers. [4] [5]. The fabrication of complex micro/nano-structures on the surface of non-transparent materials or within the volume of optically transparent materials is widely acknowledged as an important advancement in innovating advanced components. This is particularly relevant in the fields of photonics for the development of micro-devices and sensors. In addition, the femtosecond laser micro-machining stands out due to its flexibility, simplicity, and ability to generate a diverse array of surface structures suitable for a broad range of applications when compared to standard lithographic techniques. Other than fabricating photonic components, the method finds applications in diverse fields of plasmonics [6], micro/nano-fluidics, biochemical sensing, and many other related fields [7].

The interaction of the short pulses (femtosecond, usually <10 picosecond) with material gives rise to several intensity-dependent nonlinear absorption processes, such as multiphoton absorption, avalanche ionization (dominant mainly for dielectrics) which lead to the modification of its physical, chemical and optical properties. When a *fs* pulse interacts with a dielectric material, the energy is absorbed at the focal volume of interaction in a non-linear manner. Therefore, any induced change is spatially confined at the focal volume. Thus, it enables precise micro-structuring at a particular region of the material. This spatially confined energy, coupled with the flexibility of a laser beam scanning system or sample translation system helps to create structures of arbitrary geometry in three dimensions. This property provides a huge advantage in machining 3D photonic devices.

In addition, there is an opportunity to machine optical components in different materials. The structuring was accomplished on a variety of materials, including semiconductors [8] [9] [10], glasses [11] [12], metals [13] [14] [15], polymers [16], and other materials [17] [18]. In addition to its material-independent structuring advantage, this process has garnered attention from researchers due to its capacity for processing non-planar surfaces [19].

The laser-matter interaction, controlled by adjusting the laser parameters like wavelength, pulse duration, and beam shapes can ultimately influence the material structuring, especially at the micron or sub-micron scale. The Gaussian intensity distribution from a laser has a disadvantage in machining nanostructures with rather small spatial elongation, as the focal zone is limited by the focusing optics. Additionally, the interaction of the laser with the material creates plasma which restricts the Gaussian beam from propagating further into the sample, limiting the depth of the structure. By taking advantage of spatial beam shaping, we can transform the Gaussian intensity distribution into a Bessel beam. Bessel beams are known to be "non-diffracting" and it has a "self-healing" property, which further allows the beam to move beyond the obstacle as shown in Figure 1.

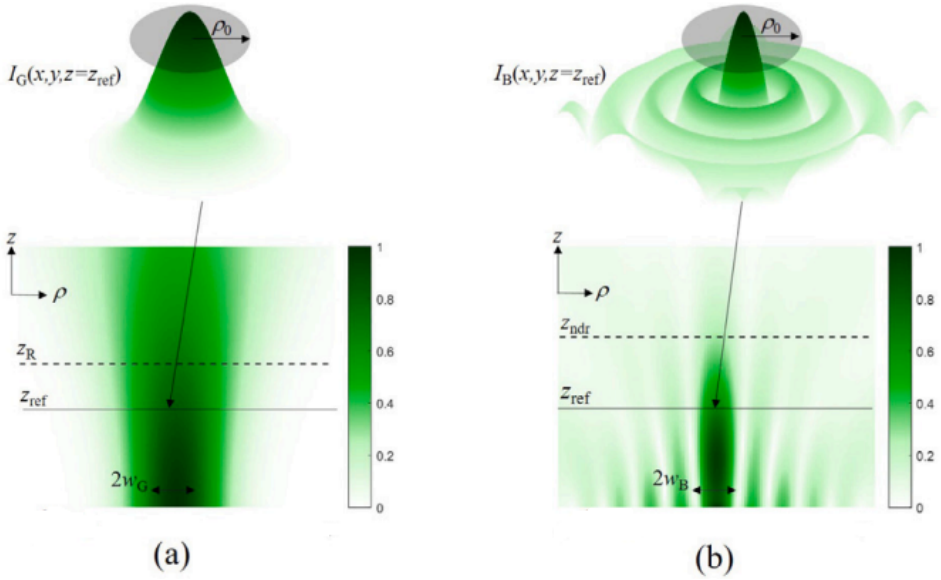

Figure 1 – The propagation of (a) a Gaussian beam, and (b) a Bessel beam generated through a finite aperture of diameter. The Perspective view (top) and contour plot over the ρz plane (bottom), adapted from [20]

.

Thus, it can overcome the plasma shielding effect. Bessel beams are proven to machine nanochannels with high [21] [22] to moderate aspect ratio [23] [24](ratio between channel length and channel diameter), which finds application in fabricating several photonic components.

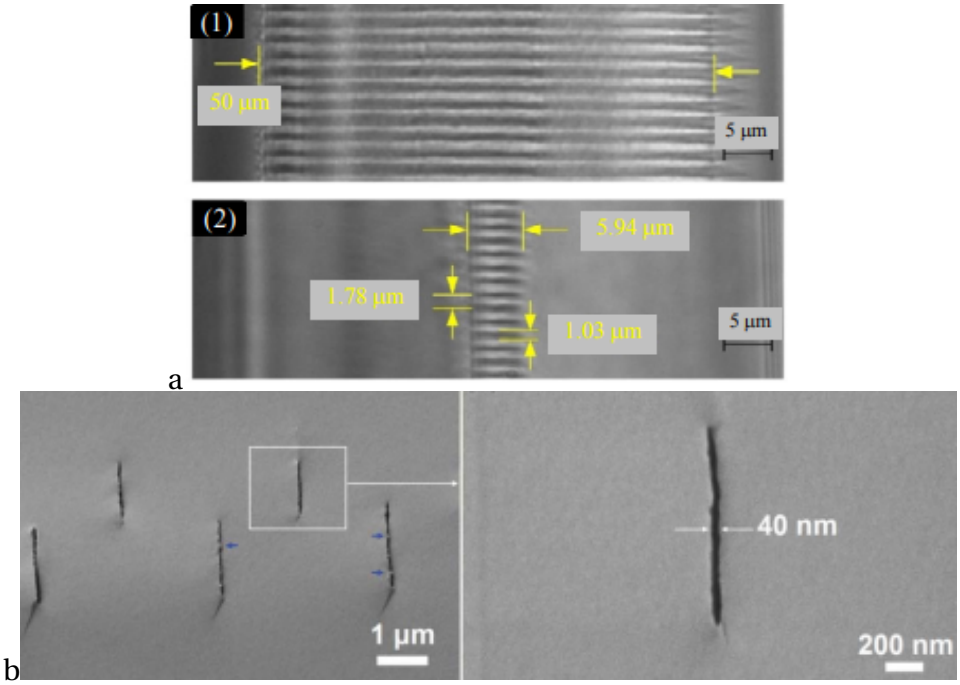

Figure 2 – a) Microscope images of the inscribed Sapphire Fiber Bragg Grating (SFBG), adapted from [25]; b) Cross-sectional view of nanofluidic channels directly buried in silicate glass, adapted from [26], machined with direct laser machining techniques.

The spatial beam shaping technique combined with controlled laser-matter interaction has evoked innovative micro and nano components for future industrial applications. Here, two examples of laser direct writing of Fiber Bragg Grating (FBG) and nanochannels buried in silicate glass are shown in Figure 2.

This thesis is divided into four chapters as described below.

Chapter 1 provides an introduction to the general aspect of micro and nano structuring. After providing a short overview of laser-matter interaction, it briefly discusses the role of beam shaping in laser machining. Later, we explore the literature about methods of micro/nano-structuring achieved so far. We compare different conventional and non-conventional techniques and then discuss mostly the advantages of direct laser writing techniques over others for micro and nano-structuring.

Chapter 2 discusses the generation of the Bessel beam, the idea of a segmented Bessel beam adapted for micro-machining, and the experimental characterization of the truncated beam through different annular apertures. It gives an estimation of choosing the optimized aperture for laser machining of our desired structure.

Chapter 3 deals with the micro-machining at the surface of fused silica. A detailed study of the hole characteristics both at the surface and in depth has been provided

here. A comparative study between front and rear surface machining has been carried out in this chapter. Here, we also discuss the issue of crosstalk between channels when machining at the micron to sub-micron scale.

In Chapter 4, we present the experimental results of laser machining in the bulk of dielectrics, and the advantage of such techniques over machining the surface. Later, we demonstrate the successful writing of photonic components with micron and sub-micron structures.

Lastly, we sum up the results of this work and conclude it by proposing some future experiments and, presenting some perspectives for its possible implementation for applications and laser-based processes.

1 Introduction to Micro/Nano-structuring with Short Pulse lasers

This chapter discusses the fundamentals of micro/nano-structuring with ultrafast laser machining. To start with, we explain the fundamental aspect of laser-matter interaction also adaptable to our machining conditions. Later on, we discuss the beam shaping methods from which we have taken advantage in the thesis. After, we present some previous research in machining structures of such micro/nano-scale dimensions. We discuss the limitation in further downscaling and fabricating photonic devices at such a scale, which is crucial to address the issue of miniaturization in today's world. In the end, we discuss our proposed methods of fabrication with direct laser writing benefiting from the short pulse duration of the femtosecond laser.

In this thesis, to machine our desired structure, we have taken advantage of short pulse durations (1ps, 30fs and 200fs) of the ultrafast laser system ASUR (which will be described in Chapter 2). Therefore, we will discuss the fundamental physics behind the laser-matter interaction of ultrashort pulses. In this thesis work, the experiments are carried out with dielectrics (fused silica). Therefore, we will discuss the laser-matter interaction mostly related to this material.

1.1 Fundamental aspects of light-matter interaction

A dielectric is characterized by a wide band gap E_g (($\approx 10^{14}\Omega$.cm to $\approx 10^{22}\Omega$.cm) [27], defined by the energy difference between the maximum of the valence band (VB) (outermost band in the band structure filled with bound electrons) and the minimum of the conduction band (CB) (the upper state in the band structure filled with conduction electrons). In pulsed laser-matter interaction of a dielectric with a femtosecond laser, the energy is absorbed through nonlinear mechanisms. For example, the band gap of fused silica is $\approx 9\ eV$ which is far superior to the photon energy (800-nm NIR wavelength) used in this work. The transition of an electron from VB to the CB is only possible if the energy gained by that electron (through nonlinear absorption) is greater than the band gap energy [28].

The femtosecond (fs) pulses, upon interacting with transparent dielectric material generate a large amount of excited electrons which are able to modify locally the material properties such as refractive index. The refractive index of the medium may

become intensity-dependent (will be discussed later). In wide band gap materials like dielectric, the relaxation channels of electronic excitation (discussed later) can lead to photo-induced damages. These optical processes are fundamentally nonlinear and are able to modify the microscopic structure of a material, making them appropriate for innovative material fabrication. By adjusting the incident pulse energy, repetition rate, or focusing condition the material modification can be controlled. The fact that materials may become locally absorbing under the excitation with a high-intensity laser pulse, makes the ultrashort pulses highly versatile for any kind of material fabrication.

Next, we will discuss the fundamental physical processes behind laser-matter interaction mostly focused on dielectrics. We also discuss briefly the nonlinear interaction and propagation of the Bessel beam.

1.1.1 Carrier excitation

The femtosecond pulses deposit energy into a material by creating electron-hole plasma through the mechanism of photon absorption. However, in the case of dielectrics the energy is linearly absorbed into an extremely small cross-section (that is related to the presence of residual defects in the band gap) and under the intense femtosecond irradiation nonlinear processes such as multiphoton ionization, tunnel ionization, and avalanche ionization are the dominant processes which create free carriers inside the material. All these processes together contribute to the carrier excitation, which will be discussed below.

1.1.1.1 Photoionization

Two/Multiphoton ionization In the case of wide band gap materials, a single photon does not have sufficient energy to excite the electrons from the valence band to the conduction band. Simultaneous absorption of the photons is required creating an energy higher (sum of the individual photons) than the band gap energy [29], and thus helping the electrons to reach the conduction band from the valence band.

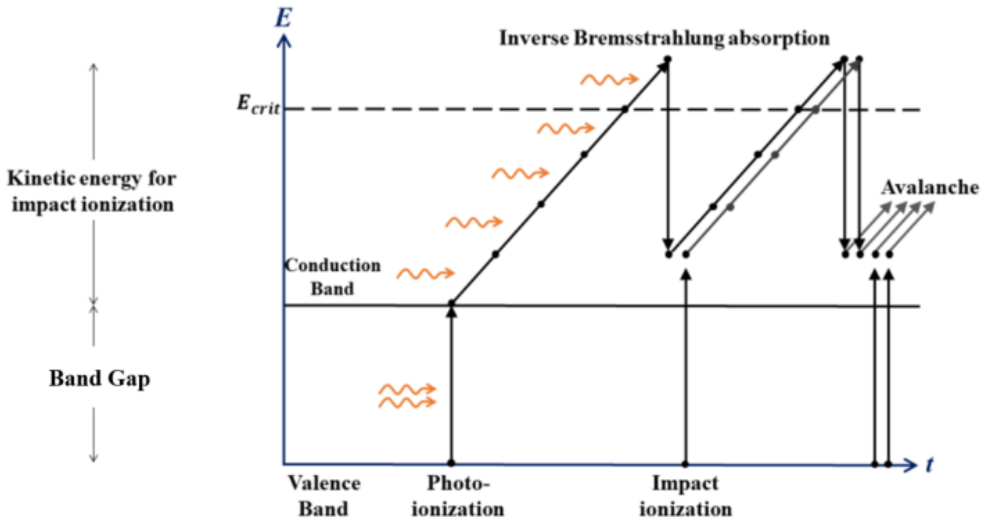

Figure 1.1 – Schematic of different types of ionization process in dielectrics, adapted from [30].

We have described different ionization processes in Figure 1.1.

The absorption rate is related directly to the optical intensity in the view of linear absorption. Conversely, for nonlinear multiphoton absorption, it aligns with the intensity raised to the power of "n", as indicated in the literature [1]. As a result, employing a highly intense focused laser with a shorter duration proves to be the most efficient approach for the nonlinear multiphoton absorption regime. The fundamental mechanism of nonlinear absorption is the two-photon absorption process, where two photons are absorbed simultaneously from the optical field. The occurrence of higher-order absorption processes is dependent upon the material's band gap energy. Specifically, if the band gap energy surpasses the incident energy of the laser beams by a factor of 2.8, it leads to three-photon absorption or even higher-order photon absorption [1].

The number of photons incident from laser N required for the excitation process of electronic transition from VB to CB is described by [28],

$$N = \frac{E_g}{\hbar\omega}, \tag{1.1}$$

where E_g is the band gap, $\hbar = h/2\pi$ with h being the Planck constant, and ω is the frequency of the photon involved in the process.

Tunneling ionization The tunnel ionization starts to happen when the laser field is very strong. The Coulomb potential can be overturned in the circumstance of a strong electric field. This in turn allows the valence electron to tunnel to the conduction band

1. https://www.rp-photonics.com/multiphoton_absorption.html

in a time which is less than the laser period. The probability of an electron excited through this ionization process is given by [31],

$$W(I) \approx exp(\frac{-2E_g^{\frac{3}{2}}\sqrt{m}}{3e\hbar E}), \tag{1.2}$$

where m corresponds to the mass of electron ($9.1*10^{-31}\ kg$) and E is the electric field. In our work, we are working with a laser beam of 800 nm and of rather long pulse duration (from 30 fs to 1 ps), and therefore multiphoton ionization is supposed to be the dominant ionization mechanism in such conditions.

The multiphoton and tunneling ionization can be described under the Keldysh theory which accounts for the probability of ionization of atoms and solids under a strong electromagnetic field [32]. Keyldsh built a model which describes different domains of ionization in which he introduced a parameter γ, also known as Keyldsh parameter. It is defined as [32],

$$\gamma = \omega\frac{\sqrt{mE_g}}{eE}, \tag{1.3}$$

where e is defined as the electronic charge. When $\gamma << 1$, tunnel ionization dominates. Contrarily, when $\gamma >> 1$, the rate of ionization is given by multiphoton ionization. In our work, we used moderate electric field ("long" fs pulses) and fused silica for material processing purposes, and it is the multiphoton ionization that is significant for our situation.

Free carrier absorption After reaching the conduction band, an excited electron in the conduction band can absorb several photons and can transport it to the higher energy states. This process also called Inverse Bremsstrahlung is efficient for free carrier absorption. The absorption coefficient depends on the imaginary part of the refractive index κ. It is equal to the inverse of the absorption depth.This coefficient is defined as [27],

$$\alpha = \frac{2\omega\kappa}{c}, \tag{1.4}$$

where c is the speed of light.
The complex refractive index can be expressed as [27],

$$\tilde{n} = n + i\kappa, \tag{1.5}$$

And in relation to the Drude model and the complex refractive index, the dielectric function can be presented as [27],

$$\widetilde{n} = \sqrt{\widetilde{\varepsilon}}, \widetilde{\varepsilon} = 1 - \omega_p^2 [\frac{\tau^2}{1+\omega^2\tau^2} + i\frac{\tau^2}{\omega\tau(1+\omega^2\tau^2)}], \tag{1.6}$$

where τ is the scattering time usually in the order of fraction of femtosecond. In this expression, ω_p is named as plasma frequency and is defined as [33],

$$\omega_p = \sqrt{\frac{e^2 N}{\varepsilon_0 m_e}}, \tag{1.7}$$

In this expression, N is expressed as electron density, m_e is the electronic mass, and ε_0 is the vacuum dielectric permittivity. When the plasma frequency is lower than the frequency of light ($\omega_p << \omega$), the absorption coefficient can be derived as,

$$\alpha = \frac{\tau}{nc}\frac{\omega_p^2}{1+\omega^2\tau^2}, \tag{1.8}$$

As soon as the electron density generated by photoionization reaches a high density ($\omega_p \sim \omega$), the rest of the femtosecond laser pulse can be absorbed.

Collisional ionization The excitation caused by the photo-ionization process is responsible for the generation of free electron carriers inside the focal volume of the medium. The free electrons that are generated in the conduction band are then able to absorb photons in a non-resonant process named inverse Bremsstrahlung [30] absorption (as described before). When the electrons in the conduction band gain enough kinetic energy during the absorption process, there is again generation of free electrons (as the kinetic energy is large enough) through impact ionization [30]. This process generates an avalanche growth of electrons. The whole process is named avalanche ionization or cascaded ionization [30]. It is the avalanche ionization that is known to produce damage within glasses.

1.1.2 Nonlinear propagation

Optical Kerr effect When an intense femtosecond pulse propagates through a dielectric material, an instantaneous nonlinear response is recorded as a result of the formation of oscillating electric dipoles which contributes to macroscopic polarization. For an isotropic dielectric material like fused silica, the resulting index of refraction can be expressed as [34] [35],

$$n = \sqrt{1 + \chi^1 + \frac{3}{4}\chi^3 E^2}, \tag{1.9}$$

where the linear and nonlinear susceptibilities are defined as χ^1 and χ^3. In more standard form, it can be presented as [36],

$$n = n_0 + n_2 I, \tag{1.10}$$

Here, the laser intensity is defined by $I = \frac{1}{2}\varepsilon_0 c n_0 E^2$. n_0 and n_2 are the linear and nonlinear part of the refractive index and defined as $n_0 = \sqrt{1+\chi^1}$ and $n_2 = 3\chi^3/4\varepsilon_0 c n_0^2$, respectively. Nonlinear refractive index causes different nonlinear optical effects (like self-focusing, defocusing) when the intense femtosecond pulse propagates through dielectric materials.

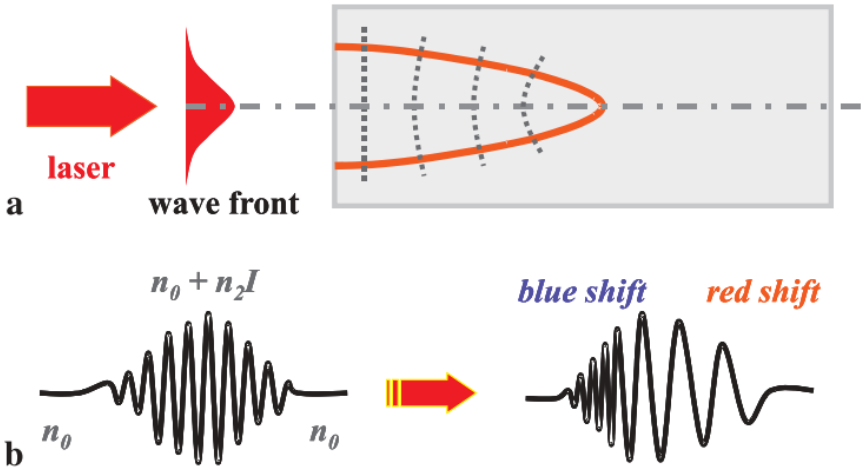

Figure 1.2 – Schematic description for a) self-focusing and b) self-phase modulation resulting from a nonlinear refractive index, adapted from [35].

Self focusing and Self phase modulation The spatial distribution of laser intensity $I(r)$ induces a corresponding spatial variation in the refractive index of dielectric materials. The spatial variation in the refractive index (which is larger towards the center considering the shape of the Gaussian profile), creates a lens-like effect within the dielectric as shown in Figure 1.2(a). This effect causes the laser beam to be focused inside the dielectric material. There is a critical power (P_{cr}) associated with the self focusing which is defined as [34],

$$P_{cr} = \frac{3.77\lambda^2}{8\pi n_0 n_2}, \tag{1.11}$$

If the peak power of a femtosecond pulse exceeds this critical power of self-focusing, the pulse collapses inside the dielectric. The intensity at the focus becomes high enough to ionize the medium. As a result, plasma is produced. However, in the case of dielectric, the nonlinear ionization will cause the effect of self-defocusing (which will be discussed later in this section) which further will prevent the pulse from collapsing inside the dielectric. The pulse propagates after.

For example, when one machines a channel in fused silica with such condition, depending upon the self-focusing and defocusing condition, the morphology of the channel could be different (we will present some results in Chapter 4, where we predicted this phenomenon to be probable in some of our experimental situations.)

The intensity depends also on the time and thus the nonlinear refractive index is also dependent on time during the pulse propagation inside the material. The change in refractive index induces a phase shift in the pulse, which causes a modification in the frequency spectrum of the pulse. The phase derivative of the pulse with respect to time can be defined as [34],

$$\frac{d\phi}{dt} = \omega - \frac{n_2 z}{c}\frac{dI(t)}{dt}, \tag{1.12}$$

The spectral broadening of the pulse is dependent on the nonlinear refractive index n_2 of the medium and the time derivative of the intensity of the propagating pulse as shown in Figure 1.2(b). There comes a frequency shift in addition to the phase modulation, which ultimately causes the broadening of the spectrum of the pulse.

Plasma defocusing As a consequence of the interaction of the femtosecond pulse with the matter, the nonlinear ionization mechanism generates an electron-hole plasma for dielectrics. The density of the electrons is maximum at the center and decreases radially outwards, thanks to the Gaussian beam. This phenomenon causes the linear refractive index of the dielectric to be modified.

The existence of electron–hole plasma leads to a decrease in the refractive index. Consequently, the minimal refractive index along the beam axis makes the plasma act similar to a diverging lens. Thus, this divergence effect may potentially counterbalance the self-focusing effect as it is described earlier.

Plasma defocusing is a serious issue encountered in the machining of long nanochannels in material. To overcome that, in our thesis, we have worked with the Bessel beam. The properties of the Bessel beam (which will be discussed in detail in Chapter 2) give an advantage to overcome the plasma effects unlike the Gaussian beam.

1.1.3 Relaxation mechanism

Once the laser energy is absorbed by the solids, the energy can be converted into elementary electronic and ionic excitations. Through these processes, the electron and hole relax and dissipate their energy into the solid. Electronic transport (however largely inhibited in dielectrics) and heat diffusion also contribute to evacuate the absorbed energy from the focal volume. In certain dielectric materials, an important relaxation mechanism involves the localization of energy within electron–hole pairs. This phenomenon gives rise to the formation of self-trapped carriers, particularly self-trapped excitons (STE).

1.1.4 Modification regimes

The material upon absorbing an energy in excess of an enthalpy of transformation gets modified. In femtosecond laser-matter interaction, there are different regimes of modification. If the energy is at the threshold (the minimum of energy which is

required to modify a material), a smooth change of refractive index occurs and at an energy above the threshold a void is created. These two regimes are interesting for this thesis which will be discussed below.

1.1.4.1 Index modification

The modification in refractive index occurs due to rapid thermal changes, which leads to alteration in local density and refractive index of the material [37] [38]. The material determines if the refractive index change is positive or negative. In fused silica (the material used in this thesis), this change of refractive index is noted as positive (10^{-2} to 10^{-3}) [39] which occurs through a quenching mechanism [40] [41] after the energy deposition.

The key to the capability of material modification lies in the remarkable potential of tightly focused ultrashort laser pulses to induce highly nonlinear material ionization at precise locations within the transparent material. The high intensity, often exceeding 10^{13} W/cm^2, can be achieved with relatively modest pulse energy in the microjoule range, resulting in exceedingly localized material modifications with minimal impact on the surrounding areas [42]. Depending on the experimental parameters, the induced material modification can manifest as a change in refractive index (homogeneous or birefringent) [43] [44] [45], or as material ablation in a confined micro-explosion regime, resulting in the creation of voids (will be discussed in next section) within the pristine material [46] [47]. For the change to occur through birefringence, when an irradiated material volume undergoes through densification process [48], the surrounding bulk material is subjected to stress, resulting in the formation of birefringence. This birefringence further leads to the refractive index change for glass medium.

In some cases, the index modification could also happen through the formation of colour center formation [49]. The nonlinear absorption of the energy creates a high electron density which in turn leads to the formation of coloured centers. It has been reported that in fused silica such a mechanism can induce the change of the refractive index [50].

1.1.4.2 Void formation and ablation

When the material is exposed to high-intensity irradiation, the modification created in the bulk is referred to as the void-like structure [51] [46]. In this thesis, the voids are formed at the surface (in that case, the matter is removed and we have an ablated crater or hole) and in the bulk of fused silica. We identify the voids as channels (as discussed in detail in Chapter 3 and Chapter 4). In Chapter 4, these voids inside the bulk are used to demonstrate photonic structures in the bulk.

So far we have discussed the fundamentals of laser-matter interaction which initiates modification and ablation in the material. All the formalism presented above has been mainly carried out for the standard Gaussian profile. In this thesis, we have spatially shaped the Gaussian profile to the Bessel profile. Although the fundamental physics of interaction is similar to the standard Gaussian one, the Bessel beam gives an advantage in overcoming certain obstacles caused by the plasma. Indeed, taking advantage of the "self-healing" property of the Bessel beam, it can propagate beyond the obstacle. In the next section, we will briefly discuss the nonlinear propagation for a Bessel beam.

1.1.5 Nonlinear interaction for Bessel beam

When intense Bessel beams interact with transparent materials, various nonlinear optical effects come into play. Indeed, as a general fact, the propagation of femtosecond laser pulses within Kerr media results in the formation of an intense, highly focused filament. The filament arises from a complex phenomenon in between self-focusing due to the optical Kerr effect and the counteractive influence of multiphoton absorption (MPA) [52].

In the case of the Bessel beam, the nonlinear interaction regimes could be divided into three regimes, as described in the article of [52]:

Weakly Nonlinear Bessel Filamentation Regime: In this regime, the resulting Bessel beam intensity is high enough to cause self-focusing. Still, it does not trigger the collapsing of the beam due to multiphoton ionization (MPA). This regime allows for controlled self-focusing without causing extreme damage to the material. A detailed study of this regime has been carried out in the work of [53] in air.

Unsteady Bessel Filamentation Regime: The power content in the central peak of the Bessel beam is slightly higher than in the previous regime. The power is sufficient to induce collapse, thus a stronger MPA. Therefore, the damage is obtained in this regime in the material.

Steady Bessel Filamentation: The steady Bessel filamentation occurs when the beam smoothly reshapes into nonlinear unbalanced beams [54] [55]. It was shown in the work of [55] that this occurs when an axicon remains in contact with the material and the Bessel beam forms inside the material rather than forming in the air. When the Gaussian beam propagates through an axicon and transforms into a Bessel beam before entering the material, it results in strong self-focusing of the central peak which leads to multiphoton absorption and intermittent reduction of peak intensity. The Kerr self-focusing periodically restores energy to the core, causing this process to repeat. This regime has further been thoroughly investigated in the work of [52].

In the study of [52], it has been demonstrated that the transition between the unsteady and steady filamentation regime is governed by the base angle of the axicon. Indeed, a similar fundamental spatial dynamics is present in these two regimes as shown in the work of [56].

In this thesis, we have worked with pulse durations ($1ps$, $200fs$) for which the peak power is much below the critical power (as described by Eq. 1.11) to evoke any nonlinear interaction of the pulse with the matter.

Laser-matter interaction is the fundamental aspect of laser machining of structures. Controlling the interaction regimes has a great influence on the micro-structuring of material. It has been observed that the variation of laser parameters like wavelength, pulse duration, or beam shapes could affect this interaction regime thus providing more control over the machining of the structures with different dimensional scales and geometry. One of the key parameters among them is the laser beam shape. In this thesis, we spatially shape the incident Gaussian beam to the Bessel beam for our machining experiment.

Therefore, in the next section, we will discuss the different beam shaping techniques available for laser machining.

1.2 Beam shaping

1.2.1 A Brief History

Classical beam shaping has a long history starting with Roman and Greek Philosophers. The first beam shaping idea emerged by combining several pieces of metals, which acted as mirrors, and paved the way for beam shaping [57]. The small pieces of metals divided the incoming beam into small segments, which in the end were targeted to one object. In practice, the Fresnel lens was the first beam-shaping optic, introduced in human history. Fresnel used the idea of joining separately polished concentric elements together to make the big lens for lighthouses [57]. This strategy also helped to reduce the weight of the lens. Modern beam shaping advanced with the invention of the laser. The first lossless beam shaping was reported by Friden in 1965, where he calculated the curvature of aspheric lenses which reshaped the single-mode Gaussian beam into a beam with a uniform profile [57]. To shape the laser beam profile into a uniform profile is important for applications like holography, material processing, and lithography. All these processes require a uniform illumination of the target. Various researches have been carried out using both reflective and refractive optics. Friden first reported that the phase of the beam over the output plane could vary by 20λ, after redistribution of the beam intensity [58]. Several other authors from the past have reported lossless beam shaping of a single-mode laser beam. Among other notable works, Aleksoff et al. reported the development of a holographic system with the help of the geometrical optics approximation, that allows the mapping of a Gaussian beam into a rectangularly shaped beam with uniform amplitude and phase

[59]. Later Veldkamp developed an iterative technique to design binary gratings to achieve the shaping of beam profile [60] [61]. Further, Kosoburd and Kedini, with the help of geometrical optics designed a diffractive system that shapes the Gaussian beams into beams with uniform irradiance[62]. Deployed on a geometrically derived phase function, Golub et al. presented results both numerically and experimentally [63].

1.2.2 Necessity for Beam Shaping

In laser micromachining, there is a constant need for machining structures and devices at a miniaturised scale of micron and sub-micrometric dimension. It has been shown in various research that among several laser parameters (wavelength, pulse duration, beam shape), shaping the intensity distribution of a beam can highly affect the processing efficiency and material structuring. Also, considering the dimension and diverse properties of the structures which are required for the industrial application, the standard Gaussian mode of the laser poses certain limitations (will be discussed later in this section and also in Chapter 2). The spatial shaping of the beam could bring robustness of the machining system to fabricate versatile structures (different functionalities, different dimensions) on a micron or sub-micron scale.

In the next section, we will give an overview of the applications of different beam shapes mostly used for laser machining applications, research which has been carried out so far, and we will mention the beam shape and its advantage over others for our machining purpose.

1.2.2.1 Uniform Beam shapes for laser machining application

Several beam shapes are able to provide uniform and particular illumination like Bessel, annular, and top-hat. Among them, top-hat beam has been largely used in the initial days of beam shaping for laser micro-structuring. The high uniformity in the transverse energy distribution of the top-hat beam compared to its Gaussian counterpart facilitated efficient laser processing with reduced surface roughness and side wall tapering effect [64]. The square top-hat beam's consistent energy profile enabled the utilization of a reduced pulse overlap, resulting in an increment in scribing speed up to 900% compared to Gaussian beam processing while maintaining a similar level of quality [65]. This in turn helps several micro-structuring techniques including micro-hole drilling and scribing micro-channels. For example, Coutts et al. employed a nanosecond laser with a square top-hat beam profile to create micro-holes in brass and ceramic substrates [66], where they demonstrated a noteworthy enhancement in the quality of the drilled holes, in contrast to the conventional Gaussian beam profile. The uniform intensity is locally maintained, near the focal zone or at the imaging plane of the optical system. Considering the beam spot size, necessary improvements in processing performance are needed to be executed [67].

In our work, there remain a few difficulties in using a top hat beam. They are,

1. The large spectral bandwidth we are using.

2. We intend to access sub-micrometer spots which cannot be reached with top-hat strategy which is limited to a few times the diffraction limit size.
3. Top-hat strategy is submitted to screening effects induced by the material because it is a small-angularly concentrated directed energy.

In short, top-hat is good for transverse uniform illumination not longitudinal while other beam shapes like Bessel/Airy are devoted to longitudinal beam shaping.

1.2.3 Beam shaping methods

This section discusses the different beam shaping techniques which have been used so far in the research and in the end we will talk about our chosen technique for beam shaping.

1.2.3.1 Laser beam shaping

The laser beam shape is defined by the intensity distribution and phase of the beam. The shaping of a beam requires the redistribution of intensity and phase. The phase is an important factor in determining the uniformity of a beam profile over its propagation distance. The intensity distribution of the beam profile is defined with various profiles like Gaussian, annular, rectangular, or circular. Beam shapers are usually designed for redistribution of the intensity and phase of the optical beam to a desired beam profile which is maintained along a required propagation distance.

Mostly, the output beam profile of a solid-state laser system resembles to Gaussian function. The Gaussian beam is not always advantageous in laser machining. For example, in the machining of nanochannels, the depth is limited to $\approx 1\ \mu m$ with a Gaussian beam [68]. The beam shaping allows us to transform the Gaussian profile into other profiles like Airy, Bessel, Annular and Top-hat beams. To extend the laser machining capabilities, for instance, towards the fabrication of transverse or longitudinally elongated non-tapered structures or the controlled manipulation (as for trapping) of particles along a trajectory, we will discuss later more the advantage of other beam shapes over Gaussian one.

Laser beam shaping methods can be divided into two categories: field mappers employing diffractive and refractive optical elements and beam integrators based on reflective phase elements [57]. Field mappers reshape the beam with a known field distribution, usually suitable for beams which are highly sensitive to beam alignment and beam dimensions. This is an effective lossless method that works well for Gaussian beams. Beam integrators work for both coherent and multi-mode beams, where the input field distribution may not be known [58]. A beam integrator utilizes a lens array to partition the incoming beam into numerous facets, subsequently endeavouring to distribute the energy across the output region within each facet. The resultant output beam profile is derived from the summation of the diffraction patterns originating

from each aperture within the lens array [57].

The beam shaping techniques are versatile and do not depend on one single parameter. Several parameters like the nature of the input beam, the system geometry, and the quality of the desired output beam affect the choice of beam shaping method [58]. For single-mode Gaussian beams calculating a parameter β helps to choose whether the geometrical or physical optics need to be chosen for describing the beam shaping. This parameter is defined as [57],

$$\beta = \frac{2\sqrt{2\pi}\, r_0\, y_0}{f\lambda}, \tag{1.13}$$

where λ is the wavelength, r_0 is the radius at $1/e^2$ position of the input beam, y_0 is the half-width of the desired output dimension, and f is focal length of the focusing optic, or the working distance of the target plane for systems without a defined focusing optics from the optical system. For a single-mode Gaussian beam, this parameter helps to evaluate the quality of the solution available and to choose whether the geometrical or physical optics methods should be used. A rule of thumb has been developed for simple output geometries like circular, and rectangular [57] [58].

β**<4** , the beam shaping system will not produce acceptable results.

4<β**<32** , diffraction effects are significant and it should be included under the beam shaping system.

β**>32** , the output beam shape is not affected by the diffraction. Geometrical optics should be sufficient for designing the beam-shaping system.

This equation suggests that designing beam shapers becomes easier when dealing with larger beams, shorter wavelengths, and shorter focal distances.

Field mapping technology, which employs complex surface elements to reshape the energy distribution of Gaussian beams into various other shapes like Airy, donut or top-hat, has its advantage in delivering collimated and low-divergence output beams. This technique thus helps to maintain a uniform irradiation profile over a given plane/distance [57]. In practice, two types of optical elements are used for field mapping solutions. In this thesis, we have used one of these techniques and therefore we will be discussing them in the next sections.

1.2.3.2 Refractive Beam Shaping

A field mapping phase element which works with the principle of refraction (for example lenses), is able to redistribute either the intensity distribution or phase of the input beam. This kind of system is known as a refractive beam shaper. Refractive elements are well-known to produce either uniform irradiance distribution or flat phase front. A class of field-mapping systems which uses Refractive Optical Element (ROE) generates a particular profile at the output plane by transforming the irradiance distribution of the input beam [69]. The output beam provides low divergence

and maintains a flat phase front with a reduced amount of aberrations [69]. This has advantages in laser micro-machining including 3D laser machining [70]. They provide advantages with their simpler design, ease of manufacturing, high transmission efficiency and their ability to be easily integrated to a laser system [71]. In low-performance systems, where cost is a driving factor, an aperture could be used to truncate the Gaussian beam profile and convert it into a flat-top profile beam. This shaping method helps to achieve a flat-top beam with a minimum energy loss and misalignment [72].

1.2.3.3 Diffractive Beam Shaping

Diffractive beam shapers use diffraction, to reshape the irradiation of the input beam. Typically, a diffractive optical element consists of microstructures on the face of an optical material. The structures diffract the light in a pre-designed manner. The characteristics of these micro-structures are customized to achieve a specific spatial phase delay for a designated design wavelength. Consequently, a Diffractive Optical Element (DOE) is usually crafted to fulfil a precise optical purpose at a particular wavelength, such as its application in laser systems that emit monochromatic light [2]. In contrast to refractive beam shapers, diffractive elements exhibit a higher sensitivity to factors such as alignment, divergence, and the beam's position within the nominal working distance plane. The diffractive optical elements offer significant benefits in laser setups with limited space, as they typically consist of a single element, as opposed to multiple refractive lenses.

1.2.3.4 Laser Beam Integrators

Primarily, a laser beam integrator is used when the laser modes are unknown or change with time and the beam collimation is less important. Usually, excimer lasers, laser diode arrays, multi-mode beams, and light sources with irregular intensity distributions utilize this mode of beam shaping. A laser beam integrator, also known as a homogenizer, consists of numerous lenslets that split the laser beam into a grid of smaller beams called beamlets, which are then combined at the target plane using a lens or another focusing component [57].

Laser beam integrators usually are divided into two categories called diffracting and imaging [57]. In the case of a diffracting beam integrator, the spatial coherence of the source over lenslet arrays is important to achieve a diffraction spot over an imaging plane that will closely replicate the shape of the sub-aperture with diffraction rings superimposed. In the case of an incoherent beam, it is impossible to obtain a reasonable replica of the lenslet aperture. Beam integrators that do not rely on diffraction, such as imaging integrators or waveguides, are effective for spatially incoherent incident light. Beam integrators normally experience random fluctuations in irradiance, resulting in a beam profile that is not entirely uniform or flat.

2. https://www.edmundoptics.eu/knowledge-center/application-notes/optics/laser-beam-shaping-overview/

In our thesis, we have used the refractive beam shaping technique by taking advantage of an axicon lens. We will talk in detail about the Bessel beam generation with an axicon in Chapter 2.

By taking advantage of the spatial beam shaping to gain control over the interaction regime, we intend to explore the material structuring primarily focused on micron to sub-micrometric scale. Therefore, in the next sections, we will give an overview of material structuring at micron to sub-micron/nanoscale by means of laser and also other standard techniques which have already been explored in various research.

1.3 Material structuring at micrometric scale

The micro-structures are usually 2D or 3D structures which are fabricated at the micrometer scale, typically at the scale of (1 μm-500 μm) [73]. Microfabrication techniques are dedicated to fabricating new structures or reconstructing the existing structures in down-sized versions, typically at sub-micrometric (below 1 μm) or even in nano-metric (1 nm-100 nm) scale [74]. Miniaturization is a key process in today's world which mostly impacts the microelectronics industry.

Research has been focused on many microelectronic devices as well as in various other applications like systems for microanalysis [75] [76] [77], microelectromechanical systems (MEMS) [78] [79] and optical components [80] [81]. The system for microanalysis finds important application in the separation and analysis of biological and chemical substances [75] [76]. Besides the biological and chemical uses of microstructures, those which are employed in MEMS have undergone swift advancements (their fabrication techniques and the type of devices), enabling seamless integration of electronics for the use of engineering applications. In recent times, there has been major progress in the fabrication of miniaturized optical components with surface and bulk micro-machining techniques. These techniques imply the structuring of the surface morphology or modifying the material in bulk, respectively. These miniaturized optical components are key parts of "integrated optics" as envisioned primarily by Miller in 1969 [82], where he proposed a similar idea of an electronic integrated circuit (where transistors are interconnected by wires), but here the active optical elements are interconnected with optical waveguides. This kind of waveguide-based integrated optics has later been termed photonic integrated circuit [83]. Photonic integrated circuits (PIC) find an advantage over standard integrated circuits as they use photons, which have no mass. Therefore, they are smaller, and faster (higher resonant frequencies) compared to the electronic integrated circuits and find their importance in the microfabrication industry where miniaturization is a primary driving factor. Besides, microfabrication has also opened up the possibilities for the fabrication of free-space optical elements. For example, a free space optical element comprising three-dimensional micrograting, micromirrors and microlenses [81] [84]. These optical devices are interesting for applications like free-space optical interconnects, optical display, data storage, sensors, and optoelectronic applications [85]. Addition-

ally, free-space optics have the capability to conduct optical imaging and produce focused spots with diffraction-limited precision [83].

In this thesis, our main focus lies in the fabrication of optical components at the sub-micron scale. These free-space optical components can subsequently be incorporated into Photonic Integrated Circuits (PICs). Some studies have explored the fabrication of these components directly within the circuit. Therefore, in the following section, we will delve into the conventional methods that have predominantly succeeded in designing photonic components at the micron scale.

1.3.1 Conventional Fabrication techniques

The most standard technique which was used in earlier days to fabricate micro and nano-structures is the lithographic technique. Initially, the most conventional photolithographic techniques [86] were used to fabricate structures for nanoscience applications. It has also been a prominent technology in fabricating MEMS systems for commercial purposes. Besides, optical MEMS technology, also known as micro-optoelectromechanical systems (MOEMS) [87] or micro-optomechanical systems (MOMS), enables the creation of highly effective light modulators, switches, widely tunable semiconductor lasers, detectors, and filters [88] [83].

With the miniaturization process, as the feature size decreases, this becomes a major limitation for the photolithography process to be used for device manufacturing purposes. Because the standard photolithographic process involves UV light exposure within the range of 350–430 nm [89], the minimum device dimension is constrained by the diffraction effects involved in this procedure [89]. Also, this technique relies on photosensitive polymers, and the masks required for it come with a substantial cost. Thus the situation required the development of new lithographic methods to meet the dimensions and precision demands of future device generations. Later, several advanced lithographic techniques, some of which we will be discussing below were introduced to address these challenges.

Extreme ultra-violet lithography (EUVL) [90] [91] technique was successful in writing structures with a further down-sized dimension of <100 nm by using extreme ultraviolet light of 10-14 nm [89]. However, EUVL encounters difficulties with line edge roughness (LER) [92] and resist resolution [93], with the absorption of EUV in resist material posing a constraint on its effective implementation. Additionally, the necessity for a high-vacuum environment imposes limitations on the practical application of EUV lithography [89].

After, as a result of ongoing miniaturization and performance enhancements, a new lithographic technique using an electron beam was proposed. Electron beam lithography (EBL) [94] is implemented due to its ability to achieve the highest practical resolution, attributable to the small wavelength of electrons (usually <0.1 nm) [89]. The resolution of EBL is determined by the resolution of the resists used in the process.

The EBL is a well-known process to create high aspect ratio nano grooves [95]. The disadvantage associated with this kind of technique is the throughput [89]. The low throughput of this procedure makes it incompatible with the mass production of components suitable for industrial applications. Also, the resolution here is limited by the generation of secondary electrons [96].

To overcome certain limitations faced by photolithography or EBL, new techniques like X-ray lithography [97] [98] were proposed. X-ray lithography offers advantages over photolithography, featuring shorter wavelengths (0.1–10 nm) for higher resolution and thus overcoming the diffraction limit caused by photolithography. This results in the formation of exceptionally precise patterns. Additionally, X-ray lithography is more cost-effective and has higher throughput [99] compared to electron beam lithography (EBL). It offers the advantage of further downsizing the feature size compared to what is offered by EBL. This technique resolves the problem of scattering encountered in EBL and is able to produce components with a high aspect ratio [99]. On the contrary, X-ray lithography also suffers from difficulties in the fabrication of X-ray masks which depends on EBL [100]. Therefore, the time taken is much longer and it makes this process not suitable for industrial applications.

Further fabrication processes included nanoimprint lithography [101] [102], and ion beam lithography techniques [103]. The ion beam lithography facilitates the fabrication of better quality high aspect ratio 3D structures [104] compared to the EBL. The electron beam technique suffers from a significant spreading while entering the resist while the ion beam is more collimated in terms of delivering energy to the resist. There exist several ion beam techniques. One of them is the focused ion beam technique (FIB). FIB has enabled to fabricate patterns in sub-100 nm regime [105]. Nanochannels even with a dimension of sub-5 nm were fabricated using FIB technique [106]. However, the FIB technique is extremely time-consuming and therefore not acceptable for industrial purposes.

Another lithographic technique has emerged with the advancement in laser technology, which is called Laser beam lithography [107]. This technique was first reported and then optimized by Gale and Knop in 1983 [108]. They also reported fabricating micro-optical components without a need for sub-micron alignment of multiple exposures. In terms of directly creating structures in photoresists, various optical components have been successfully demonstrated with this technique. Micro-Fresnel lenses (MFLs) with a thickness of 9.64 mm and 1 μm were produced, exhibiting superior resolution compared to equivalent components created using E-beam lithography [109]. More recently, continuous optical components have been showcased, such as the fabrication of a continuous f/15 Fresnel microlens array [110]. Optical components designed for communication purposes, such as a beam coupler directing a diode-laser into a multimode fiber, were created using two diffractive optical elements (DOEs) assembled through laser beam lithography. This assembly demonstrated an average efficiency of 74% according to [111]. In a separate study, the fabrication of structures

with aspect ratios of 130:1 was achieved through laser lithography, as reported by [112].

In contrast to E-beam lithography, this approach relies on photon radiation absorption without scattering effects in the photoresist bulk [113]. An advantageous feature is the freedom to design optimized structures using computer techniques [114]. Nevertheless, challenges encompass the straightness of scan lines and an exposure time that scales with pattern size, rendering it less conducive to collective fabrication or mass production [113].

So far we have reviewed different lithographic techniques as a standard microfabrication tool. All of the previously described lithographic techniques suffer from several issues in implementing them for industrial applications. As reported in the review of [89], optical lithography faces challenges with depth of focus, field size, and overlay accuracy. EUV projection encounters fundamental issues that require resolution. In electron beam lithography, a key obstacle is enhancing throughput, as using a single fine beam to simultaneously achieve higher resolution and throughput proves to be extremely challenging.

Besides these standard lithographic techniques, there exist non-conventional techniques using laser for micro/nano-structuring. The techniques using laser yield a significant advantage over the conventional techniques, which we will describe in the next section.

1.3.2 Non-conventional fabrication method

Here in this thesis, we are mainly interested in fabricating optical components for further implementing them into photonic devices. Although the lithographic techniques are successful in fabricating high-resolution components, it is not very effective for mass production of the components. The processes are relatively slow, and need a vacuum to perform the process. Therefore, it is rather costly. It is difficult to fabricate complex structures on any material as the processes are material-dependent. To pattern in 3D configuration is complicated, thus limited to the flexibility of fabrication. Ultrafast laser (usually with picosecond and femtosecond pulses) is one of the most promising tools to fabricate such components with the requirement of the industry by allowing fabricating complex structures on any material in a rather fast, cost-effective, and flexible way. Some other advantages of femtosecond laser machining include a point-by-point machining approach and the capability of creating structures with diverse geometry at a time.

Therefore, in this section, we will concentrate on optical structures fabricated with various ultrafast laser machining techniques.

1.3.2.1 Ultrafast laser processing

The generation of femtosecond pulses allowed for creation of downsized features with high density. The material exposed to traditional Q-switched laser or nanosec-

ond pulses suffer from the problem of thermal diffusion and therefore are unable to fabricate small feature sizes. The small thermal effects associated with the use of femtosecond pulse energy are an advantage in laser machining. This helps to modify the material with precision as a consequence of the controlled energy deposition of femtosecond pulses. Also, the advancement of ultrafast laser processing boasted remarkable spatial resolution for processed feature sizes by avoiding optical and thermal limits. This is one of the reasons that femtosecond material processing enables the creation of accurate 3D micro and nano-structures. The reduced thermal effects in femtosecond laser technology make it suitable for producing highly regular damages. Two types of structuring (surface and bulk) have majorly drawn attention for decades.

A diverse range of femtosecond laser-based techniques has been utilized for generating micro/nano-scale structures. One of them is near-field enhancement by particle lens array (PLA) [115]. PLA-based technologies are limited to only surface structuring and additionally, this technique requires the presence of micro/nanoparticles on the surface. Holographic technology [116] is constrained by the diffraction pattern created by the interfering beams. There exists parallel diffractive multi-beam technology [117] which is also limited to surface structuring. In addition, it also requires an extra diffractive optical element. Compared to these complex technologies, the Single-beam direct laser writing (SBDLW) technique [118] [119] [120] [121] [51] has been successful in structuring periodic patterns on the surface and in the bulk of the material.

These studies show that the femtosecond laser has innovative applications in material modification with different techniques. In our thesis, we have modified the surface and bulk of dielectric material (fused silica) by taking advantage of the SBDLW technique. Next, we will be discussing applications on surface and bulk structuring mostly focusing on the applications with this technique.

Material structuring with direct laser writing A major area of research in nano/micro-structuring is the machining of arrays of nano and microchannels on the surface and in the bulk of the material. The interest in studying this specific structure lies in its ability to serve as a building block of many photonic devices. Also, the periodic structure of long holes is the basis for photonic crystal structures or metamaterials. In this thesis, we concentrated on fabricating such structures in fused silica. Therefore, now we will discuss some research conducted before showing such results.

Nanochannels-based devices have been a very well-known area of research in the photonic industry. Pronko et al. [3] first showed that a femtosecond Gaussian beam is able to machine nanoholes with a diameter of 300 nm and a depth of 52 nm. Later, arrays of nanoholes were created by Vestentoft et al. [122] through the utilization of a self-assembled microlens array formed by depositing quartz microspheres onto a metal surface. Microchannels have been demonstrated in different materials of fused silica and BK-7 glass. It has been shown that in BK7 glass, the high aspect ratio channels are not possible, and machining in this material is limited by its morphology.

The certain type morphology is determined by the laser writing parameters [123]. In view of laser machining, aspect ratio is an important factor which is defined as the ratio of channel length to channel diameter. Ahsan and his colleagues [124] recorded the fabrication of regular nano-scale holes/voids both on the surface and in the bulk of soda-lime glass through the application of single-pulse irradiation at specific locations. Based on the applications, research has been carried out for both low or high-aspect ratio nanochannels. Single nanoholes on chalcogenide glass have been reported by [119]. Joglekar et al. [120] also presented single nanohole structuring on the cover glass. Nanochannels buried inside the glass with a transverse width of ≈40 nm have been reported by [125]. Research has been conducted to machine nanochannels in fused silica with a diameter of 200-500 nm [121]. A combination of three cylindrical channel lenses facilitated to machine of nanochannels up to 40 μm depth. They were fabricated in fused silica as shown in [126].

In surface micro/nanostructuring, research has also been carried out to show the influence of laser parameters (wavelength, pulse duration, pulse energy, polarization of the beam, beam profile and others) on the geometry and size of machining structures. By adjusting one of the parameters it is possible to fabricate structures even in sub-micrometric dimension. It has been found that there is significant influence of laser pulse duration in drilling micro/nanochannels. A comparison between nanosecond (ns), picosecond (ps) and femtosecond (fs) pulses in drilling sub-10μm holes has been presented by Zhu and his colleagues [127]. It is reported that at the micron scale, femtosecond laser pulses are best suited for material removal unlike liquid phase contamination faced by nano/picosecond pulses. Laser processing power has an influence on the crater morphology and the debris formation as shown by [128]. It is observed that, with reduced processing power, the generated recoil pressure lacked the necessary force to expel debris from the micro-holes. Consequently, there was a growth of particles on the walls and the bottom of the holes, significantly impeding the subsequent absorption of laser energy. Laser fluence is an important parameter which controls the depth of the micro holes, shown in the studies of [129]. Cylindrical structures are one of the most processed structures with a femtosecond laser. It has been reported by Nayak et al. [130] that below the threshold fluence, multiple pulses restrain the formation of regular cylindrical structures. Also, the impact of varying the number of pulses on the formation of cylindrical structures was investigated on titanium within a vacuum setting [131]. Besides, the polarization of the beam also influences the periodic structures. The influence of polarization on the development of cylindrical structures on nickel was explored using four different polarizations: linear, P-polarization, circular polarization, +45° and -45° as reported in [132]. It has been observed that the beam polarization controls both the geometry and orientation of the oval base of the periodic structures. In addition to the laser parameters, the environments of machining affect the properties of the structures as shown by [133] [134]. It is observed that the cylindrical structure density was greater in a vacuum compared to air or helium environments.

Another crucial factor influencing the machining of nanochannels, as documented in [135] [136] [23] [137], is the use of a Bessel intensity profile instead of a Gaussian one through laser beam shaping. In our thesis, we have similarly utilized a Bessel beam for machining the desired structures. The following section will present various applications of microstructuring employing the Bessel beam.

1.3.3 Micro-structuring application with Bessel beam

Bessel and Airy beams find significant applications in laser micro-structuring. For example, it has been reported that Bessel beams are capable of producing elongated atom traps which are not possible by Gaussian beams [138]. In optical manipulation, Bessel [139] and Airy beam [140] showed prominent results in trapping various particles at the same time. This performance is difficult to reach by Gaussian or top-hat beam because of their limited depth of focus. Moreover, in novel biological applications, such as optoinjection for cell transfection, employing Bessel beams eliminates the requirement for precise focusing on the delicate cell membrane, ultimately enhancing the overall efficiency of the process [141].

Besides, the elongated "non-diffracting" depth of focus of the Bessel beam has drawn interest in machining structures in micron and nanoscale from earlier times [142] [143] [144]. From the review paper of [144], glass has been recognized as an interesting material to be used for writing photonic structures like waveguides, power splitters, directional couplers, and many other photonic components for decades. Among notable works, femtosecond Bessel-Gauss laser beams have been employed to fabricate waveguides, each measuring 1 cm in length, with minimal loss, within bulk SiO_2 and BK7 glasses [145]. This was achieved through the direct modification of the refractive index. Kudryashov and colleagues [68] effectively generated nanochannels with lengths of up to 1 μm through front-surface machining. Herbstman and co-authors [146], on the other hand, achieved nanochannels as long as 10 μm using a combination of front- and reverse-surface machining methods. Also, later channels with >10 μm length have been demonstrated, but the beam distortion causes irregular structure in channels [121] as the beam suffers from non-linear effects. These studies have been performed with Gaussian beam initially, and nonlinear effects like filamentation are the main reason behind producing such long nanochannels. Nonetheless, as reported by Bhuyan et al., [136] this machining technique is not consistently convenient or reproducible, mainly due to the challenging control of the highly nonlinear filamentation process when utilizing an incident Gaussian beam. They have observed a solution to this problem and demonstrated a more controlled approach to nanochannel formation [21].

Additionally, the Bessel beam shows significant advantages in drilling long nanochannels in solid materials with a controllable approach. This is because one of the dramatic advantages of Bessel beams is that they deliver energy to the workpiece by the sides in an axially elongated manner, thereby immediately minimizing the problem

of screening effects related to Gaussian beam energy deposition along the optical axis. By taking advantage of the high stability of the Bessel filaments compared to the Gaussian one [52], nanochannels of length of 43 μm have been fabricated in glass. Later, higher aspect ratio (100:1) channels have been machined and reported by Courvoisier et al. [22]. Besides applications, numerical studies to understand the laser-matter interaction inside dielectrics have been carried out. Beuton et al. [147] have shown that even if it has a "self-healing" property, the femtosecond Bessel beam is not completely immune from the material ionization effect. Indeed, the formation of the beam is perturbed by the laser-ionized matter, which creates a screening effect that further limits the energy deposition in the material. It was suggested that this screening effect could be bypassed by using bursts of femtosecond pulses or pulses with picosecond duration. In another study, Bhuyan et al. identified a window of laser pulse energy and duration for single-shot bulk nanostructuring, over which it would be possible to fabricate nanovoids with an ultra-high aspect ratio of 1000 retaining a nanovoid diameter of 200-400 nm [148]. A chirp-controlled ultrafast Bessel beam would be favorable for such machining.

Besides the Bessel beam, research has shown favorable results for annular beams as well. Bessel and annular beams are closely related by the Fourier transform. As reported in the review of Duocastella [149], the combination of Gaussian beams with annular beams has facilitated the development of innovative imaging methods like stimulated emission depletion (STED) microscopy [150] [151].

In this thesis, we have used a Bessel beam along with an advanced beam shaping technique for micro-structuring in fused silica. Our aim is to machine small aspect ratio (≈1:10) channels with cylindrical walls for future application in making photonic components. As shown in literature previously, several advantages like small focused spot size, uniform illumination over an elongated DOF, and its ability to overcome plasma shielding effect make the Bessel beam profile a good choice for our purpose.

Now, after studying the development in the fabrication of single structures, we are eager to look forward to completing photonic components and devices. This is one of the aims of this thesis to demonstrate the possibility of fabricating photonic components in transparent material. Therefore, in the next section, we will concentrate on the research that have already been carried out for such fabrication.

1.3.4 Micro-structuring of photonic components and devices

Besides periodic patterning either on the surface or in the bulk of the material, research has also been conducted that investigated creating photonic components like waveguides, couplers, gratings and other components. These are crucial components for fabricating a photonic integrated circuit. In the pioneering work of Hirao et al. [152] [153], they studied optical characteristics of waveguides based on the laser writing condition and also they aimed to fabricate the photonic devices. Following that work, several other researches have been carried out lately. Many have tried to study

the fundamentals of structural modification which is directed towards the refractive index change in fused silica. Later, this has been the basis of writing waveguides in the fused silica [154] [155]. Besides studying the fundamental interaction regime, much research has been carried out to study the writing possibilities of waveguides in different materials like doped silica, borosilicate glass, phosphate and chalcogenide glasses [156] [157] [158] [159]. Investigation has also been carried out for linear [160] [161] and nonlinear [162] [163] crystals.

Among other photonic devices, the successful writing of a Y-coupler to divide power into two branches was demonstrated in fused silica by taking benefits from a low repetition rate (1 KHz) laser and longitudinal writing geometry, as reported in the review of [164]. In advanced work, Liu and his colleagues [165] have demonstrated a high-quality power splitter. Optical splitter inside fused silica [166], as well as in lithium niobate [167] have been machined with femtosecond laser pulses. Taking advantage of the flexibility of the femtosecond system, power splitters are designed in 3D configurations [168]. The optical and directional couplers are usually the basis for waveguide interferometers which is an important device in telecommunication and sensing applications. There have also been demonstrations of directional couplers in soda-lime glasses [169]. Among other devices, a Mach-Zehnder (MZI) interferometer composed of two X-couplers has also been demonstrated in soda-lime glasses [170]. A three-dimensional Mach-Zehnder interferometer (3D MZI) was utilized to demonstrate an electro-optic modulator in fused silica [171].

Femtosecond laser has also been successful in writing high-quality diffraction and Bragg gratings [172]. A fiber Bragg grating constituted of a Bragg reflector helps to reflect a particular wavelength. Diffraction gratings have been reported in several glasses [173] [174], particularly in fused silica [175] [176] and also in polymers [177]. By exploiting the point-by-point writing technique, the femtosecond laser has demonstrated the micro-structuring of optical Bragg grating. There is also an interesting demonstration of writing both the optical waveguide and Bragg grating by direct laser writing technique in fused silica, reported by Marshall and co-workers [178]. By using a double-step writing method, and varying the pulse energy in each writing turn, they were successful in writing the waveguide and the grating at the same time. A further achievement of writing the Bragg grating and optical waveguide together (periodic-structured waveguide) with low propagation loss has been reported by Zhang and his colleagues [179] with a single-step process. Also, Wavelength Bragg Gratings (WBGs) were created in fused silica using another single-step femtosecond laser writing technique involving a high repetition rate laser system which was equipped with an external acousto-optic modulator (AOM) [180].

Several studies have already been conducted on the fabrication of structures at the micron scale. The progress in laser machining technology has facilitated further exploration of sub-micrometric and nanometric scale structures with greater flexibility compared to conventional fabrication methods discussed earlier. The main objective

of this thesis is to showcase the feasibility of achieving dimensions in micro/nano-structuring suitable for the fabrication of photonic devices, both on the surface and within the bulk of dielectrics. Consequently, the next section will look into the advancements in the sub-micro/nano-metric writing regime.

1.4 Structuring at nanoscale using conventional methods

Besides the standard techniques of lithography as discussed earlier, some advanced lithographic techniques have been invented in recent days to facilitate machining at an even smaller nanometric scale. For example, recent methods of parallel irradiation technique which take advantage of multibeam interference or colloidal lithography have been successful in machining large surface area at nanometric scale [181] [182]. Another advanced technique named laser interference lithography was used to fabricate a large area of nano cone structure [183]. The development of the two-photon polymerization (TPP) [184] method has initiated the fabrication of 3D micro-structures with high resolution. The first proposed 3D components using TPP were reported by Mauro et al. [185]. As reported in the review of [186], even though the idea of employing Two-Photon Polymerization (TPP) for 3D data storage was initially suggested in 1989 using two beams [187], the resolution of TPP saw continuous enhancement in subsequent years. The first nano-scale TPP of 3D structures, with a feature size of 120 nm, was successfully demonstrated by Kawata et al. [188]. The simultaneous fabrication of periodic 3D micro/nanostructures has been achieved through the utilization of micro-lens arrays in conjunction with the TPP technique [189].

Further development in nanoscience has facilitated in fabrication of metamaterial and photonic crystal structures. The study of photonic crystals (PhCs) has gained significant attention due to their unconventional characteristics, particularly their capacity to guide and confine electromagnetic waves. The distinctive structural features of PhCs set them apart from other optical media by the fact that they exhibit periodic alterations in refractive indices (RIs) at the sub-wavelength scale [190] [186]. Based on their geometric structures, PhCs are classified as one-dimensional (1D), two-dimensional (2D), and three-dimensional (3D) PhCs [191]. Depending on the dimensions, the periodic variation of the refractive index is defined. The electromagnetic wave is guided according to this periodic variation of refractive index.

Metamaterials are structures which have negative electrical permittivity and thus a negative refractive index [186]. Usually, they are composed of sub-wavelength building blocks. As reported in the review of Li [186], "Rill et al. employed the TPP direct laser writing (DLW) technique for the creation of polymeric templates. Subsequently, they coated the templates with metal using either silver chemical vapor deposition (CVD) or silver shadow evaporation. This approach enabled the fabrication of diverse pho-

tonic metamaterials, including a planar magnetic metamaterial and a negative-index bianisotropic photonic metamaterial [192]. Additionally, the TPP DLW technology was utilized to produce various structures such as 3D gold-helix photonic metamaterials [193], three-dimensional bi-chiral helical photonic crystals [194], and 3D invisibility-cloaking structures [195]."

The current methods for producing all-dielectric meta-photonic components, such as photolithography and electron-beam lithography combined with reactive-ion etching [196], are inherently limited to planar, two-dimensional patterning. Consequently, the scope of fabrication is constrained to the material surface [196] [197] [198].

1.5 Towards the direct laser writing at sub-micrometric scale

The non-conventional techniques using laser are more flexible and easy to use for the mass production of sub-micrometric structures. Among several non-conventional techniques with laser, the digital laser machining tool has emerged as the most prominent tool for industrial applications. The reasons behind as described in the review of [199] are,

1. Simpler and less expensive production equipment by avoiding vacuum and clean room facilities.
2. Rapid prototyping facilitates changing the structure pattern easily by software control. This reduces the time and production cost compared to the standard photolithographic steps which require a generation of masks.
3. This laser direct writing technique is three-dimensional (3D), as it can induce refractive index changes at any point within the bulk of the material at a given depth from the surface. This capability can be utilized to incorporate innovative functionalities (as structuring a material generates a function) that are unattainable with conventional fabrication methods.

These advantages make this technique adapted for further sub-micrometric structuring of the material at a scale close to the optical wavelength and even at a sub-wavelength scale.

The laser-induced refractive index change, achieved through three-dimensional laser beam scanning, has facilitated the demonstration of various photonic circuitry components, including information storage, and exploration of doped glasses and crystals [200] [201] [202] [203]. However, the magnitude of refractive index change, typically obtained under multipulse, high-repetition-rate, low-energy exposure, is typically limited to a range of $\Delta n \approx 10^{-4}$ to 10^{-2} [201] [202]. While suitable for writing waveguiding structures, it falls short of meeting the requirements for creating

meta-photonic structures, which demand local index contrasts approaching unity, necessitating an increase by two orders of magnitude.

Reaching the extreme scale in laser-matter processing with optical radiation has been a limit for a long time, as the spatial dimension of the structures is predominantly controlled by the focusing optics. Therefore, diffraction becomes a limitation. The optical limit is defined as the diffraction-limited spot diameter size as D=1.22λ/NA or the limits in resolution expressed as R=0.61λ/NA [204]. This is called the Rayleigh criterion [204] for resolution for two spots to be separated. The optical wavelength is defined by λ and NA is the numerical aperture of the system. The advancement in ultrafast laser machining has brought several breakthrough developments to push the scale of fabrication beyond optical limits which could be achieved for two or three dimensions. Several techniques have been employed over the years. Among them, some notable ones as reported in the review of [199] are a)direct focusing of the laser irradiation, b)near-field threshold interaction.

For example, optical diffusers whose dimension is comparable to the wavelength of visible light have been fabricated by direct femtosecond machining of float glass as reported by [205]. Bessel beams have been used for surface structuring at sub-wavelength scale in transparent materials [21]. Direct focusing of femtosecond pulse on the glass in the presence of a nonlinear excitation mechanism induced by the infrared ultrashort pulse can generate nanoscale structures [42]. The apertureless close contact structuring was attempted using near field parallel processing [206]. Besides, using a Bessel beam, nanoscale structuring in 3D inside the volume of the glass has been reported [207].

In the essence of overcoming optical resolution limits, photonic crystal structures and metasurfaces have drawn significant attention in the last years with the conventional lithographic fabrication technique. Although there is some progress in fabricating nanostructures with digital laser machining, there remain sufficient challenges in machining a photonic component or devices with spatial dimension or resolution achieved with lithography. Further improvement in this domain can give rise to machine interesting functionalities.

1.6 Summary

The material structuring at the micron scale has been an important research area for decades. Lately, the invention of ultrafast lasers has revolutionized the area. Femtosecond laser machining has been at the forefront of machining microstructures for decades. Over time, the processing techniques are optimized to achieve new novelty. For this purpose, it is necessary to understand the physics behind laser-matter interaction and also to explore different application regimes with such techniques. Several extensive studies have already been carried out in favor of fabricating structures at micro or nano-scale and also to the theoretical aspect of laser-matter interaction. In that context, beam shaping has enabled micron-to-sub-micron scale structuring with greater control and flexibility to reach smaller dimensions, which is an important

criterion for miniaturization.

Despite remarkable achievements in machining micron/nano-sized structures, there is still a constant need to achieve a high control over the machined structures in terms of robustness of the machining system, high resolution close to the one achieved with lithographic techniques, repeatability of the patterns, easiness and flexibility of parallel processing of either one or multiple structures. The lithographic techniques pose higher resolution and smaller dimensions but find difficulties in applications for the industry where mass production within a limited period of time is constantly growing. Although machining of smaller structures and photonic devices has already been possible on a micron scale, challenges remain in gaining full control over the micro-structures. For example, the photonic waveguide writing has two geometries named longitudinal and transverse geometry [164]. In longitudinal geometry, where the sample is translated along the laser propagation distance, symmetrical features can be obtained, however, the depth of the structures is limited by the focusing objective and complex arbitrary structures are extremely limited in such a configuration. The transverse geometry offers significantly increased flexibility, enabling the creation of waveguides or photonic circuits with arbitrary length and complexity. Nevertheless, it comes with the drawback of inducing a significant asymmetry in the cross-section of the waveguide [208].

Femtosecond direct laser writing has already shown promising results in the fabrication of Fiber Bragg Grating compared to the other femtosecond laser-assisted techniques like femtosecond laser phase mask technology and femtosecond laser holographic interferometry. The developments have been reported in detail in the review of [209]. Other direct laser writing technique based on multiphoton polymerization has been used to fabricate 3D photonic devices, lenses, mirrors, and photonic crystal structures in sub-micron scale [210]. Also, as mentioned earlier, the two-photon polymerization assisted with direct laser writing has also been successful in writing photonic structures [211], especially in 3D.

The utilization of laser nano-manufacturing in commercial applications is growing, particularly within the photonic industry. Despite the cost and operational advantages (machining is possible in air, instead of vacuum) in the writing of surface nano-patterns compared to established techniques with EBL or others, it is still not fully adapted to an industrial level. This delay is primarily due to the lack of comprehensive systems which have both control over the procedure and flexibility in designing various geometrical structures with resolution and size close to the ones achieved with standard techniques. In industrial applications, the emphasis is on the adoption of extreme ultraviolet (EUV) techniques and optimize them to achieve far-field super-resolution direct writing of nano-patterns. This conditions the development of the next generation of photonic integrated circuits. Some of the challenges that still remain in reaching the nanometric or sub-wavelength scale of the structures are,

1. Better resolution ($\approx$ few nm)

2. Longer depth of writing with parallel sidewalls.
3. Larger machining area with high throughput
4. Structures with better surface finishing and clean of debris.

In this thesis, we aim to address the micrometric to sub-micrometric scale structuring with digital laser machining techniques. As discussed earlier, the advantage lies in being cost-effective, flexible to fabricate 3D structures, and fast processing speed which could benefit industrial applications majorly. The machining of a transparent material is unique to femtosecond lasers and many interesting applications like buried optofludic channels, embedded metasurfaces and waveguides. Fiber Bragg gratings and micro-fluidic channels are well-established and extensively used in various industries for micro-scale fabrications. While these technologies are already mature enough for mass-production purposes, the challenge arises when attempting sub-micrometer scale fabrication within transparent materials using lasers. Also, the challenge still remains in achieving point-by-point machining with excellent reproducibility with a digital laser writing tool.

We plan to pursue machine micro-structures with a digital laser machining tool. This tool, by employing a channel-by-channel writing strategy provides the capability to independently adjust the dimensions of each channel, including diameter and length, as well as the periodicity of the pattern (pitch). The targeted spatial resolution is $<1\ \mu m$ and a depth $>>1\ \mu m$ for structures at the surface and in the bulk of fused silica. This kind of long micro/nano-channels with a spatial separation of $<<1\ \mu m$ are suitable to make the basis for demonstrating sub-micro/nano-metric features. In this thesis, the primary interest lies in exploring the writing condition of such spatially resolved structures. The highest degree of controlled laser parameters is required to achieve sub-micron structures. Advanced spatial shaping helped to create a micro-Bessel beam, which helps us to avoid simple point-by-point stitching of overlapping tightly-focused laser spots while scanning the material subject to beam pointing, positioning and mechanical stability issues [212]. This allows for the direct creation of an entire channel with a single laser pulse, offering advantages such as time savings and process quality. This also allows the utilization of a localized and digital approach, which constitutes a pivotal benefit of the laser method.

2 Bessel beam and additional shaping method

In this chapter, we discuss the fundamentals of the Bessel beam and the further beam shaping technique used in this thesis. In addition, we explain how we chose the optimized beam shaping method which helped us in machining our desired photonic structures.

2.1 Bessel beam

Beam divergence is a significant phenomenon that causes the laser beam to expand as it propagates. The Rayleigh range of a Gaussian beam is defined as the value of z (from the waist position z_0) where the cross-sectional area of the beam is doubled. There exists a special class of beam that inherits a bright central core, whose width is very narrow and surrounded by concentric rings. Zeroth order Bessel beams, ideally are extended over an infinite distance and the "non-diffracting" effects occur as a result of the minimum spreading of the central core over a given propagation distance called depth of field (DOF) [213]. The DOF of the Bessel beam can be compared with the Rayleigh range of the Gaussian beam. At a particular position, only a part of the plane waves composing the beam interferes and contributes to form the central core. The rest of the wave generates side lobes. Thus when the Bessel beam encounters an obstacle, the Bessel beam will be blocked locally but will approach from the side and reconstruct itself. Thus it exhibits a 'self-healing' property.

2.1.1 Generation of Bessel Beam

The profile of a Bessel beam is defined by the Bessel function, which is an exact and invariant solution of the Helmholtz equation. The quasi-homogeneous energy distribution of the Bessel beam along the propagation distance prevents any spread out of the beam as it propagates, thus retaining a 'diffraction-free' beam. An ideal Bessel beam requires an infinite amount of energy to sustain. However, under finite energy approximation, there have been practical demonstrations of the Bessel beam. When Durnin et al. [214] first presented an experimental demonstration to generate a Bessel beam, they placed an annular slit at the back focal plane of a converging lens which was illuminated by plane waves. This simple technique of truncation of the beam with an aperture suffers several drawbacks like,

a , the slit truncation method allows only a part of the beam, thus it encounters high loss.

b , due to the hard aperturing by the slit, diffraction causes oscillation in the on-axis intensity of the Bessel beam.

Research has been carried out to optimize the depth of focus of the Bessel beam. Classical techniques have their disadvantage of generating a Bessel beam with not perfect on-axis uniformity and thus with the presence of oscillation in the on-axis profile, as reported by Durnin et al. [214]. Vetter et al. [137] proposed a technique to generate the Bessel beam using a simple optical component that closely resembles a cylindrical lens changed into a closed ring-shape form. This lens focuses the incoming beam into a sharp-ring-shaped focal plane, after which its Fourier transform gives a high-quality zeroth-order Bessel beam with an extremely narrow ring of light. This is a similar technique used by Durnin but they managed to overcome the inherent loss of an annular aperture. Recently, Stoyanov et al.[215] have used the idea of Optical Vortex (OV) and presented an innovative method for producing extended-range Gauss–Bessel beams, which significantly surpass the conventional techniques that typically result in only a few centimeters of beam propagation. As these beams travel over long distances, their quality greatly outperforms Gauss–Bessel beams generated by low-angle axicons and is comparable to the beams described by Vetter.

Here, in our thesis, we have used an axicon because of its simplicity, low cost, ease of implementation, and good results obtained before, creating a Bessel-Gauss beam. In addition, the Bessel beam generated by an axicon finds important applications in laser machining due to the high damage threshold and broad wavelength coverage offered by them [216]. Therefore, we will discuss in detail the Bessel beam generated by an axicon.

For the laser system, we use the ASUR (Applications des Sources laser Ultra-Rapides) platform [217] to explore the capabilities of Bessel beam shaping for micromachining at the (sub)-micrometer scale. ASUR delivers large spectral bandwidth ultrashort laser pulses in the near-infrared (800 nm 23 fs nominal, 760-840 nm spectral bandwidth, 1 mJ, 100 Hz). In particular, it provides the advantage of easily studying the interest of varying the pulse duration on a large temporal range (from femtosecond to picoseconds) for Bessel beam micromachining (as explored in Chapter 4) through simple detuning of the optical compressor of the laser system. We also benefit from the previous studies and optical developments on this laser system and its micromachining test-bench [23] [218] [24].

2.1.2 Fundamentals of Bessel beam

The mathematical construction of the Bessel beam was first proposed by Durnin [219][213] as a solution to the Helmholtz equation. The electric field of the Bessel

beam is defined as [220],

$$E(r,\phi,z) = a_0 J_n(k_r.r).exp(i(k_z z).exp(\pm n\phi), \tag{2.1}$$

where r, ϕ, and z represent the radial, azimuthal, and longitudinal coordinates respectively. a_0 is the amplitude of the electric field and J_n defines the nth order of Bessel function. k_r ($k\perp$)=$ksin\theta$ & k_z($k\parallel$)=$kcos\theta$ are the radial and longitudinal wave vectors respectively. Here θ is referred to as the half-cone angle of the Bessel beam, which we will describe later. This transverse and longitudinal wave vector is related to k as,

$$k = \sqrt{(k_r^2 + k_z^2)} = \frac{2\pi}{\lambda}, \tag{2.2}$$

In this thesis, we will deal with only zeroth-order Bessel beam (n=0), and the electric field for a zeroth-order Bessel beam is defined as follows,

$$E(r,\phi,z) = a_0 J_0(k_r.r).exp(i(k_z z) = a_0 exp(ikzcos\theta) J_0(krsin\theta), \tag{2.3}$$

Here, the intensity associated with the Bessel beam is proportional to J_0^2 which can be expressed as,

$$I(r,z) \propto J_0^2(krsin\theta), \tag{2.4}$$

This expression represents a beam whose central core is surrounded by the concentric lobes shown in Figure 2.1 (right). This is often called the transverse intensity profile of the beam.

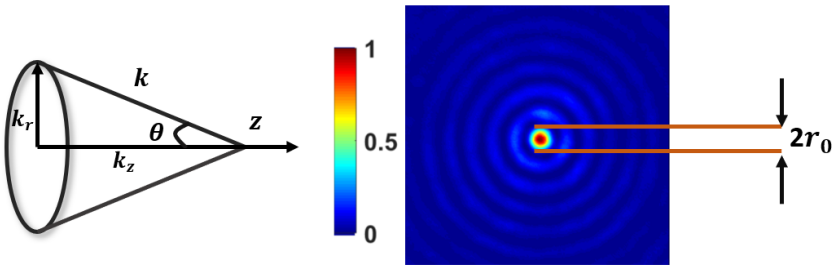

Figure 2.1 – Schematic to show the relation between wave vectors that form a Bessel beam (left) and the transverse intensity profile of Bessel beam with a central core size of $2r_0$ (right)

The propagation of the Bessel beam can be considered as a superposition of an infinite number of plane waves. The wave vectors of these plane waves can be imagined as distributed over a cone that is centered on the propagation(z) axis as shown in Figure 2.1(left). As we see from Figure 2.1(left), the angle θ of the zeroth-order Bessel beam, often referred to as the half-conical angle is expressed as,

$$\theta = tan^{-1}(\frac{k_r}{k_z}), \tag{2.5}$$

2.1.3 Axicon generated Bessel beam

The standard refractive axicons are made of conical lenses or prisms. In an ultrafast laser system, to avoid chromatic dispersion, reflective axicons are preferred over refractive ones. In our work, we have used a refractive axicon. When a collimated monochromatic Gaussian laser beam with a flat phase front is directed straight onto an axicon lens with a specific refractive index (n) and base angle (α), the beam splits into parts having a circular symmetry. The beam deviates toward the central axis, following the direction of propagation, and intersects, creating an interference effect. In essence, the interferences between the two beam portions as they converge on the central axis are responsible for generating the Bessel beam properties.

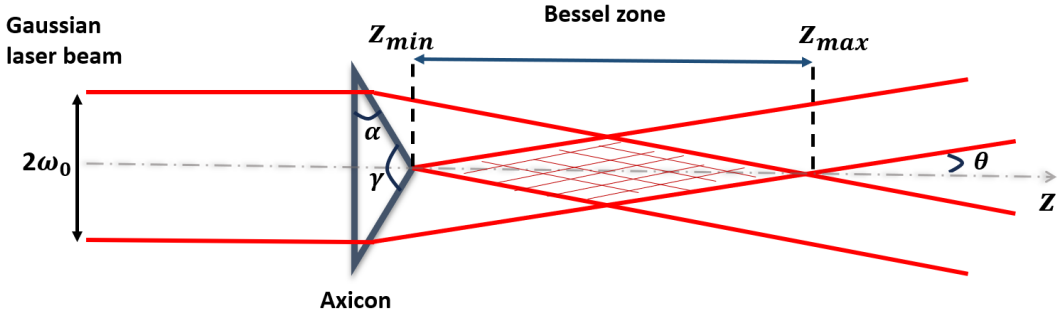

Figure 2.2 – Schematic of generation of Bessel beam with an axicon of base angle α, and tip angle γ=$\pi - 2\alpha$, from an incident Gaussian beam with waist ω_0

Figure 2.2 shows the schematic of the principle of Bessel beam generation through an axicon.

The base angle (α) is linked with the tip angle (γ) by the expression,

$$\alpha = (\pi - \gamma)/2, \tag{2.6}$$

With geometrical optics consideration, Snell's law at the inclined surface of an axicon gives rise to the following expression of the cone angle,

$$\theta = arcsin(nsin\alpha) - \alpha, \tag{2.7}$$

where n is the refractive index of the axicon. The refractive index at 800 nm is considered as 1.45 for fused silica.

The half-conical angle affects the machining of densely spaced nanochannels, which is our primary aim to carry on in this thesis. The conical angle of the Bessel beam is important as the capability to write down high-quality regular channels depends on the focusing (Bessel beam angle) because of sensitivity to nonlinear propagation. The use of high angle Bessel beam to drill nano-channels shows good resistance to the Kerr effect (when lower energy is used), limits the energy losses, and reduces the plasma screening effect as shown in the work of [147]. This is because the energy is

going by the sides with energy widespread along the transverse axis when propagating thus limiting the clamping effect occurring when the axial energy deposition is at play. In addition, literature has shown that increased conical angle results in increasing the nano-channel diameter. A larger channel diameter is indeed obtained when increasing the conical angle as expressed by Eq. 2.8 (given page 70) and experimentally demonstrated from 11° to 17° [21]. Conversely, a small conical angle yields a reduced diameter of the central lobe of the Bessel beam.

In our work, we expect a channel diameter to be small (~200 nm) and adjacent channels to be densely spaced. In light of the latter, a high angle of the Bessel beam can be a disadvantage as the energy is spread over a large transverse distance thus propagating along (previous) perturbed/machined zones and thus 'testing' the self-healing capability of the Bessel beam. On the other hand, the research shows that small conical angles (~5° inside the sample) exhibit a disadvantage for ultrashort pulses because of the nonlinear dynamics played for this regime, compared to the longer ones [221]. The larger cone angles help to retain the propagation invariance of the Bessel beam and thus a uniform deposition of energy along the propagation results. For example, the machining of borosilicate glass with a small conical angle has resulted in discrete damage spots as shown by [222].

To show the influence of the conical angle on the machining with a Bessel beam, we present a few literatures. It was reported for the first time that an aspect ratio of 60-100 in transparent material was machined by varying the conical angle [22] of the Bessel beam. Vetter et al. have machined channels with a length of 170±10 μm in fused silica with a Bessel beam of the conical angle of 19.5° in the air [223]. A Bessel beam conical angle of 10° has resulted in machining channels with a high aspect ratio of 40 as reported in [224]. In practice, when machining the transparent materials, Bessel beams with angles ranging from 17° to 26° in air are employed. These angles, influenced by refraction, result in angles between 10° and 16° when the medium has a refractive index of ~1.5 at 800 nm wavelength [21] [225]. In the previous work of [218], the Bessel beam with the conical angle of 21.4° machined channels with depth of 9 μm at the front surface of the fused silica. The depth corresponds to an aspect ratio of 8, which is suitable for the fabrication of advanced optical components like photonic crystal structures with further downscaling of the spatial resolution. Based on these previous studies we carried out our machining experiment with a half-cone angle of 21.4° in air, which corresponds to an angle of 14.6° upon propagating through a medium of refractive index of 1.45 at 800 nm.

In Eq. 2.4, we depict the intensity profile of the zero-order Bessel beam. By examining the characteristics of the zeros in a Bessel function, the initial cancellation occurs at a specific value of 'r' where[220],

$$r_0 = \frac{2.405}{ksin\theta}, \tag{2.8}$$

This is the full radius of the central core. This amount is also often regarded as being equal to the FWHM (as it is usually done with diffraction-limited spots) and it is

therefore named the core diameter of the Bessel beam.

Now, we define the Depth of focus (DOF) of the Bessel beam. For an ideal Bessel beam, the intensity will no longer depend on the z-position along the propagation axis. Thus, according to Eq. 2.4, $I(r,z)$ becomes $I(r)$ for any z position of the beam. This is the reason we call the Bessel beam a "diffraction-free" or "propagation invariant" beam. But, in reality, the limitation of generating such a beam is caused by the optical elements of finite aperture. When a Gaussian beam with a half-width ω_0 is incident on the axicon, a Bessel beam with a DOF is produced up to z_{max} starting from the tip of the axicon (z_{min}=0). From Figure 2.2, we can express the DOF as,

$$DOF = z_{max} - z_{min} = \frac{\omega_0}{tan\theta} \tag{2.9}$$

Here, the "non-diffracting" length is established by the size of the input beam and the axicon's half-conical angle. The depth of field (DOF) of the Bessel beam is larger in several order magnitude (nearly 10 times larger) than the Rayleigh range of the Gaussian beams of the same spot size.

Advantage of Bessel beam over Gaussian beam There are certain advantages of the Bessel beam in controlling the depth of focus of the beam which the Gaussian beam lacks. We have shown a comparison of two beams in Figure 2.3.

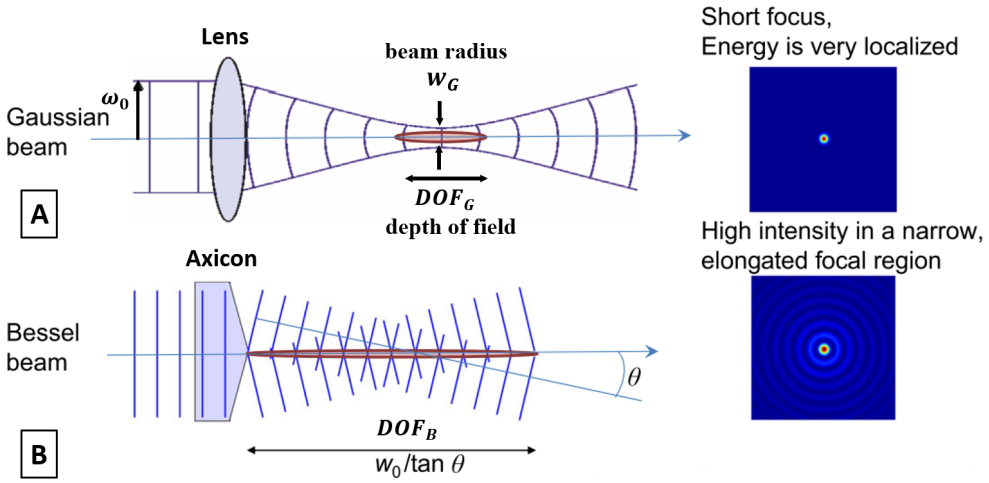

Figure 2.3 – A) Focusing of Gaussian beam with a lens and B) Generation of the Bessel beam [226].

A Gaussian beam with an incident waist of ω_0 which is focused through a lens as shown in Figure(A), can be mathematically expressed as [227],

$$I(r) = I_0 e^{\frac{-2r^2}{\omega_0^2}} \tag{2.10}$$

After the focus, the beam radius w_G and the DOF (given by twice the Rayleigh range) are expressed as,

$$w_G \sim \frac{\lambda f}{\pi \omega_0} \sim \frac{2}{ksin\phi}; DOF_G = \frac{2\pi w_G^2}{\lambda} \sim k w_G^2, \tag{2.11}$$

Here, λ is the wavelength, the wavevector k is defined as k=2π/λ, and ϕ is the diverging angle expressed as $tan\phi = \omega_0/f$.

The Gaussian beam radius w_G is defined at $1/e^2$. However, this is not convenient to compare to the Bessel beams, whose diameter is defined as FWHM. To address this, we use a coefficient derived from Gaussian beams, where the ratio between the radius at $1/e^2$ of maximum intensity (typical waist definition) and the diameter FWHM is approximately $(1/\sqrt{2ln(2)}) \sim 0.85$. Applying the same coefficient as the two distributions well overlap (central lobe), we define the waist at $1/e^2$ for the Bessel beam

$$w_B = \frac{r_0}{\sqrt{2ln(2)}} \sim \frac{2}{ksin\theta} \tag{2.12}$$

Thus we arrive at an identical expression as that of the Gaussian beam:$w_B \sim w_G$ Consequently, the diameter of the central core in a Bessel beam closely matches the diameter of a Gaussian beam focused at the same angle θ.

Then the DOF therefore writes as,

$$DOF_B = 2z_r = \frac{\omega_0}{tan\theta} \sim k w_B \omega_0, \tag{2.13}$$

Compared to the expression of Eq. 2.12 for the Gaussian beam, this expression indicates that for the Bessel beam, there is an extra control parameter of incident beam waist ω_0 to adjust the DOF, along with the base angle α which is directly linked to the half cone angle θ. For a Gaussian beam, the beam waist solely determines the DOF. With a Gaussian beam, it is impossible to change the DOF without changing the beam waist and thus the optical elements (lens in our case) through which the beam is focused. Bessel beam shows advantage by overcoming this limitation and thus we can also conserve the core diameter of the beam while changing the DOF.

Placing ourselves in the experimental condition, for example, with an incident beam size (ω_0) of 3 mm, with an axicon of $\alpha = 1°$, the value of θ=0.45°. With this beam size, we find the DOF of the Gaussian beam as ~8 mm when it is focused with a lens of equivalent numerical aperture. Whereas, the DOF of the Bessel beam is ~382 mm. This confirms the longer DOF for the Bessel beam over Gaussian one.

We have performed experiments to show the influence of the incident beam size over the DOF, where we have changed the incident beam size from 3 mm to 6 mm, to control the DOF of the generated Bessel beam as shown in Figure 2.4. The DOF measured with a 3 mm incident beam is 28.2 cm at FWHM, whereas a 6 mm beam yields a DOF of 53.2 cm at FWHM. Therefore, the DOF changes in proportion to the incident beam size ω_0. This process proved to keep the core diameter of the beam unchanged as the measured core size is the same (45 μm) for both cases. We have

simulated the experimental results with a homemade simulation tool that we will be discussing in the next section.

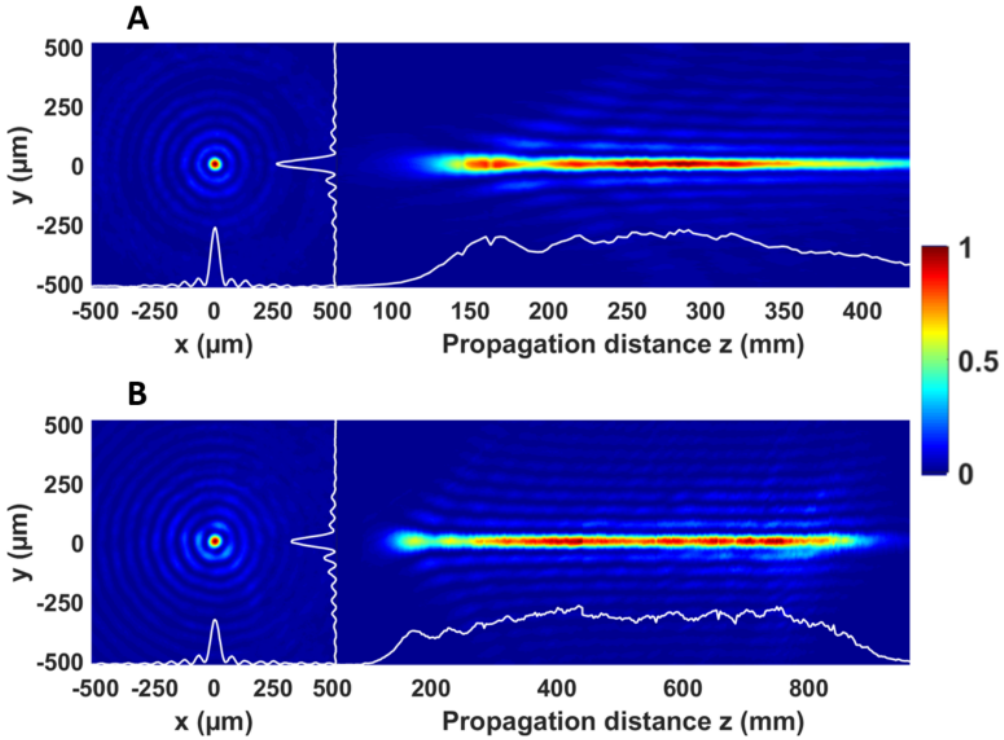

Figure 2.4 – A) Bessel beam generated with an incident beam waist of 3 mm and B) Bessel beam generation from a 6 mm incident beam. The DOF measured with a 3 mm incident beam is 28.2 cm, whereas a 6 mm beam yields a DOF of 53.2 cm.

Besides the control over DOF, the Gaussian beam limits the crater depth (≤500 nm) in machined materials because of executing a short depth of focus. Also, the plasma shielding effect [228] [229] [230] is difficult to avoid with the Gaussian beam. The way the laser energy is deposited by the sides coupled with the "self-healing" capability of the Bessel beam helps to overcome this plasma shielding effect. Bessel beam is thus the tool of choice to produce a long cylindrical channel compared to a Gaussian beam.

2.1.4 Simulation tool

We have developed a simulation tool at LP3 with the help of Matlab software. As it will be justified later, we use a Gaussian beam with a waist of 3 mm and a wavelength of 800 nm is passed through an axicon of base angle (α=1°) to generate a Bessel beam. The refractive index of glass at this wavelength is 1.45.

The simulation tool is developed for the first Bessel region due to the paraxial approximation required by the scalar Fresnel diffraction theory. However, the beam

propagation in the second Bessel region (which will be defined later in section 2.5.2) is closely related to the first region by a $4f$ demagnification system by taking into account the image relay function with a demagnification factor of 49.5.

Modeling of propagation As it has been developed in a previous work from lab [218], "According to the Fresnel theory, the optical field at a position z is depicted by a 2D complex amplitude $A(x,y,z)$. In the Fourier plane, this can be decomposed as a sum of plane waves (the "angular spectrum"). Each of the plane waves is defined by a wavevector $\vec{k} = (k_x, k_y, k_z)$. If the optical field encounters an obstacle, then $A(x,y,z)$ is multiplied by the corresponding complex transmittance function $T(x,y)$. This enables us to depict within the same formalism pure phase elements (the axicon, the air/glass interface) as well as obstacles that affect the amplitude (annular aperture, pre-existing nanoholes in case of machining) placed in any plane z along propagation. In the Fourier space, propagation along a distance dz is calculated by multiplying the angular spectrum by the Fourier Kernel propagator,

$$P(x,y,dz) = e^{ik_z dz} = exp[i\,dz\sqrt{k^2 - k_x^2 - k_y^2}], \tag{2.14}$$

Note that we neglect here the effects of the spectral bandwidth of our laser pulse. The optical field after propagation can be written as

$$A(x,y,z+dz) = \mathscr{F}^{-1}\{P(x,y,dz).\mathscr{F}\{A(x,y,z).T(x,y)\}\} \tag{2.15}$$

where $\mathscr{F}$ denotes the Fourier transform. The 3D complex amplitude along propagation is obtained by applying this algorithm step by step along z, and the intensity is finally obtained by $I(x,y,z) = |A(x,y,z)|^2$."

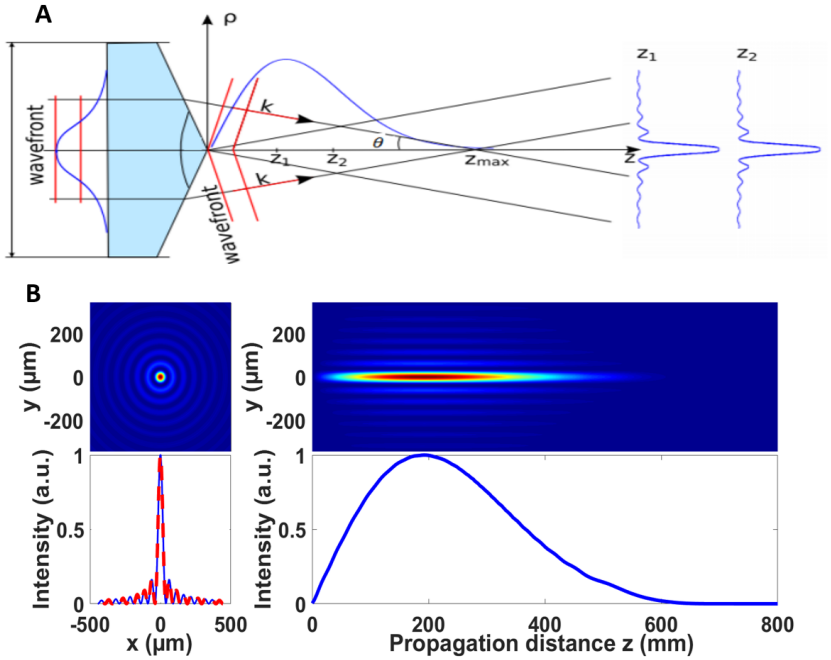

Figure 2.5 – A) Creating a Bessel beam (BB) involves using an ideal axicon to illuminate a Gaussian beam with its beam waist located at the front surface of the axicon. The flat wavefronts of the Gaussian beam in the vicinity of its beam waist are represented by straight red lines. The wavevectors $'k'$ of the plane waves composing the Bessel beams are situated on the surface of a cone with a semi-apex angle of θ. z_{max} represents the maximum distance of propagation where the Bessel beam persists. B) Bessel beam generated through a perfect axicon of 1° base angle.

We have displayed the schematic of Bessel beam generation and our simulation of the beam with a perfect axicon in Figure 2.5. The propagation of the Bessel beam right after the axicon is shown in Figure 2.5. The left part of Figure 2.5(B) shows the transverse profile of the Bessel beam with an intense central core surrounded by rings named the lobes of the Bessel beam. The intensity of the lobes decreases as we move away from the center. The right part of the image shows the propagation of the beam along the optical z-axis called the longitudinal profile of the beam.

On-axis oscillation In practice, using an industrial axicon gives rise to the undesired modulation in intensity profile which affects the results after. The on-axis intensity profile of the Bessel beam is not only caused by the hard aperturing but also by the tip of the axicon that is defined by the conical geometry. Usually, the tip loses this conical shape and exhibits a round tip instead. The on-axis intensity modulation and the propagation of the Bessel beam are affected by the round tip. We have simulated the beam propagation through the axicon by keeping in mind these two factors. As we can observe in Figure 2.5(B), the beam through perfect axicon shows a smooth on-axis intensity profile. We have simulated two cases here to show the dependence

of DOF and the on-axis oscillation on the round tip width ('a' as described in Figure 2.6(a)) and also on the imperfection of the base angle α.

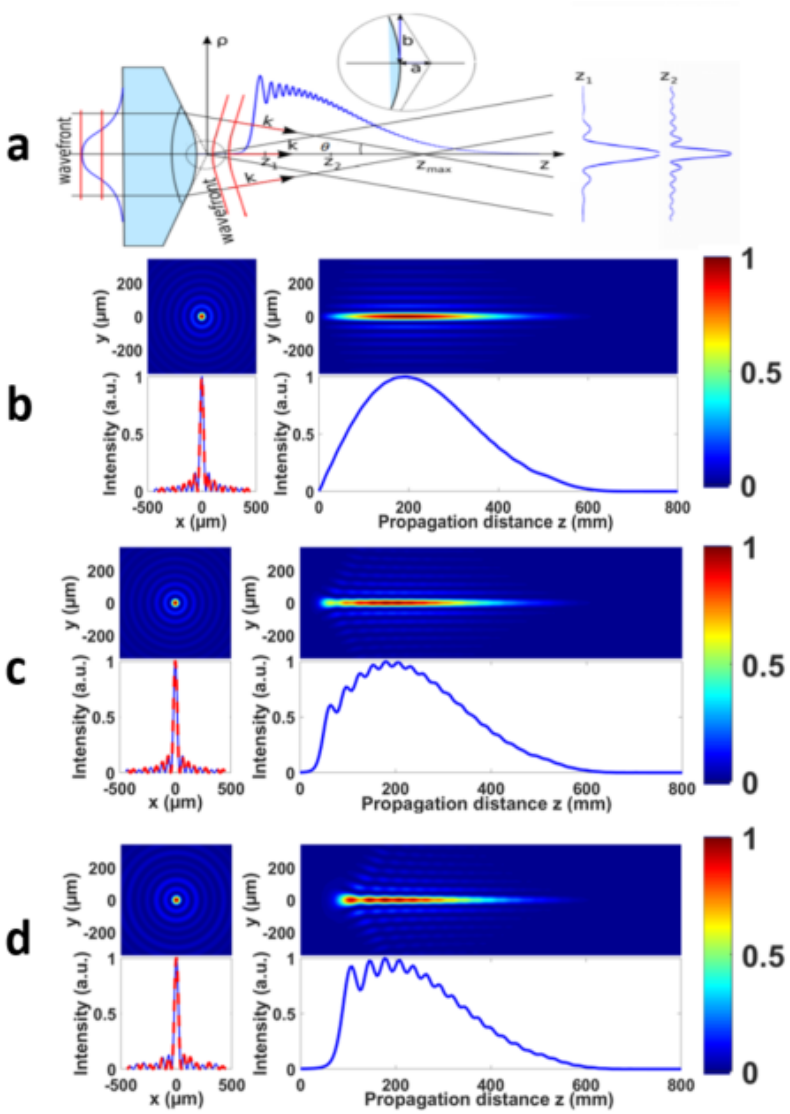

Figure 2.6 – a) Schematic of the impact of the rounded tip of the axicon: The new wave refracted by the round tip travels beyond the axicon and interacts with the Bessel beam, causing axial modulation of the optical intensity with a period of $[\lambda/(1-cos\theta)]$, where λ represents the wavelength of the wave within the medium. The round tip of the axicon was approximated by a hyperbola of revolution with two parameters 'a' and 'b', as detailed in [231] b) Generation of Bessel beam with a perfect axicon of the base angle of 1° and a round tip width of a=0 μm; c) Generation of Bessel beam with a round tip axicon of the base angle of 1° and a round tip width of a=5 μm; d) Bessel beam generated with round tip axicon of a=10 μm, with the same base angle. The DOF gets shortened with larger values of tip width.

Axicon Parameters	Perfect (a=0μm)	round tip (a=5μm)	round tip (a=10μm)
DOF (cm)	30.4	29.2	26.5

Table 2.1 – DOF measurement of Bessel beam with different round tip widths obtained from experiment and simulation.

Figure 2.6 shows the impact of the round tip width a. When we change the round tip width from a=0 μm (see Figure 2.6(b))to a=5 μm (see Figure 2.6(c)) and a=10 μm (see Figure 2.6(d)), we observe distinguishable intensity fluctuations along the propagation z-axis.

In Figure 2.6 we observe that along with the on-axis intensity oscillations, the DOF of the beam also gets shorter with increasing values of tip width(a). We have listed the values of DOF for the three cases shown in Figure 2.6(b), Figure 2.6(c), and Figure 2.6(d), in the table below.

Next, we have tested another imperfection which is caused by the imperfect base angle (α) usually encountered with an industrial axicon.

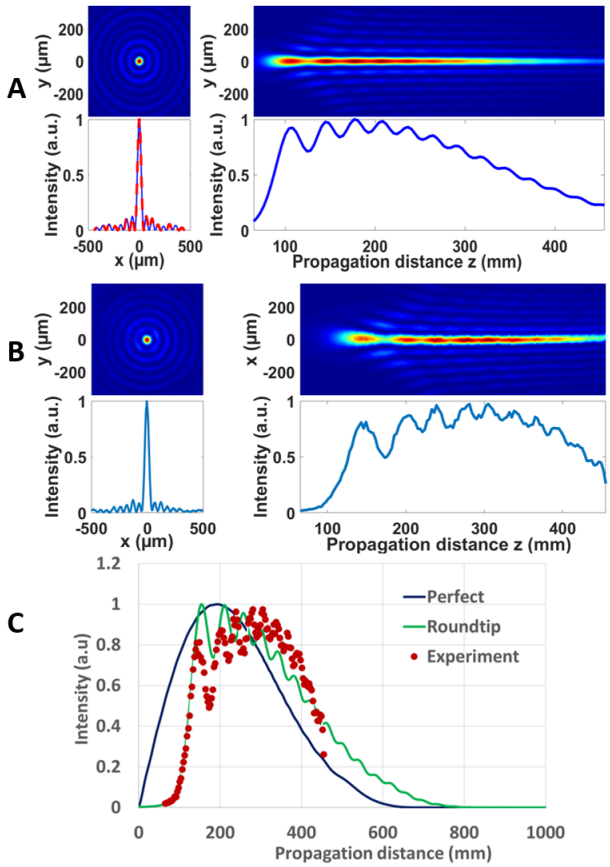

Figure 2.7 – A) Bessel beam simulation with a round tip axicon with α=0.83°, a=10 μm. The values of α and a are adapted according to the experimental beam profile; B) Experimental beam profile showing the imperfect nature of the axicon tip. C) Compared longitudinal propagation profiles of Bessel beam of three cases of perfect (α=1°, a=0 μm), round tip (α=0.83°, a=10 μm), and experimental one.

We have obtained the beam experimentally as shown in Figure 2.7(B). Next, the simulation was carried out according to the beam profile which was obtained in experimental configuration (see Figure 2.7(A)). The base angle α was adjusted to α=0.83° instead of 1°, to obtain the best match between the experiment and simulation. In the following, we have kept the constant value of a=10 μm.

We have further compared the values of core diameter and DOF which were obtained from Figure 2.7(A) and Figure 2.7(B), with the theoretical value of core diameter and DOF calculated from Eq. 2.8 and Eq. 2.9, respectively. The theoretical value of the core diameter of a 1° axicon is 39 μm measured at the first zero of the transverse profile from the center, and the DOF is 38 cm. The best match of the DOF with the theoretical value is also found with the perfect axicon (30.4 cm). The difference mainly comes from the quality of the axicon used (the accuracy of the 1° expected angle is questionable, as well as the perfect sharpness of the tip).

Numerous researches have been done to study the Bessel beam generation through round tip axicon. Detailed theoretical studies of the spatial distribution of the Bessel beam generated from a round tip axicon have been conducted by Brzobohatý et al. [231]. They have shown a spatial filtering at the Fourier plane helps to recover spatial distribution and could remove the undesired on-axis intensity modulation. Müller et al. [**MÃijller2016**] have also shown that the Bessel beam generated from the round tip axicon is suffering modulation including the core diameter of the beam. In addition, they have also discussed about effects of astigmatism on Bessel beam generation [**MÃijller2016**]. The round tip of the axicon causes the ellipticity of the central core diameter [**MÃijller2016**]. Dudutis et al. [232] have demonstrated that ellipticity can favor the creation and propagation of cracks in the transverse direction in the bulk of glass with positive effects in the applications of glass cutting.

2.2 Further beam shaping method: Segmented Bessel Beam

In light of further advancement in Bessel beam research, there has been a constant need for modifying the depth of field of the beam. Indeed, the DOF determines the length of the machined structures fabricated with laser micro-machining. The advantage of a segmented beam generated by placing an object in front of the axicon gives flexibility to control the position and size of DOF while keeping the core size of the beam constant. In our work, we had to shorten the length of the Bessel beam for our interest in machining small aspect ratio nanochannels.

Among some notable works on segmented Bessel beams, Rao et al. [216] generated high on-axis peak intensity, segmented, smooth, zero-order quasi-Bessel beams with tunable ranges by illuminating the axicon with hollow Gaussian beams (HGB) of different orders. In their approach, they have overcome the loss of energy issues which was present in the case of placing a ring aperture. Additionally as reported by Rao et al., "several other works have been carried out to remove on-axis oscillations with techniques like Fourier filter [233], or by blocking the beam passing through the tip of axicon [**MÃijller17**], but all these methods lower the beam energy. This drawback is acceptable if we use a large amount of energy. There is also a lack of control to generate a Bessel beam at a desired axial position along the propagation with an axicon because the beam is created right after the axicon and in the tunability of the Bessel beam".

This property to control the focal zone is important for applications like depth-selective material processing or for structured illumination in optical imaging which requires a Bessel beam with shorter focal zone. A new approach to beam shaping was proposed by Müller et al. [**MÃijller17**] by placing a ring aperture after the axicon, and thus by generating a segmented Bessel beam as shown in Figure 2.8. The width of the apertures has been optimized to have the shortest possible depth of focus of the Bessel beam.

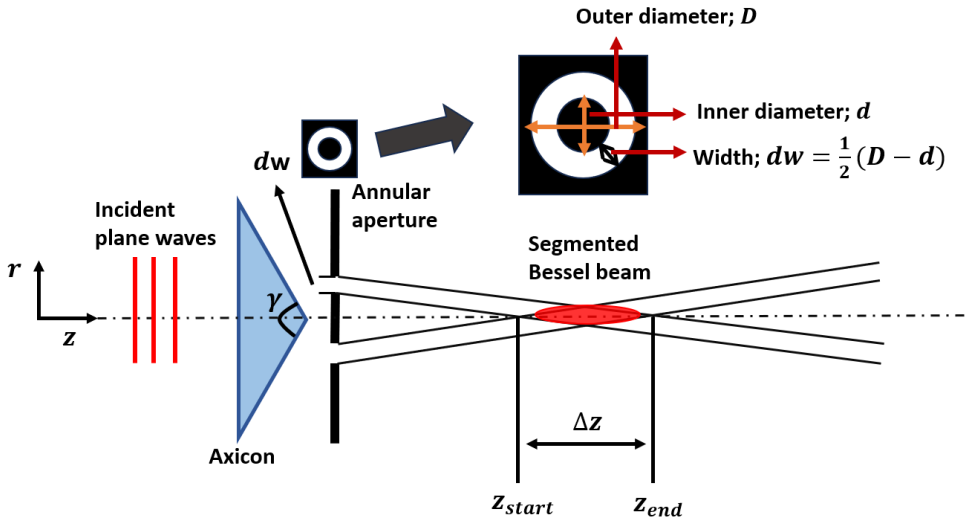

Figure 2.8 – Schematic drawing of the segmented Bessel beam region using annular aperture with aperture width dw. The tip angle of the axicon is γ. The annular aperture in the front of the axicon restricts the Bessel beam region such that we get a smaller, segmented Bessel beam region Δz at position z_{start} until z_{end}.

The outer and inner diameters are noted as D and d respectively, and the width is calculated as $dw = \frac{1}{2}(D-d)$. The width determines the interference region over which the Bessel beam would form, and its transverse positioning also determines the position of the segment along the optical axis.

2.2.1 Customization of the depth of focus

Since we know that the length of the channels through machining is controlled partly by the DOF of the beam, we looked into optimizing the annular apertures to obtain the preferred DOF (~20 μm) of the segmented Bessel beam to machine channels with desired length and small aspect ratio (~1:10). Müller et al. [**MÃijller17**] have performed an analytical calculation to find the aperture width for having the shortest segmented Bessel beam. The aperture producing the shortest Bessel beam depends on its radius, the conical angle of the axicon, and the wavelength of the incident beam. In the classical regime, the length of the segmented beam is proportional to the aperture width dw. However, when decreasing dw to a narrow aperture, the opposite trend is observed (i.e., lengthening of the DOF) due to the effect of diffraction. Hence, the optimal aperture width is to be found between the Fraunhofer and classical limit. Müller et al. [**MÃijller17**] tried to derive a scale-invariant analytical estimate in a simple expression by finding an intersection of the Fraunhofer and classical limits. The optimal aperture width is found to be 200 μm for the shortest segment (15 μm) of the Bessel beam, which lies in between the Fraunhofer (100 μm) and classical (800

μm) limit.

We carried out a numerical simulation to test the beam truncation with different aperture widths. This numerical study provides us with a range (4 mm - 100 μm) of the width of the annular aperture (starting from no truncation of the beam) which can make an optimized segmented Bessel beam as shown in Figure 2.9. This numerical simulation helped to justify the choice of annular width and also to find out the limitations of the truncation method for achieving a short segment of DOF. The optimized aperture width is around 500 μm and below and upper of this value, it gets longer again.

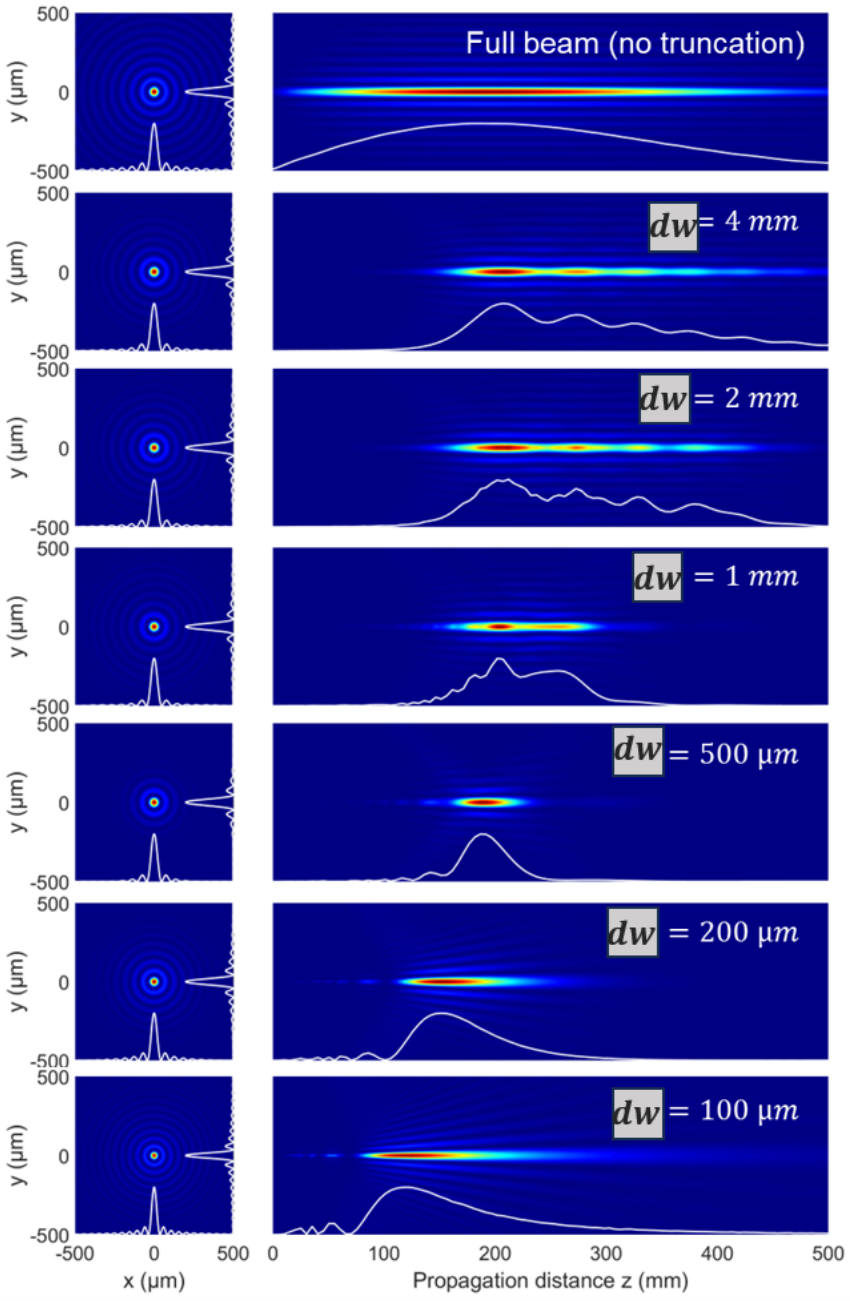

Figure 2.9 – Simulations of beam propagation of the truncated Bessel beam right after the axicon and the annular aperture (i.e. before the $4f$ demagnification system) for different values of the width dw of the annular aperture. The incident beam comes from the left.

These numerical studies provided us with information on a range of widths that can be explored in experimental configurations.

2.3 Experimental arrangements

In this section, we will discuss in detail how we performed our experiment, starting from the initial Gaussian beam to generating a segmented Bessel beam with an advanced beam shaping method, inspired by the work of Müller et al. [**MÃijller17**] After implementation of demagnification set-up with a reducing factor of 49.5 has been realized to create the micro-Bessel beam. This micro-Bessel beam has later been utilized for machining purposes with different configurations in fused silica.

2.3.1 Beam waist retrieval of incident Gaussian beam

The beam waist of the incident Gaussian beam influences the DOF of the generated Bessel beam as we can see from Equation 2.13. Therefore, it is important to measure the beam waist of the incident Gaussian beam. We have followed the transmission measurement through an aperture when a Gaussian beam is incident on it. The schematic of the beam transmission is shown in Figure 2.10.

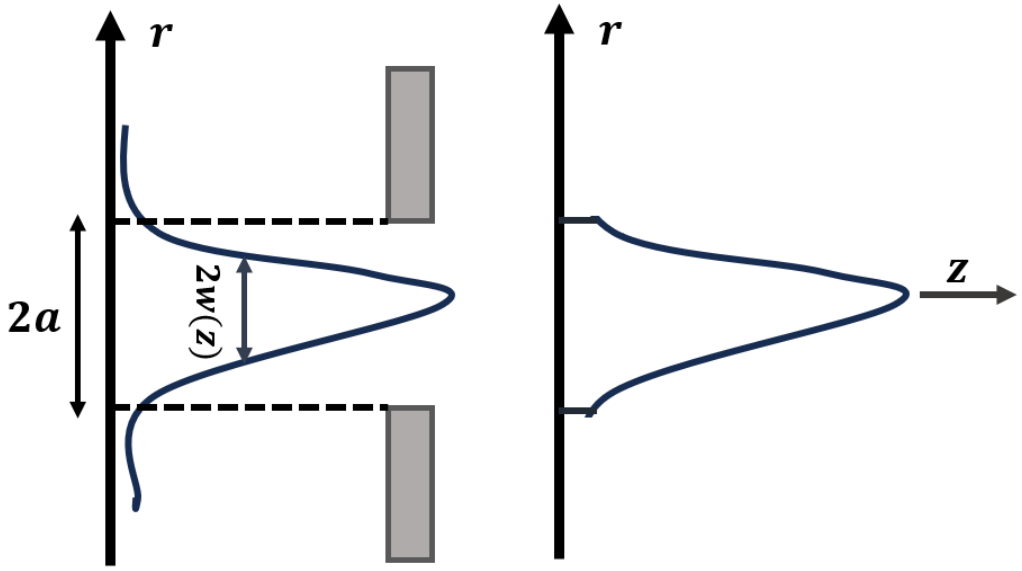

Figure 2.10 – Schematic of the Gaussian beam passing through an aperture of diameter of $2a$.

When a Gaussian beam is traveling through an aperture, the transmission through the aperture is calculated as the ratio of transmitted power to incident beam power. This is further expressed in terms of beam diameter as [234],

$$T = 1 - e^{\frac{-2a^2}{w_0^2}}, \tag{2.16}$$

Here $2a$ is the total aperture diameter that has been inserted in the beam path and w_0 is the Gaussian beam waist. When the aperture is larger than the beam size,

the power is constant, and as the aperture size keeps diminishing, the power starts to decrease and then it reaches near zero. For the Gaussian beam with 1 *ps* pulse duration, we obtain a curve that is shown in Figure 2.11.

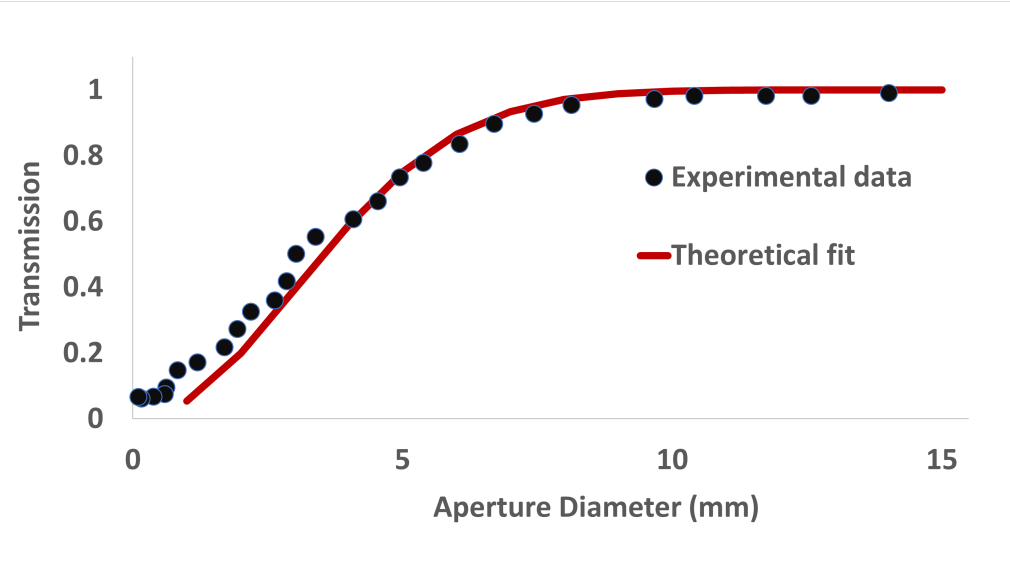

Figure 2.11 – Synthesis curve for the Beam waist retrieval. It has been compared and best fit against the theoretical curve calculated from Equation 2.16. The beam waist defined concerning $1/e^2$ is determined to be 3 mm.

We fit this curve with a numerically calculated curve with the help of Equation 2.16 and with w_0 as a free-fitting parameter. The best fit gives $w_0 = 3\ mm$.

2.3.2 Experimental Set-up

Using the ASUR platform, we generate a Bessel beam (core size of 0.96 μm at FWHM, Depth of field of 15 μm) with the help of an axicon (1°, Altechna, $1-APX-2-H254-P$, $n = 1.45$). The entire beam shaping set-up is shown in Figure 2.12.

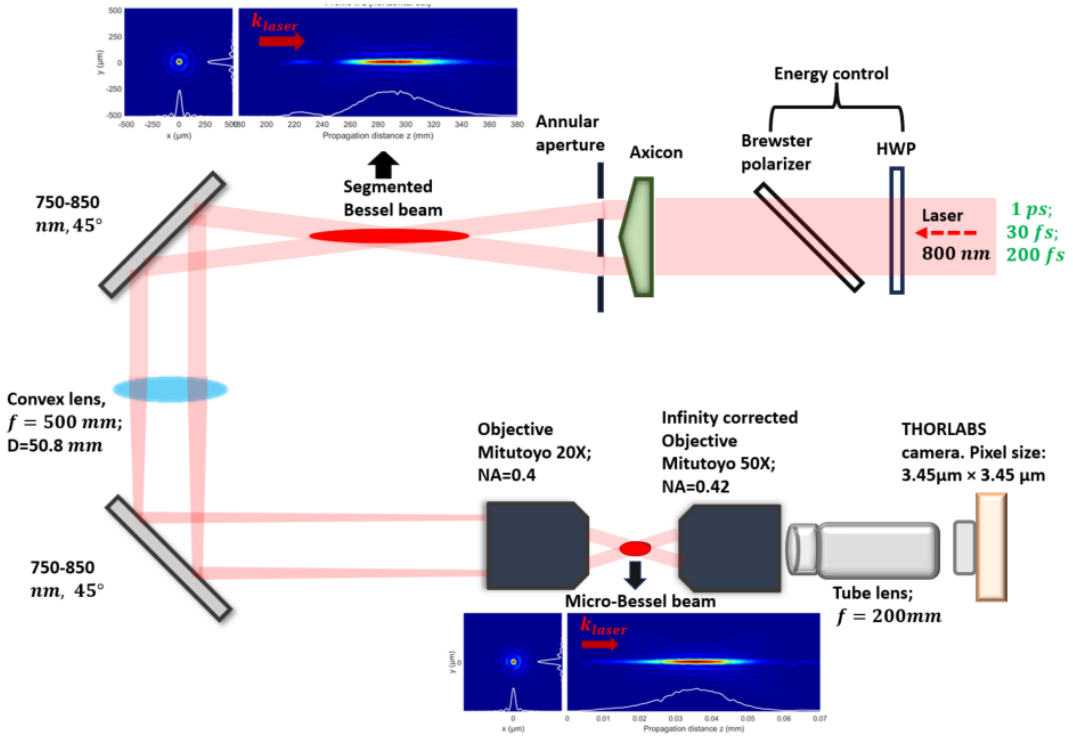

Figure 2.12 – Schematic of experimental set-up showing the beam shaping arrangement with an axicon of base angle of 1°. The demagnification setup with a 500 mm lens and an objective lens of 20X helps to form the micro-Bessel beam. This beam is imaged with a homemade telescopic system comprised of a 50X objective and a 200 mm tube lens. A Thorlabs camera was used to image the profile afterward.

Before the axicon, we place the combination of a half-wave plate and a polarizer to control the energy of the incident beam. We add an annular aperture to generate the truncated Bessel beam with an extra control of the non-diffracting length. In our work, we have tested apertures with widths of 200 μm, 300 μm, 400 μm, 500 μm and 600 μm, varying from classical to Fraunhofer diffraction limit. We have tested these annular apertures of different widths by characterizing the beam profile through them. To further downscale the shaped beam, we build up a demagnification set-up as shown in Figure 2.12, made up of a lens of focal length of 500 mm and an objective lens with a magnification of 20X (20X, $NA = 0.4$, $f = 10\ mm$, Mitutoyo NIR, working distance 20 mm). This demagnification set-up along with an axicon of the base angle of 1° helps to generate a micro-Bessel beam of core size of 0.96 μm, which is favorable to create short microchannels. After we have placed an imaging system that comprises another infinity-corrected objective lens with a magnification of 50X (50X, $NA = 0.42$, $f = 4\ mm$, Mitutoyo NIR, working distance 17 mm) and a tube lens of the focal length of 200 mm, along with a THORLABS camera. The micro-Bessel beam forms in the air in between two microscopic objectives. We recorded the 2D intensity distribution of the beam by axially scanning and recording the transverse intensity distribution at

each plane by translating the $50X$ objective on a motorized stage along the optical axis with 1 μm steps. After we stack all the images together. These images are numerically treated to measure the central core size and depth of field of the beam, and also to reconstruct the entire beam. Recording the beam requires high mechanical stability when translating with the motorized stage with the camera for beam imaging. Since this was not the case, we reconstructed the beam numerically, stitching all the images plane by plane to suppress the distortion due to vibration.

The translation axis of the camera was not perfectly parallel to the laser beam, which has been treated numerically while reconstructing the 2D beam profile. The intensity distribution of the micro-Bessel beam remains constant for the three different (1 *ps*, 30 *fs* and 200 *fs*) pulse durations which we are going to use in our machining experiments as described in the next chapters. This is normal as the spectral content characteristics of the ASUR beamline used are the same whatever the pulse duration (use of chirped pulses to get the long pulse durations) and the spatial beam shaping method does not have any influence on the temporal profile of the beam.

2.3.3 Annular aperture calibration

The characterization of the beam through annular apertures of various width have been performed. We have followed our previous work [23] and further characterized annular apertures in more detail with width around ~400 μm. For each width of the aperture, we have tested three different sets of the annular aperture by varying the outer diameter and keeping the values of inner diameter as 2 mm,3 mm, and 4 mm except for the smaller width aperture (200 μm) where a smaller value was also tested. We have used three different combinations of inner and outer diameter for five different widths of the aperture, whose characteristics are summarized in the Table below. We have defined the parameters dw, d, and D in the Figure 2.8.

We placed these apertures at the back of the axicon and recorded the beam through them in several propagation planes, each of them equally separated with a given step adapted for one particular aperture. For example, to record the beam in the Bessel zone through the aperture of 2/2.8 (d/D), we have set a step of 3 mm and we have recorded 131 propagation planes of the beam. Later, we processed these images as described in section 2.3.2, to construct the 2D beam profile and the DOF profile. The interest in changing the diameter value for one single aperture width lies in showing the flexibility in selecting different regions to form the Bessel beam while keeping its core width constant. This property finds its applications in depth-selective material processing.

2.3.4 Beam characterization through various aperture widths

In this section, we will compare the profiles of segmented beams for different aperture widths and three different inner and outer diameters for a certain width. We check the beam profile, the value of core diameter, and the DOF of the beam for different apertures and compare them with their theoretical simulation to confirm

$dw(\mu m)$	$d(\mu m)$	$D(\mu m)$
200	1700	2100
	2000	2400
	3000	3400
300	2000	2600
	3000	3600
	4000	4600
400	2000	2800
	3000	3800
	4000	4800
500	2000	3000
	3000	4000
	4000	5000
600	2000	3200
	3000	4200
	4000	5200

Table 2.2 – List of annular apertures with their inner (d)/outer (D) diameters and widths used in the experiment. We characterized the beam propagation through them to find the optimized aperture width.

our experimental results. This procedure helps us to find the optimum aperture width with given diameters for machining further in fused silica.

200 μm

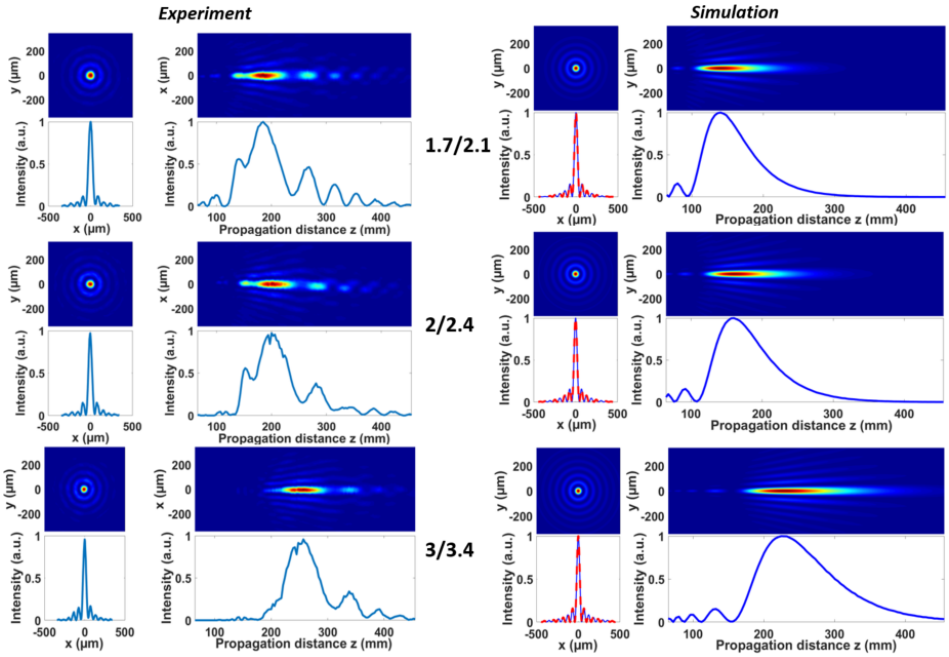

Figure 2.13 – Beam characterization through 200 μm aperture for three different sets of aperture with varied inner and outer diameter

300 μm

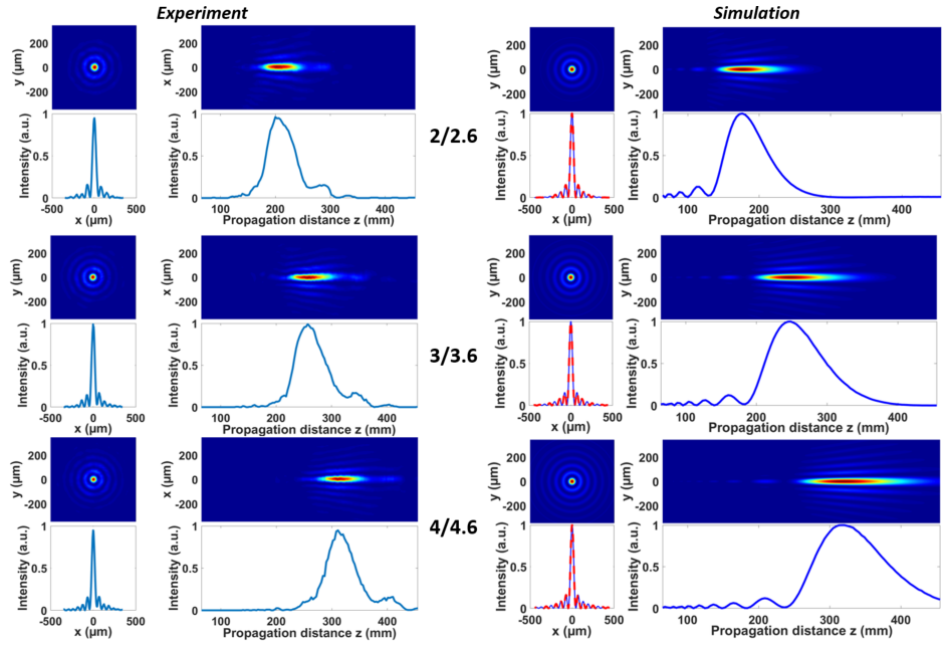

Figure 2.14 – Beam characterization through 300 μm aperture for three different sets of aperture with varied inner and outer diameter

400 μm

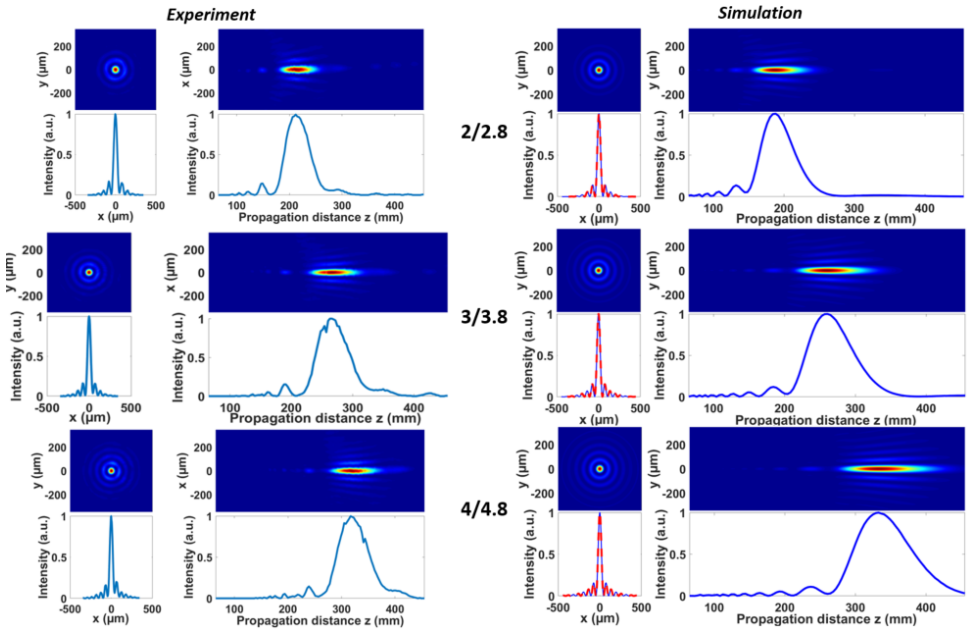

Figure 2.15 – Beam characterization through 400 μm aperture for three different sets of aperture with varied inner and outer diameter.

500 μm

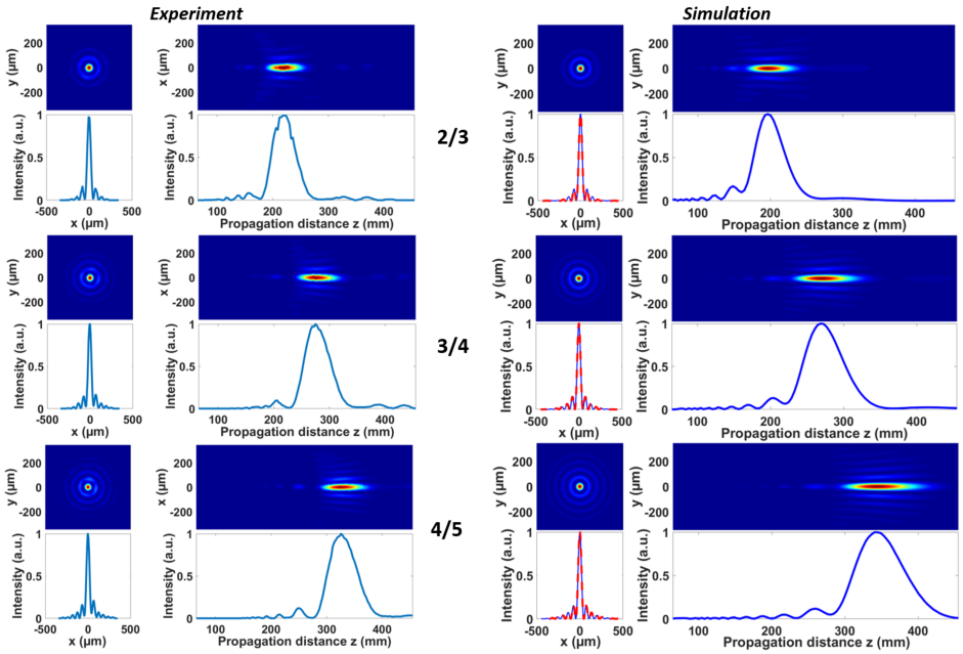

Figure 2.16 – Beam characterization through 500 μm aperture for three different sets of aperture with varied inner and outer diameter

600 μm

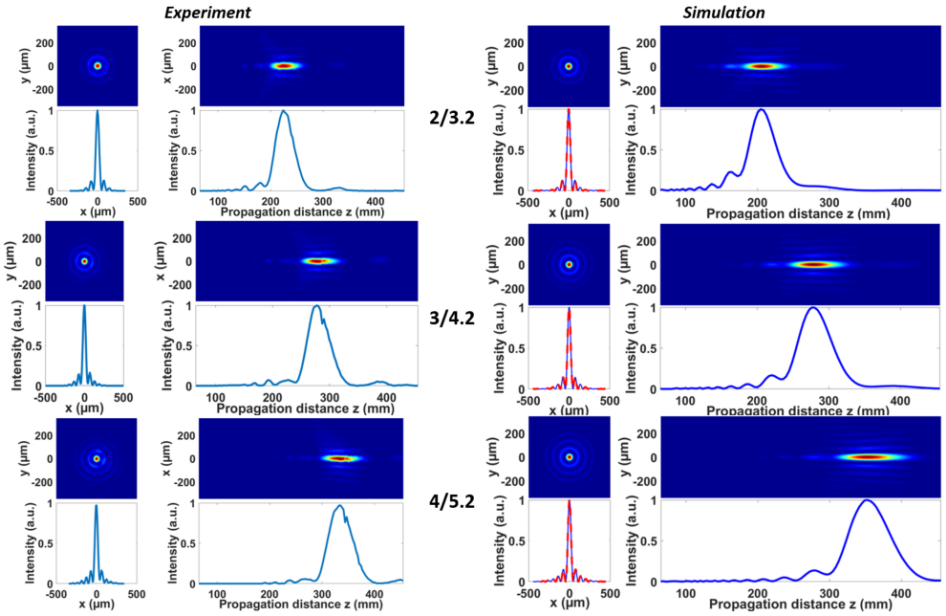

Figure 2.17 – Beam characterization through 600 μm aperture for three different sets of aperture with varied inner and outer diameter

The Bessel beam characterization through the three different apertures for each width has been shown in Figure 2.13 - Figure 2.17. We have measured the core diameter and DOF for each case as listed in the table (see Figure 2.18) below.

Aperture Width (µm)	Aperture (Inner/Outer diameter) (mm/mm)	Core diameter (µm)		Depth of Field (DOF) (mm)	
		Experiment	Simulation	Experiment	Simulation
	1.7/2.1	48	45	81	76
200	2/2.4	48	45	87	88
	3/3.4	48	45	66	112
	2/2.6	48	45	57	66
300	3/3.6	45	45	63	86
	4/4.6	45	45	59	109
	2/2.8	45	49	54	66
400	3/3.8	48	45	57	80
	4/4.8	45	45	69	98
	2/3	48	45	47	54
500	3/4	48	45	55	70
	4/5	45	45	63	82
	2/3.2	48	45	42	46
600	3/4.2	49	45	48	52
	4/5.2	45	45	55	72

Figure 2.18 – Measurement of Core diameter and DOF (measured at FWHM) for each of the apertures. The experimental values are compared with the numerical simulation.

We verified both experimentally and numerically the following key driving parameters for segmented Bessel beam control associated with the use of engineered annular apertures.

— The inner and outer diameters respectively allow for control of the longitudinal coordinate from which (respectively to which) laser machining can be performed, providing flexibility for in-depth selective processing.

— The width of the annular aperture controls the DOF extent. In the numerical studies described in Figure 2.9, we did observe that the DOF decreases with a reduction of the aperture width starting from the no truncation of the Bessel beam. The DOF begins to increase once again after reducing the width further beyond 500 μm. This observation would be at first glance counter-intuitive as according to Eq. 2.9 the DOF is expected to scale with the beam width (as selected by an aperture increasing size) and thus to be reduced for small apertures. However, as it was already numerically (Figure 2.9) and experimentally outlined [23] [**MÃijller17**], diffraction effects come into play when small aperture widths are used (going to the Fraunhofer limit) causing the beam to diverge and so con-

tributing to the DOF extension. This is perfectly shown here in our experiments (see Figure 2.13 - 2.17 where a more and more divergent beam is observed for smaller apertures) and corresponding simulations. In a way completing our analysis, we did observe in [23] that the DOF decreases with the reduction of the aperture width starting with no truncation of the Bessel beam but further is also large for small apertures. We here analyze with more precision this transition region given determining an optimized aperture for our targeted applications devoted to small aspect ratio machining.

— Concerning the DOF, some discrepancies exist between experimentally obtained and simulated values. In addition, for a given aperture width, its lateral distance from the laser axis (related to the inner diameter) provides a supplementary flexibility, with as predicted by the simulation an extension of the DOF when the annulus is located towards the edges of the beam.

— As expected, we also verify that the core diameter of the Bessel beam does not depend on the characteristics of the annular aperture (as shown in the table, Figure 2.18). A good agreement is observed between the experimental and simulated values for the core diameter for the ensemble of the aperture configurations that were tested.

We observed that the positioning of the apertures (of a certain constant width) concerning the incident beam influences the DOF. This last point is not intuitive. One possible explanation could be that since the incident beam is transversely Gaussian. The transverse positioning of the aperture may have an impact because it selects different parts of the Gaussian intensity distribution. Below, we study this specific question numerically, by testing a top-hat beam instead of a Gaussian incident beam (see Figure 2.19). To explore such a hypothesis, we simulated the aperture of 600 μm width for three different cases of inner/outer diameter with a top-hat incident beam with constant intensity all over the envelope of the beam.

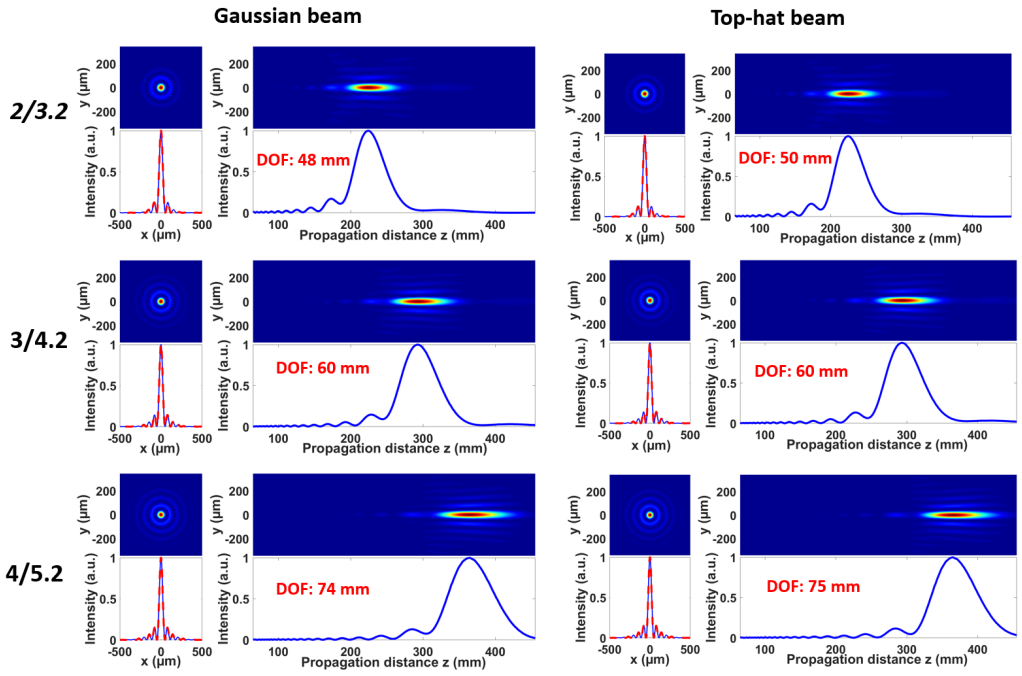

Figure 2.19 – Simulation of the beam propagation for the case of 600μm aperture width, in three different conditions of inner/outer diameter. The DOF remains similar for both of the beams in every case. The core size is also measured as constant (44μm everywhere).

Figure 2.19 shows the simulation when the incident beam has a top hat distribution and compares it with the Gaussian beam. We obtained almost similar DOF in both cases. Therefore, we can conclude that the energy distribution of the beam does not impact the DOF of the beam.

Next, we aim to choose the optimized aperture which could help us in machining micro channels of small aspect ratio with parallel sidewalls, excluding the tapering effect. To choose the best aperture, we selected a few criteria that need to be fulfilled. They are described as,

1. The beam has to have a smooth on-axis online intensity profile.
2. The beam keeps a transverse size that is close to the original Bessel beam's transverse size before truncation.
3. The arrangement that preserves the diffraction-free feature of the Bessel beam over a spatial extent that is sufficiently small (~ 20 μm).

Based upon these criteria we can see that the configurations with 200 μm and 300 μm apertures are poor choices. As we see from Figure 2.13 and Figure 2.14, the beam propagation through those apertures does not fulfill our criterion 1 & 3.

As shown in the simulation (see Figure 2.9) and also in the work of [**MÃijller17**], the optimized aperture lies between the classical (4 mm) and Fraunhofer (200 μm) limit.

Further work in controlling (shortening) the depth-of-focus has been performed from the lab by Liu et al. [23]. They found the optimal aperture to be 420 μm to generate a segmented Bessel beam with the attributes described earlier.

After reviewing the study by [23] and our numerical study (as described in Figure 2.9), we decided on a further optimized scan around 500 μm aperture width with increased precision. We plotted a curve between the aperture width and DOF (measured at FWHM) as shown in Figure 2.20(A). We have selected a constant inner diameter of 3 mm for the case of every aperture width.

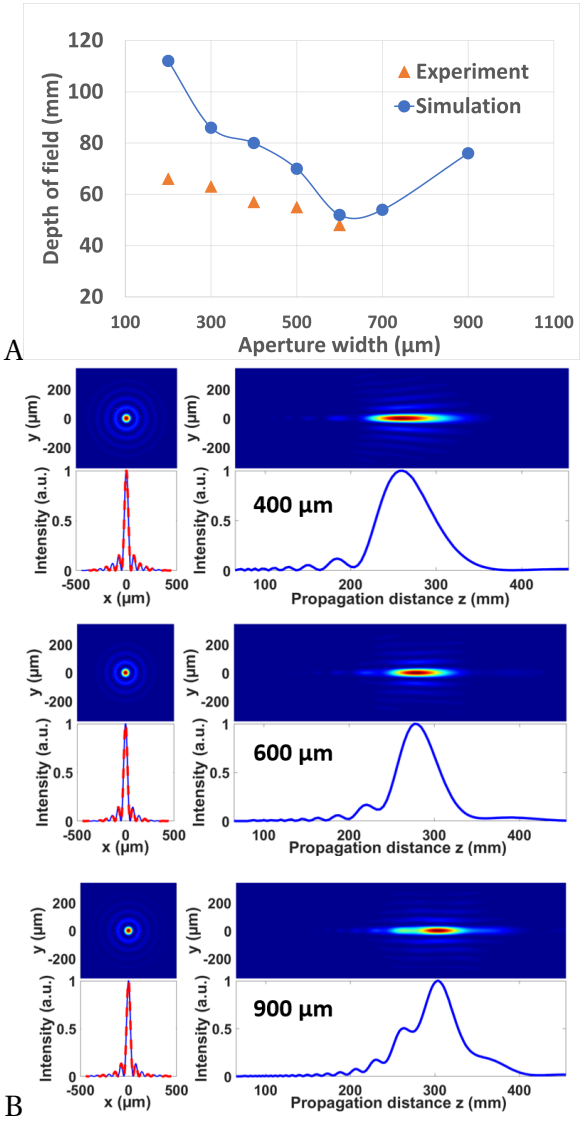

Figure 2.20 – A) The plot between aperture width and DOF. We have selected a constant inner diameter of 3 mm for all the aperture widths. The optimized aperture width is 600 μm, tested both experimentally and with simulation. B) Simulation of beam propagation through 400 μm, 600 μm, 900 μm.

As commented before, the DOF decreases with the aperture width first, and then again starts increasing just after a certain width. The optimized aperture width is obtained at the minimum of the curve (see Figure 2.20(A)). Both the simulation and experimental curves confirm that 600 μm is the optimized width of the aperture to generate a segmented Bessel beam. It is also shown from the simulation that above 600 μm (for 900 μm as shown in Figure 2.20(B)), the beam suffers from increased oscillation along with the increment in DOF (as shown in Figure 2.20(A)). The oscillation and increased diffraction effect made this not a suitable choice for our purpose.

Now, the 600 μm was identified as the optimal aperture width. There were three different combinations of inner/outer diameters for this aperture width. To choose one among them for our machining purpose, we compared them by plotting the beam propagation profile for each of them. The beam propagation has a smooth profile through these apertures as shown in Figure 2.21.

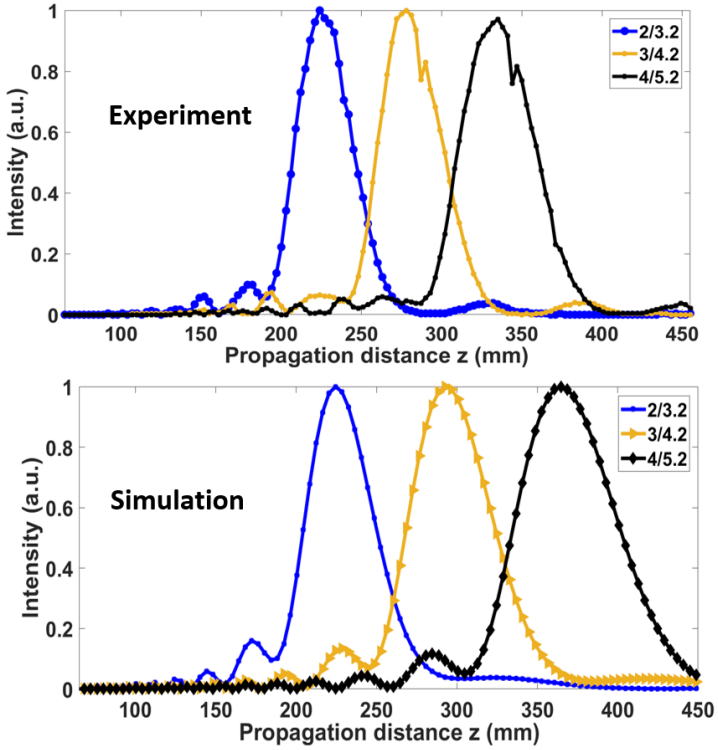

Figure 2.21 – Experimentally obtained results of beam propagation through three different (inner/outer diameter) sets of apertures (top) and Simulation of beam propagation through the three apertures (bottom) for an aperture width of 600 μm.

The simulation corresponds to the experimental results in terms of DOF value and the beam distribution profile. The largest value of DOF is obtained with the highest value of inner diameter (4 mm). To further analyze critically, we take into

consideration of Full width at half maxima (FWHM) of the profile. The measurement of this parameter helps to determine the sharpness of the central profile, which in turn helps to machine channels with sharp boundaries for the Bessel beam. A lower value of FWHM defines the higher sharpness.

Finally, a superposition of the three propagation profiles as shown in Figure 2.22 helped us to choose the particular combination of inner/outer diameter for the experiment. It is observed that the FWHM varies with different values of the inner aperture. The lowest FWHM DOF is measured for the aperture of 600 μm with the value of inner/outer diameter as 2/3.2.

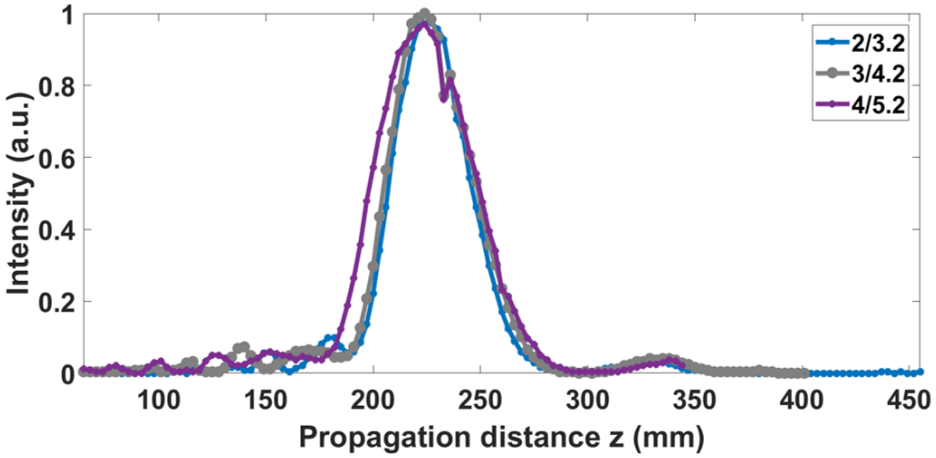

Figure 2.22 – Comparison of intensity distribution along the propagation axis of the experimentally obtained beam, after superimposing the profiles for the aperture width 600 μm apertures. This indicates that the smallest FWHM corresponds to the lowest value of inner diameter.

Therefore, we finalized our choice in keeping the configuration 2/3.2 (600 μm aperture width) and we used this aperture for the rest of our machining experiments that will be described in the next two chapters.

2.3.5 Micro-Bessel beam characterization

After selecting the right aperture, we placed it in the front of the axicon, and with the help of the further demagnification set-up (as shown in Figure 2.12) we generated the micro-Bessel beam with 1-*ps* configuration of the laser system, shown in Figure 2.23.

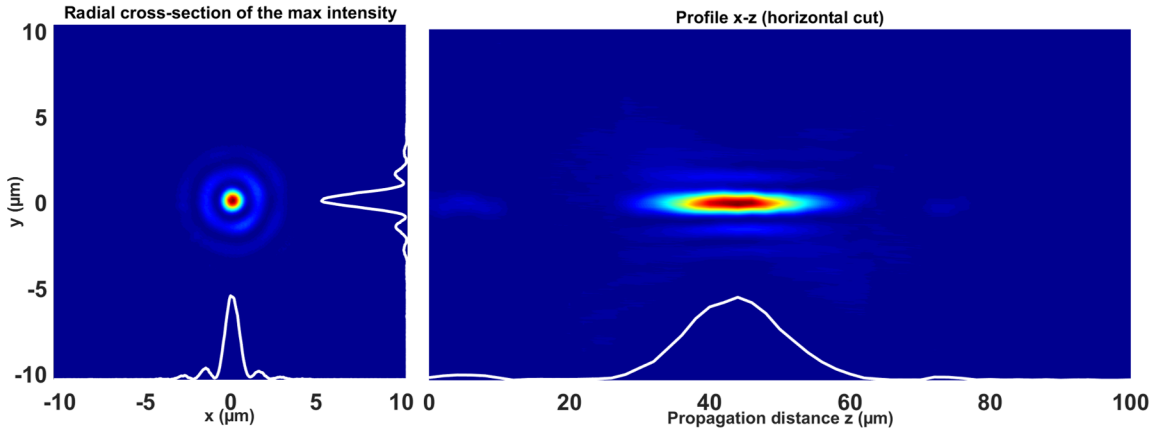

Figure 2.23 – Generation of the micro-Bessel beam through the aperture of 2/3.2 (width 600 μm) with a core size of 0.96 μm and a DOF of 17 μm.

This micro-Bessel beam is imaged with the telescopic system made of a $50X$ objective lens and a 200 mm tube lens. We measured the longitudinal beam profile with a step of 1 μm along the propagation axis. The starting of the z-axis was randomly chosen as we were unable to detect the exact starting position of the beam in the air between the two microscopic objectives. We corrected the tilt with a numerical method (developed with MATLAB at the lab) while we reconstructed the 2D profile of the beam. The characterization allows us to define the two important parameters (0.96 μm core size, DOF of 17 μm). It also shows that a smooth not axially modulated micrometric Bessel beam can be delivered to the workpiece.

2.4 Summary

In the end, we have created a micro-Bessel beam with a core size of 0.96 μm at FWHM and DOF of ~15 μm with the help of the demagnification setup. In this thesis, this micro-Bessel beam is used with *ps* and *fs* pulse durations to machine the channels at the surface or inside the bulk of fused silica.

To get such Bessel beam characteristics, we adapted from the work of Müller [**MÃijller17**] and Liu et al. [23], to shape the incident Gaussian beam by placing an annular aperture in the front of the axicon. This method gives us the liberty to change the depth of field of the beam while keeping the core size constant concerning the original Bessel beam ($45\mu m$). We have tested our homemade specially designed annular apertures of 200 μm, 300 μm, 400 μm, 500 μm and 600 μm widths by studying the Bessel beam characteristics generated by 1° axicon. We check the propagation profiles through each aperture (numerically and experimentally) and analyze them with our defined criteria described as i)smooth on-axis online intensity profile, ii) the beam keeps a transverse size that is close to the original Bessel beam's transverse size before truncation, iii) the arrangement that preserves the diffraction-free feature of

the Bessel beam over a spatial extent that is sufficiently small (~20 μm). Based on that, we selected the best width of the aperture to be 600 μm.

3 Material processing at the surface of the dielectrics

3.1 Introduction

The building blocks for photonic components rely on creating periodic structures of holes. Periodic hole structures in an opaque metal film have so far been the structures that have found the most applications owing to the simplicity with which their spectral properties can be tuned and scaled. Among other things, they can act as filters for which the transmitted color can be selected by merely adjusting the period [235]. The extraordinary optical transmission (EOT) property of nanohole arrays initiated more applications from sensors to optoelectronic devices [235]. The arrays of nanoholes with depths reaching several micrometers hold the potential to write designs and functionalities of nanophotonic structures. Being able to do that in a simple, flexible, and versatile way on every kind of material is not demonstrated yet. Concerning optical materials, it remains a challenge to drill ultradeep holes at the surface of dielectrics. One of the key interests in writing arrays of deep and cylindrical air holes is for light-confining structures (Bragg Grating, Photonic Crystals) at the surface of photonic integrated circuits. For example, the structures written on the surface of lithium niobate chips [236]. To the current date, the design of nanostructures with periodic holes majorly relies on techniques like focused ion beams, electron beams, and photo-lithography. These procedures are very mature and highly efficient; however, the drawback lies in being very slow and the fabrication requires several steps. The development of masks is required often and the experiment needs to be conducted in a vacuum which makes such methods more complicated. Also, the techniques need to be optimized for each material, which makes them to be costly and complex in terms of writing different patterns.

Research has been carried out to investigate the possibilities of direct laser writing techniques in fabricating nanohole arrays. Dedicated research has been carried out on the production of long, continuous nanostructures in glass and sapphire, those are designated as channels. For example, Kudryashov et al. [68] successfully produced nanochannels up to 1 μm long using front-surface machining. Herbstman et al. [146] managed to achieve nanochannels up to 10 μm long using both front- and rear-surface machining techniques. Vertical nano-holes starting at the surface of fused silica of depths exceeding 11 μm and diameters of 200-500 nm have been machined by focusing a 200 fs laser pulse with a high numerical aperture objective with spherical aberration. However, the limitation remained in achieving long channels due to the

lack of control over the filamentation regime, which plays a key role in achieving longer lengths of channels, with a Gaussian profile of the incident beam.

The beam shaping technique allows us to spatially shape the incident Gaussian profile. Among several other beam shapes, the Bessel beam showed promising results in drilling high aspect ratio controllable nanochannels. Non-diffracting beams like Bessel beams can retain the maximum intensity over a localized zone which exceeds the usual Rayleigh range of a Gaussian beam by a few orders of magnitude. This property has attracted many interests in both linear and non-linear optics. The properties like self-reconstruction, and stability under non-linear propagation make the beam suitable for energy deposition in dielectrics in a highly localized elongated and controlled manner [135]. By taking advantage of stable Bessel filaments long channels up to 43 μm have been drilled in glass [136]. Further advancements in beam shaping techniques using a Spatial light modulator (SLM) have helped to achieve channels with a high aspect ratio of 100 [22]. A high aspect ratio with a value of more than 100 has been machined very close to the rear surface of the glass however with a visible tapering effect. The tapering effect is defined with respect to the hole itself. When it is perfectly cylindrical (same diameter over the entire length), we speak of the non-tapered hole. When the sidewalls of the hole are not perpendicular to the surface, we have a tapering effect (which can be positive or negative). The reasons for that can be manifold, also coming from the beam distribution. With a Gaussian beam, we may have a strong tapering effect because of the non-homogeneous transverse distribution of the intensity leading to non-uniform ablation and this can be emphasized when a high NA objective is used. It also comes from possible redeposition of ablation products on the sidewalls (especially when long holes are machined), etc. Next, by increasing the half conical angle from 17° to 26°, Bhuyan et al. reported channel length up to 100 μm by rear surface structuring in glass with improved sidewall quality. The influence of energy on the length and diameter of the channel have also been studied [136]. Using a different strategy, rear surface machining with further improvement in beam shaping techniques has facilitated the machining of channels with taper-free profiles. Different laser shot regimes like single and multishot have been investigated and channels with taper-free profiles have been found in single shot regimes [237]. Rear surface machining with post-processing techniques like immersing the surface under machining inside water has been also successful in creating taper-free microchannels and micro-trenches. High aspect ratio channels are well suited to make microfluidic devices, a lab-on-chip DNA sequencing system needs high aspect ratio sub-10 μm wide channels with no taper [238]. Courvoisier et al. have demonstrated the machining of micro-channels with ~2 μm diameter and of 40 μm length [238]. Liu et al. reported the fabrication of taper-free channels of length ~40 μm with a diameter of ~1.2 μm with single-shot beam of 1 ps pulse duration in fused silica [218]. This new beam shaping technique which helped to create a truncated Gaussian-Bessel beam, assisted machining of densely packed channels with aspect ratio ~5 and a spatial period down to 1.5 μm, which further opens the prospective demonstration of direct laser writing of 2D photonic structures [23]. This study opens a new window for the machining of channels controllable via pulse energy, pulse

duration, and truncation factor [23].

In this chapter, we primarily study the limitations and solutions of achieving such spatial periodicity while retaining sub-micron resolution in between adjacent channels, taper-free profile, and good quality opening diameter with different pulse energies. To target high quality and efficiency, we focus on the single-shot irradiation regime and we explore both front and rear surface machining with pitches down to the sub-micron range (~0.8 μm). Post-processing techniques like plasma torch cleaning, ultrasonic cleaning, and polishing have been performed after the machining to further enhance the channel quality. As previous studies confirmed that 1 *ps* pulse duration is performant to machine controllable channels, all the results shown here represent the machining of fused silica sample with 1 *ps* duration. With the advancement of the beam shaping technique that produces a truncated Bessel beam, our work intends to further downscale the spatial periodicity in the sub-micron range with more optimized beam shaping conditions.

3.2 Experimental arrangement

We generate a Bessel beam to go further from the Gaussian beam provided by the ASUR platform (1 mJ, 100 Hz, 1 *ps*, linearly polarized, 800nm) with the help of an axicon (1°, Altechna, 1-APX-2-H254-P, n=1.45). We add an annular aperture (600μm width, 2 mm inner diameter, 3.2 mm outer diameter) to generate a truncated Bessel beam with an extra control of the non-diffracting length. To further downscale the shaped beam, we build up a de-magnification set-up as shown in Figure 3.1, made up of a lens of focal length of 500 mm and an objective lens with a magnification of 20X (20X, NA = 0.4, f2=10 mm, Mitutoyo NIR, working distance 20 mm). This generates a micro-Bessel beam of core diameter of 0.96 μm with a depth of field (DOF) of 15±2 μm, which is favorable for creating micro-channels. We place our fused silica sample (15 × 5 mm; thickness 3 mm) on a system made of translational stages which allows movements in micro-metric and nanometric range. We use the MFA-CC (from Newport-MKS) stage to locate the surface of the samples with micro-metric precision and we used the nano-positioner stage for moving the material during the laser machining. The resolution of the nanopositioner stage is 0.2 nm, which provides confidence in machining the material with nanometric positioning precision. We transversely machine the material with a single-shot micro-Bessel beam. We implement an in-situ imaging setup composed of a 500 mm focal length telephoto objective lens along with a doubler. A doubler is a device that helps to make the focal length of the lens two times the initial focal length of the lens used. This makes the total focal length 1 m. We adjust this set-up with a Thorlabs camera (pixel size: 5.2 μm X 5.2 μm). This imaging setup is used to image the channels during machining.

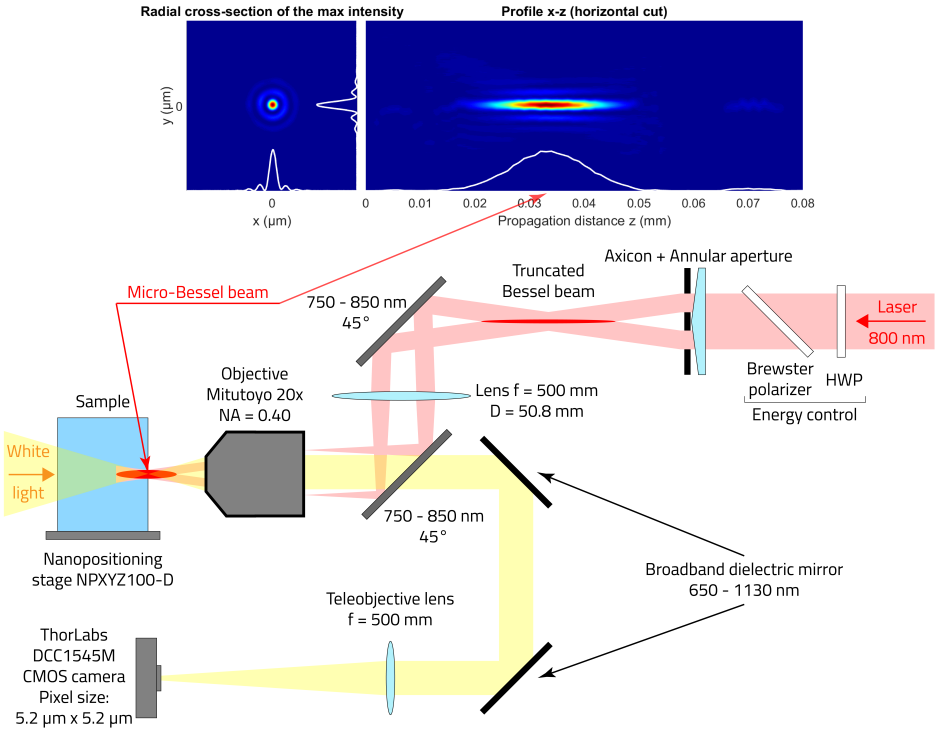

Figure 3.1 – Experimental set-up showing the machining and in-situ imaging arrangement.

The laser machining characteristics depend on several process parameters; among them, for a given laser pulse duration and laser wavelength, the most important is the fluence. To ensure the optimum delivery of energy at the focus position and control the experiment, we adjust the perpendicularity of the material to the incident beam. To do that, we adapt the vertical and horizontal tilt of the sample using an iterative procedure in which the tilt and z-position of the sample holder were optimized with respect to the sharpness of the in-situ imaging system (see Figure 3.1). After a few iterations, the tuning converges to the situation where we have perfect sharpness over a sample surface of 1 mm area in both horizontal and vertical directions.

Since the Bessel beam has a longer depth of field compared to a Gaussian beam, there remains another freedom of choice for machining which is how to place the maximum of the beam on the sample. We distinguished five different possibilities for choosing the beam position on the surface as shown in Figure 3.2. Case 1 is when the beam profile is placed entirely in the bulk (suitable for bulk modification); Case 2 corresponds to the maximum beam intensity positioned on the front surface; Case 3 corresponds to the maximum placed below the front surface. Case 4 corresponds to the case when the maximum is out of the sample and last, Case 5 corresponds to the situation when the maximum of the beam is placed at the rear surface of the sample (suitable for rear surface structuring). In this chapter, we focus on the machining of

the front and rear surfaces. Therefore, we are interested in Case 2 and Case 5.

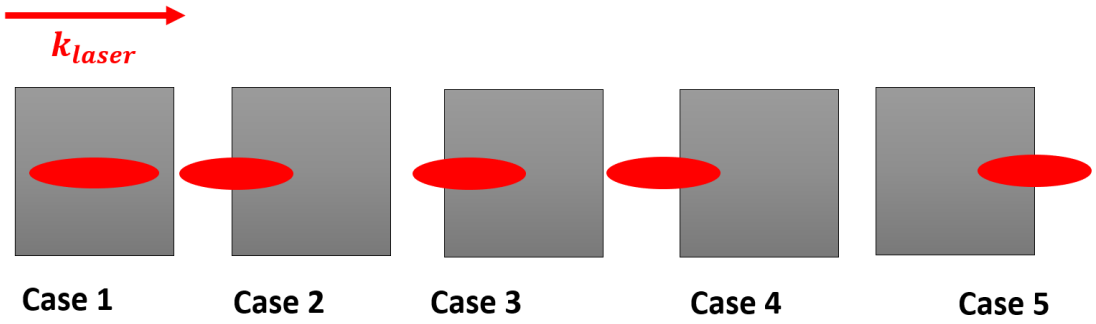

Figure 3.2 – Different configurations of placing the sample surface with respect to the micro-Bessel beam. Case 1: The beam is entirely placed inside the sample; Case 2: The maximum of the beam is placed on the front surface; Case 3: The maximum of the beam is placed right below the surface; Case 4: The maximum of the beam is outside the surface; Case 5: The maximum of the beam is placed at the rear surface. We mention the laser propagation direction with k_{laser}.

To precisely locate the maximum at the surface, we performed a combined energy- and z- scan experiment, thanks to our in-situ imaging system. We translate the sample transversely to the beam with 5 μm steps to ensure a fresh location for each case. Along the optical axis, we change the z-position of the sample with 2 μm steps around a range where we can machine the material. We move the sample in a direction where the beam starts machining inside the bulk and then gradually moves outside in the air. This range is chosen around the z-position when the sample is placed at a distance equal to the working distance of the microscope objective (20 mm for our objective). We perform the scanning with different energies. To locate the beam focal zone at the surface of the material with precision, we lower the energy down to the ablation threshold of machining.

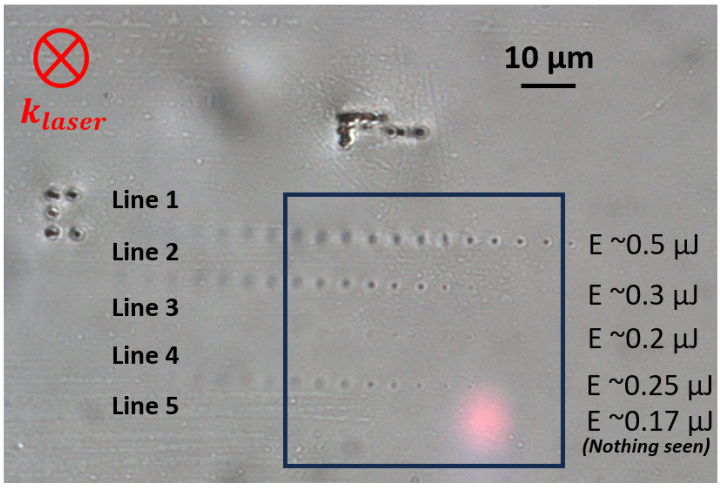

Figure 3.3 – Z-scan procedure followed to position the sample at the maximum intensity of the micro-Bessel beam. Line 1 to Line 5 refers to the different energy values on the sample in descending order except line 4. Line 1: E~0.5 μJ; Line 2: 0.3 μJ; Line 3: 0.21 μJ; Line 4: 0.25 μJ ; Line 5: 0.17 μJ. The range of z explored here is ~20 μm on both sides encircling the value which corresponds to the working distance of the microscope objective from the end of the objective lens to the surface of the material.

As we reach an energy close to the threshold energy of machining, only one small black hole can be seen sharp on the surface (as shown in Figure 3.3). We then choose the z-value corresponding to this spot for performing the machining experiment. This experiment enables also us to obtain a rough estimate of the threshold, which corresponds to the smallest energy for which we detect a damage with our in-situ imaging system. A more precise and dedicated procedure is desirable for obtaining reliable values, as we present in section 3.3 below.

3.3 Crater Morphology

In this section, we present a study on the crater profile depending on various energies. All the results presented here are done in a single-shot regime, i.e., one laser shot produces one hole at a given surface position. We also determine the surface ablation threshold using the Liu method [239]. Liu method helps to retrieve the threshold by measuring the diameter (squared) of the modification versus the pulse energy (logarithmic scale). This method is useful as it could be applied to any material to derive the modification fluence threshold. To this aim, we need statistics done on several craters realized in the same conditions. We therefore machine a large area by creating matrices of 10 × 10 holes that are spaced enough to ensure that the formation of a crater by a single shot is independent of the previous one. Accounting for the transverse Bessel beam profile (see Figure 2.18 of Chapter 2 or Figure 3.1) that exhibits a core diameter of 0.96 μm, we choose a separation distance of 5 μm between two

adjacent holes. We performed several experiments while gradually decreasing the energy to the ablation threshold. The explored energy range is 0.2 μJ – 0.6 μJ.

3.3.1 Determination of ablation threshold

The ablation threshold is an important parameter in machining as it defines the level of energy (fluence) from which the sample is permanently modified. To find out the threshold, we measured the averaged values of inner diameter 'de' over four different craters and studied their evolution with energy. We define the inner diameter of the craters in section 3.3.2 (Figure 3.6). We have carried out the threshold determination for front and rear surfaces.

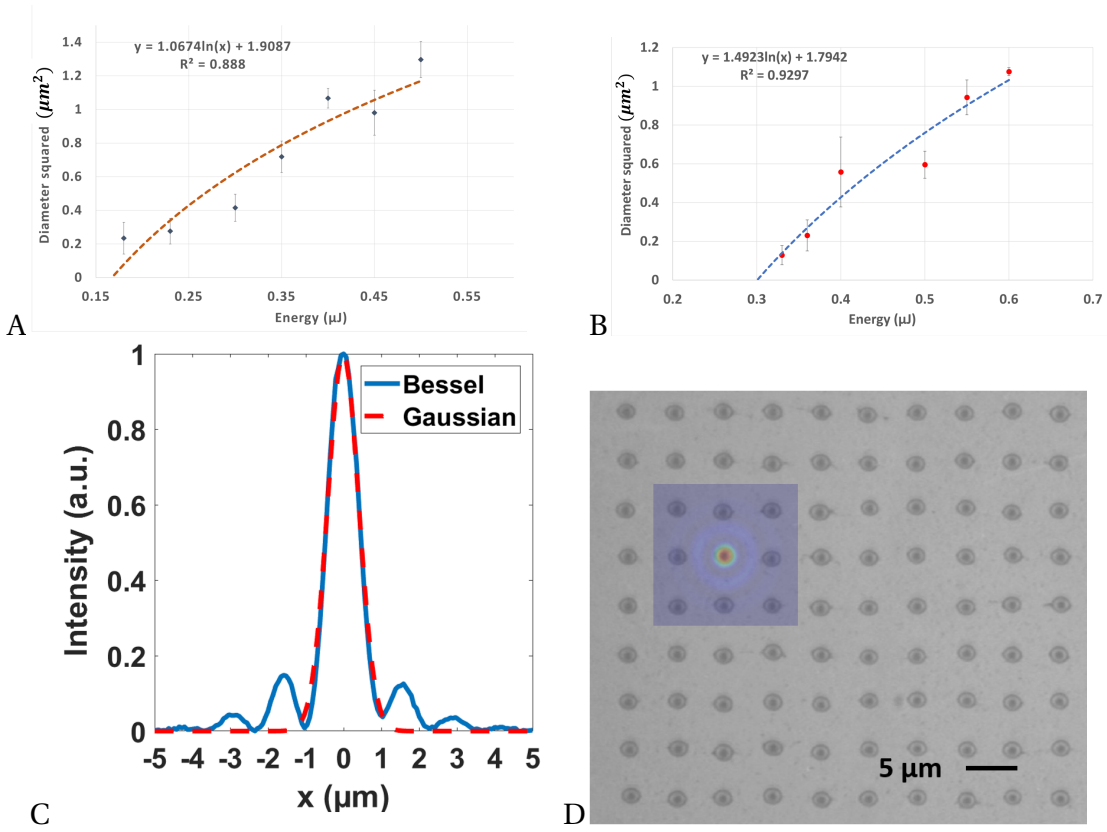

Figure 3.4 – Ablation threshold determination from Liu method. A) Evolution of measured inner diameters d with incident laser energy for front surface; B) Evolution of measured inner diameters d with incident laser energy for rear surface; C) Transverse profile of experimental Bessel beam (blue), numerical Gaussian fit of central peak (red dashed); D) Superimposing the beam profile onto the holes with 5 μm pitch to illustrate the interaction of laser beam core with the material

To use the Liu method for threshold determination, we approximate the central peak to a Gaussian function as shown in Figure 3.4(c) The numerical fit gives an

equivalent beam waist of ω_0=0.84 μm (radius at $1/e^2$) for the Gaussian beam. This enables us to use the Liu method for calculating the surface ablation threshold under the assumption that ablation is a strict threshold-based and deterministic mechanism. The diameter of the ablated crater could be written as [239],

$$de^2 = 2\omega_0^2(\ln E - \ln E_{th}) \tag{3.1}$$

Using this expression to fit the experimental data in Figure 3.4(A) for the front surface and in Figure 3.4(B) for the rear surface, we find the threshold value (the energy for which de^2=0) as 168 ± 12% nJ and 300 ± 11% nJ for front and rear surface respectively. Note that the given error bar is only composed of energy fluctuations (~6% peak to peak) and the measured variations of diameter (~ ±3%) (fluctuations over four different diameters) for a given energy. We observe a difference in threshold values for the front and rear surfaces of the sample. Among the reasons for that, propagation losses inside the sample (as well as the reflection on the second face and also refraction) are not accounted for in the rear surface case precluding a direct comparison between them. Nevertheless, both estimates provide important observables to dimension the machining processes and their limitations that can be reached in both geometries.

3.3.2 Crater Characterization

To start with, we machined independent craters on the front surface with micrometric (5 μm) pitch (center-to-center distance between two adjacent holes) and studied them with different tools like confocal, scanning electron microscope (SEM) and with atomic force microscopy (AFM) as shown in Figure 3.5.

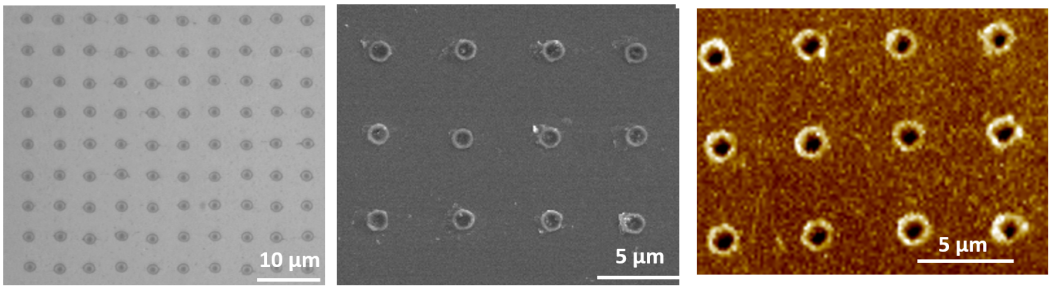

Figure 3.5 – Matrices with 5 μm pitch at the front surface imaged under a) Confocal microscope (E~0.45 μJ); b) Scanning electron microscope (E~0.2 μJ); c) Atomic force microscope (E~0.45 μJ).

We observed craters with round openings with the presence of a rim around them. The craters are free of any debris with this pitch and independent of each other. To detail the crater profile, we take a horizontal line through the craters as shown in Figure 3.6. We have characterized the different parameters of craters like crater diameter, rim

width, and rim height from the line profile, as displayed in Figure 3.6 both schematically and experimentally. The precision of the AFM scan has been calibrated with a test grating with array characteristics of 3 μm transverse pitch and 20 nm depth, confirming that good accuracy can be obtained for the transverse measurements made at the sample surface. However, considering the small diameter($<<$ 1 μm) and long elongated depth($>>$ 1 μm) of the crater drilled with a Bessel beam pulse compared to AFM tip characteristics, no accuracy can be reached for the measurement of the depth. Because the tip cannot penetrate deep inside the channels. Even if it is shown on the AFM graph, those data will not be considered in the following. This limitation of the AFM tool also justifies our efforts to quantify the length of the micro-channel using another measurement approach (see paragraph 3.7).

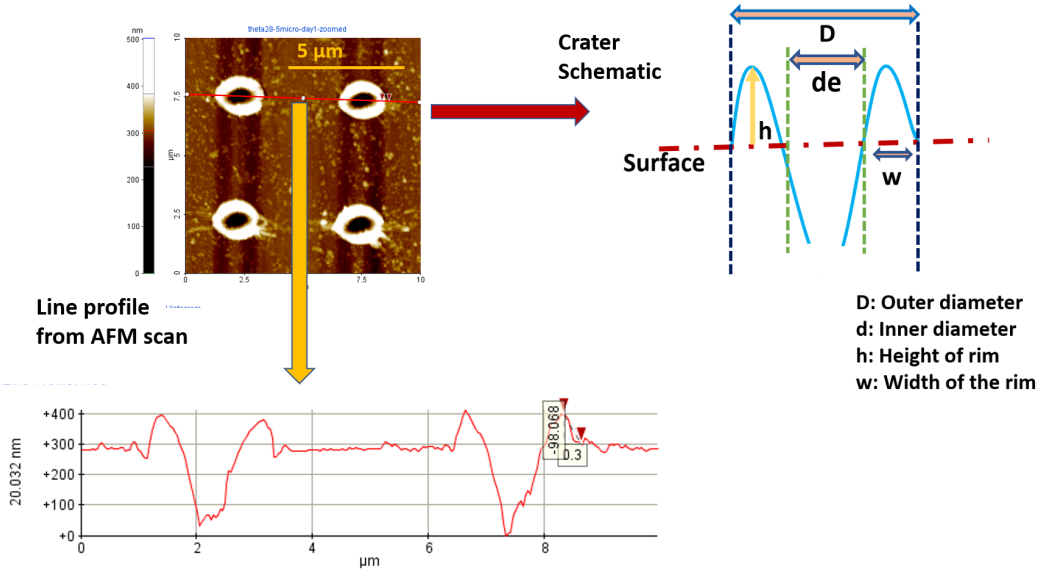

Figure 3.6 – The crater profile with 5 μm pitch and E~0.5 μJ imaged with AFM and the line profile was analyzed from the analysis software provided by AFM. Also, we made a schematic of the crater profile to show the different parameters linked to the crater profile. Depth should not be considered from the AFM profile.

3.4 Towards sub-micron spacing of channels

We performed an experiment at the front surface of our fused silica sample, where we decreased the pitch of the two craters starting from 5 μm to 1 μm with a step of 1 μm, and from 1 μm we have finely tuned the pitch down to 0 μm, which means when the two holes overlap. This we named the two-line experiment, as we machine two lines of holes with a gradually decreasing horizontal distance between them, as shown in Figure 3.7(a)(b)(c). We have repeated the experiment for several energy conditions to show the influence of energy on the smallest achievable spacing between two holes.

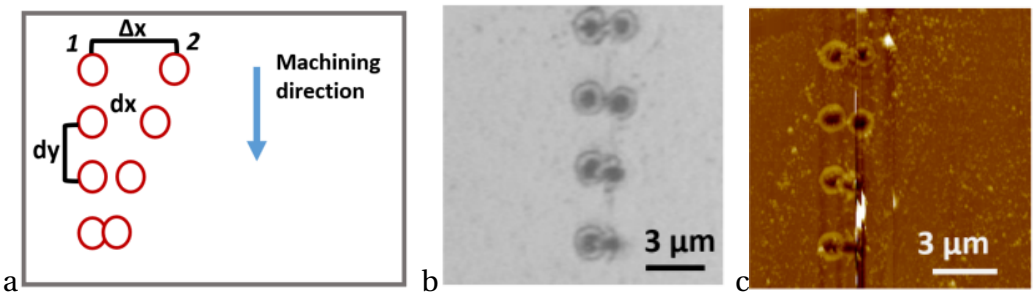

Figure 3.7 – a) Schematic of two-line experiment. 1 refers to line 1, and 2 refers to line 2. dy refers to the spacing in the vertical direction. Δx is the first center-to-center spacing when starting the experiment, and dx is the value of decrement (dx = 0.1 μm) in the horizontal direction; b) Experimental results of a two-line experiment performed for a range of ΔX=1.6 μm - 1.3 μm with energy E~0.5 μJ imaged with confocal microscopy; c) Same holes imaged with atomic force microscopy.

The two-line experiment provides us with a clear view to assess the dependence of the minimum resolvable pitch with energy. We define the minimum resolvable pitch as the pitch that corresponds to the situation where two adjacent holes of a given inner diameter are physically separated, independently of any formed rim. To identify the minimum resolvable distance between two holes, we take a line profile and measure the precise distance over which the material surface between two holes is at an altitude higher than or equal to the reference level marked as surface as shown in Figure 3.8. The Atomic Force microscopy technique provides a resolution which is enough to analyze our results with precision.

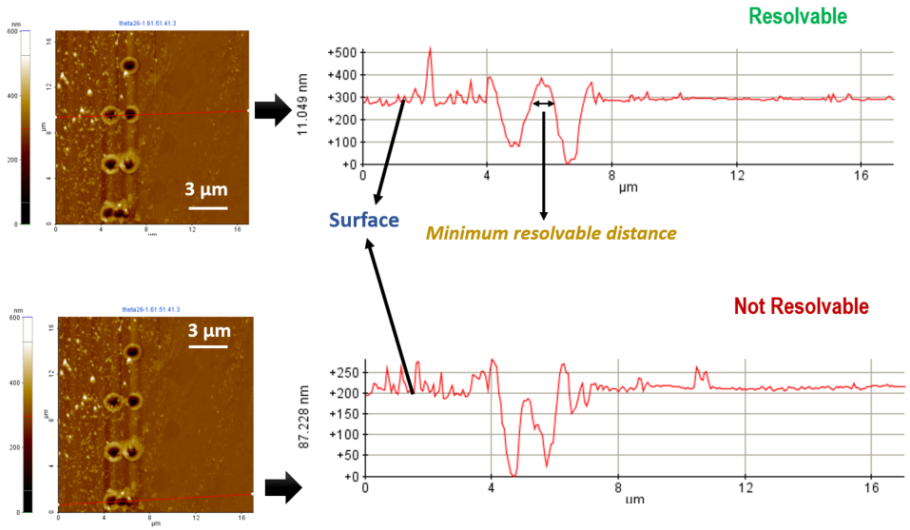

Figure 3.8 – Line profile of a series of two-line experiment performed at E~0.4 μJ; resolvable (top) for 1.5 μm pitch and not resolvable for 1.3 μm pitch (bottom).

Next, we performed this two-line experiment for different energies to understand the dependence of minimum resolvable pitch on energy, as presented in the graph in Figure 3.9 below.

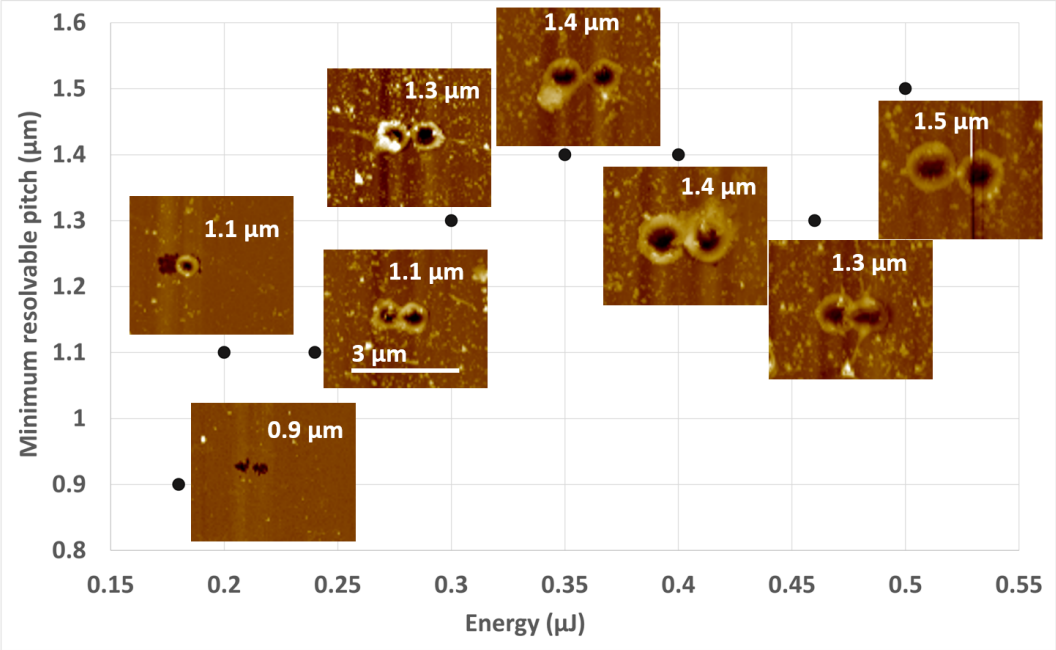

Figure 3.9 – Evolution of minimum resolvable pitch with energy.

Figure 3.9 suggests that decreasing the energy helps to access sub-micron meter pitch. We found that near the threshold (168 nJ), 0.9 μm pitch is possible to machine. Also, the minimum resolvable pitch increases with the energy and decreases when we lower the energy.

The resolution of writing increases at lower energy at the expense of the surface morphology. We can summarize the results as,

— Structuring with sub-micrometer periodicity is only possible with processing energy very close to the threshold energy (see Figure 3.9). However, with this processing energy, the machined holes, even though being of sub-micron diameter, appear to be irregular and we lose control over the surface morphology structuring.

— To keep control in this 1-μm domain, it is mandatory to work close but slightly above the threshold energy (a few % above). However, in this case, the presence of a rim precludes getting into the perspective of periodic structuring with optimal hole stacking and quality. The best performance demonstrating nearly 1 μm periodic structuring is reached with E=0.25 μJ processing energy yielding a minimum resolvable pitch of 1.1 μm.

— At higher energies, the minimum resolvable pitch increases significantly above 1 μm, but the surface morphology improves. Also, we have noticed the presence of a rim around the craters as the energy increases. We discuss below the source

and evolution of the rim around the craters. The crater morphology at the higher energy allows the user to envision controlled periodic surface structuring in the 1 μm range with different hole spatial filing ratios providing the possibility of ajustment of the macroscopic response of a surface.

As it is shown, the rim limits the sub-micron spacing at higher energy. As explained in the reference [240], the rim is formed as a result of a complex interplay of nonlinear interaction of the ultrafast laser pulse with the matter. A plasma is created at the surface when an ultrashort pulse interacts with the dielectrics. The plasma extends after and most of the absorbed energy is used by the expanding plasma to move into ambient gas. The rest small portion of the energy remains in the target as thermal energy. This thermal energy creates a shallow molten zone beneath the plasma which is on the walls of the channels. Later, as a result of heat diffusion, the front part of the molten layer propagates laterally in the bulk of the material, i.e., perpendicularly to the channel axis. As the temperature decreases below the melting temperature, the melt re-solidifies. During re-solidification, forces act on the liquid molten material driving them towards edges and creating elevated rim around the ablated craters. The plasma also retains large pressure gradients which also contributes to the formation of the rim near the edges as it drives the molten layer near the edge. Next, we have studied the influence of incident laser energy on the rim parameters.

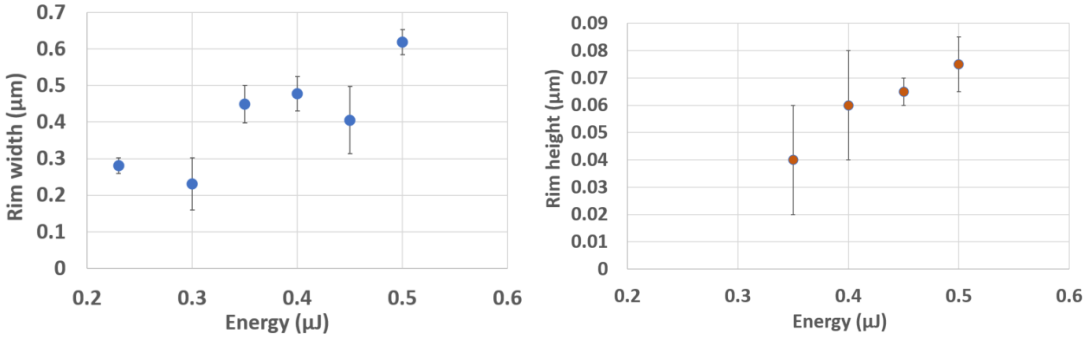

(a) Rim Width

(b) Rim height

Figure 3.10 – Variation of Rim width and height with energy from the two-line experiment. The rim height was not measurable with trusted value for the case of E~0.3 μJ and E~0.23 μJ.

The thermal consequence of the laser-matter interaction induces the formation of the rim which thus appears unavoidable. As shown in Figure 3.10, it gains importance (increasing writing limitation) when increasing the incident energy. Indeed, the amount of energy dissipated thermally is first approximation proportional to the incident energy. When the incident energy is very low (close to the threshold), there is even no rim (as shown in Figure 3.9) because the energy thermally dissipated is too low to yield a measurable rim. Note that, ablation with minimized thermal effects

or even suppression of them (so including the rim) could occur when conditions of electronic ablation can be reached in the dielectrics by adjusting the working fluence of the ultrashort pulse very close to the threshold [241] [242][243] [244]. This was presumably approached when working extremely close to the energy threshold showing no rim but at the expense of an irregular not-controllable surface morphology. New developments using much shorter pulse durations and extremely energy-stable pulses to enhance electronic ablation and deterministic selectivity could be tested to address such limitations.

3.5 High Spatial density matrices of channels

The two-line experiment demonstrates as shown in Figure 3.9 that the sub-micron pitch structuring could be attained if we carefully adjust the energy. Next, we have machined matrices with various pitches depending upon the energies at the front surface of fused silica (see Figure 3.11 (a),(b),(c)). The presence of a rim was evident. We machine up to a pitch of 1.2 μm starting from 5 μm at the front surface, but faced limitation with 1 μm pitch. Next, we carried out another quantitative study on the rim characteristics by measuring the rim height and width for a range of pitches (averaged over four craters) with several energies as shown in Figure 3.11 (d),(e).

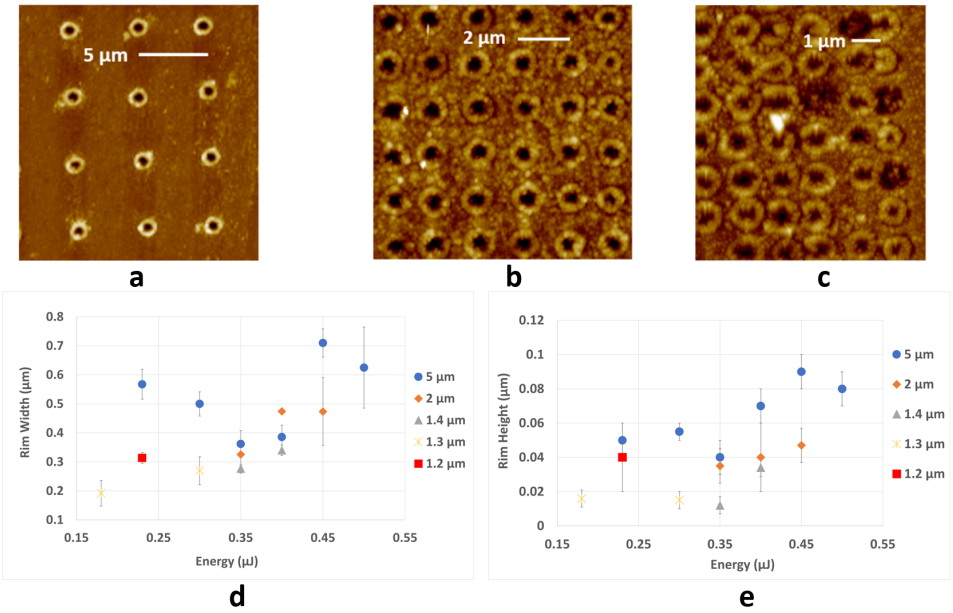

Figure 3.11 – a: Front surface machining of matrices with 5 μm pitches at E~0.3 μJ imaged with AFM technique; b: With 2 μm pitch at E~0.35 μJ; c: With 1.2 μm pitch at E~0.23 μJ; d: Evolution of Rim width with energy for various pitches measured from the machined matrices at front surface; e: Evolution of Rim height with energy for various pitches measured from the machined matrices at front surface.

The dependence of rim parameters on energy is similar to two-line experiments. This study of rims is also important technically because the presence of rims around the craters can be an obstacle to the spatial densification of crater stacking given the design of an optical component. We have faced an obstacle to reaching 1 μm or sub-μm dimension at the front surface. The first reason we have suspected is the presence of a rim. To overcome the limitation posed by the rim in achieving sub-micron pitch, we decided to machine the rear surface of fused silica. The rear surface configuration could help in overcoming the resolution limitations caused by the rims by considering the beam propagation through fused silica. Indeed, at the front surface, the rim around the craters poses a limitation when machining the next channel by the beam. When interacting with the front surface, the beam extends over a region of X=5.63 μm size (see Figure 3.12). This is calculated considering the half conical angle of our Bessel beam (θ = 21.4°) and refraction at the surface of air and fused silica as shown in the schematic in Figure 3.12.

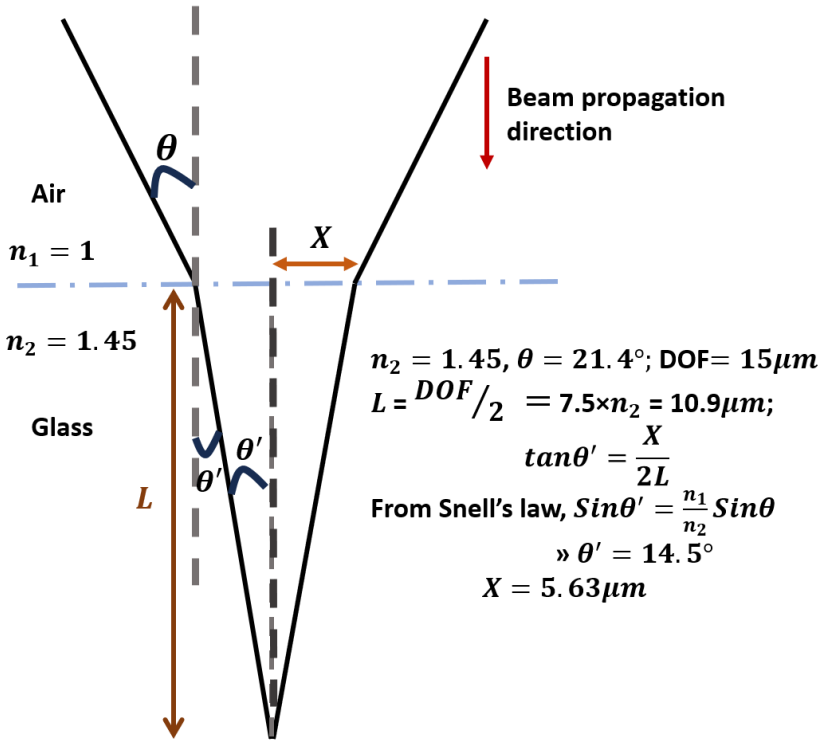

Figure 3.12 – Schematic of beam interaction at the surface of fused silica

By considering the geometry of beam interaction, the perturbation of the Bessel beam is less when we are at the rear surface (interaction only with the pre-machined channels) (see Figure 3.13(b)) compared to the front surface (interaction first with the rim and then with the rest of the pre-machined channels) (see Figure 3.13(a)). Therefore, machining at the rear surface could be beneficial for the incident beam to avoid the presence of the rim from pre-machined zones.

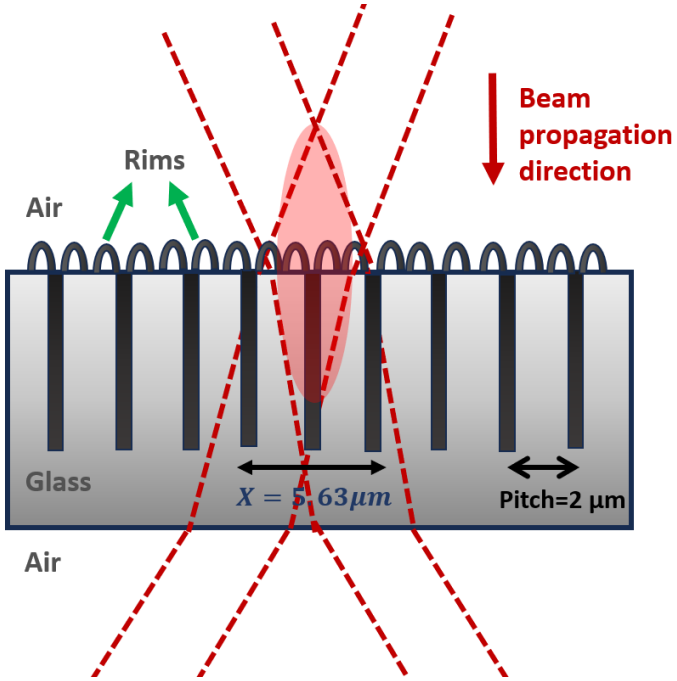

(a) Front face

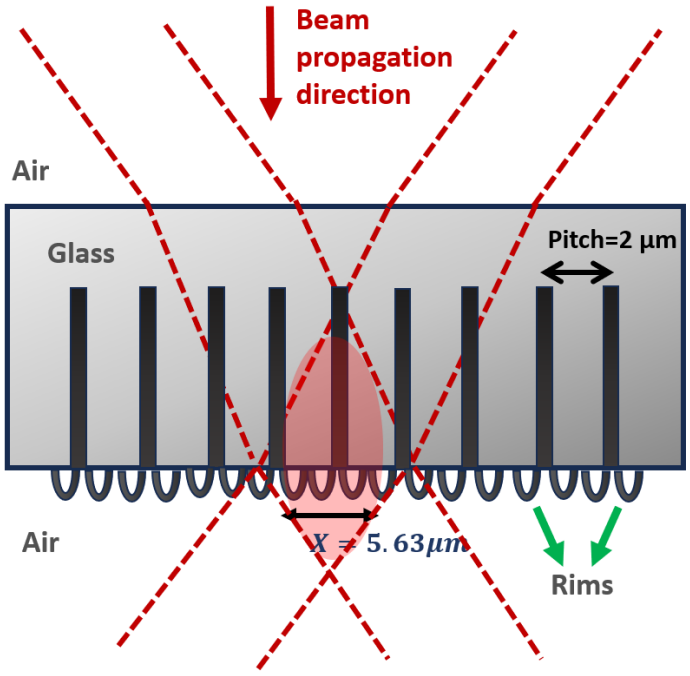

(b) Rear face

Figure 3.13 – Schematic of the interaction of Bessel beam with the channels at a) front face and at the b) rear face (bottom). At the front face, the beam is perturbed by the presence of rim and channels while at the rear surface configuration, the beam is only perturbed by the pre-existing channels.

Keeping this benefit in mind, by moving to the rear surface we machine matrices with varying pitches ranging from 5 μm to 0.9 μm with different energies. Figure 3.14(c) shows that sub-micron pitch structuring is attainable in this configuration, demonstrating that the rear surface configuration can be an advantage for high-density stacking.

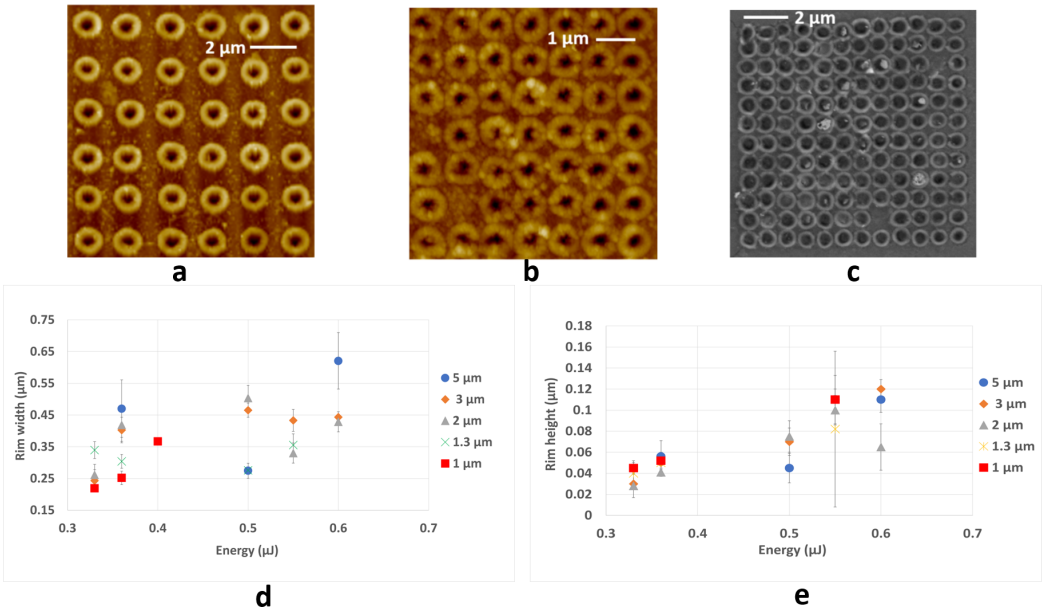

Figure 3.14 – a) Rear surface machining of matrices with 2 μm pitches at E~0.55 μJ imaged with AFM technique; b) Rear surface machining of matrices with 1 μm pitches at E~0.33 μJ imaged with AFM technique; c) Rear surface machining of matrices with 0.9 μm pitches at E~0.33 μJ imaged with SEM technique; d) Evolution of Rim width with energy for various pitches measured from the machined matrices at rear surface; e) Evolution of Rim height with energy for various pitches measured from the machined matrices at rear surface. Good laser shot-to-shot reproducibility is also demonstrated.

However, the matrix experiment done in the rear surface configuration again confirms the presence of a rim. As we decrease the pitch to 0.9 μm, we find the rim of adjacent holes touching each other. This defines the first limitation in placing holes in the sub-micron regime as shown in Figure 3.14(c).

So now comparing the results obtained on the front and rear surface, we show that sub-micrometer pitch (0.9 μm and even 0.8 μm as later shown in Figure 3.26) can only be obtained for the rear surface configuration. We also find that the rim width varies from 0.25 μm to 0.6 μm irrespective of front and rear surface cases as could be seen in Figure 3.11(d) and Figure 3.14(d). The rim height varies also in the same way for both surface configurations.

Apart from the presence of the rim which could be mitigated using dedicated strategies (as said before), the limitation of machining at the front surface comes also from other reasons. One of them is the pollution. The pollution occurs during the machining when ablated material is sputtered around the matrices and poses limitations on resolving matrices as shown in Figure 3.15. Also, here lies another advantage of machining at the rear surface which is that the beam is less perturbed by the pollution at the rear surface.

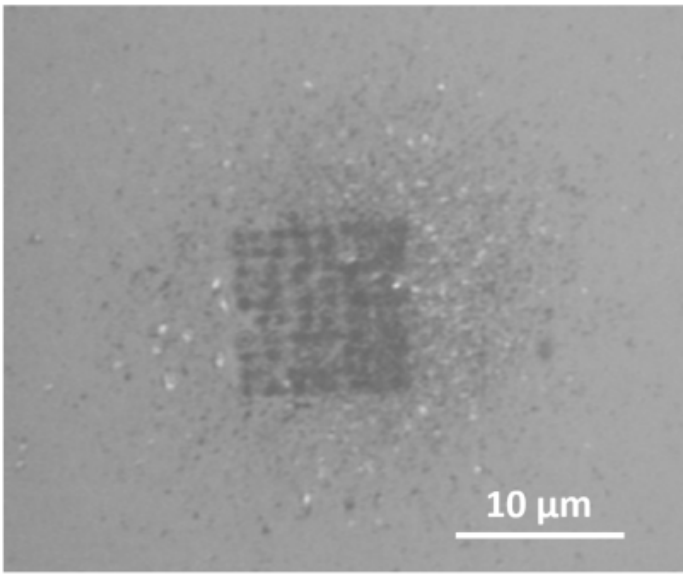

Figure 3.15 – Machining of matrices with 1 μm pitch at the front surface of fused silica at E~0.35 μJ. The pollution occurs at the surface

3.6 Post Processing techniques

The machining of matrices on the sample created debris around the processed area. The debris highly depends on the energy and number of shots used for machining the matrices. After the effect of debris becomes more intense for smaller pitches as the same amount of pollution arises for a smaller surface. In our experiment, to clean the debris from matrices, we used a plasma torch and ultrasonic cleaning.

3.6.1 Cleaning with Plasma torch

The ultraviolet light generated in plasma is very effective in breaking most of the organic bonds of surface contaminants and pollution. Plasma torch ULS V12 series from AcXys Technology as shown in Figure 3.16 is used for our cleaning purpose. The compressed air is attached to the unit. The plasma torch can be moved and controlled as per the required distance and processing speed. In plasma torch, it is the atmospheric gas like nitrogen that is used, and this ensures surface treatment by plasma cleaning to be an environment-friendly technology.

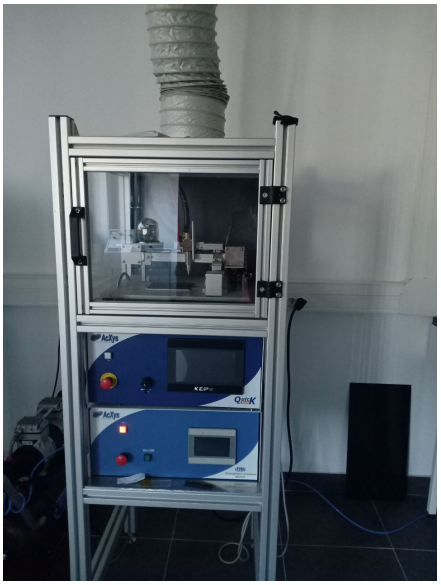

Figure 3.16 – Plasma torch setup of ULS Series

We cleaned the surface two times sequentially with the plasma torch with a flow of 35 l/min for ≤20 s each time with a power of ~600 W. The cleaning left traces of plasma inside the matrices as seen in Figure 3.17 and as shown from the examination of the surrounding areas, it also appears not at all efficient for removing debris. Therefore, we abandoned this process of cleaning.

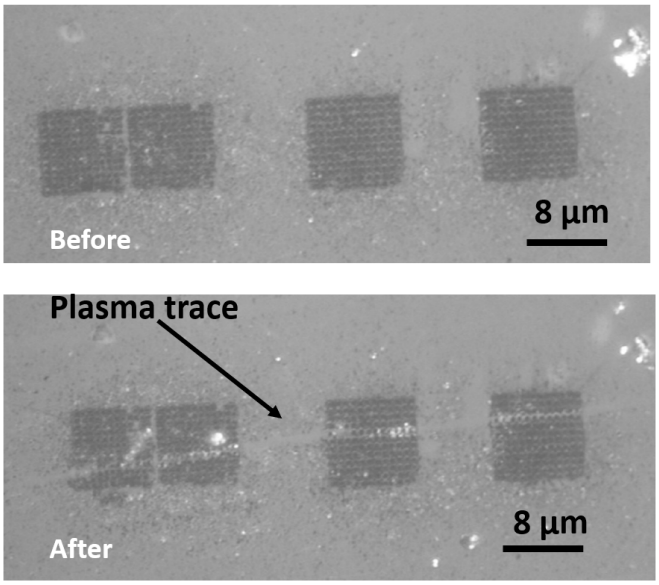

Figure 3.17 – Matrices of 0.9 μm (top-right) and 0.8 μm (top-left) pitches machined with E~0.3 μJ. Plasma cleaning was tried successively by applying it two times using the same operating conditions of the plasma torch. The results shown correspond to the surface finish after the second passage.

3.6.2 Ultrasonic Cleaning

We test another cleaning strategy based on the use of an ultrasonic bath. To clean the sample, we followed a protocol composed of 4 successive steps "clean/observe/decide and act" steps. After each step, we looked with the confocal microscope and decided on the procedure for the next step after comparing the images of the new step with the previous step. We carried out a dedicated cleaning with an Isopropanol bath at room temperature and with higher temperatures like 50°C. The choice of a liquid for cleaning was based on the wettability characteristics of liquids. Isopropanol and acetone both have low values of contact angle for glass, whereas water demonstrates moderate wettability depending on the surface preparation procedure. Another critical parameter is the solubility of contaminated substances in the solution. For some inorganic compounds (e.g. $NaCl$) water demonstrates excellent solubility. In this case, isopropanol and especially acetone almost does not dissolve salt contaminants. Moreover, in our case, most of the experiments were carried out in isopropanol, since it is a less “aggressive” solvent than acetone.

The solubility of contaminants in general increases as the solution is heated up. Therefore, raising the temperature could help to remove the debris which is caused by the redeposited matter around the matrices and contains silica mostly. We tried different temperature regimes to reveal if this affected the quality of the surface after cleaning.

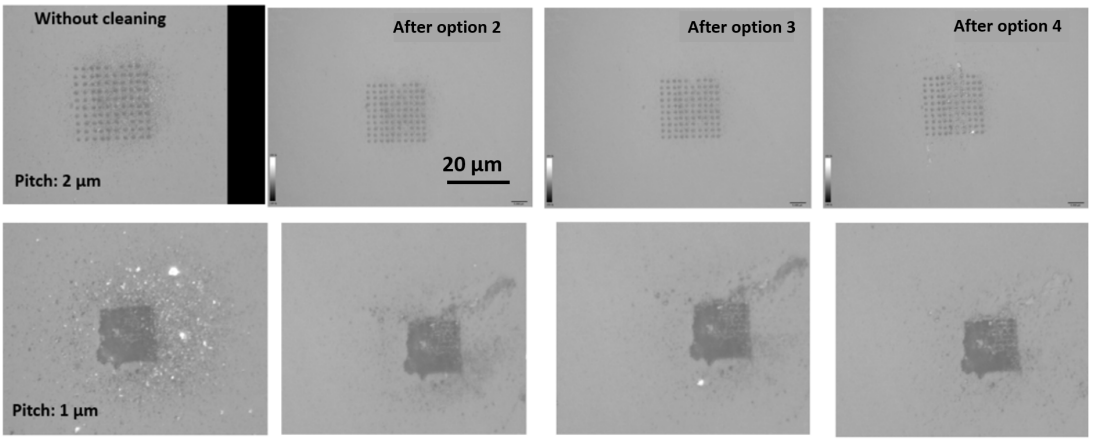

Figure 3.18 – Matrices of 2 μm and 1 μm pitches are machined at an energy of 0.3 μJ shown here after cleaning options described above.

The different options we followed are described below and the matrix after different steps is shown in Figure 3.18.

— Option 1 Started with a delicate cleaning with Isopropanol at room temperature.
— Option 2 Proceeded with a full cleaning with Acetone at room temperature.
— Option 3 Performed a delicate cleaning with Isopropanol at 40°C. (Suggested 65% of the boiling point) The boiling point for acetone: is 56°C, whereas the boiling point for Isopropanol is 82.5°C.

— Option 4 After noticing the effect it might clean some of the debris from the inner line of the matrices, especially 2 μm ones (that shows good craters with reproducibility for any energies). Carried out a full cleaning for 1 hour at 50°C again with Isopropanol.

Figure 3.18 shows that the matrix with larger pitches compared to the smaller one was cleaned more effectively than the matrix with smaller pitches. Thus, even though some benefit is observed, the limitation remains with this approach in cleaning 1 μm or sub-micron pitches when the density of debris is higher in between the matrix.

3.7 Channel characteristics determination below the surface

After carrying out a detailed study on the opening of the channels of the surface, we concentrate on characterizing other parameters which are the characteristics of the channels in bulk like their length. The length is embedded in the bulk of the sample and we need some techniques that could help to access the channels in depth. We use the focus ion beam (FIB) technique combined with SEM analysis to characterize the quality of the entrance of the channels just below the surface, the length of the channels, their sidewall characteristic, and the separability of the adjacent channels in microns and sub-micron resolution.

3.7.1 FIB milling procedure for SEM analysis

Focused ion beam technique incorporated with SEM imaging utilizes focused beams of gallium ions to modify the material under investigation at nanoscale [1]. Depending upon the current intensity of the ion source, FIB can be used in two following modes. The gallium ion beam can operate at low beam currents for imaging purposes and or at high beam currents for sputtering or milling purposes [1]. Along with the milling potential of FIB, the ion implantation method of FIB allows the modification of materials to create micro-structures [1].

We have milled our sample with the following procedure.

— 1. The region of interest for FIB is coated with a platinum layer to avoid the milling of the targeted region.

— 2. The target region is milled with a high current (~9.3 nA) to mill a depth of 15-20 μm significantly larger than the length of channels.

— 3. Later when we approached the selected line of holes, the current was reduced to 2.3 nA and finally, we reduced it to 0.28 nA when coming very close to the holes.

1. https://en.wikipedia.org/wiki/Focused_ion_beam

To start our milling procedure on a matrix, first we selected a specific line from the matrix as shown in Figure 3.19.

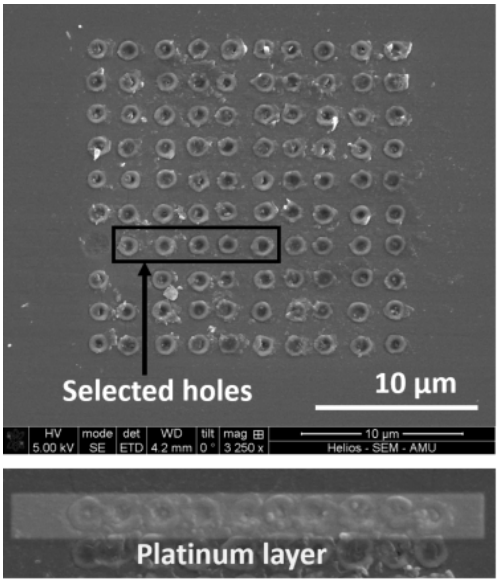

Figure 3.19 – Machining of holes with 2 μm pitch with E~0.33 μJ. The region of interest to drill is shown with the rectangular box. We deposited the platinum layer on that region.

Then we followed the steps mentioned before to mill the channels. The various stages of step 3 are shown in Figure 3.20. We gradually progressed towards our selected lines from Step 1 to Step 4 with a moderate current of 2.3 nA. In Step 5, we reached the channel and afterward drilled until Step 8 with a very low current of 0.28 nA. Next, from Step 9 to Step 12, we gradually moved away from the selected line and approached the other line.

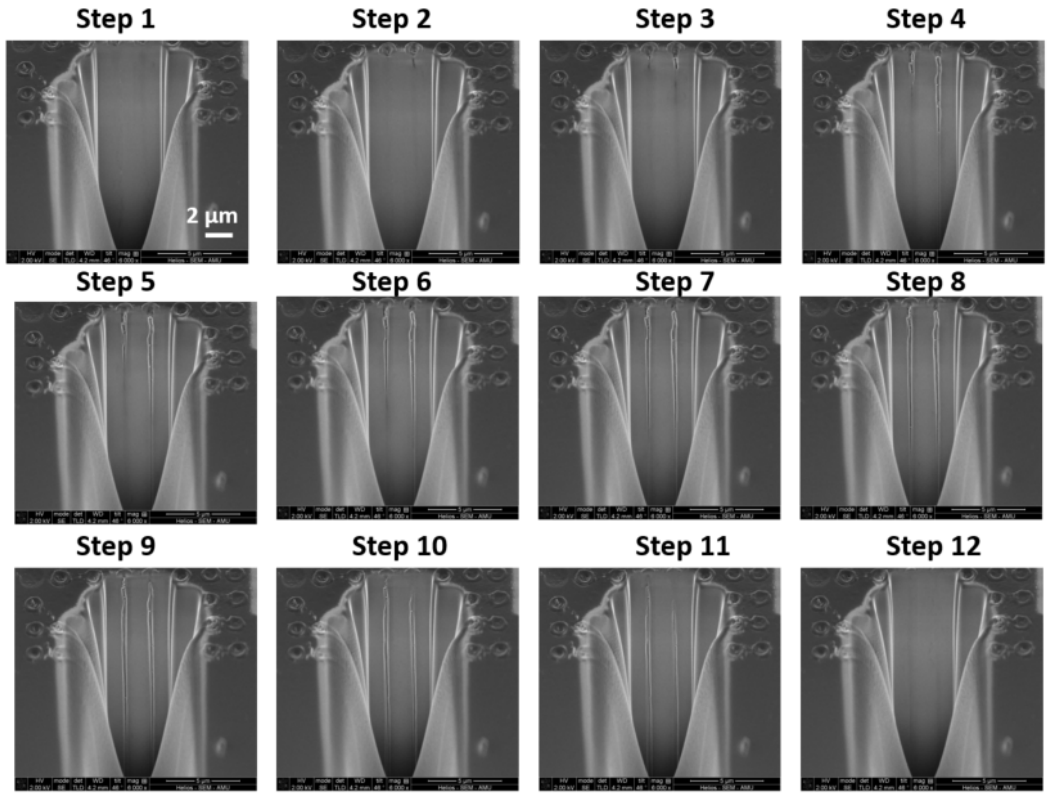

Figure 3.20 – Steps of FIB milling procedure

This procedure helps us to see the channel diameter as shown in Figure 3.20 (Step 7 and Step 8).

3.7.2 Analysis of Channel Entrance

We have analyzed the entrance of the channels both for the front and rear surfaces. The top-view entrance as shown in Figure 3.22 (c) both for the front and rear face is circular. Then, from the side view, as we move towards beneath the surface (see Figure 3.22(d) Front and Rear face), in the beginning, we observe a non-cylindrical shape which is attributed to the existence of a rim, which eventually is caused by the ejected matter during machining at the surface. To investigate this further, we have selected a cross-section of the channel (see Figure 3.21). Next, we calculated the area of ejected matter averaged over two channels from the walls (by taking a triangular shape as shown in Figure 3.21) and compared it with the area of the rim (by taking a parabolic area as shown in Figure 3.21). These two measurements show good correspondence (measured area ~0.01 μm^2) and thus it justifies our argument. We have taken these measurements of the corresponding areas by using the software ImageJ.

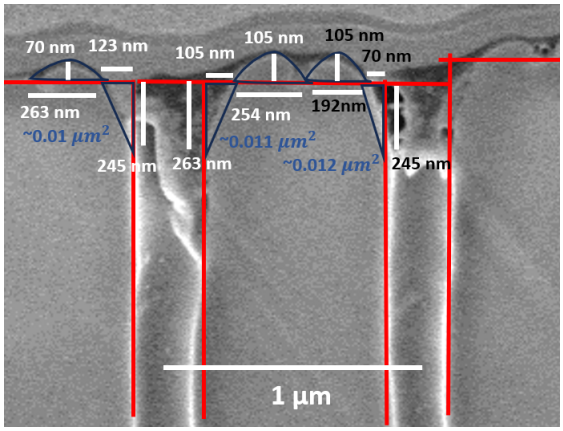

Figure 3.21 – Comparison of the area of the rim with the area of the ejected matter which caused funnel shape. The channels are machined at the rear surface with a pitch of 1 μm at an energy of E~0.33 μJ. The calculated comparable area between the rim and ejected matter which caused funnel shape is ~0.01 μm^2.

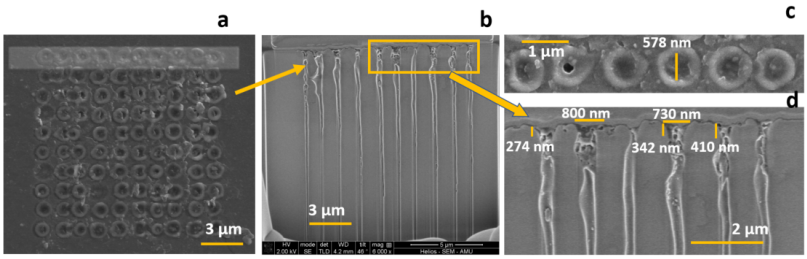

(a) Front face

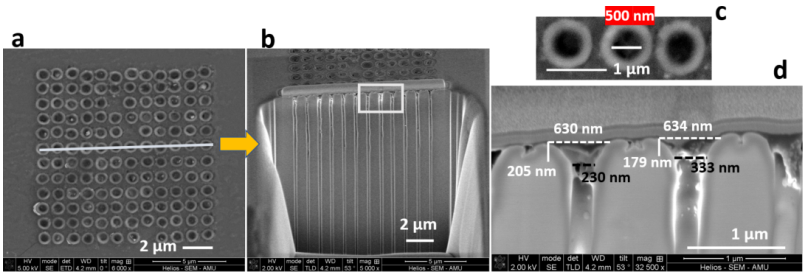

(b) Rear face

Figure 3.22 – (Top) Funnel shaped entrance for channels with 1.3 μm pitch at E~0.3 μJ at front surface. From the front view of the channels shown in a) we milled the line highlighted in gray. The channel profile is shown in b) and we see a close-up view of the front of the channels in c) and their profile in depth in d); (Bottom) a) Front view of matrices with 1 μm pitch machined at the rear surface with E~0.33 μJ. b) The profile of the channels milled with FIB. c) Front view of 3 selected craters and the channel profile is shown in d)

Entrance Characteristics	Front Surface	Rear Surface
Funnel length shape (nm)	342±68	192±18

Table 3.1 – Measurement of the funnel shape entrance at the front and rear surface of fused silica.

During the rim formation, the molten matter generated by the laser-matter interaction is driven from the center to the edges of the crater. This contributes to the entrance not being straight but funnel-shaped. Therefore, the entrance of the holes of the matrices exhibits a funnel-like shape (see Figure 3.22(d) Front and Rear face). The funnel shape continues up to a few hundred nanometers from the surface as seen in Figure 3.22 and then disappears. We have measured the length up to which the funnel shape exists, defining the funnel shape length parameter (as shown in Figure 3.22(d)). We have listed the quantitative value of the parameter averaged over at least two of the channels for both machining the (rear and front) surface configurations in Table 3.1.

The table shows that the funnel shape is reduced for the rear surface configuration. As mentioned before in section 3.5, the beam formation is less perturbed for the rear surface compared to the front surface. For machining in rear surface configuration, the beam does not interact with the rims, therefore it could provide less beam distortion while machining the channels.

3.7.3 Channel diameter, quality of sidewalls

After analyzing the entrance, we looked into depth to determine the sidewall quality and diameter of the channels. We have measured the diameter of the channels machined at both front and rear surfaces as shown in Figure 3.23. We relied on the central part of the channel to measure with precision and confidence (the framed area in Figure 3.23(a)(b)).

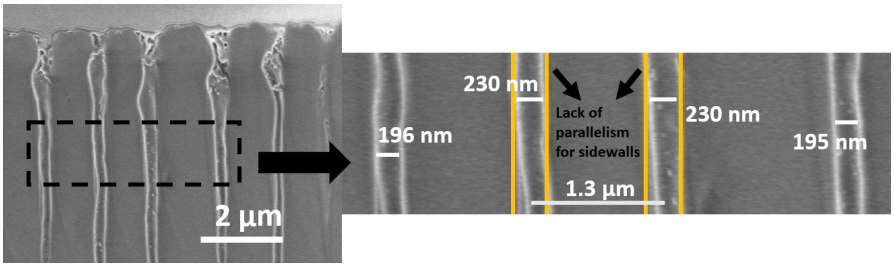

(a) Front face

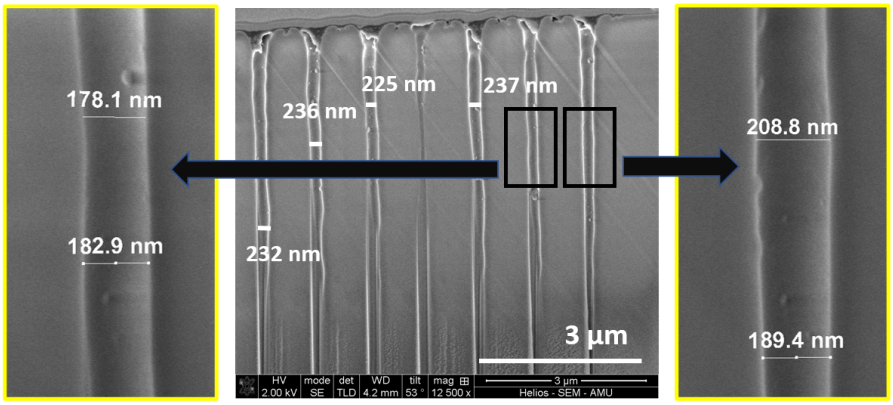

(b) Rear face

Figure 3.23 – Cylindrical channel profile with a diameter of ~200 nm for a) front surface with 1.3 μm pitch at E~0.3 μJ and b) rear surface with 1 μm pitch at E~0.33 μJ .

We have measured the diameter of channels by taking horizontal lines between two boundaries (see Figure 3.23). We have repeated the measurements for four different channels machined at the front surface as shown in Figure 3.23(a) and concluded the diameter of the channels as an average of four different measurements. The same procedure has been carried out for the rear surface channels shown in Figure 3.23(b) for six different channels. The measured diameter for the front and rear surfaces appears to be of the same order of magnitude with an average diameter value of ~200 nm at an energy close to the threshold. Note that, we used a beam radius (at FWHM) of 0.96 μm to machine channels whose diameter is ~0.2 μm. The channel loses its cylindrical profile for sidewalls, mentioned as the loss of parallelism in Figure 3.23(a) at many places along its length. We achieve comparatively better parallel profiles of sidewalls for channels machined at the rear surface, compared to the front surface.

3.7.4 Channel Length

The length of the channel is an important parameter while we are machining with a Bessel beam. The segmented Bessel beam that we use for machining, is also an advanced tool to control the length of the channels. Besides exploring the channel diameter, sidewall quality, and entrance shape, FIB machining allows us to access

the length of the channels. However, during the FIB milling process, there arises an artifact named the curtaining effect which imposes a limitation in measuring the length of the channels with accuracy.

In FIB milling, the curtaining effect manifests itself as increasing the milling depth on interfaces, i.e. in particular at the end of the channels. In our analysis, the detrimental effect of the curtaining effect is that it artificially increases the length of the channels (see Figure 3.24(left)).

To mitigate the curtaining effect, there exist several ways. For example, adjusting the milling parameters, such as the ion beam current, exposure time, and scanning speed, can help to minimize the curtaining effect. Another option could be the rotation of the sample. Rotating the sample during milling can promote more uniform material removal and reduce the impact of channel lengthening due to curtaining. Therefore, this solution helped us to mitigate the curtaining effect, as can be seen on the right side of Figure 3.24.

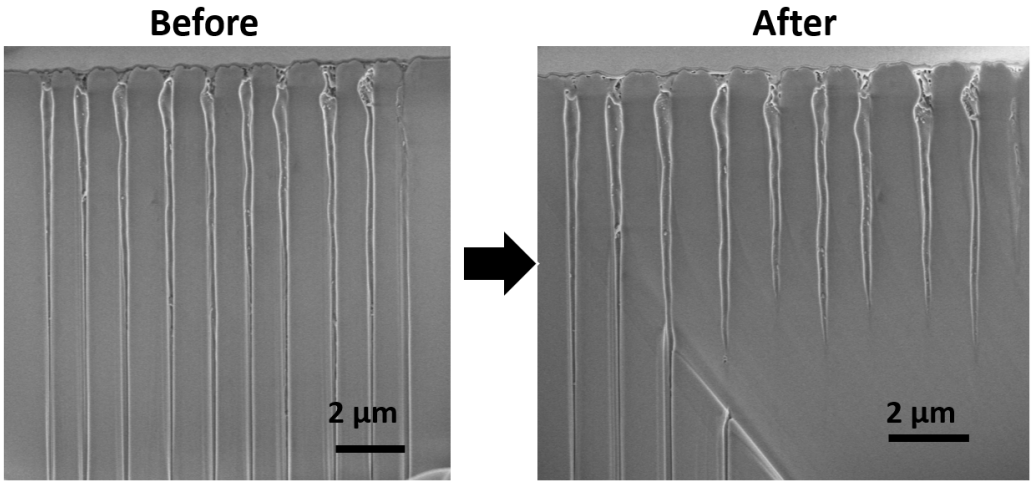

Figure 3.24 – Curtaining effect during FIB milling. The left shows the artifact due to the effect which makes the channel look extremely parallel, and the right after the attempt to remove the curtaining effect.

As we can see from Figure 3.24, removing the curtaining effect is not always easy to achieve. However, there remains another way to measure the length that could avoid the errors introduced by the curtaining. This is why we relied on measuring the length of the channels in transparency as shown in Figure 3.25. By transparency, we do not measure the length by reaching the channels, but we stop before the channels, look at them from a distance, and capture them in transparency.

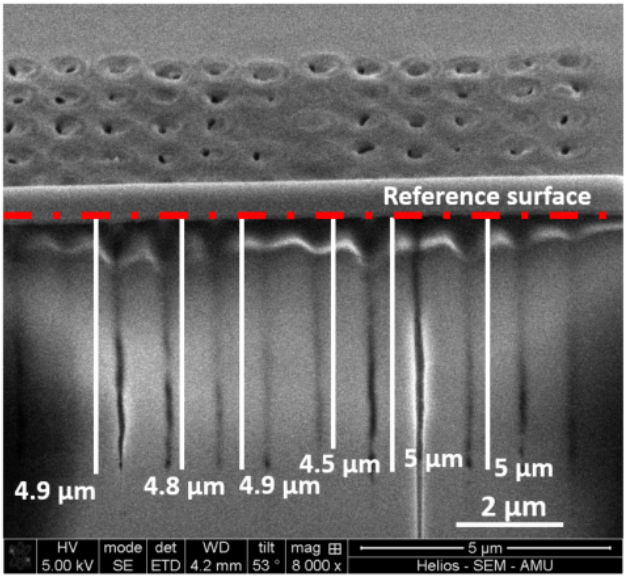

(a) Rear face

Figure 3.25 – Length of the channel measured in transparency obtained in rear face writing configuration with 1 μm pitch machined at E ~0.33 μJ

The recording is done by taking images of the channels before we reach the channels. We have measured the lengths over six different channels machined at the rear surface close to the threshold energy (E~0.33 μJ). The average length is calculated as 4.85 μm which is much smaller than the DOF of the Bessel beam. This is explained later in the paragraph 3.7.4. We have also measured the length of the channels machined at the front surface with similar energy, and the length is also ~5 μm. However, measuring in transparency implies a low resolution. Nonetheless, the length of channels shows good shot-to-shot reproducibility as well.

3.7.5 Crosstalk effect

Using the FIB/SEM characterization technique, we also examine the cases of dense spatial structuring (corresponding to sub-micron pitches like 0.8 μm and 0.7 μm) obtained in the rear surface configuration to evaluate its characteristics below the surface and the capability of the Bessel Beam laser tool in this difficult writing regime. The front view of 0.8 μm pitch channels looks separated with rims touching each other as shown in Figure 3.26(a). The cross-section of the channels loses the quality to be straight as shown in Figure 3.26(b) and this occurs due to the presence of a crosstalk effect between channels.

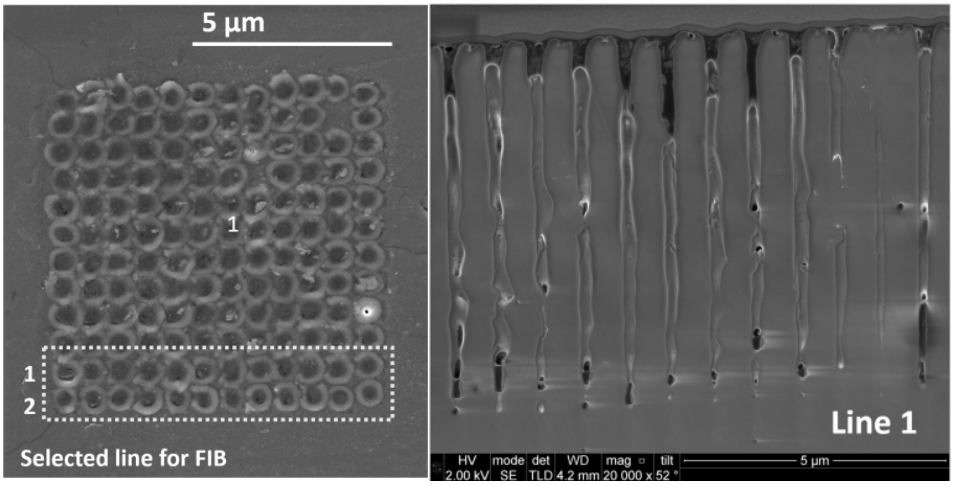

(a) Front view (b) Depth profile

Figure 3.26 – a)Front view of matrix with 0.8 μm pitch machined at E~0.33 μJ. We show the lines chosen to be machined. b) Cross section of channels showing the lengths and distortion due to crosstalk effect.

The crosstalk effect between channels refers to the unwanted beam perturbation that occurs when multiple channels are close to each other. The crosstalk effect could be a limitation on the achievable density of the produced close-packed array holes. As shown from previous work of the lab by Liu et al. [218], from numerical simulation, we see that the presence of previous channels affects the propagation of the Bessel beam to write the next channel. This study is shown in Figure 3.27.

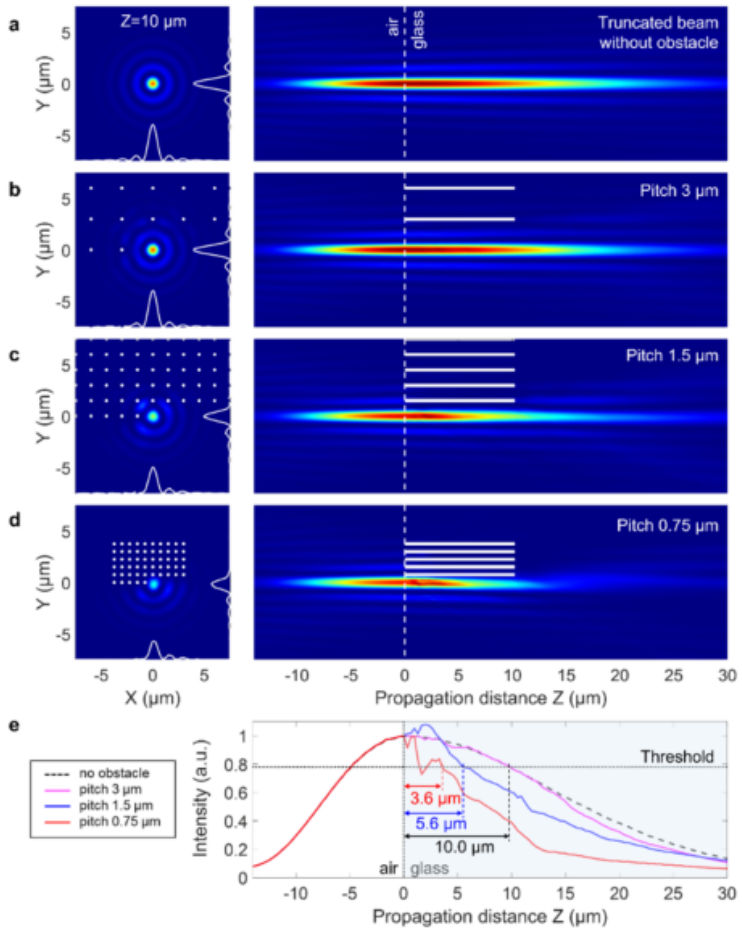

Figure 3.27 – "Numerical study of crosstalk: simulations of beam propagation and distortions in presence of preexisting holes at the surface of the sample, for decreasing pitches. a) no obstacle, b) pitch a = 3 μm, c) pitch a = 1.5 μm, d) pitch a = 0.75 μm. The coordinate Z = 0 is the surface of the fused silica glass sample, placed at the maximum intensity of the incoming beam. All images are normalized to this value and they are therefore directly comparable. The XY beam intensities (left panel) are taken at Z = 10 μm; this enables us to compare the beam distortions and drop of intensity at the end of the hole for each case studied. The YZ intensity distributions (right panel) display the beam propagation. The white disks and the white tracks represent the preexisting holes. The intensity profiles along Z are plotted on the graph e) for all cases. By direct comparison with experiments, the ablation threshold is obtained for a normalized intensity of 78%." [218]

The micro-Bessel beam does not form properly anymore, thereby affecting the processing of the next hole. Also, another reason lies in possible modifications of the material properties between the holes (densification, index change, structural

reorganization, etc.). This could influence on uncontrolled material fracture, thus forbidding the formation of straight and regular holes. In the previous work by Liu et al. [218], the numerical simulation shows how the length of the micro-Bessel beam gets shorter when the beam propagates through densely packed channels with a pitch down to 0.75 μm. Decreasing the pitch from 1.5 μm to 0.75 μm yields several beam distortions, amongst which are intensity modulations, increased beam divergence, and shortening the length of the Bessel beam for ablation. As found out in their work, due to the existence of a previous hole, the intense central core of the Bessel beam can no longer be formed without perturbation. For a pitch of 0.75 μm (case d), the intensity along the propagation axis decreases which yields a reduced depth of a hole, where only the first 3.6 μm overpasses the threshold.

The beam whose length gets shortened affects the next channel to be written. Therefore, if we consider the machining direction, the first channel will always have a straight and long profile compared to the rest of the channels machined after as shown in Figure 3.28. As also shown in Figure 3.28, the quality of the sidewalls and entrance of the next channels get degraded.

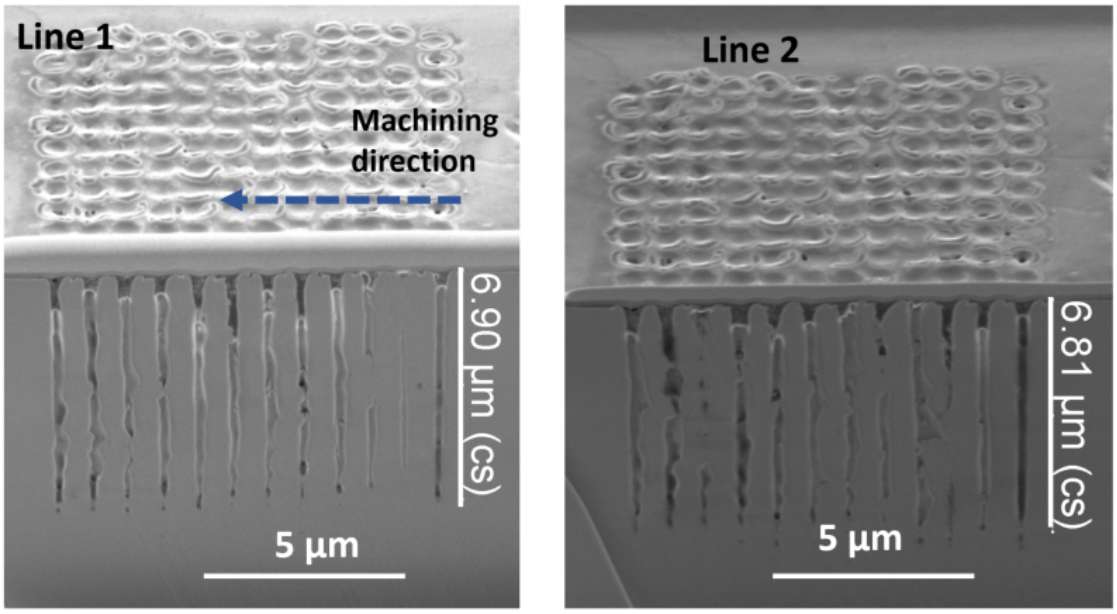

Figure 3.28 – Channel lengths seen in transparency with 0.8 μm pitch machined with E~0.33 μJ. The length of the first channel for both lines 1 and 2 is similar which is measured as ~6.85 μm. The sidewall quality of channels gets distorted gradually afterward, providing the proof of presence of the cross-talk effect.

We also tried channels with 0.7 μm pitch as shown in Figure 3.29. We observe clear limitation of writing channels with sub-wavelength (800 nm wavelength is used to write structures) feature. Again demonstrating the crosstalk perturbation of the

previous channel on the next one, the first channel looks comparatively well machined than the rest of the channels.

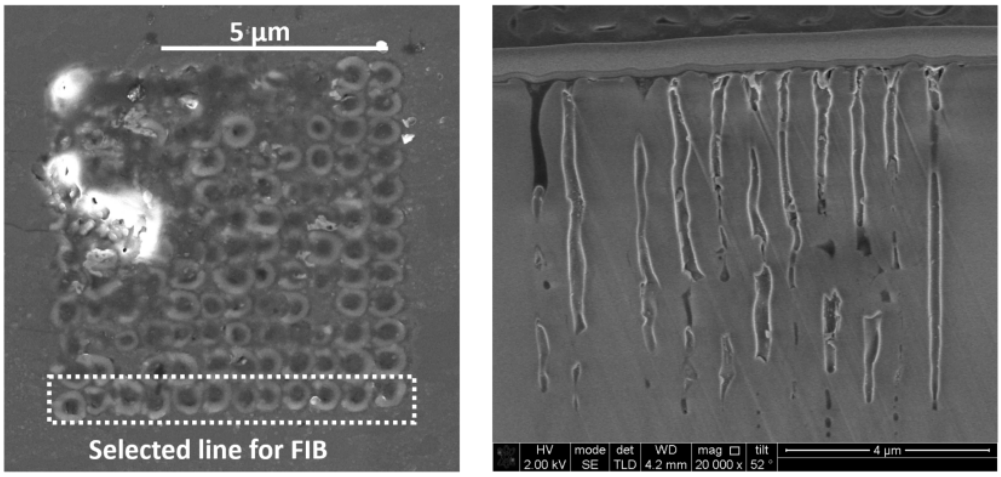

Figure 3.29 – Channels with 0.7 μm pitch at E~0.33 μJ.

These results show us the limitation of the writing of the channels, that is the wavelength of the beam used for structuring. Matrices written with a pitch below or equal to the wavelength are not well separable anymore.

As suggested by [240], there should be a minimum spacing of writing wavelength for the rim to not influence the beam propagation and writing, which again suggests that the diffraction of light imposes a crucial role. This limitation we find true for the length of the channels, since the channel profile, and the sidewalls get destroyed by the influence of pre-existing channels.

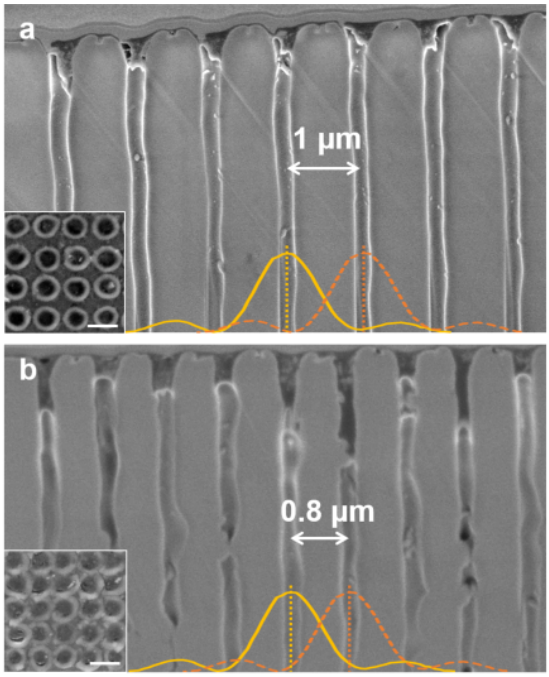

Figure 3.30 – Channels with a) 1 μm and b) 0.8 μm pitch at E~0.33 μJ machined at rear surface.

In Figure 3.30, we have compared the beam profile with the channel spacing for 1 μm and 0.8 μm channels at the rear surface. It is observed that we can resolve until 1 μm channels and for 0.8 μm the channels are separable but we compromise on the sidewall quality. This ensures the limitation by beam core size which is measured as 0.96 μm and finally, this limits the pitch of the channels with the desired profile to 1 μm.

Let us now summarize the main findings related to this paragraph. The FIB was performed on the channels machined both at the front and rear face of fused silica. We have successfully measured the channel diameter, entrance quality, sidewall quality, and length of channels in both cases. The entrance of the channel looked like a funnel shape which we attributed to the presence of a rim around the craters. The funnel length shape is larger for the channels machined at the front surface compared to the channels at the rear surface as the presence of a rim affects the front surface channels more. The channel diameters are similar ~200 nm for an energy E~1.7E_{th} for the channels at the front surface and E~1.1E_{th} for the channels at the rear surface. The measured diameters are significantly smaller than the Bessel beam core diameter (0.96 μm). We observed more parallel sidewalls for channels at the rear surface compared to the front surface. The length of channels measured at two surfaces near the threshold energy is also similar. We can machine separated channels with a spatial pitch lower (0.8 μm) than the beam core radius (see Figure 3.26(b)). We observed even when the rims of the craters touch each other at the surface (see Figure 3.26(a)), the channels remain separated in depth, although their quality degrades. We can conclude that the

rim may limit the channels to reach sub-micron spacing at the surface, but overlapping rims are not a limitation for channels to be separated in depth as we see for channels with 0.7 μm pitch near the threshold energy (see Figure 3.29).

3.8 Summary

We have fabricated and characterized deep holes with micrometer spacing between two adjacent holes at the front and rear surface of fused silica with the ASUR system of 800 nm wavelength and 1 ps pulse duration. An ablation threshold of 0.2 μJ for the front surface and of 0.3 μJ at the rear surface was detected with the Liu method allowing us to calibrate in energy the machining processes for micrometric surface structuring. Then using dedicated methodology, we show that dense sub-micrometric surface structuring (until 0.8 μm pitch) can be reached by using rear surface configuration only. This is mainly due to a crosstalk effect which is more important for the front surface configuration compared to the rear surface one.

We have also encountered the problem of pollution at the front surface (see Figure 3.15), which we tried to clean with techniques like plasma cleaning and ultrasonic cleaning. Plasma cleaning was not promising, but with ultrasonic cleaning with adjusted parameters, we achieved comparatively better cleaning of the debris around the matrix. Cleaning the small pitches remains a problem (see Figure 3.18). Finally, the pollution could be reduced with machining at the rear surface.

After, we decided to characterize the channel characteristics in depth. In vision to characterization, an extensive FIB-SEM analysis was performed to study the channel sidewall qualities, diameter, and length. We demonstrate that we can machine channels with ~200 nm diameter with parallel side walls and with a pitch of 1 μm. This is much smaller than the beam size (0.96 μm) showing the thresholding effect of laser writing. We also confirm that the rear surface configuration is bringing advantages for small size and high-quality structuring with more regular parallel channels and reduced funnel shape compared to the front surface arrangements. This again is due to the crosstalk effect which has more impact on the front surface configuration.

Concerning surface structuring, we conclude that a spatial limitation for high-density stacking comes from the presence of a rim related to the thermal dissipation of depositing energy. This limitation could be removed by polishing the surface in the future. In particular, if we can remove the depth corresponding to the funnel shape length characterizing the hole entrance, we could reach surface structuring with a hole diameter of ~200 nm.

4 Material processing in the bulk of the dielectrics

4.1 Introduction

Typically, all-dielectric meta-photonic devices and optical functionalities, such as photonic crystals or metalenses, are crafted by etching arrays of nanoholes onto the material surface. Two-dimensional photonic-crystal structures offer precise control over light confinement, facilitating controlled waveguiding [245]. Conversely, photonic two-dimensional metamaterials, known as metasurfaces, provide the ability to locally manipulate the phase, polarization, and amplitude of transmitted light [245] [246]. Consequently, they can generate innovative optical effects such as meta-lensing [247] and meta-holography [248], which are gaining rapid integration into microchips today [249] [250].

In the work of P. Barton et al., they presented an innovative method for the direct laser fabrication of metal nanostructures for plasmonics, with potential applications in sonophoresis and micro-nanoelectronics [6]. Also, the use of surface plasmon (SP) assistance metal optical nanofabrication technology has demonstrated its capability for achieving 3D and exact structural fabrication on nanoelectronic devices and optical metamaterials [251]. These structures have been demonstrated on the surface.

Now, extending the capabilities of surface meta-devices into the bulk material offers several advantages. Firstly, it enhances mechanical robustness and resistance to external contaminants and aggressions. More importantly, it unlocks the potential for designing more intricate architectures by introducing an additional spatial dimension as a novel degree of freedom [252]. Additionally, this approach paves the way for the three-dimensional integration of multiple functionalities within a single chip, all manufactured within a unified material platform.

Laser-based methods have proven effective in accessing the volume of transparent dielectric materials. Specifically, direct ultrafast laser processing has emerged as a robust and versatile top-down approach for achieving three-dimensional fabrication within such materials. Notably, this method stands out as a single-step technological process, eliminating the need for additional post-processing techniques or specific materials, as seen in other approaches like two-photon laser writing in photoresists followed by chemical etching [253] [254] [255]. Also, proposing a digital laser-processing technology solution for the flexible in-volume fabrication of embedded nanochannel-

based meta-photonic structures holds significant potential for creating new devices and enhancing broader applications.

In the current study, our focus is on the ultrashort ablation regime, showcasing the in-volume laser machining of flexible configurations of nanochannels. Ablation inherently offers the most significant possible index change (Δn=$n_0 - 1$), as the refractive index of the remaining void equals 1. This natural advantage provides access to high contrasts, with values approaching unity or even surpassing it, contingent upon the refractive index of the original material, denoted as n_0. In this research, fused silica glass, a widely used optical material, serves as the test material. Nevertheless, ultrashort-pulse direct laser ablation is a versatile technique easily applicable to any dielectric or semiconductor material, with the sole requirement being the material transparency to the laser wavelength [256][257].

Our previous experiments performed on the surface find several challenges too. One of our primary aims, to space the array of holes with micron to sub-micron spatial resolution (limited $\sim 1\ \mu m$) faced challenges due to the debris issues around the structures, which raised from very localized femtosecond laser-matter interaction. With the help of FIB analysis, we have observed that the channels in-depth exhibit parallel walls with diameter ~200 nm. This dimension of the channel diameter is suitable for the fabrication of photonic structures. The surface structuring includes the presence of rims which limits to achieving spatial resolution much below 1 μm at the surface. Usually, the photonic crystal structures are holes with a spatial resolution of ~500 nm at the surface and cylindrical channels beneath the surface. The funneling effect that we have observed beneath the surface, (see Figure 3.21 in Chapter 3) also imposed a limitation in achieving cylindrical walls which is also crucial for photonic crystal structures. However, the funneling effects exist only until 300-400 nm down from the surface as shown in Figure 3.21 and Figure 3.22 in Chapter 3. Therefore, machining in the bulk could help to avoid these two limitations caused by the rims at the surface and funnel shapes beneath the surface and therefore to achieve the dimensions usually suitable for photonic crystal structures.

Our initial investigation focuses on assessing the control over individual channel characteristics within the bulk material by varying laser pulse duration and pulse energy relative to the ablation threshold. Subsequently, we tackle the crucial challenge of creating densely stacked structures, demonstrating the feasibility of achieving sub-micron spacing between adjacent channels. Drawing from these findings, we illustrate three different variations of integrated meta-photonic-type structures that can be realized using our method, and we evaluate their relevance through numerical analysis. This marks the first step in showcasing the potential of direct ultrashort laser ablation as a versatile and single-step solution for crafting embedded nanophotonic structures with agility.

4.2 Experimental arrangements

We placed ourselves in similar experimental conditions as mentioned in Chapter 3. The Bessel beam is placed inside the sample which refers to Case 1 (see Figure 3.2 in Chapter 3) of positioning the sample. We take advantage of the same truncated Bessel beam used for the surface machining as shown in Figure 4.1.

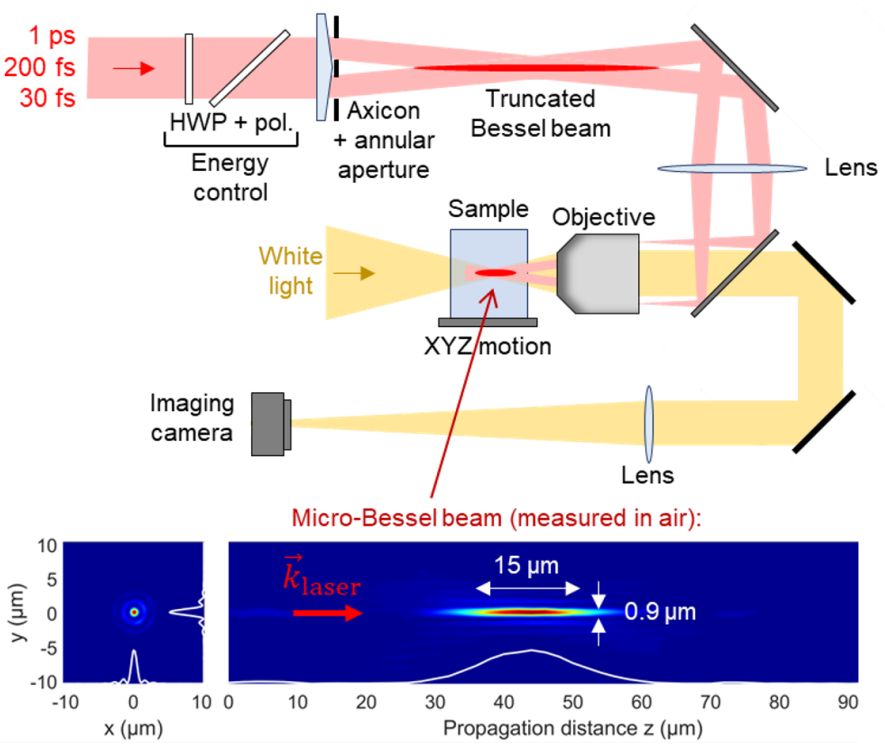

Figure 4.1 – The experimental arrangement for bulk machining.

This Bessel beam has a half conical angle of 21.4° in air, resulting in 14.6° in the bulk upon propagating through the fused silica with a refractive index of 1.45 at 800 nm (as mentioned in Chapter 2).

We have machined 10 individual channels under several irradiation conditions. To start with the machining experiment in the bulk, we performed the Z-scan procedure as mentioned in section 3.2, to locate the surface of the sample. The sample is further translated by 100 μm such that the peak intensity of the beam is located ~145 μm inside from the surface (due to refraction) i.e., completely inside the sample. The sample is a synthetic (spectrosil) fused silica cube of 1 cm edge length, all sides polished. The experiment is performed near a lateral edge of the sample to facilitate further ex-situ transverse imaging by optical microscopy (distance ~150 μm, smaller than the working distance of the imaging microscope objective). The channels are machined one by one in a single-shot regime, the sample is translated laterally by a piezo-electric stage ($NPXYZ100$) from Newport-MKS with a nanometric spatial resolution after each shot.

After machining, we observed the channels under the oil immersion optical microscopy technique. The increased resolution of oil immersion microscopy helped us to resolve the sub-micron structure with accuracy. Later, we have taken advantage of a side view of the microscopy technique to determine the length of the channels.

4.2.1 Adjustment to the shortest pulse duration

In the following experiments, we explore three different pulse durations, including the nominal and chirped pulse durations (30 *fs*, 200 *fs*, and 1 *ps*). Achieving a 30 *fs* effective pulse duration at the focal point necessitates precise pre-compensation for the unknown dispersion introduced by the focusing microscope objective. However, measurement of the pulse duration at the focus is impossible without extra beam recollimation – that would inevitably introduce again dispersion and then skew the measurement. To circumvent this technical difficulty and adjust experimentally the adequate amount of negative dispersion that should be introduced by tuning the laser compressor, we rely on a nonlinear effect, sensitive to the intensity and thus to the pulse duration. We place a thin (200 μm) BBO crystal at the focus at low energy; the shortest pulse duration of 30 *fs* is ensured when the second-harmonic signal is maximum while tuning the laser compressor. Further, the durations of 200 *fs* and 1 *ps* are obtained by adjusting the compressor by an experimentally pre-calibrated amount concerning the 30 *fs* pulse duration.

4.2.1.1 Pulse width measurement

We used the auto-correlator device BONSAI (Amplitude technologies) to measure the pulse width of our beamline provided by the ASUR system.

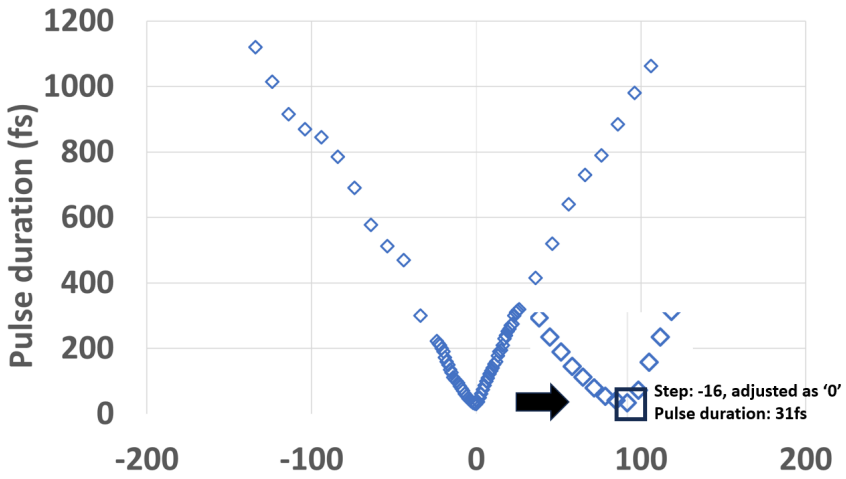

Figure 4.2 – a) Pulse width measurement with the auto-correlation system BONSAI. The figure shows the parabolic curve between grating translation steps and pulse duration.

By changing the distance between the two gratings of the compressor, we change the compression rate and thus the pulse duration. We started with a grating step of 90, which gave us a pulse duration of ~1 ps. After we reduced the steps and noted a corresponding decrease in the pulse duration. Upon reaching near the nominal pulse duration of ASUR, which was measured before as 23 fs (when everything was optimized in the system and in particular the compression system), we performed a scan with a translation step of unity of the compressor. After we continued the scan until we reached ~1 ps again. The nominal pulse duration of 31 fs was obtained for a grating step of −16 in our experimental configuration. Later, we set the step corresponding to this nominal pulse duration as the minimum (as zero) and obtained a parabolic curve as shown in Figure 4.1.

4.3 Parametric study of channels

The primary aim is to evaluate the role of pulse duration on Bessel beam laser writing. The fundamental reason underlying that is the necessity to deposit energy in a dielectric medium which requires nonlinear absorption, but also poses the question of nonlinear propagation inside bulk material which is inherently sensitive to the pulse duration. Lamperti et al. [221] carried out a study, where they numerically presented the nonlinear energy absorption in fused silica for a Gaussian pulse as a function of fluence (the measured energy delivered per unit area) and pulse duration. It has been reported that the highest absorption was found for pulses with duration <100 fs. However, the energy deposition in the material is more robust and finally more efficient for the longer picosecond pulses when a comparable fluence (w.r.t Gaussian beam) is attained by the Bessel beam. Indeed, the study has reported that at longer picosecond pulse duration the nonlinear absorption is homogeneous within the Bessel zone (within the DOF) and the propagation invariance property of the Bessel beam is retained efficiently. But, at shorter femtosecond pulse duration the non-stationary fluence gives rise to cycles of rapid nonlinear absorption, which finally affects the Bessel beam propagation inside dielectrics [52].

This study helped us to choose our pulse durations to perform the experiment where we explored the writing conditions for regular, well-separated, and high-quality nanochannels.

Next, we have carried out the parametric study on the channel laser writing for different pulse durations of 1 ps, 30 fs and 200 fs (see Figure 4.2). The channels were fabricated in the single-shot mode for several pitches starting from 5 μm to 0.5 μm. The energy is varied over a range from threshold (E_{th}) to five times of threshold ($5E_{th}$).

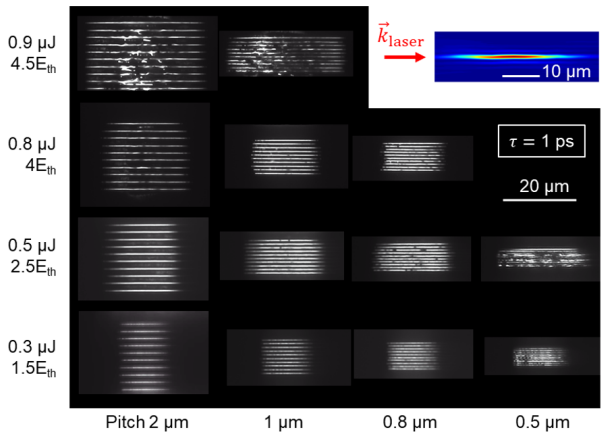

(a) 1 *ps*

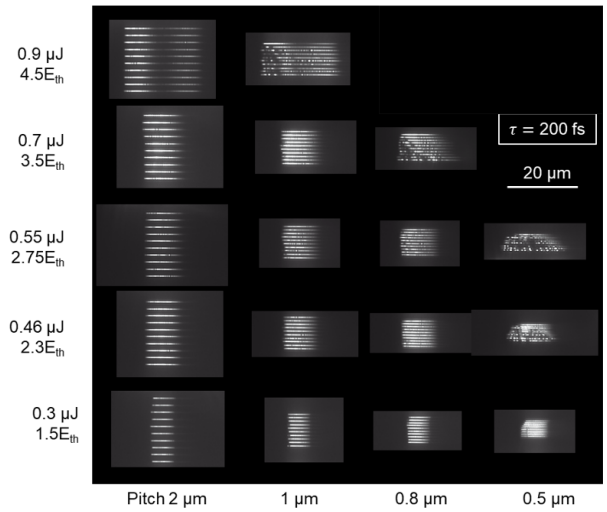

(b) 200 *fs*

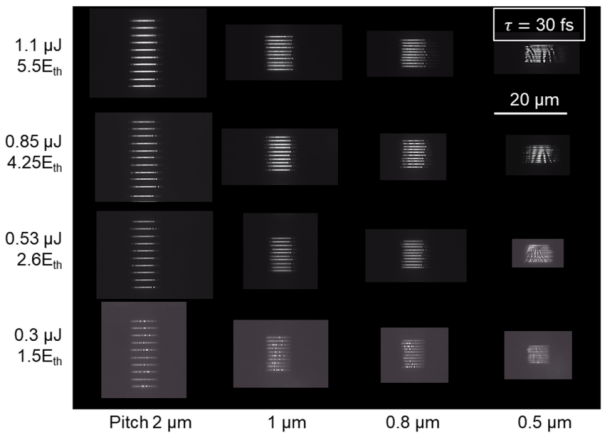

(c) 30 *fs*

Figure 4.3 – Parametric study of channels in bulk for a)1 *ps*; b)200 *fs*; c)30 *fs*. For 1 *ps*, 0.8 μm, 0.5 μm was not done for higher energies. The energy range explored here is between E_{th}=0.2 μJ and $5E_{th}$=1 μJ. The pitch has been varied from 5 μm to 0.5 μm for three different pulse durations.

From the parametric studies, we concluded as listed below,

1. From Figure 4.3, we observed the white modification tracks under the epi-illumination mode of optical microscopy. These modifications seen under trans-illumination (see Figure 4.5 (left column)) are similar to the modifications found in Sapphire as shown by [258], in glass as presented in the work of [224]. Also, in our experiment of surface machining, we observed the channel profile in depth (see section 3.7 of Chapter 3), similar to the one found in the literature mentioned above. Therefore, these studies give us full confidence to conclude these white tracks (seen under epi/trans-illumination) to be the nanochannels formed either by refractive index modification or by void creation (as described in section 1.1.4 of Chapter 1).

2. Reducing pulse duration allows to obtain regular structures even at high energy contrary to what is observed for longer pulses. However, the structures obtained are much shorter. As mentioned in the work of R. Beuton [147], this should be attributed to the higher intensity used inducing a stronger intensity clamping effect and also stronger screening and diffraction effects, constraining an efficient 'over-the-threshold' energy deposition to the central Rayleigh zone (DOF) only of the Bessel beam. The structures obtained seem to be regular (even at high energy, no degradation / low energy) showing very good resistance (no sensitivity) to the optical Kerr effect. For 1 ps case, the structures obtained are much longer (no clamping effect), but irregular at high energy mainly in the central zone (except the first one), so expressing the limitation of the self-healing capability of a Bessel beam when a too large amount of obstacle (modified material) is present on the beam path. The irregularities could also appear from post-mortem modification of the material and the necessity for the Bessel beam to propagate through them (when drilling successive channels): the cross-talk effect.
3. Interestingly, the use of shorter pulse duration appears as a technical solution given dense stacking (at the expense of shorter length and a few adjustable structures obtained because of the clamping effect). Changing (increasing) the pulse duration in *fs* range and adapting the energy can provide satisfactory flexibility to circumvent this technical limitation (in terms of patterning) seen for ultrashort pulses.

4. A shadowing effect was observed in the imaging of channels at 200 *fs* (see Figure 4.3 (c), case 0.9 μJ, 2 μm). This is attributed to the perturbation of illumination by other marks, structures that were close to the series of interest.

The parametric studies confirm that the sub-micrometric pitch was attained close to threshold energy while machining. The observation under high-resolution optical microscopy (with an oil immersion objective) shows that a pitch of 0.8 μm remained the last resolvable pitch for any pulse duration achieved with E~1.5E_{Th}.

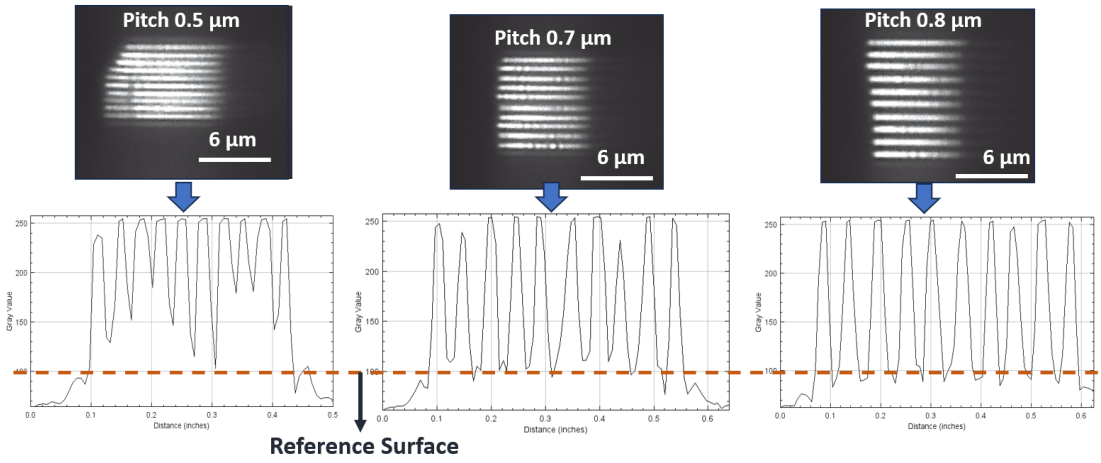

Figure 4.4 – The resolvability of the nanochannels (measured against the reference surface) based on the pitch of structured 10-channels. A pitch of 0.8 μm, 0.7 μm and 0.5 μm was machined with E~1.5E_{Th} at 200 *fs* pulse duration. The pitch of 0.5 μm remains unresolved while 0.8 μm and 0.7 μm remain resolvable. We provided the microscopic images and the profile of 10 channels taken with the software ImageJ.

The 200 *fs* and 30 *fs* allowed us to reach down to 0.7 μm, but 0.5 μm remained a limitation irrespective of the pulse durations as shown in Figure 4.4. Not only we can access the sub-micrometric range with near-threshold energy, but this parametric study also confirmed that the energy range of 1.5 - 2E_{Th} could be a good choice for the future structuring of photonic components.

We have seen that the length of the channels varies with energy and different pulse duration. To investigate further the characteristics of channel length with 1 ps, 30 *fs* and 200 *fs*, we recorded two kinds of images under brightfield optical microscopy, using respectively trans-illumination and epi-illumination modes. In trans-illumination, the incident light is transmitted through the channels and the contrast is created based on the absorption. The modified areas (channels) absorb more light than the surrounding unmodified areas. Therefore, in trans-illumination mode, the channels are visualized as dark tracks against a gray backdrop as shown in Figure 4.5 (left column). In epi-illumination mode, the light is reflected from the channels to create the contrast. The morphology of the channels appears different in these two modes. While, the epi-illumination mode shows us only the voids (the channels), in trans-illumination modes the modifications before and after the channels are also visible, especially for 30 *fs* and 200 *fs* (see Figure 4.5 (left column)). We previously verified that the dark regions in trans-illumination mode correspond to regions where the material has been removed [24].

Within the range of energies examined in this study, the typical channel diameter (determined using SEM) falls within the range of (190-340 nm), varying based on the

pulse energy, as detailed in prior research [218]. This dimension is notably smaller than the central core diameter of the truncated Bessel beam. In this context of confined ablation, the volume of ablated material cannot escape the sample and is consequently redeposited along the channel sidewalls, thus constraining their diameter.

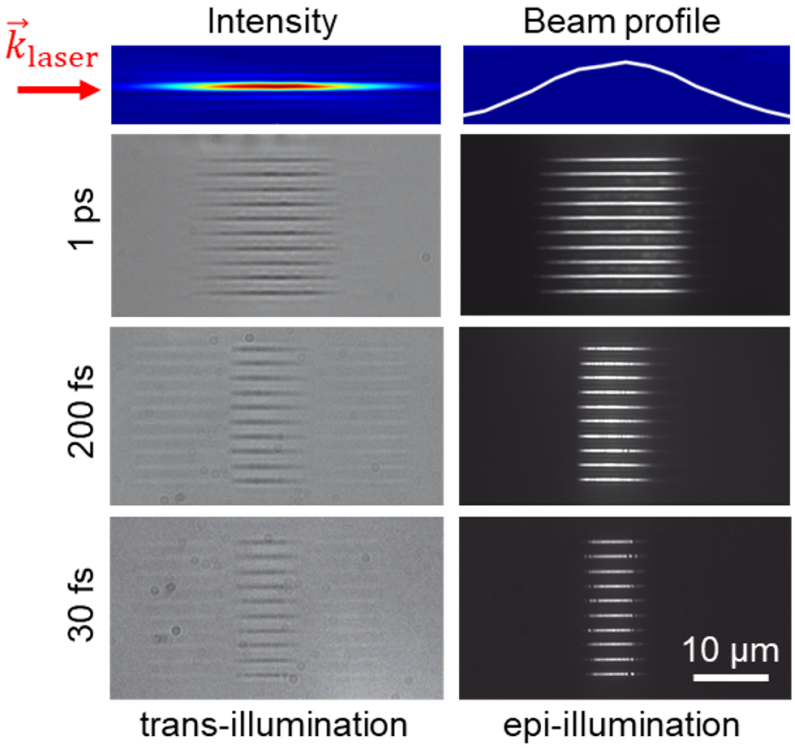

Figure 4.5 – Side-view images of a series of 10 channels in the volume of fused silica, with a pitch (spacing) of 2 μm. Each channel is machined by single-shot ablation, with the energy ~0.5 μJ. For each pulse duration (1 ps, 200 fs, 30 fs), trans-illumination images (left column) and epi-illumination images (right column) are shown. The laser beam is incident from the left (k_{laser}). The scale bar holds for all images, including the beam intensity and its longitudinal profile.

In the case of 1 ps pulse duration, both images display a consistent and uniform channel morphology that extends continuously along the entire length of the channel. This morphology faithfully reproduces the distribution of the beam's intensity. However, when we examine shorter pulse durations (200 fs and 30 fs) at the same pulse energy, we also identify ablated regions, which are evident in the epi-illumination images. Nevertheless, these ablated regions are noticeably shorter in their longitudinal extent compared to the 1 ps case.

Furthermore, in the trans-illumination images, we observe faint white tracks on either side of the laser axis along with the channels, particularly pronounced in the 30 fs case, as illustrated in Figure 4.5 (bottom). These tracks are characteristic indicators

of index modification rather than ablation, as documented and characterized in other studies [259] [260]. This is corroborated by the fact that these tracks do not appear in epi-illumination images, which exclusively reveal the ablated regions.

The first mechanism relates to the likelihood of nonlinear propagation effects that can significantly distort the beam's behavior inside the sample. This is a plausible occurrence, given that the critical power for Kerr self-focusing (P_{cr}=3.77$\lambda^2/8\pi n_0 n_2 \sim 1$ MW for fused silica at 800 nm) is surpassed only for the 200 fs and 30fs cases, reaching peak powers of 2.5 MW and 16.7 MW, respectively.

The second mechanism is linked to ionization physics: shorter pulses generate higher intensity and faster ionization, leading to intensity clamping [261]. Under similar experimental conditions, previous studies with numerical simulations [259] [260] [221] have demonstrated less efficient absorption of laser energy within fused silica for shorter pulses, resulting in a lower and spatially non-uniform excitation density.

4.3.1 Individual channel characterization

By employing epi-illumination images and profiles, we have conducted measurements of the channel length while varying the pulse energy for each pulse duration, as shown in Figure 4.6. The graph in Figure 4.6 summarizes the results obtained.

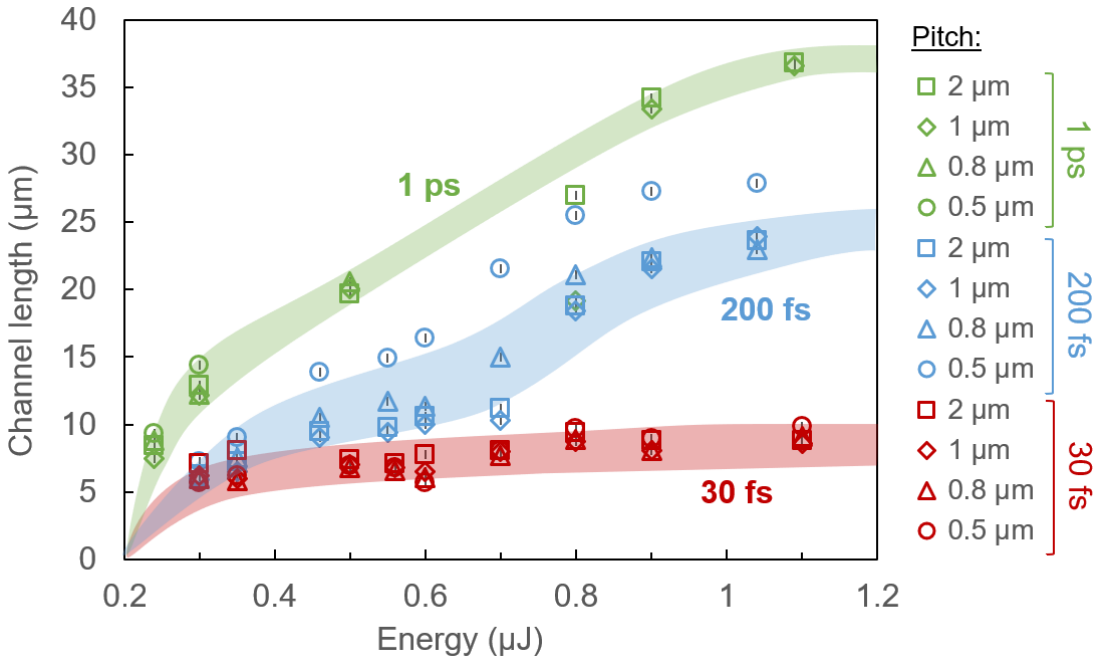

Figure 4.6 – Nanochannels characteristics. Channel length as a function of incident energy of the laser pulse. Normalized energy E/E_{th} (E_{th} = 0.2 μJ). For each pulse duration and energy, channels are measured for four different pitches.

In the case of a 1 ps pulse, we can achieve channel lengths ranging from below 10 μm to approximately 35 μm. Conversely, with a 30 *fs* pulse duration, we observe that the ablated channel length exhibits a near-independence concerning the pulse energy, providing access to a narrow/selective processing window with a channel length of 5 μm in our experimental Bessel beam configuration. Meanwhile, the 200 *fs* series falls into an intermediate regime.

The data presented in the graph also suggest that, despite the differences in pulse durations, the threshold energy required to create a hollow channel within the fused silica material appears to be approximately consistent across all three cases studied here, approximately around E_{th}~0.2 μJ. However, it's worth noting that a precise determination of ablation thresholds for each pulse duration would necessitate conducting a meticulous energy scan around this threshold energy range.

In summary, both pulse energy and pulse duration emerge as significant parameters for accurately controlling the lengths of the channels created.

4.4 Dense stacking of channels down to sub-micron pitch

After successfully controlling individual channels, our objective is to achieve the smallest spacing between channels when fabricating closely packed channel assemblies. To accomplish this, we systematically explore a 3D parameter space encompassing pitch (p), energy (E), and pulse duration (τ). The parametric studies showed us that to access the dense stacking of channels, lower energy close to the threshold (E~1.5E_{th}) is favorable. As an illustrative example, Figure 4.7(a) presents specific results for a chosen energy level (E~0.5 μJ), with variations in pitch and pulse duration.

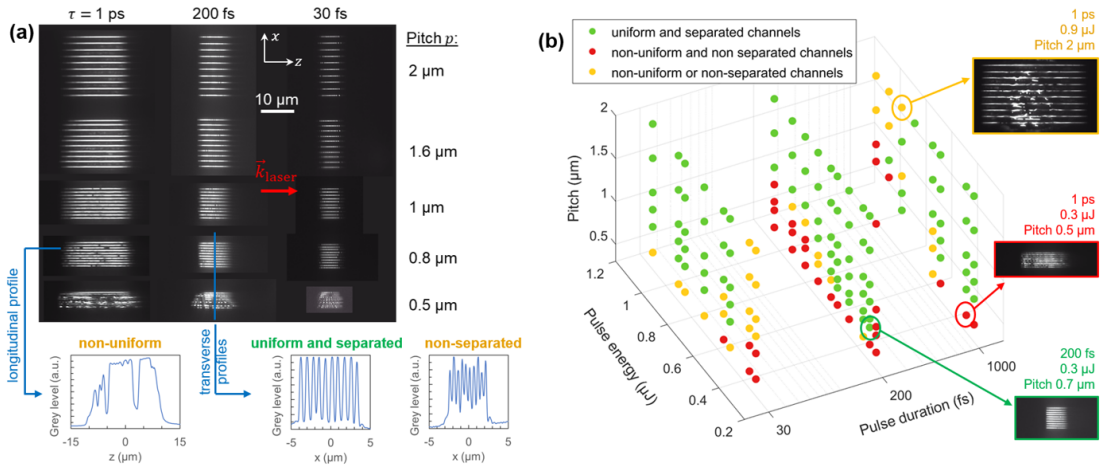

Figure 4.7 – Parametric study to reach the dense channel stacking. a) Series of 10 channels in the volume of fused silica, with a decreasing pitch (from $p = 2$ μm to 0.5 μm) and for various pulse durations. Each channel is processed by single-shot ablation, with a constant energy (here $E \sim 0.5$ μJ). Longitudinal and transverse profiles of channels are extracted from images. It enables to define and assess the criteria to define uniform and separated channels. b) Results of the parametric study in a $3D$ space (pitch, pulse energy, pulse duration). Experimental conditions corresponding to green points are accepted whereas yellow and red points are rejected. Insets show examples of corresponding channels (same scale as for Figure a).

Figure 4.7(a) reveals that regular and separated channels can be achieved for all three pulse durations when the pitch is larger than 1 µm. However, as shown in the insets of Figure 4.7(b), it becomes apparent that for a given pulse duration, it is advisable to avoid high energy levels and/or small pitches, a notion that aligns with intuitive expectations. To precisely determine the suitable range of experimental conditions, we introduce two criteria.

The first criterion pertains to the uniformity of channels along their length. This is exemplified, for instance, in the case of a 1 ps pulse duration in Figure 4.7(a) when the pitch decreases to 0.8 μm: some channels within the series exhibit interruptions, manifesting as dips in the longitudinal profile along the z-axis. We define any drop of >10% in image intensity as a discontinuity, leading us to discard the corresponding series.

The second criterion concerns the separability of channels, which we assess by plotting transverse profiles along the x-axis for a series of 10 channels. We determine that channels are adequately separated when the intensity between adjacent channels returns to zero within a 10% tolerance. This is demonstrated in the case of a 200 fs pulse duration as shown in Figure 4.7(a), where a pitch of 0.8 μm is deemed acceptable, while a pitch of 0.5 μm is rejected.

By applying these criteria across the range of experimental conditions explored, we generate the graph in Figure 4.7(b), which delineates the appropriate parameter combinations (green points) for producing high-quality, well-separated channels. If one of the two criteria is not met, the points are represented in yellow, while red indicates a failure to meet both conditions, such as in the case of a pitch of p=0.5 μm for all pulse durations in Figure 4.7(a).

In conclusion, we can achieve submicron pitches with the three pulse durations examined here by carefully selecting the appropriate combinations of energy and pulse duration. For those seeking the highest tunability (in terms of accessing various channel lengths) and density of channel assemblies, using a 200 *fs* pulse duration is preferable, allowing for the fabrication of separated good-quality channels with pitches over an extended spatial range, from as small as 0.7 μm and as high as 2 μm (see Figure 4.7(b)). Notably, this value is slightly less than the wavelength of the writing femtosecond laser. This achievement surpasses previous results obtained with a shorter wavelength (515 nm), which initially seemed advantageous but encountered limitations such as beam distortions and hole breakage when attempting to densely pack holes below a spatial pitch of 1 μm [262]. Our work demonstrates the robustness of micro-Bessel beams as a solution to overcome existing limitations.

The limit we encounter in this study is primarily associated with a "crosstalk effect" during laser machining, a phenomenon we have previously identified [218]. Since the channels are machined one by one sequentially, the presence of previously machined channels disrupts the proper propagation of the Bessel beam when machining the next adjacent channel. This is qualitatively illustrated by examining a series of channels fabricated with a 200 *fs* pulse and a pitch of 0.5 μm in Figure 4.7(a). Upon careful examination, it becomes apparent that the channels systematically lengthen and show irregular morphology from the first channel in the series (the top one in the image, with the same length as those at larger pitches) to the last one (which is longer). The quantitative values are reported in the graph in Figure 4.6, revealing a deviation in measured lengths when the pitch is reduced to 0.5 μm (blue circles), accompanied by significantly larger error bars. This is probably due to the redistribution of energy during beam propagation in the previous post-mortem zone (thus except the first one), which further contributes to increasing irregularity and the channel length, sometimes even exceeding the DOF of the Bessel beam. Additionally, this underscores the adverse impact of crosstalk during laser processing when reducing the pitch significantly below the laser wavelength, corroborating our numerical simulations [218] as detailed in section 3.7.5 of Chapter 3. To overcome this limitation and achieve pitches down to a few hundred nanometers, strategies such as using smaller wavelengths by frequency-converted beams (for example by generating the second harmonic of the fundamental beam) or parallel processing should be explored. The parallel processing can induce low-level perturbation in the machined zones which are only affected by the beam propagation, but mostly eliminates the perturbation from post-mortem zones.

4.5 Fabrication of embedded basic and meta-photonic structures

The above-mentioned studies performed with varied laser parameters (pulse duration, energy) helped us to develop a versatile writing pencil laser tool. The Bessel beam writing tool is efficient in patterning basic structures like squares, and hexagons in the bulk as shown in Figure 4.8. The three pulse durations previously used for parametric studies have been explored to fabricate the structures with micron and sub-micron pitches. These geometries are basic units for advanced photonic components like waveguides, and metalenses which allowed us to demonstrate the first possibility of writing such photonic components.

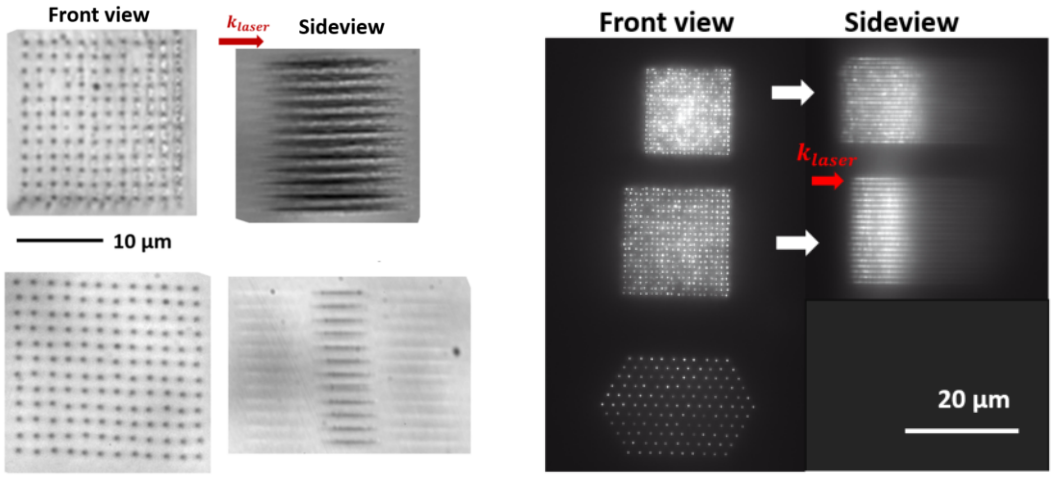

(a) (b)

Figure 4.8 – Photonic structures written inside the bulk of dielectrics at E~2.5 E_{th}, imaged under optical microscope for a) 2 μm square lattice with 1 ps (top); 2 μm square lattice at 30 fs(bottom); b) 0.8 μm square, 1 μm square and 2 μm hexagon lattice at 200 fs. We present the front and side view with trans-(a) and epi-(b) illumination modes.

After, the Bessel beam writing tool was also capable of fabricating embedded meta-photonic structures, thanks to its versatility and agility. This will be discussed in the next section.

4.5.1 Fabrication of embedded meta-photonic structure

Finally, having successfully demonstrated the feasibility of creating precise arrays of channels, our focus now turns toward the fabrication of more intricate structures embedded within fused silica (as depicted in Figure 4.9). Given our ability to achieve sub-micron pitches, which correspond to a fraction of the short-wave infrared (SWIR) or

mid-infrared (MIR) wavelength range, our objective here is to offer a proof-of-concept demonstration of how our approach can pave the way for the direct manufacturing of integrated nanophotonic components. In this section, we showcase this potential by constructing structures whose arrangements and dimensions mimic meta-photonic devices, which, depending on their characteristics, can serve as photonic crystals or metamaterials. These structures are fabricated at a depth of 145 μm within the sample, with each channel being sequentially created using a single laser shot without moving the workpiece along the z-axis.

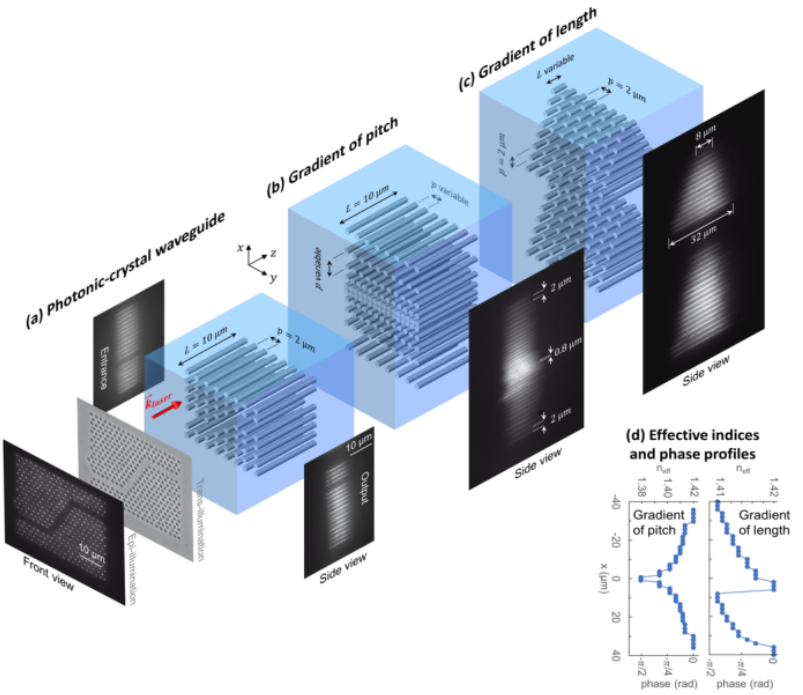

Figure 4.9 – Integrated photonic metastructures composed of hollow nanochannels machined inside the volume of fused silica. For each case, the design is schematically represented, whereas experimental optical microscopy images of channel assemblies are displayed. Each channel is drilled by a single laser shot, without moving the workpiece along the z direction. (a) A photonic-crystal waveguide arrangement, composed of channels of 10 μm length (pulse duration 200 fs, pulse energy 0.5 μJ) with a pitch of 2 μm. (b) Gradient of pitch along the vertical (x) direction, obtained by variation of interchannel spacing from p=2 μm to p=0.8 μm (pulse duration 200 fs, energy 0.5 μJ). (c) Gradient of channel length along the vertical (x) direction, from L=8 μm to L=32 μm, obtained by laser pulse energy variation from 0.2 μJ to 0.9 μJ (pulse duration 1 ps). (d) Calculated effective refractive indices and corresponding phase profiles along the vertical axis (x) for the two metamaterial structures (cases b and c).

In Figure 4.9, we produce a photonic-crystal (PC) waveguide within a triangular

lattice with a pitch of p=2 μm. The figure encompasses both a conceptual schematic and experimental images from the front and side views. The side views highlight the 'entrance' and 'output' of the waveguide for a reading beam incident along the y-direction. These integrated nanochannels function precisely like their counterparts composed of arrays of nanoholes fabricated on the surface of a dielectric or semiconductor device but with unique advantages. Firstly, the channels can be much longer, as demonstrated here with a length of 10 μm, in contrast to the typical ~1 μm depths achievable with conventional nanofabrication techniques [263]. Secondly, laser machining utilizing Bessel beams provides a direct technological approach to creating cylindrical channels, thus avoiding tapered hole profiles [24]. This aspect is significant for enhancing the efficiency of light confinement within the guided reading beam and minimizing losses [264]. Thirdly, these structures can be flexibly embedded within the bulk of the material, providing inherent protection against external contaminants or degradation factors.

Beyond structures based on regular lattices, the channel-by-channel laser machining approach's flexibility extends the potential for fabricating more complex designs. By adjusting either the individual channel dimensions (diameter and length) or their spacing (pitch), we can generate structures with spatial gradients.

Figure 4.9(b) presents a structure of the 'gradient-index photonic crystal' (GRIN PC) type. While maintaining a constant individual channel template, we progressively increase the pitch along the ±x directions (from p=0.8 μm to p=2 μm, with 0.2 μm increments). This approach opens up possibilities for crafting GRIN lenses. With proper optimization, this gradient in lattice pitch along the lateral distance can controllably manipulate the wavefront of a reading light beam [265],[266] incident along the y-direction.

Alternatively, when illuminated by a reading beam directed along the z-direction (parallel to the channel's axis), the structure in Figure 4.9(b) can function as a 2D photonic metamaterial. The reading beam would undergo a local optical phase delay dependent on the accumulated phase along the entire length of the structures. Variations in the pattern within the transverse xy plane offer the capability to locally manipulate the effective refractive index and, consequently, shape the wavefront of the reading beam as needed. This is analogous to the principles underlying metasurfaces, including structures such as holey metalenses [267][268]. In principle, three fundamental approaches exist to locally modulate the properties of these structures: varying the hole diameter, the hole depth, or the hole spatial density. Our laser direct processing method provides direct access to the two other degrees of freedom besides hole diameter modulation. To illustrate this, we create two different scenarios as described below,

1. A gradient of pitch along the transverse direction (x) while maintaining constant channel length (Figure 4.9(b)).
2. A gradient of channel length while keeping pitch constant (Figure 4.9(c)). These

structures serve as proof-of-concept and have not been experimentally tested.

However, in the following discussion, we anticipate their performance in terms of the magnitude of achievable phase functions and their relevance for metamaterials applications.

We introduce the effective index theory in the next paragraph which was used to anticipate the performances of these structures.

Effective refractive index of the laser-written structures The effective medium theory is a conceptual framework. This enables us to depict a macroscopic dielectric response to an electromagnetic excitation of a heterogenous material, as if it were homogeneous [269]. For this description to be valid, the size of the inclusions inside the native material must be small compared to the wavelength, and their volume fraction (spatial density) should correspond to a dilute concentration. These conditions apply to our case of meta-structures composed of cylindrical air holes with sub-wavelength diameters embedded in a uniform host material (fused silica). The Maxwell-Garnett mixing rule enables us to get an estimate of the effective refractive index of the laser-created structures. Based on Mie's theory considering inclusions inside a homogeneous host material, the exact formulation should be adapted to the specific geometrical shape of inclusions. Apart from spherical inclusions, the only shapes for which simple analytical solutions can be found are ellipsoids. It is an interesting case to us since it encompasses cylindrical channels as a limit case. The Maxwell Garnett formula [270] for composites made of aligned ellipsoidal inclusions of permittivity ε_i inside a uniform environment material of permittivity ε_e writes [271] [270] [272]:

$$\varepsilon_{eff,x} = \varepsilon_e + f\varepsilon_e \frac{\varepsilon_i - \varepsilon_e}{\varepsilon_e + (1-f)N_x(\varepsilon_i - \varepsilon_e)}, \tag{4.1}$$

with f the volumic filling fraction of inclusions. This formulation depicts the fact that the effective permittivity of the mixture is anisotropic, in other words, it has different permittivity components in the different directions x, y, and z, that can be calculated by considering the appropriate depolarization factors (N_x,N_y,N_z). Regarding our practical realizations, as they appear in Figures 4.9(a) and 4.9(b) of the manuscript, the channels are appropriately depicted by ellipsoids of circular section and infinite length in the z dimension (in other words: cylinders), corresponding to depolarization factors of (1/2,1/2,0). Thus, depending on the propagation direction and the polarization of the reading beam, different effective indices must be attributed to the two categories of structures that we have fabricated with nanochannels assembly: metamaterials and photonic crystals. Accounting also for the fact that we machined cylindrical 'air holes' (ε_i=1) inside fused silica ($\varepsilon_e = n_0^2$), the effective indices are then expressed by the following formulas:

1. 'Metamaterial configuration'(case of Figure 4.9(b) and 4.9(c)). The reading beam

propagates along z at a test wavelength of 1.55 μm (corresponding to a refractive index of n_0=1.42 for fused silica), i.e. parallel to the channels. It is therefore polarized in the transverse xy plane (for which depolarization factors N_x=N_y=1/2) so that the effective permittivity writes:

$$\varepsilon_{eff} = \varepsilon_e(1 + f\frac{2\alpha}{1-\alpha f}) = \varepsilon_e\frac{1+\alpha f}{1-\alpha f}, \tag{4.2}$$

with,

$$\alpha = \frac{\varepsilon_i - \varepsilon_e}{\varepsilon_i + \varepsilon_e} = \frac{1-n_0^2}{1+n_0^2}, \tag{4.3}$$

The effective index is therefore written as,

$$n_{eff} = n_0\sqrt{\frac{1+f(1-n_0^2)/(1+n_0^2)}{1-f(1-n_0^2)/(1+n_0^2)}}, \tag{4.4}$$

This expression is classically used in designing nanohole-based metamaterial devices like metalenses [268] [273].

2. 'Photonic crystal configuration'(case of Figure 4.9(a) and Figure 4.9(b)) with the appropriate reading beam). The reading beam propagates along y direction at a test wavelength of 1.55 μm (corresponding to a refractive index of n_0=1.42 for fused silica), i.e. perpendicular to the channels. If the incident polarization is TE (the electric field is oriented along the x direction, perpendicular to the channels), then the corresponding effective index has the same expression as established in the above section because N_x=1/2. If the incident polarization is TM (the electric field is oriented along the z direction, parallel to the channels), then the corresponding effective permittivity is calculated using N_z=0, which yields:

$$\varepsilon_{eff,z} = \varepsilon_e + f(\varepsilon_i - \varepsilon_e) = f\varepsilon_i + (1-f)\varepsilon_e, \tag{4.5}$$

Note that this can be straightforwardly interpreted as the average permittivity of a mixture of two materials weighted by the respective filling factors f and $(1-f)$. The effective index is therefore written as,

$$n_{eff} = \sqrt{f + n_0^2(1-f)}, \tag{4.6}$$

This expression is usually used to depict photonic crystal structures, for example, graded index photonic crystals [274].

Next, we need to calculate the filling factor f. It is calculated by considering a unit (basic) cell linking 4 holes. Therefore, it depends on the pitch p, but also the lattice geometry. For a triangular lattice (as depicted in Figure 4.9(a)), the filling factor is expressed as,

$$f = \frac{\pi}{2\sqrt{3}} \frac{d^2}{p^2}, \tag{4.7}$$

where d represents the channel diameter.

The required value of channel diameter was calculated using our previous work reported by Liu et al. [218]. We presented the measurement of channel diameter as a function of energy in Figure 4.10. In addition to the previous work done by Liu et al., we have also added our measured value of channel diameter at an energy 0.5 μJ in the plot. For example, for an energy of 0.5 μJ, the energy we used to write our photonic structure, the channel diameter has been calculated as 200 nm.

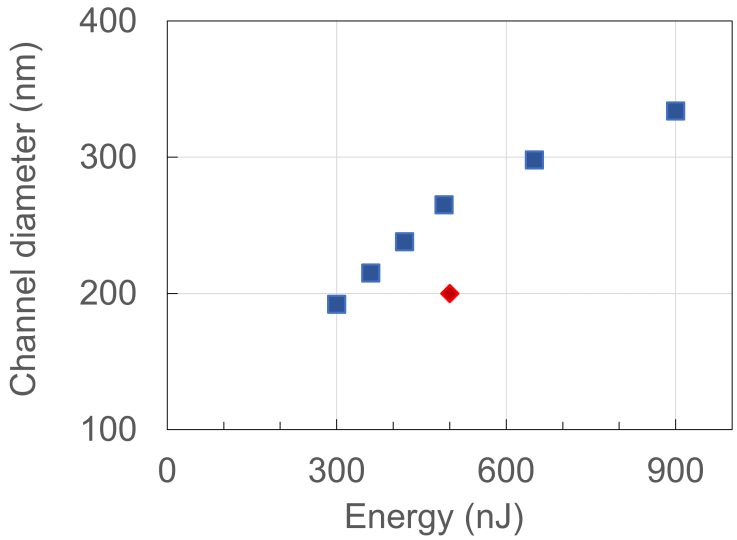

Figure 4.10 – Evolution of channel diameter with laser pulse energy, adapted from [218]. We added our measured value of diameter at 0.5 μJ, which we used for writing structures.

We used this obtained value of d at 0.5 μJ for calculating the filling factor. For the triangular lattice of Figure 4.9(a), with pitch p as 2 μm and d as 200 nm, according to Eq. 4.7, the filling factor was calculated as 0.9%. Whereas for the square lattices of structures represented in Figure 4.9(b) and Figure 4.9(c), the filling factor is written as,

$$f = \frac{\pi}{4} \frac{d^2}{p^2}, \tag{4.8}$$

According to Eq. 4.8, considering the same diameter value at E=0.5 μJ, for the varying pitch as shown in Figure 4.9(b), the filling factor varies from 0.78% (when p=2 μm at the top of the structure) to 4.9% (when p=0.8 μm at the center of the structure).

Figure 4.9(d) displays the calculated effective indices for the two gradient-index metastructures, plotted along the x-direction (vertical). For the gradient of the pitch

case (Figure 4.9(b)), all channels are identical, with a diameter of d=265 nm, employing a pulse energy of 0.5 μJ. Starting from the center of the structure (corresponding to x=0), where the pitch is at its minimum (p=0.8 μm), we increment the pitch every three channels in steps of δx=0.25 p=0.2 μm in both the $+x$ and $-x$ directions. This leads to a gradual variation in effective index ranging from n_{eff}=1.40 at the center of the structure to n_{eff}=1.41 at the extremities. The change in the index relative to the initial value n_0=1.42 appears relatively small compared to typical 2D metamaterials (where the index contrast can reach unity [267] [268] [275]). However, by calculating the phase ϕ(r)=$\frac{2\pi}{\lambda} n_{eff} L$ accumulated over the entire length L=10 μm of the structure, we can achieve a phase difference as substantial as $\sim\pi/2$. Thus, the channel length provides a direct means to control the optical phase delay and, consequently, the magnitude of the generated phase.

In the case of the gradient of channel length (Figure 4.9(c)), variations in pulse energy lead to concurrent changes in channel diameter (affecting the effective index) and channel length (influencing the accumulated phase). By employing measured channel lengths and diameters [218], we also find that a maximum attainable phase of approximately $\pi/2$ can be achieved, despite the small effective index difference. As depicted in the graph, the phase profile along the x-axis exhibits two regions of gradual increase separated by a "phase jump."

Several key takeaways emerge from the analysis of these two case studies. The primary insight is that the additional degree of freedom offered by varying channel length through our approach provides a direct means to compensate for small variations in effective index. Even with a low-index material like simple glass and a small filling factor (here <10%), we obtain phase values that fall within the range of [0-$\pi/2$]. Although we do not achieve complete 2π phase coverage in this instance, there is potential for future enhancements, such as increasing the Bessel beam length or boosting spatial density through downscaling the writing beam's core size (potentially through second harmonic generation). Importantly, this capability cannot be realized with a Gaussian beam, whose inherent confocal length is too short. Furthermore, our methodology offers the possibility to fabricate such structures in standard materials like fused silica, opening the exciting prospect of engraving 2D metastructures across a broader range of material platforms, beyond specific high-index materials [275].

Secondly, the digital writing approach enables the independent scaling of each channel. Unlike conventional 2D metamaterials or photonic crystals, which often rely on altering only the hole diameter (with pitch and depth kept constant) or solely the pitch (with hole diameter and depth held constant), our approach allows for more intricate designs due to the flexibility to adjust pitch, diameter, and depth on-demand. In the two examples presented, we varied the gradient in only one lateral direction, which serves as the foundation for meta-prisms or beam-steering structures. Expanding these designs to include radial gradients in pitch or length would enable the fabrication of 2D metalenses. Looking ahead, combining both pitch and length

gradients could unlock a wide array of design possibilities, drawing from a rich library of elementary unit cells or 'meta-atoms.'

Lastly, extending optical functionalities from the surface to the bulk of the material offers a direct solution for creating robust components. Such components exhibit mechanical stiffness and resistance to external environmental factors while retaining the compact and lightweight attributes of flat optics. Additionally, bulk fabrication opens up the potential to integrate numerous optical functions within a monolithic device. For example, layering various functions (such as beam focusing to inject light into a waveguide, followed by a Y-coupler and beam recollimation at the exit) provides advanced beam shaping and delivery capabilities within a self-aligned integrated device.

4.6 Summary

In this study, we have showcased the direct laser-based fabrication of precisely controlled arrays of nanochannels within the bulk of fused silica. Utilizing a specialized truncated Bessel beam shaping technique, we systematically explored the characteristics of these channels that can be realized with varying pulse durations from 1 ps to the femtosecond range (30 fs and 200 fs), and carefully adjusted laser pulse energies. Our results have demonstrated the ability to achieve an inter-channel spacing as small as 0.7 μm, which is even less than the wavelength of the laser employed for the machining process. The crucial factor for achieving this high resolution and sub-micrometer spatial period structuring lies in the proficient combination of the doublet (energy, pulse duration) for a given Bessel beam angle laser focusing.

Furthermore, we have exemplified the versatility of this method in crafting well-defined arrays of hollow nanochannels, representing a pivotal initial step toward the future fabrication of meta-photonic devices. Leveraging a channel-by-channel machining approach, which uniquely grants individual control over channel properties such as diameter and length within a digital framework, we have successfully produced various buried structures. With a view to their potential applications in manipulating near-infrared reading light, our calculations have indicated a substantial phase coverage of approximately $\sim\pi/2$. This underscores the promise of our proposed approach, particularly the novel and significant use of the third dimension (channel length) as an innovative degree of freedom for tailoring the characteristics of these novel "embedded metasurfaces."

Importantly, our demonstration has been conducted using fused silica glass, one of the most commonly used optical materials. However, this groundbreaking capability extends beyond fused silica to encompass a broad spectrum of standard optical materials (e.g., borosilicate glass, sapphire) as well as other material platforms highly relevant to integrated photonics, such as chalcogenide glasses [276], silicon [277], or

lithium niobate [278].

Finally, the combined advantages of in-volume and digital machining present two distinctive potentials that synergize for future technological advancements. Together, they open up the exciting prospect of a novel array of customized effective-index engineering capabilities, enabling the creation of new 3D designs and unconventional complex architectures. Laser writing crosstalk effect which remains an issue in the view of dense stacking structuring could be avoided by taking advantage of parallel processing. Building on our successful proof of concept, and considering that suitable femtosecond laser sources are widely available commercially, our proposed method holds the potential to access mesoscopic structuring (hundreds of nm) using the Bessel beam approach which is fast, adaptable, applicable to multiple materials, environmentally friendly, cost-effective, and equipped with 3D capabilities for manufacturing the next generation of advanced meta-photonic integrated chips.

Conclusion and Perspective

The femtosecond laser machining tool has made its mark in the realm of fabricating photonic structures, offering certain advantages over standard lithographic techniques. The digital laser machining technique has garnered attention for its ability to precisely shape nanoscale structures, a crucial factor in the microelectronics and photonics industry. Despite its notable advancements, the writing tool requires optimization to reach the desired resolution comparable to that achieved with standard lithographic techniques. Enhancing the writing tool's performance is essential for gaining greater flexibility in crafting controlled nanochannels. To achieve this goal, a thorough understanding and manipulation of laser-matter interaction are crucial, involving careful adjustments to laser parameters.

A spatial beam shaping system using an axicon was built up which transforms the incident Gaussian beam from the ASUR system into a Bessel beam with a long DOF (~30 cm). In a Bessel beam, the energy is distributed on a wide angle and not directed (as energy is arriving by the sides at different locations which is not possible for a Gaussian beam), this beam should be more robust for the machining of material. To adapt the long DOF of the axicon-generated beam for our machining purpose, we further tailored the DOF by placing an annular aperture in front of the axicon. The axicon-annular aperture set-up allowed us to develop a depth-selective formation of a segmented Bessel beam which provided us the freedom to freely choose the machining location in the sample. We optimized this composed beam shaping system (axicon+annulus) by characterizing the beam through it to choose the desired width of the annular aperture (600 μm) suitable for machining our targeted structure. Finally, by using a $4f$ demagnification set-up (with a demagnifying factor ~49.5) after the beam shaping assembly, we managed to generate a micro-bessel beam with a core diameter of 0.96 μm and a DOF of 15 μm which we further used to machine in fused silica.

After developing the beam shaping system, we fabricated arrays of nanoholes at the front and rear surface of the dielectrics with $1ps$ pulse duration. Then using a dedicated methodology, we show that dense sub-micrometric surface structuring (until 0.8 μm pitch) can be reached by using rear surface configuration only. This is mainly due to a crosstalk effect which is more important for the front surface configuration compared to the rear surface one. We also encountered the problem of debris at the front surface, which was reduced at the rear surface configuration. An in-depth characterization of the channels has also been carried out with FIB analysis. We also confirm that the rear surface configuration brings advantages for small size (channel

diameter of ~200 nm) and high-quality structuring with more regular parallel channels and reduced funnel shape compared to the front surface arrangements. In surface structuring, the spatial limitation in density stacking appears from the presence of a rim related to the thermal dissipation of depositing energy. This limitation in the future could be encountered by polishing the surface up to a few hundred nanometers.

One of the unique capabilities of femtosecond machining lies in its capacity to machine locally in the volume of transparent material. This process is possible, thanks to the nonlinear absorption process associated with short pulses. By taking advantage of this property, we machined nanochannels at a depth of 150 μm inside fused silica. A parametric study with three different pulse durations of 1 *ps*, 30 *fs*, and 200 *fs* was carried out within an energy range of 0.2 μJ - 1 μJ. The key to achieving high resolution and sub-micrometer spatial period structuring lies in the proficient combination of doublet parameters (energy, pulse duration) for a given Bessel beam angle during laser focusing. The results showed the ability to achieve an inter-channel spacing as small as 0.7 μm, even smaller than the laser wavelength (800 nm) that was used. A presence of crosstalk again was identified here, which limits the regularity of the channels, especially for dense stacking of pitches below 1 μm. The knowledge of the parametric study provided us with an energy value of ~$2E_{th}$ (0.5 μJ) which was further used to machine photonic structures in the bulk irrespective of pulse duration. By varying the pulse durations from picoseconds to femtoseconds, and adjusting laser pulse energies we first demonstrated the writing of basic geometrical structures like square and hexagon with a pitch down to 0.8 μm in the bulk. In addition, we finally managed to demonstrate the meta-photonic structures and photonic crystal waveguide embedded in the fused silica. We carried out an effective index study for our laser-written structures and showed that the meta-photonic structures offered an effective index variation of n_{eff}~ 1.41 - 1.40. We also indicated that this variation of the effective index contributes to a phase change of $\frac{\pi}{2}$ to the incident beam. Therefore, the study highlights the potential applications of these structures in manipulating near-infrared light, with calculations indicating substantial phase coverage. Importantly, the demonstrated capability extends beyond fused silica to include a broad spectrum of standard optical materials and materials relevant to integrated photonics, such as borosilicate glass, sapphire, chalcogenide glasses, silicon, and lithium niobate.

In summary, we have demonstrated an improved method for direct laser-based fabrication of precisely controlled arrays of nanochannels within and at the surface of the fused silica, a commonly used optical material. A specialized truncated Bessel beam was used for the shaping technique and we systematically managed to explore the characteristics of individual nanochannels. The versatility of this method was exemplified in the fabrication of meta-photonic devices in the bulk of fused silica. A channel-by-channel machining approach allowed individual control over channel properties within a digital framework, enabling the production of various buried structures. To add on, this research introduces the prospect of employing the third dimension (channel length) as an innovative and significant parameter for adjust-

ing the characteristics of these emerging "embedded metasurfaces." Moreover, the entire fabrication process is laser-based, eliminating the need for chemicals or a vacuum environment. This makes this method fast, adaptable, environmentally friendly, and cost-effective. This technique applies to a wide range of low-index standard optical materials, expanding the selection of suitable material platforms for meta-photonic devices. Additionally, there is an opportunity to facilitate the 3D integration of components within material volumes, promising dense monolithic integration for multifunctional photonic chips.

To conclude, the combined advantages of in-volume and digital machining offer at least two distinctive potentials for future technological advancements, enabling customized effective-index engineering capabilities and the creation of new 3D designs and unconventional complex architectures. The challenge of laser writing crosstalk, particularly concerning dense stacking structuring, can be circumvented by leveraging parallel processing. Drawing from our successful proof of concept and recognizing the widespread commercial availability of suitable femtosecond laser sources, our proposed method has the potential to achieve mesoscopic structuring (on the scale of hundreds of nanometers) using the Bessel beam approach. This technique is rapid, adaptable, applicable to various materials, environmentally friendly, cost-effective, and possesses 3D capabilities, positioning it as a promising avenue for manufacturing the next generation of advanced meta-photonic integrated chips.

References

1. Strickland, D. & Mourou, G. Compression of amplified chirped optical pulses. *Optics communications* **55,** 447–449 (1985).
2. Du, D., Liu, X., Korn, G., *et al.* Laser-induced breakdown by impact ionization in SiO_2 with pulse widths from $7ns$ to $150fs$. *Applied physics letters* **64,** 3071–3073 (1994).
3. Pronko, P., Dutta, S., Squier, J., *et al.* Machining of sub-micron holes using a femtosecond laser at 800 nm. *Optics Communications* **114,** 106–110 (1995).
4. Chimmalgi, A., Choi, T., Grigoropoulos, C., *et al.* Femtosecond laser aperturless near-field nanomachining of metals assisted by scanning probe microscopy. *Applied Physics Letters* **82,** 1146–1148 (2003).
5. Joglekar, A. P., Liu, H.-h., Spooner, G., *et al.* A study of the deterministic character of optical damage by femtosecond laser pulses and applications to nanomachining. *Applied Physics B* **77,** 25–30 (2003).
6. Barton, P., Mukherjee, S., Prabha, J., *et al.* Fabrication of silver nanostructures using femtosecond laser-induced photoreduction. *Nanotechnology* **28,** 505302 (2017).
7. Yang, L., Wei, J., Ma, Z., *et al.* The Fabrication of Micro/Nano Structures by Laser Machining. *Nanomaterials* **9,** 1789 (2019).
8. Borowiec, A. & Haugen, H. Subwavelength ripple formation on the surfaces of compound semiconductors irradiated with femtosecond laser pulses. *Applied Physics Letters* **82,** 4462–4464 (2003).
9. Bonse, J., Munz, M. & Sturm, H. Structure formation on the surface of indium phosphide irradiated by femtosecond laser pulses. *Journal of Applied Physics* **97,** 013538 (2004).
10. Harzic, R. L., Schuck, H., Sauer, D., *et al.* Sub-100 nm nanostructuring of silicon by ultrashort laser pulses. *Opt. Express* **13,** 6651–6656 (2005).
11. Taylor, R., Hnatovsky, C., Simova, E., *et al.* Femtosecond laser fabrication of nanostructures in silica glass. *Optics letters* **28,** 1043–1045 (2003).
12. Höhm, S., Rosenfeld, A., Krüger, J., *et al.* Femtosecond diffraction dynamics of laser-induced periodic surface structures on fused silica. *Applied Physics Letters* **102,** 054102 (2013).

13. Vorobyev, A., Makin, V. & Guo, C. Periodic ordering of random surface nanostructures induced by femtosecond laser pulses on metals. *Journal of Applied Physics* **101,** 034903 (2007).

14. Paivasaari, K., Kaakkunen, J., Kuittinen, M., *et al.* Enhanced optical absorptance of metals using interferometric femtosecond ablation. *Optics express* **15,** 13838–13843 (2007).

15. Weck, A., Crawford, T., Wilkinson, D., *et al.* Ripple formation during deep hole drilling in copper with ultrashort laser pulses. *Applied Physics A* **89,** 1001–1003 (2007).

16. Pérez, S., Rebollar, E., Oujja, M., *et al.* Laser-induced periodic surface structuring of biopolymers. *Applied Physics A* **110,** 683–690 (2013).

17. Ionin, A., Klimachev, Y., Kozlov, A., *et al.* Direct femtosecond laser fabrication of antireflective layer on GaAs surface. *Applied Physics B* **111,** 419 (2013).

18. Dumitru, G., Romano, V., Weber, H., *et al.* Femtosecond ablation of ultrahard materials. *Applied Physics A: Materials Science & Processing* **74,** 729–739 (2002).

19. Tao, H., Tan, X., Diao, L., *et al. Extending femtosecond laser fabrication of micro- and nanoscale structures from a planar to non-planar metal surface* in *2012 International Conference on Manipulation, Manufacturing and Measurement on the Nanoscale (3M-NANO)* (2012), 1–4. doi:10.3390/ma14092413.

20. Fuscaldo, W., Burghignoli, P. & Galli, A. A comparative analysis of Bessel and Gaussian beams beyond the paraxial approximation. *Optik* **240,** 166834 (2021).

21. Bhuyan, M., Courvoisier, F., Lacourt, P., *et al.* High aspect ratio nanochannel machining using single shot femtosecond Bessel beams. *Applied Physics Letters* **97,** 081102 (2010).

22. Courvoisier, F., Bhuyan, M., Jacquot, M., *et al. High aspect ratio taper-free micro and nano-channel fabrication in glass with ultrafast nondiffracting Bessel beams* in *Laser-based Micro-and Nanopackaging and Assembly V* (2011). doi:10.1117/12.875409.

23. Liu, X., Li, Q., Sikora, A., *et al.* Truncated Gaussian-Bessel beams for short-pulse processing of small-aspect-ratio micro-channels in dielectrics. *Optics Express* **27,** 6996 (2019).

24. Liu, X., Sanner, N., Sentis, M., *et al.* Front-surface fabrication of moderate aspect ratio micro-channels in fused silica by single picosecond Gaussian-Bessel laser pulse. *Applied Physics A* **124,** 1–6 (2018).

25. Xu, X., He, J., Liao, C., *et al.* Multi-layer, offset-coupled sapphire fiber Bragg gratings for high-temperature measurements. *Optics letters* **44,** 4211–4214 (2019).

26. Liao, Y., Cheng, Y., Liu, C., *et al.* Direct laser writing of sub-50 nm nanofluidic channels buried in glass for three-dimensional micro-nanofluidic integration. *Lab on a Chip* **13,** 1626–1631 (2013).

27. Ashcroft, N. & Mermin, N. *Solid State Physics* (Cengage Learning, 2011).

28. Kittel, C. & McEuen, P. *Introduction to Solid State Physics* (John Wiley & Sons, 2015).

29. Ammosov, M. V. Tunnel ionization of complex atoms and of atomic ions in an altemating electromagnetic field. *Sov. Phys. JETP* **64,** 1191 (1987).

30. Vogel, A. & Rockwell, B. A. Roles of tunneling, multiphoton ionization, and cascade ionization for femtosecond optical breakdown in aqueous media. *Lübeck Medical University (Germany) Medical Laser Center* (2009).

31. Popov, V. Tunnel and multiphoton ionization of atoms and ions in a intense laser field (Keldysh theory). *Uspekhi Fizicheskikh Nauk* **174,** 921–951 (2004).

32. Keldysh, L. *et al.* Ionization in the field of a strong electromagnetic wave. *Sov. Phys. JETP* **20,** 1307–1314 (1965).

33. Fox, M. *Optical properties of solids* (American Association of Physics Teachers, 2002).

34. Shen, Y. *The Principles of Nonlinear Optics* (Wiley, 2003).

35. Mao, S., Quere, F., Guizard, S., *et al.* Dynamics of Femtosecond Laser Interactions with Dielectrics. *Applied Physics A* **79,** 1695–1709 (2004).

36. Boyd, R. *Contemporary Nonlinear Optics* (Elsevier Science, 2012).

37. Chan, J. W., Huser, T., Risbud, S., *et al.* Structural changes in fused silica after exposure to focused femtosecond laser pulses. *Optics letters* **26,** 1726–1728 (2001).

38. Chan, J. W., Huser, T. R., Risbud, S., *et al.* Modification of the fused silica glass network associated with waveguide fabrication using femtosecond laser pulses. *Applied Physics A* **76,** 367–372 (2003).

39. Homoelle, D., Wielandy, S., Gaeta, A. L., *et al.* Infrared photosensitivity in silica glasses exposed to femtosecond laser pulses. *Optics Letters* **24,** 1311–1313 (1999).

40. Brueckner, R. Properties and structure of vitreous silica. I. *Journal of non-crystalline solids* **5,** 123–175 (1970).

41. Haken, U., Humbach, O., Ortner, S., *et al.* Refractive index of silica glass: influence of fictive temperature. *Journal of non-crystalline solids* **265,** 9–18 (2000).

42. Joglekar, A. P., Liu, H.-h., Meyhöfer, E., *et al.* Optics at critical intensity: Applications to nanomorphing. *Proceedings of the National Academy of Sciences* **101,** 5856–5861 (2004).

43. Davis, K. M., Miura, K., Sugimoto, N., *et al.* Writing waveguides in glass with a femtosecond laser. *Optics letters* **21,** 1729–1731 (1996).

44. Miura, K., Qiu, J., Inouye, H., *et al.* Photowritten optical waveguides in various glasses with ultrashort pulse laser. *Applied Physics Letters* **71,** 3329–3331 (1997).

45. Hnatovsky, C., Taylor, R., Pattathil, R., *et al.* Pulse Duration Dependence of Femtosecond-Laser-Fabricated Nanogratings in Fused Silica. *Applied Physics Letters* **87,** 014104 (2005).

46. Glezer, E. N. & Mazur, E. Ultrafast-laser driven micro-explosions in transparent materials. *Applied Physics Letters* **71,** 882–884 (1997).

47. Gamaly, E. G., Juodkazis, S., Nishimura, K., *et al.* Laser-matter interaction in the bulk of a transparent solid: Confined microexplosion and void formation. *Physical Review B* **73,** 214101 (2006).

48. Lancry, M. & Poumellec, B. UV laser processing and multiphoton absorption processes in optical telecommunication fiber materials. *Physics Reports* **523,** 207–229 (2013).

49. Wortmann, D., Ramme, M. & Gottmann, J. Refractive index modification using *fs*-laser double pulses. *Optics Express* **15,** 10149–10153 (2007).

50. Albert, J., Malo, B., Hill, K. O., *et al.* Refractive-index changes in fused silica produced by heavy-ion implantation followed by photobleaching. *Optics letters* **17,** 1652–1654 (1992).

51. Glezer, E. N., Milosavljevic, M., Huang, L., *et al.* Three-dimensional optical storage inside transparent materials. *Opt. Lett.* **21,** 2023–2025 (1996).

52. Polesana, P., Franco, M., Couairon, A., *et al.* Filamentation in Kerr media from pulsed Bessel beams. *Phys. Rev. A* **77,** 043814 (2008).

53. Roskey, D., Kolesik, M., Moloney, J., *et al.* Self-action and regularized self-guiding of pulsed Bessel-like beams in air. *Opt. Express* **15,** 9893–9907 (2007).

54. Porras, M. A., Parola, A., Faccio, D., *et al.* Nonlinear unbalanced Bessel beams: stationary conical waves supported by nonlinear losses. *Physical review letters* **93,** 153902 (2004).

55. Polesana, P., Couairon, A., Faccio, D., *et al.* Observation of Conical Waves in Focusing, Dispersive, and Dissipative Kerr Media. *Phys. Rev. Lett.* **99,** 223902 (22 2007).

56. Porras, M. A., Ruiz-Jiménez, C. & Losada, J. C. Underlying conservation and stability laws in nonlinear propagation of axicon-generated Bessel beams. *Physical Review A* **92,** 063826 (2015).

57. Dickey, F. *Laser Beam Shaping: Theory and Techniques, Second Edition* (CRC Press, 2018).

58. Shealy, D. L. *Historical perspective of laser beam shaping* in *Laser Beam Shaping III* **4770** (2002), 28–47. doi:10.1117/12.453505.

59. Aleksoff, C. C., Ellis, K. K. & Neagle, B. D. *Holographic Conversion Of A Gaussian Beam To A Uniform Beam* in *Holographic Optics: Design and Applications* (ed Cindrich, I.) **0883** (SPIE, 1988), 220–229. doi:10.1117/12.944148.

60. Veldkamp, W. B. Laser beam profile shaping with binary diffraction gratings. *Optics Communications* **38,** 381–386 (1981).

61. Veldkamp, W. B. Laser beam profile shaping with interlaced binary diffraction gratings. *Appl. Opt.* **21,** 3209–3212 (1982).

62. Kosoburd, T. & Kedmi, J. *Beam shaping with diffractive optical elements* in *8th Meeting on Optical Engineering in Israel: Optical Engineering and Remote Sensing* (eds Oron, M., Shladov, I. & Weissman, Y.) **1971** (SPIE, 1993), 390–399. doi:10.1117/12.151002.

63. Golub, M. A., Duparre, M. R., Kley, E.-B., *et al.* New diffractive beam shaper generated with the aid of e-beam lithography. *Optical Engineering* **35,** 1400–1406 (1996).

64. Li, B., Xiong, S. & Zhang, Y. Fresnel diffraction model for mode-mismatched thermal lens with top-hat beam excitation. *Applied Physics B* **80,** 527–534 (2005).

65. Rung, S., Rexhepi, M., Bischoff, C., *et al.* Laserscribing of Thin Films Using Top-Hat Laser Beam Profiles. *Journal of Laser Micro / Nanoengineering* **8,** 309 (2013).

66. Coutts, D., Withford, M., Piper, J., *et al. Generation of flat-top focussed beams for percussion drilling of ceramic and metal* in *International Congress on Applications of Lasers & Electro-Optics* (2002), 1–10.

67. Mishra, S. & Yadava, V. Laser Beam MicroMachining (LBMM) – A review. *Optics and Lasers in Engineering* **73,** 89–122 (2015).

68. Kudryashov, S. I., Mourou, G., Joglekar, A., *et al.* Nanochannels fabricated by high-intensity femtosecond laser pulses on dielectric surfaces. *Applied Physics Letters* **91,** 141111 (2007).

69. Laskin, A. & Laskin, V. *Refractive beam shapers for material processing with high power single mode and multimode lasers* in *Laser Resonators, Microresonators, and Beam Control XV* **8600** (2013), 140–150. doi:10.1117/12.2001390.

70. Le, H., Penchev, P., Henrottin, A., *et al.* Effects of top-hat laser beam processing and scanning strategies in laser micro-structuring. *Micromachines* **11,** 221 (2020).

71. Delaporte, P., Karnakis, D. & Zergioti, I. Laser processing of flexible organic electronic materials. *Handbook of flexible organic electronics: Materials. Manufacturing and Applications. UK: Woodhead Publishing,* 285–313 (2014).

72. Laskin, A. & Laskin, V. πShaper Refractive Beam Shaping Optics for Advanced Laser Technologies. *Journal of Physics: Conference Series* **276,** 012171 (2011).

73. Dongre, S., Gujrathi, A., Nandan, H., *et al.* A review of laser micromachining. *Int. J. Eng. Sci* **6,** 2416–2420 (2016).

74. Hatzakis, M. Materials and processes for microstructure fabrication. *IBM Journal of Research and Development* **32,** 441–453 (1988).

75. Manz, A. What Can Chips Technology Offer for Next Century's Chemistry and Life Sciences? *CHIMIA* **50,** 140–143 (1996).

76. Bratten, C. D., Cobbold, P. H. & Cooper, J. M. Micromachining sensors for electrochemical measurement in subnanoliter volumes. *Analytical Chemistry* **69,** 253–258 (1997).

77. Clark, R. A., Hietpas, P. B. & Ewing, A. G. Electrochemical analysis in picoliter microvials. *Analytical Chemistry* **69,** 259–263 (1997).

78. Kovacs, G. T., Petersen, K. & Albin, M. Peer reviewed: Silicon micromachining: Sensors to systems. *Analytical Chemistry* **68,** 407A–412A (1996).

79. MacDonald, N. C. SCREAM microelectromechanical systems. *Microelectronic Engineering* **32,** 49–73 (1996).

80. Lee, S., Lin, L. & Wu, M. Surface-micromachined free-space micro-optical systems containing three-dimensional microgratings. *Applied Physics Letters* **67,** 2135–2137 (1995).

81. Lin, L., Lee, S., Pister, K., *et al.* Micro-machined three-dimensional micro-optics for integrated free-space optical system. *IEEE Photonics Technology Letters* **6,** 1445–1447 (1994).

82. Miller, S. E. Integrated Optics: An Introduction. *Bell System Technical Journal* **48,** 2059–2069 (1969).

83. Wu, M. C. Micromachining for optical and optoelectronic systems. *Proceedings of the IEEE* **85,** 1833–1856 (1997).

84. Wu, M. C., Lin, L.-Y., Lee, S.-S., *et al.* Micromachined free-space integrated micro-optics. *Sensors and Actuators A: Physical* **50,** 127–134 (1995).

85. Qin, D., Xia, Y., Rogers, J. A., *et al.* Microfabrication, microstructures and microsystems. *Microsystem technology in chemistry and life science,* 1–20 (1998).

86. Gates, B. D., Xu, Q., Stewart, M., *et al.* New approaches to nanofabrication: molding, printing, and other techniques. *Chemical reviews* **105,** 1171–1196 (2005).

87. Motamedi, M. E. Micro-opto-electro-mechanical systems. *Optical Engineering* **33,** 3505–3517 (1994).

88. BRIGHT, V. M., COMTOIS, J. H., REID, J. R., *et al.* Surface micromachined micro-opto-electro-mechanical systems. *IEICE transactions on electronics* **80,** 206–213 (1997).

89. Sharma, E., Rathi, R., Misharwal, J., *et al.* Evolution in Lithography Techniques: Microlithography to Nanolithography. *Nanomaterials* **12,** 2754 (2022).

90. Meiling, H., Benschop, J. P., Dinger, U., *et al. Progress of the EUVL alpha tool* in *Emerging Lithographic Technologies V* **4343** (2001), 38–50. doi:10.1117/12.436675.

91. Bakshi, V. *EUV Lithography* (SPIE Press, 2009).

92. Brunner, T. A., Chen, X., Gabor, A., *et al. Line-edge roughness performance targets for EUV lithography* in *Extreme Ultraviolet (EUV) Lithography VIII* **10143** (2017), 48–57. doi:10.1117/12.2258660.

93. AM, G., Gronheld, R., LHA, L., *et al.* EUV resist screening: current performance and issues. *Journal of photopolymer science and technology* **18,** 647–654 (2005).

94. Altissimo, M. E-beam lithography for micro-/nanofabrication. *Biomicrofluidics* **4,** 026503 (2010).

95. Sugihara, T., Nagai, S. & Kaneko, A. High-aspect nano-groove fabrication in thick film resists using 150-kV high acceleration voltage electron beam lithography. *Precision Engineering* **74,** 205–208 (2022).

96. Bolorizadeh, M. & Joy, D. C. Effects of fast secondary electrons to low-voltage electron beam lithography. *Journal of Micro/Nanolithography, MEMS and MOEMS* **6,** 023004–023004 (2007).

97. Silverman, J. P. Challenges and progress in x-ray lithography. *Journal of Vacuum Science & Technology B: Microelectronics and Nanometer Structures Processing, Measurement, and Phenomena* **16,** 3137–3141 (1998).

98. Maldonado, J. R. & Peckerar, M. X-ray lithography: Some history, current status and future prospects. *Microelectronic Engineering* **161,** 87–93 (2016).

99. Guckel, H. High-aspect-ratio micromachining via deep X-ray lithography. *Proceedings of the IEEE* **86,** 1586–1593 (1998).

100. Gentili, M. in *NANOLITHOGRAPHY: A Borderland between STM, EB, IB, and X-Ray Lithographies* 129–136 (Springer, 1994).

101. Chou, S. Y., Krauss, P. R. & Renstrom, P. J. Nanoimprint lithography. *Journal of Vacuum Science & Technology B: Microelectronics and Nanometer Structures Processing, Measurement, and Phenomena* **14,** 4129–4133 (1996).

102. Guo, L. J. Nanoimprint lithography: methods and material requirements. *Advanced materials* **19,** 495–513 (2007).

103. Watt, F., Bettiol, A., Van Kan, J., *et al.* Ion beam lithography and nanofabrication: a review. *International Journal of Nanoscience* **4,** 269–286 (2005).

104. Li, P., Chen, S., Dai, H., *et al.* Recent advances in focused ion beam nanofabrication for nanostructures and devices: Fundamentals and applications. *Nanoscale* **13,** 1529–1565 (2021).

105. Hoffmann, P., Utke, I., Perentes, A., *et al. Comparison of fabrication methods of sub-100nm nano-optical structures and devices* in *Nanophotonic Materials and Systems II* **5925** (2005), 592506. doi:10.1117/12.617142.

106. Menard, L. D. & Ramsey, J. M. Fabrication of sub-5 nm nanochannels in insulating substrates using focused ion beam milling. *Nano letters* **11,** 512–517 (2011).

107. Bernardeschi, I., Ilyas, M. & Beccai, L. A review on active 3D microstructures via direct laser lithography. *Advanced Intelligent Systems* **3,** 2100051 (2021).

108. Gale, M. T. & Knop, K. *The fabrication of fine lens arrays by laser beam writing* in *Industrial Applications of Laser Technology* **398** (1983), 347–353. doi:10.1117/12.935397.

109. Haruna, M., Takahashi, M., Wakahayashi, K., *et al.* Laser beam lithographed micro-Fresnel lenses. *Applied optics* **29,** 5120–5126 (1990).

110. Aristizabal, S. L., Cirino, G. A., Montagnoli, A. N., *et al.* Microlens array fabricated by a low-cost grayscale lithography maskless system. *Optical Engineering* **52,** 125101–125101 (2013).

111. Herzig, H. *Micro-Optics: Elements, Systems And Applications* (CRC Press, 1997).

112. Aebersold, J., Walsh, K. & Beggans, M. *Utilization of Direct Write Lithography to Develop Ultra High Aspect Ratio (> 100: 1) DRIE Silicon Pillars* in *2010 18th Biennial University/Government/Industry Micro/Nano Symposium* (2010), 1–5. doi:10.1109/UGIM.2010.5508920.

113. Carrion Perez, J. V. *Design and fabrication of micro optical components for miniaturized optical imagers* 2016BESA2034. PhD thesis (2016).

114. Gale, M. T., Lang, G., Raynor, J., *et al.* Fabrication of kinoform structures for optical computing. *Applied optics* **31,** 5712–5715 (1992).

115. Zhou, Y., Hong, M., Fuh, J., *et al.* Near-field enhanced femtosecond laser nano-drilling of glass substrate. *Journal of alloys and compounds* **449,** 246–249 (2008).

116. Kurobori, T., SAKAI, T. & AOSHIMA, S.-i. Femtosecond Laser Interferometric Processing of Transparent Materials and Its Application to a Visible Laser. *The Review of Laser Engineering* **37,** 521–527 (2009).

117. Liu, D., Kuang, Z., Shang, S., *et al. Ultrafast parallel laser processing of materials for high throughput manufacturing* in *Proceedings of LAMP 2009—The 5th International Congress on Laser Advanced Materials Processing* (2009), 09–021.

118. Ahsan, M. S., Kim, Y. & Lee, M.-S. Formation mechanism of nanostructures in soda–lime glass using femtosecond laser. *Journal of Non-Crystalline Solids* **357,** 851–857 (2011).

119. Zhang, Q., Lin, H., Jia, B., *et al.* Nanogratings and nanoholes fabricated by direct femtosecond laser writing in chalcogenide glasses. *Opt. Express* **18,** 6885–6890 (2010).

120. Kudryashov, S. I., Joglekar, A., Mourou, G., *et al. Mechanisms of femtosecond laser nanomachining of dielectric surfaces* in *Laser-based Micro-and Nanopackaging and Assembly* **6459** (2007), 173–181. doi:10.1117/12.697663.

121. White, Y. V., Li, X., Sikorski, Z., *et al.* Single-pulse ultrafast-laser machining of high aspect nano-holes at the surface of SiO_2. *Optics Express* **16,** 14411–14420 (2008).

122. Vestentoft, K. & Balling, P. Formation of an extended nanostructured metal surface by ultra-short laser pulses: single-pulse ablation in the high-fluence limit. *Applied Physics A* **84,** 207–213 (2006).

123. Hnatovsky, C., Taylor, R., Simova, E., *et al.* Fabrication of Microchannels in Glass Using Focused Femtosecond Laser Radiation and Selective Chemical Etching. *Applied Physics A* **84,** 47–61 (2006).

124. Ahsan, M. S., Kim, Y. G. & Lee, M. S. Formation mechanism of nanostructures in sodalime glass using femtosecond laser. *Journal of Non-Crystalline Solids* **357,** 851–857 (2011).

125. Liao, Y., Cheng, Y., Liu, C., *et al.* Direct laser writing of sub-50 nm nanofluidic channels buried in glass for three-dimensional micro-nanofluidic integration. *Lab on a Chip* **13,** 1626–1631 (2013).

126. Canfield, B. K., Bowman, T. S., Costa, L., *et al. Machining High Aspect Ratio Features with Single Femtosecond Laser Pulses* in *Frontiers in Optics 2014* (Optica Publishing Group, 2014), FTh4G.4. doi:10.1364/FIO.2014.FTh4G.4.

127. Zhu, X., Naumov, A. Y., Villeneuve, D., *et al.* Influence of laser parameters and material properties on micro drilling with femtosecond laser pulses. *Applied Physics A* **69,** S367–S371 (1999).

128. Liu, Y., Zhang, R., Li, W., *et al.* Effect of machining parameter on femtosecond laser drilling processing on SiC/SiC composites. *The International Journal of Advanced Manufacturing Technology* **96,** 1795–1811 (2018).

129. Lei, C., Pan, Z., Jianxiong, C., *et al.* Influence of processing parameters on the structure size of microchannel processed by femtosecond laser. *Optics & Laser Technology* **106,** 47–51 (2018).

130. Nayak, B. K. & Gupta, M. C. Self-organized micro/nano structures in metal surfaces by ultrafast laser irradiation. *Optics and Lasers in Engineering* **48,** 940–949 (2010).

131. Tsukamoto, M., Asuka, K., Nakano, H., *et al.* Periodic microstructures produced by femtosecond laser irradiation on titanium plate. *Vacuum* **80,** 1346–1350 (2006).

132. Yong Hwang, T. & Guo, C. Polarization and angular effects of femtosecond laser-induced conical microstructures on Ni. *Journal of Applied Physics* **111,** 083518 (2012).

133. Lehr, J., De Marchi, F., Matus, L., *et al.* The influence of the gas environment on morphology and chemical composition of surfaces micro-machined with a femtosecond laser. *Applied Surface Science* **320,** 455–465 (2014).

134. Nayak, B., Gupta, M. & Kolasinski, K. Formation of nano-textured conical microstructures in titanium metal surface by femtosecond laser irradiation. *Applied Physics A* **90,** 399–402 (2008).

135. Courvoisier, F., Zhang, J., Bhuyan, M., *et al.* Applications of femtosecond Bessel beams to laser ablation. *Applied Physics A* **112,** 29–34 (2013).

136. Bhuyan, M. K., Courvoisier, F., Phing, H. S., *et al.* Laser micro and nanostructuring using femtosecond Bessel beams. *The European Physical Journal Special Topics* **199,** 101–110 (2011).

137. Vetter, C., Steinkopf, R., Bergner, K., *et al.* Realization of Free-Space Long-Distance Self-Healing Bessel Beams. *Laser and Photonics Reviews* **13,** 1900103 (2019).

138. Mazilu, M., Stevenson, D., Gunn-Moore, F., *et al.* Light beats the spread: "non-diffracting" beams. *Laser and Photonics Reviews* **4,** 529–547 (2010).

139. Garcés-Chávez, V., McGloin, D., Melville, H., *et al.* Simultaneous micromanipulation in multiple planes using a self-reconstructing light beam. *Nature* **419,** 145–147 (2002).

140. Shvedov, V. G., Rode, A. V., Izdebskaya, Y. V., *et al.* Giant Optical Manipulation. *Phys. Rev. Lett.* **105,** 118103 (11 2010).

141. Tsampoula, X., Taguchi, K., Čižmár, T., *et al.* Fibre based cellular transfection. *Optics express* **16,** 17007–17013 (2008).

142. Ladabaum, I., Jin, X., Soh, H. T., *et al.* Surface micromachined capacitive ultrasonic transducers. *IEEE transactions on ultrasonics, ferroelectrics, and frequency control* **45,** 678–690 (1998).

143. Reinhardt, C., Kiyan, R., Passinger, S., *et al.* Rapid laser prototyping of plasmonic components. *Applied Physics A* **89,** 321–325 (2007).

144. Della Valle, G., Osellame, R. & Laporta, P. Micromachining of photonic devices by femtosecond laser pulses. *Journal of Optics A: Pure and Applied Optics* **11,** 013001 (2008).

145. Zambon, V., McCarthy, N. & Piché, M. *Fabrication of photonic devices directly written in glass using ultrafast Bessel beams* in *Photonics North 2008* **7099** (2008), 720–724. doi:10.1117/12.807194.

146. Herbstman, J. F. & Hunt, A. J. High-aspect ratio nanochannel formation by single femtosecond laser pulses. *Optics express* **18,** 16840–16848 (2010).

147. Beuton, R., Chimier, B., Quinoman, P., *et al.* Numerical studies of dielectric material modifications by a femtosecond Bessel–Gauss laser beam. *Applied Physics A* **127,** 334 (2021).

148. Bhuyan, M. K., Velpula, P. K., Colombier, J. P., *et al.* Single-shot high aspect ratio bulk nanostructuring of fused silica using chirp-controlled ultrafast laser Bessel beams. *Applied Physics Letters* **104,** 021107 (2014).

149. Duocastella, M. & Arnold, C. Bessel and annular beams for materials processing. *Laser & Photonics Reviews* **6,** 607–621 (2012).

150. Blow, N. New ways to see a smaller world. *Nature* **456,** 825–826 (2008).

151. Hell, S. W. Microscopy and its focal switch. *Nature Methods* **6,** 24–32 (2009).

152. Davis, J. A., Carcole, E. & Cottrell, D. M. Nondiffracting interference patterns generated with programmable spatial light modulators. *Applied optics* **35,** 599–602 (1996).

153. Miura, K., Inouye, H., Qiu, J., *et al.* Optical waveguides induced in inorganic glasses by a femtosecond laser. *Nuclear Instruments and Methods in Physics Research Section B: Beam interactions with materials and atoms* **141,** 726–732 (1998).

154. Schaffer, C. B., Brodeur, A., Garcia, J. F., *et al.* Micromachining bulk glass by use of femtosecond laser pulses with nanojoule energy. *Optics letters* **26,** 93–95 (2001).

155. Streltsov, A. M. & Borrelli, N. F. Study of femtosecond-laser-written waveguides in glasses. *JOSA B* **19,** 2496–2504 (2002).

156. Zoubir, A., Richardson, M., Rivero, C., *et al.* Direct femtosecond laser writing of waveguides in AS_2S_3 thin films. *Optics letters* **29,** 748–750 (2004).

157. Hirao, K. & Miura, K. Writing waveguides and gratings in silica and related materials by a femtosecond laser. *Journal of non-crystalline solids* **239,** 91–95 (1998).

158. Chan, J. W., Huser, T. R., Risbud, S. H., *et al.* Waveguide fabrication in phosphate glasses using femtosecond laser pulses. *Applied physics letters* **82,** 2371–2373 (2003).

159. Bhardwaj, V. R., Simova, E., Corkum, P. B., *et al.* Femtosecond laser-induced refractive index modification in multicomponent glasses. *Journal of Applied Physics* **97,** 083102 (2005).

160. Gorelik, T., Will, M., Nolte, S., *et al.* Transmission electron microscopy studies of femtosecond laser induced modifications in quartz. *Applied Physics A* **76,** 309–311 (2003).

161. Apostolopoulos, V., Laversenne, L., Colomb, T., *et al.* Femtosecond-irradiation-induced refractive-index changes and channel waveguiding in bulk Titanium doped Sapphire. *Applied Physics Letters* **85,** 1122–1124 (2004).

162. Thomson, R. R., Campbell, S., Blewett, I. J., *et al.* Optical waveguide fabrication in z-cut lithium niobate (LiNbO3) using femtosecond pulses in the low repetition rate regime. *Applied Physics Letters* **88,** 111109 (2006).

163. Nejadmalayeri, A. H. & Herman, P. R. Ultrafast laser waveguide writing: lithium niobate and the role of circular polarization and picosecond pulse width. *Optics letters* **31,** 2987–2989 (2006).

164. Della Valle, G., Osellame, R. & Laporta, P. Micromachining of photonic devices by femtosecond laser pulses. *Journal of Optics A: Pure and Applied Optics* **11,** 013001 (2008).

165. Liu, J., Zhang, Z., Chang, S., *et al.* Directly writing of $1-to-N$ optical waveguide power splitters in fused silica glass using a femtosecond laser. *Optics communications* **253,** 315–319 (2005).

166. Sohn, I.-B., Lee, M.-S. & Chung, J.-Y. Fabrication of optical splitter and passive alignment technique with a femtosecond laser. *IEEE photonics technology letters* **17,** 2349–2351 (2005).

167. Gui, L., Xu, B. & Chong, T. C. Microstructure in lithium niobate by use of focused femtosecond laser pulses. *IEEE Photonics Technology Letters* **16,** 1337–1339 (2004).

168. Nolte, S., Will, M., Burghoff, J., *et al.* Femtosecond waveguide writing: a new avenue to three-dimensional integrated optics. *Applied Physics A* **77,** 109–111 (2003).

169. Kowalevicz, A., Sharma, V., Ippen, E., *et al.* Three-dimensional photonic devices fabricated in glass by use of a femtosecond laser oscillator. *Optics letters* **30,** 1060–1062 (2005).

170. Minoshima, K., Kowalevicz, A. M., Ippen, E. P., *et al.* Fabrication of coupled mode photonic devices in glass by nonlinear femtosecond laser materials processing. *Optics Express* **10,** 645–652 (2002).

171. Li, G., Winick, K. A., Said, A. A., *et al.* Waveguide electro-optic modulator in fused silica fabricated by femtosecond laser direct writing and thermal poling. *Optics letters* **31,** 739–741 (2006).

172. Martinez, A., Dubov, M., Khrushchev, I., *et al.* Direct writing of fibre Bragg gratings by femtosecond laser. *Electronics letters* **40,** 1170–1172 (2004).

173. Li, Y., Watanabe, W., Yamada, K., *et al.* Holographic fabrication of multiple layers of grating inside soda-lime glass with femtosecond laser pulses. *Applied Physics Letters* **80,** 1508–1510 (2002).

174. Takeshima, N., Narita, Y., Tanaka, S., *et al.* Fabrication of high-efficiency diffraction gratings in glass. *Optics letters* **30,** 352–354 (2005).

175. Florea, C. & Winick, K. A. Fabrication and characterization of photonic devices directly written in glass using femtosecond laser pulses. *Journal of lightwave technology* **21,** 246–253 (2003).

176. Liu, J., Zhang, Z., Lu, Z., *et al.* Fabrication and stitching of embedded multi-layer micro-gratings in fused silica glass by *fs* laser pulses. *Applied Physics B* **86,** 151–154 (2007).

177. Ding, L., Blackwell, R., Kunzler, J. F., *et al.* Large refractive index change in silicone-based and non-silicone-based hydrogel polymers induced by femtosecond laser micro-machining. *Optics express* **14,** 11901–11909 (2006).

178. Marshall, G. D., Ams, M. & Withford, M. J. Direct laser written waveguide-Bragg gratings in bulk fused silica. *Optics Letters* **31,** 2690–2691 (2006).

179. Zhang, H., Eaton, S. M., Li, J., *et al.* Femtosecond laser direct writing of multiwavelength Bragg grating waveguides in glass. *Optics letters* **31,** 3495–3497 (2006).

180. Zhang, H., Eaton, S. M. & Herman, P. R. Single-step writing of Bragg grating waveguides in fused silica with an externally modulated femtosecond fiber laser. *Optics letters* **32,** 2559–2561 (2007).

181. Khan, A., Wang, Z., Sheikh, M. A., *et al.* Laser micro/nano patterning of hydrophobic surface by contact particle lens array. *Applied surface science* **258,** 774–779 (2011).

182. Klein-Wiele, J.-H. & Simon, P. Sub-wavelength pattern generation by laser direct writing via repeated irradiation. *Optics Express* **21,** 626–630 (2013).

183. Savas, T., Farhoud, M., Smith, H. I., *et al.* Properties of large-area nanomagnet arrays with 100 nm period made by interferometric lithography. *Journal of Applied Physics* **85,** 6160–6162 (1999).

184. Ostendorf, A. & Chichkov, B. N. Two-photon polymerization: a new approach to micromachining. *Photonics spectra* **40,** 72 (2006).

185. Maruo, S., Nakamura, O. & Kawata, S. Three-dimensional microfabrication with two-photon-absorbed photopolymerization. *Optics letters* **22,** 132–134 (1997).

186. Li, L., Hong, M., Schmidt, M., *et al.* Laser nano-manufacturing-state of the art and challenges. *CIRP annals* **60,** 735–755 (2011).

187. Parthenopoulos, D. A. & Rentzepis, P. M. Three-dimensional optical storage memory. *Science* **245,** 843–845 (1989).

188. Kawata, S., Sun, H.-B., Tanaka, T., *et al.* Finer features for functional microdevices. *Nature* **412,** 697–698 (2001).

189. Tanaka, T., Ishikawa, A. & Kawata, S. *Three-dimensional metallic micro/nanostructures fabricated by two-photon-induced reduction of metal ions* in *Plasmonics: Nanoimaging, Nanofabrication, and their Applications II* **6324** (2006), 151–158. doi:10.1117/12.681508.

190. John, S. Strong localization of photons in certain disordered dielectric superlattices. *Physical review letters* **58,** 2486 (1987).

191. Zhang, Y., Sheng, Y., Zhu, S., *et al.* Nonlinear photonic crystals: from 2D to 3D. *Optica* **8,** 372–381 (2021).

192. Rill, M. S., Plet, C., Thiel, M., *et al.* Photonic metamaterials by direct laser writing and silver chemical vapour deposition. *Nature materials* **7,** 543–546 (2008).

193. Gansel, J. K., Thiel, M., Rill, M. S., *et al.* Gold helix photonic metamaterial as broadband circular polarizer. *science* **325,** 1513–1515 (2009).

194. Thiel, M., Rill, M. S., von Freymann, G., *et al.* Three-dimensional bi-chiral photonic crystals. *Advanced Materials* **21,** 4680–4682 (2009).

195. Ergin, T., Stenger, N., Brenner, P., *et al.* Three-dimensional invisibility cloak at optical wavelengths. *science* **328,** 337–339 (2010).

196. Bi, K., Qingmin, W., Jianchun, X., *et al.* All-Dielectric Metamaterial Fabrication Techniques. *Advanced Optical Materials* **9,** 2001474 (2020).

197. Walia, S., Shah, C., Gutruf, P., *et al.* Flexible metasurfaces and metamaterials: A review of materials and fabrication processes at micro- and nano-scales. *Applied Physics Reviews* **2,** 011303 (2015).

198. Busch K. Lölkes S., W. R. & H., F. *Photonic Crystals: Advances in Design, Fabrication, and Characterization* 2nd ed. (Wiley, 2006).

199. Stoian, R. & Colombier, J.-P. Advances in ultrafast laser structuring of materials at the nanoscale. *Nanophotonics* **9,** 4665–4688 (2020).

200. Meany, T., Gräfe, M., Heilmann, R., *et al.* Laser written circuits for quantum photonics. *Laser & Photonics Reviews* **9,** 363–384 (2015).

201. Gross, S. & Withford, M. Ultrafast-laser-inscribed 3D integrated photonics: challenges and emerging applications. *Nanophotonics* **4,** 332–352 (2015).

202. Corrielli, G., Crespi, A. & Osellame, R. Femtosecond laser micromachining for integrated quantum photonics. *Nanophotonics* **10,** 3789–3812 (2021).

203. Royon, A., Bourhis, K., Bellec, M., *et al.* Silver clusters embedded in glass as a perennial high capacity optical recording medium. *Advanced materials* **22,** 5282–5286 (2010).

204. Hecht, E. *Optics* (Pearson, 2012).

205. Alqurashi, T., Penchev, P., Yetisen, A. K., *et al.* Femtosecond laser directed fabrication of optical diffusers. *RSC advances* **7,** 18019–18023 (2017).

206. Kulchin, Y. N., Vitrik, O., Kuchmizhak, A., *et al.* Through nanohole formation in thin metallic film by single nanosecond laser pulses using optical dielectric apertureless probe. *Optics letters* **38,** 1452–1454 (2013).

207. Velpula, P. K., Bhuyan, M., Courvoisier, F., *et al.* Spatio-temporal dynamics in nondiffractive Bessel ultrafast laser nanoscale volume structuring. *Laser & Photonics Reviews* **10,** 230–244 (2016).

208. Will, M., Nolte, S., Chichkov, B. N., *et al.* Optical properties of waveguides fabricated in fused silica by femtosecond laser pulses. *Applied Optics* **41,** 4360–4364 (2002).

209. He, J., Xu, B., Xu, X., *et al.* Review of femtosecond-laser-inscribed fiber Bragg gratings: fabrication technologies and sensing applications. *Photonic Sensors* **11,** 203–226 (2021).

210. Lee, W., Pruzinsky, S. A. & Braun, P. V. Multi-photon polymerization of waveguide structures within three-dimensional photonic crystals. *Advanced Materials* **14,** 271–274 (2002).

211. Geng, Q., Wang, D., Chen, P., *et al.* Ultrafast multi-focus 3-D nano-fabrication based on two-photon polymerization. *Nature communications* **10,** 2179 (2019).

212. Harb, J., Talbot, L., Petit, Y., *et al.* Demonstration of Type A volume Bragg gratings inscribed with a femtosecond Gaussian-Bessel laser beam. *Optics Express* **31,** 15736–15746 (2023).

213. Durnin, J. Exact solutions for nondiffracting beams. I. The scalar theory. *J. Opt. Soc. Am. A* **4,** 651–654 (1987).

214. Durnin, J., Miceli, J. J. & Eberly, J. H. Diffraction-free beams. *Phys. Rev. Lett.* **58,** 1499–1501 (1987).

215. Stoyanov, L., Zhekova, M., Stefanov, A., *et al.* Generation of long range low-divergent Gauss–Bessel beams by annihilating optical vortices. *Optics Communications* **480,** 126510 (2021).

216. Rao, A. S. & Samanta, G. K. On-axis intensity modulation-free, segmented, zero-order Bessel beams with tunable ranges. *Opt. Lett.* **43,** 3029–3032 (2018).

217. Utéza, O., Blandin, P., Charmasson, L., *et al. ASUR: Plateforme d'Applications des Sources laser Ultra-Rapides pour l'imagerie X et l'interaction laser-matière* in *UVX 2012-11e Colloque sur les Sources Cohérentes et Incohérentes UV, VUV et X; Applications et Développements Récents* (2013), 01004. doi:10.1051/uvx/201301004.

218. Liu, X., Clady, R., Grojo, D., *et al.* Engraving Depth-Controlled Nanohole Arrays on Fused Silica by Direct Short-Pulse Laser Ablation. *Advanced Materials Interfaces* **10,** 2202189 (2023).

219. Durnin, J., Miceli, J. J. & Eberly, J. H. Durnin, Miceli, and Eberly reply. *Phys. Rev. Lett.* **66,** 838 (1991).

220. McGloin, D. & Dholakia, K. Bessel beams: Diffraction in a new light. *Contemporary Physics* **46,** 15–28 (2005).

221. Lamperti, M., Jukna, V., Jedrkiewicz, O., *et al.* Invited Article: Filamentary deposition of laser energy in glasses with Bessel beams. *APL Photonics* **3,** 120805 (2018).

222. Gaizauskas, E., Vanagas, E., Jarutis, V., *et al.* Discrete damage traces from filamentation of Gauss-Bessel pulses. *Opt. Lett.* **31,** 80–82 (2006).

223. Vetter, C., Giust, R., Furfaro, L., *et al.* High aspect ratio structuring of glass with ultrafast Bessel beams. *Materials* **14,** 6749 (2021).

224. Bhuyan, M. K., Courvoisier, F., Lacourt, P.-A., *et al.* High aspect ratio taper-free microchannel fabrication using femtosecond Bessel beams. *Opt. Express* **18,** 566–574 (2010).

225. Meyer, R., Froehly, L., Giust, R., *et al.* Extremely high-aspect-ratio ultrafast Bessel beam generation and stealth dicing of multi-millimeter thick glass. *Applied Physics Letters* **114,** 201105 (2019).

226. Courvoisier, F., Stoian, R. & Couairon, A. Ultrafast laser micro-and nano-processing with nondiffracting and curved beams: invited paper for the section: hot topics in ultrafast lasers. *Optics & Laser Technology* **80,** 125–137 (2016).

227. Siegman, A. *Lasers* (University Science Books, 1986).

228. Raciukaitis, G., Brikas, M., Gecys, P., *et al.* Use of high repetition rate and high power lasers in microfabrication: How to keep the efficiency high? *JLMN Journal of Laser Micro/Nanoengineering* **4,** 186–191 (2009).

229. Breitling, D., Ruf, A. & Dausinger, F. Fundamental aspects in machining of metals with short and ultrashort laser pulses. *Proc SPIE* **5339,** 49–63 (2004).

230. Boulmer-Leborgne, C., Hermann, J. & Dubreuil, B. Plasma formation resulting from the interaction of a laser beam with a solid metal target in an ambient gas. *Plasma Sources Science and Technology* **2,** 219 (1993).

231. Brzobohatỳ, O., Čižmár, T. & Zemánek, P. High quality quasi-Bessel beam generated by round-tip axicon. *Optics express* **16,** 12688–12700 (2008).

232. Dudutis, J., Stonys, R., Račiukaitis, G., *et al.* Glass dicing with elliptical Bessel beam. *Optics & Laser Technology* **111,** 331–337 (2019).

233. Čižmár, T. & Dholakia, K. Tunable Bessel light modes: engineering the axial propagation. *Optics express* **17,** 15558–15570 (2009).

234. Saleh, B. E. A. & Teich, M. C. *Fundamentals of Photonics* 1st ed. (John Wiley & Sons, Ltd, 1991).

235. Bravo-Abad, J., Degiron, A., Przybilla, F., *et al.* How light emerges from an illuminated array of subwavelength holes. *Nature Physics* **2,** 120–123 (2006).

236. Li, M., Ling, J., He, Y., *et al.* Lithium niobate photonic-crystal electro-optic modulator. *Nature Communications* **11,** 4123 (2020).

237. Bhuyan, M. K., Courvoisier, F., Jacquot, M., *et al. Femtosecond non-diffracting Bessel beams and controlled nanoscale ablation* in *2011 XXXth URSI General Assembly and Scientific Symposium* (2011), 1–3. doi:10.1109/URSIGASS.2011.6050591.

238. Bhuyan, M. K., Courvoisier, F., Lacourt, P.-A., *et al.* High aspect ratio taper-free microchannel fabrication using femtosecond Bessel beams. *Opt. Express* **18,** 566–574 (2010).

239. Liu, J.-M. Simple technique for measurements of pulsed Gaussian-beam spot sizes. *Optics letters* **7,** 196–198 (1982).

240. Ben-Yakar, A., Harkin, A., Ashmore, J., *et al.* Thermal and fluid processes of a thin melt zone during femtosecond laser ablation of glass: The formation of rims by single laser pulses. *J. Phys. D: Appl. Phys* **40,** 1447–1459 (2007).

241. Stoian, R., Ashkenasi, D., Rosenfeld, A., *et al.* Coulomb explosion in ultrashort pulsed laser ablation of Al_2O_3. *Physical review B* **62,** 13167 (2000).

242. Gamaly, E. G., Rode, A. V., Luther-Davies, B., *et al.* Ablation of solids by femtosecond lasers: Ablation mechanism and ablation thresholds for metals and dielectrics. *Physics of plasmas* **9,** 949–957 (2002).

243. Bulgakova, N., Stoian, R., Rosenfeld, A., *et al.* Electronic transport and consequences for material removal in ultrafast pulsed laser ablation of materials. *Physical Review B* **69,** 054102 (2004).

244. Bulgakova, N., Stoian, R., Rosenfeld, A., *et al.* A general continuum approach to describe fast electronic transport in pulsed laser irradiated materials: The problem of Coulomb explosion. *Applied Physics A* **81,** 345–356 (2005).

245. De La Rue, R. M. & Seassal, C. Photonic crystal devices: some basics and selected topics. *Laser & Photonics Reviews* **6,** 564–597 (2012).

246. Su, V., Chu, C. H., Sun, G., *et al.* Advances in optical metasurfaces: fabrication and applications. *Optics express* **26,** 13148–13182 (2018).

247. Chen, M. K., Wu, Y., Feng, L., *et al.* Principles, functions, and applications of optical meta-lens. *Advanced Optical Materials* **9,** 2001414 (2021).

248. Shi, Y., Wan, C., Dai, C., *et al.* Augmented reality enabled by on-chip metaholography multiplexing. *Laser & Photonics Reviews* **16,** 2100638 (2022).

249. Pan, M., Fu, Y., Zheng, M., *et al.* Dielectric metalens for miniaturized imaging systems: progress and challenges. *Light: Science and Applications* **11,** 195 (2022).

250. Lee, D., Gwak, J., Badloe, T., *et al.* Metasurfaces-based imaging and applications: from miniaturized optical components to functional imaging platforms. *Nanoscale Advances* **2,** 605–625 (2020).

251. Xu, B.-B., Wang, L., Ma, Z.-C., *et al.* Surface-plasmon-mediated programmable optical nanofabrication of an oriented silver nanoplate. *Acs Nano* **8,** 6682–6692 (2014).

252. Soukoulis, C. & Wegener, M. Past achievements and future challenges in the development of three-dimensional photonic metamaterials. *Nature Photonics* **5,** 523–530 (2011).

253. Jeong, H. Y., Lee, E., An, S.-C., *et al.* 3D and 4D printing for optics and metaphotonics. *Nanophotonics* **9,** 1139–1160 (2020).

254. Guo, R., Li, Z., Jiang, Z., *et al.* Log-pile photonic crystal fabricated by two-photon photopolymerization. *Journal of Optics A: Pure and Applied Optics* **7,** 396 (2005).

255. Ergin, T., Stenger, N., Brenner, P., *et al.* Three-Dimensional Invisibility Cloak at Optical Wavelengths. *Science (New York, N.Y.)* **328,** 337–9 (2010).

256. Beresna, M., Gecevičius, M. & Kazansky, P. G. Ultrafast laser direct writing and nanostructuring in transparent materials. *Advances in Optics and Photonics* **6,** 293–339 (2014).

257. Chambonneau, M., Grojo, D., Tokel, O., *et al.* In-Volume Laser Direct Writing of Silicon—Challenges and Opportunities. *Laser & Photonics Reviews* **15,** 2100140 (2021).

258. Rapp, L., Meyer, R., Giust, R., *et al.* High aspect ratio micro-explosions in the bulk of sapphire generated by femtosecond Bessel beams. *Scientific Reports* **6,** 34286 (Sept. 2016).

259. Bhuyan, M. K., Somayaji, M., Mermillod-Blondin, A., *et al.* Ultrafast laser nanostructuring in bulk silica, a slow microexplosion. *Optica* **4,** 951–958 (2017).

260. Praveen Kumar, V., Bhuyan, M., Courvoisier, F., *et al.* Spatio-temporal dynamics in nondiffractive Bessel ultrafast laser nanoscale volume structuring. *Laser and Photonics Review* **10,** 234 (2016).

261. Rayner, D., Naumov, A. & Corkum, P. Ultrashort pulse non-linear optical absorption in transparent media. *Optics express* **13,** 3208–3217 (2005).

262. Mahmoud Aghdami, K., Rahnama, A., Ertorer, E., *et al.* Laser nano-filament explosion for enabling open-grating sensing in optical fibre. *Nature Communications* **12,** 6344 (2021).

263. Genevet, P., Capasso, F., Aieta, F., *et al.* Recent advances in planar optics: From plasmonic to dielectric metasurfaces. *Optica* **4,** 139 (2017).

264. Burr, G. W., Diziain, S. & Bernal, M.-P. The impact of finite-depth cylindrical and conical holes in lithium niobate photonic crystals. *Opt. Express* **16,** 6302–6316 (2008).

265. Centeno, E. & Cassagne, D. Graded photonic crystals. *Opt. Lett.* **30,** 2278–2280 (2005).

266. Kurt, H., Colak, E., Caglayan, H., *et al.* The focusing effect of graded index photonic crystals Related Articles Design for ultrahigh-Q position-controlled nanocavities of single semiconductor nanowires in two-dimensional photonic crystals. *Applied Physics Letters* **93,** 171108–181106 (2008).

267. Lim, S. W. D., Meretska, M. L. & Capasso, F. A High Aspect Ratio Inverse-Designed Holey Metalens. *Nano Letters* **21,** 8642–8649 (2021).

268. Mikheeva, E., Claude, J.-B., Salomoni, M., *et al.* CMOS-compatible all-dielectric metalens for improving pixel photodetector arrays. *APL Photonics* **5,** 116105 (2020).

269. Choy, T. *Effective Medium Theory: Principles and Applications* 2nd ed. (International Series of Monographs on Physics, Oxford, 2015).

270. Markel, V. A. Introduction to the Maxwell Garnett approximation: tutorial. *J. Opt. Soc. Am. A* **33,** 1244–1256 (2016).

271. Sihvola, A. Mixing rules with complex dielectric coefficients. *Subsurface sensing technologies and applications* **1,** 393–415 (2000).

272. Humlicek, J. in *Ellipsometry at the Nanoscale* (eds Losurdo, M. & Hingerl, K.) 145–178 (Springer Berlin Heidelberg, Berlin, Heidelberg, 2013). doi:10.1007/978-3-642-33956-1_3.

273. Mavidis, C. P., Tasolamprou, A. C., Economou, E. N., *et al.* Polaritonic cylinders as multifunctional metamaterials: Single scattering and effective medium description. *Physical Review B* **102,** 155310 (2020).

274. Zhu, Q., Jin, L. & Fu, Y. Graded index photonic crystals: A review. *Annalen der Physik* **527,** 205–218 (2015).

275. Kim, Y.-B., Cho, J.-W., Lee, Y.-J., *et al.* High-index-contrast photonic structures: a versatile platform for photon manipulation. *Light, science and applications* **11,** 316 (2022).

276. D'Amico, C., Troles, J., Cheng, G., *et al.* Multiscale Laser Written Photonic Structures in Bulk Chalcogenide Glasses for Infrared Light Transport and Extraction. *Photonics* **8,** 211 (2021).

277. Siew, S. Y., Li, B., Gao, F., *et al.* Review of silicon photonics technology and platform development. *Journal of Lightwave Technology* **39,** 4374–4389 (2021).

278. Boes, A., Chang, L., Langrock, C., *et al.* Lithium niobate photonics: Unlocking the electromagnetic spectrum. *Science (New York, N.Y.)* **379,** eabj4396 (2023).